分类号_____ 密级_____

UDC_____ 编号_____

华中师范大学

博士学位论文

LHC/ALICE 实验上质子-质子和铅-铅碰撞中 π^0-强子关联和直接光子-强子关联的研究

学位申请人姓名: 朱祥荣

申请学位学生类别: 全日制博士

申请学位学科专业: 粒子物理与原子核物理

指导教师姓名: 周代翠 博士 教授

Constantinos Loizides 博士

殷中宝 博士 教授

博士学位论文

LHC/ALICE 实验上质子-质子和铅-铅碰撞中 π^0-强子关联和直接光子-强子关联的研究

论文作者：朱祥荣

指导教师：周代翠　博士　教授

Constantinos Loizides　博士

殷中宝　博士　教授

学科专业：粒子物理与原子核物理

研究方向：高能重离子碰撞实验

华中师范大学物理科学与技术学院

2014 年 5 月

博士学位论文
DOCTORAL DISSERTATION

Dissertation

Two-Particle Correlations with Neutral Pion and Direct Photon Triggers in pp and Pb+Pb Collisions with ALICE at the LHC

By

Xiangrong Zhu

Supervisors: Prof. Dr. Daicui Zhou

Dr. Constantinos Loizides

Prof. Dr. Zhongbao Yin

Specialty: Particle Physics and Nuclear Physics

Research Area: Heavy-Ion Collisions Experiment

College of Physical Science and Technology

Central China Normal University

May 2014

华中师范大学学位论文原创性声明和使用授权说明

原创性声明

本人郑重声明：所呈交的学位论文，是本人在导师指导下，独立进行研究工作所取得的研究成果。除文中已经标明引用的内容外，本论文不包含任何其他个人或集体已经发表或撰写过的研究成果。对本文的研究做出贡献的个人和集体，均已在文中以明确方式标明。本声明的法律结果由本人承担。

作者签名：　　日期：　　年　　月　　日

学位论文版权使用授权书

学位论文作者完全了解华中师范大学有关保留、使用学位论文的规定，即：研究生在校攻读学位期间论文工作的知识产权单位属华中师范大学。学校有权保留并向国家有关部门或机构送交论文的复印件和电子版，允许学位论文被查阅和借阅；学校可以公布学位论文的全部或部分内容，可以允许采用影印、缩印或其它复制手段保存、汇编学位论文。（保密的学位论文在解密后遵守此规定）

保密论文注释：本学位论文属于保密，在 ____ 年解密后适用本授权书。

非保密论文注释：本学位论文不属于保密范围，适用本授权书。

作者签名：　　导师签名：

日期：　　年　　月　　日　　日期：　　年　　月　　日

本人已经认真阅读“CALIS 高校学位论文全文数据库发布章程”,同意将本人的学位论文提交“CALIS 高校学位论文全文数据库”中全文发布,并可按“章程”中的规定享受相关权益。同意论文提交后滞后：□半年；□一年；□二年发布。

作者签名：　　导师签名：

日期：　　年　　月　　日　　日期：　　年　　月　　日

Dedicated to
my beloved mother, father
and to my beloved wife Kangfang

谨献给我最亲爱的父母，妻子！

摘　　要

自古以来，物质微观结构一直都是人类感兴趣并探寻的对象。从古希腊哲学家德谟克利特(Democritus)猜想的原子不可分论到 1803 年英国物理学家约翰·道尔顿(John Dalton)依据“倍比定律”提出的近代原子论，再到 1897 年英国物理学家约瑟夫·约翰·汤姆逊(Joseph John Thomson)通过测量阴极射线的荷质比发现电子以及 1911 年英国物理学家欧内斯特·卢瑟福 (Ernest Rutherford)通过α粒子散射实验提出的原子有核模型，再到之后通过各种实验陆续发现的质子、中子、夸克……。所有这些才使人们逐渐清晰地认识到：原子是由原子核和核外电子组成，原子核又是由质子和中子组成，而质子和中子又是由一定相互作用禁闭在其内的夸克与胶子组成等等。

目前普遍的观点认为，构成物质的基本粒子分为三代夸克(quark)及其反夸克(anti-quark)和三代轻子(lepton)，且这些基本粒子间通过传递胶子(gluon)、$W^{\pm}$和Z^0玻色子($W^{\pm}$ Z^0 boson)及光子发生对应的强、弱和电磁相互作用。近代物理建立了一套描述这些基本粒子及它们间的基本相互作用的理论－标准模型(Standard Model)。该模型对诸多实验结果都给出了合理的解释，同时它预言的一种解释基本粒子质量之源的粒子－希格斯玻色子(Higgs boson)，也已于 2012 年在欧洲核子研究组织(European Organization for Nuclear Research, CERN)的大型强子对撞机(Large Hadron Collider, LHC)实验中发现。在这个标准模型中，夸克胶子(部分子)间发生的强相互作用通过规范学理论－量子色动力学(Quantum ChromoDynamics, QCD)给予描述。量子色动力学存在三个显著的基本特性：1)禁闭(confinement)，在普通环境中，因部分子间交换的横动量小，强相互作用很强(耦合常数(α_s)大)，因此，夸克与胶子都被禁闭在强子内部；2)渐近自由(asymptotic freedom)，当交换的横动量越大或夸克间距离越小时，强相互作用越弱(耦合常数(α_s)越小)。在渐近自由状态下，部分子间的相互作用是微扰的。3）手征对称性恢复(chiral symmetry restoration)，希望在 QGP 物质中手征对称性是恢复的，这意味着在极端环境中夸克质量趋近于零。基于量子色动力学，采用格点方法发展的另一理论－格点量子色动力学(Lattice QCD)预言在极端高温和/或高重子数密度的条件下，禁闭在普通强子内的部分子将发生退禁闭形成一种由处于渐近自由状态的夸克和胶子组成的新物质相－夸克-胶子等离子体(Quark-Gluon Plasma, QGP)。众多研究结果表明，宇宙大爆炸早期因形成极高温的环境而可能产生这种新物质相，或在中子星内因其具有极高的重子数密度而可能存在该物质相。基于此，寻找 QGP 形成的特征信号并研究其相关特性对理解强相互作用和宇宙早期形成及演化具有重要意义。但是，随着宇宙大爆炸后极长时间的

演化，其早期信息已很难被提取，且探测遥远中子星内部亦充满巨大的挑战，因此如何在现有实验条件下通过实验产生 QGP 这种新物质相一直是科学家们思考的问题。

高能重离子碰撞被认为是在现有实验条件下实现从强子相退禁闭到 QGP 相的一种可行途径。在高能重离子碰撞实验中，两重离子束流被加速到接近光速，然后实现对撞并将大部分能量沉积在碰撞区域，这使得在碰撞区域内产生能够发生退禁闭相变所需的超高能量密度，进而在碰撞区域内产生由渐近自由夸克和胶子组成的 QGP 热密物质。随着时间推移，产生的 QGP 物质系统迅速膨胀并通过强子化形成最后实验上能够观测到的各种粒子。自上世纪 60 年代，科学家们相继建造了一系列重离子加速器，如交变梯度同步加速器(Alternating Gradient Synchrotron, AGS)、超质子同步加速度器(Super Proton Synchrotron, SPS)和相对论重离子对撞机(Relativistic Heavy Ion Collider, RHIC)，并在 QGP 特征信号的寻找及相关性质的研究方面取得了丰硕成果。欧洲核子研究组织建造了目前世界上最大的大型强子对撞机，并于 2009 年底正式运行。作为 LHC 上四大实验之一的大型重离子对撞实验(A Large Ion Collider Experiment, ALICE)，其中各子探测器的设计和性能都为重离子碰撞研究提供了前所未有的优越条件。在 2010 年运行的铅－铅碰撞中，其质心系能量达到$\sqrt{s_{NN}}$ = 2.76 TeV，该能量相当于 RHIC 最高碰撞能量的～14 倍，因此碰撞所形成的 QGP 物质相比于 RHIC 能区将持续时间更长且体积更大，这为全面而深入地研究 QGP 物质的特性提供了更加优越的条件。重离子碰撞中形成的 QGP 只存在于碰撞后的瞬间，然后就碎裂成末态强子，因此几乎不可能从实验上直接观察到 QGP 物质相，而只能通过对末态粒子的各种观察量来判断 QGP 形成并研究其相关性质。到目前为止，被认为在重离子碰撞中可能形成了 QGP 的特征信号主要有：奇异粒子的增加(Strangeness enhancement)、J/ψ 的产额压低、直接光子与热双轻子、喷注淬火(Jet quenching)、集体流(Collective flow)等等。

末态两粒子间的方位角关联被认为是研究热密物质效应的成功方法之一。该测量方法通常选取两类粒子，一类具有高横动量的粒子称作“触发粒子”，其被认为是来自于一个喷注中的领头粒子，另一类具有较低的横动量粒子称作“伴随粒子”，它可能来自于喷注中的其他粒子，也可能来自于其他信号，如集体流等。在 RHIC 和 LHC 上，相比于质子-质子碰撞中的关联分布，核－核中心碰撞中高横动量区粒子间关联在远端(away side)存在压低甚至消失，以及低横动量区关联远端出现增宽，双峰结构和近端(near side)的“脊”。这些测量结果都可解释为热密物质的相互作用，并间接表明核－核碰撞中形成了夸克－胶子等离子体这种新物质相。当触发粒子选取的是直接光子时，这种两粒子关联分析到了碰撞

中硬散射过程形成的光子－喷注事件。这类事件中，领头阶的直接光子通过夸克胶子的康普顿散射或正反夸克湮灭产生于碰撞初期的硬散射过程，这使得直接光子与其背对部分子在初始动量大小上近似平衡。同时光子的平均自由程很大且当它穿越碰撞形成的 QGP 相时与相中其他粒子只发生电磁相互作用，由此直接光子携带了碰撞初期的相关信息。当测量背对部分子碎裂的末态强子与直接关子的关联时，又可以获取部分子穿越密度物质后的相关信息，如介质效应作用下的部分子碎裂函数，进而研究密度物质的相关性质。

本文基于 LHC/ALICE 的电磁量能器(EMCal)和中心桶部径迹探测系统，利用中性粒子(中性π介子和光子)与强子关联，分析研究热密物质的介质效应，同时测量部分子碎裂函数。在中性π介子(π^0)－强子关联分析中，基于质心系能量$\sqrt{s_{NN}}$ = 2.76 TeV 的质子－质子与铅－铅碰撞数据，通过构建电磁量能器测量的π^0与径迹探测系统测量的带电强子在方位角上的关联，测量π^0－带电强子方位角分布函数和铅－铅中心碰撞中每π^0触发的带电强子产额在关联近端与远端的修正因子$I_{AA}=Y_{PbPb}/Y_{pp}$。分析结果显示在近端区这个修正因子存在～1.2 倍的增强，而在远端区则存在～0.6 倍的压低。这个结果可以用于研究热密物质的喷注淬火机制和部分子碎裂函数的改变。其中近端区的增强反应了近端部分子受热密物质的作用，这种作用主要体现在以下三点：1）受热密物质作用，近部部分子的碎裂函数被改变；2）因对热密物质的不同耦合导致末态夸克与胶子喷注比例发生变化；3）因触发粒子π^0的选择导致能量损失后的部分子谱存在偏离(bias)。而远端区的压低则是因远端部分子穿越热密物质过程中损失部分能量导致末态粒子在高横动量区内的产额压低。在直接光子－强子关联分析中，基于质心系能量为$\sqrt{s}$ = 7 TeV 的质子－质子碰撞数据，分别通过孤立分析技术和统计减除方法提取直接光子信号并与带电强子构建方位角关联，进而通过分析非平衡参数$x_E=-\vec{p}_T^{\,\gamma}\cdot\vec{p}_T^{\,h}/|\vec{p}_T^{\,\gamma}|^2$测量部分子碎裂函数。孤立分析技术是基于领头阶的直接光子周围没有或只有很少的粒子，采用该方法测量了横动量在$8.0<p_T<25.0$ GeV/c 的部分子的碎裂函数，并与理论计算进行比较。而统计减除的分析方法则是基于全部光子由直接光子和来自强子的衰变光子组成，通过从全部光子中减除强子衰变的光子的贡献而获取直接光子信号。因目前$\sqrt{s}$ = 7 TeV 质子－质子碰撞数据统计量的局限，很难利用统计减除方法提取到有意义的直接光子－强子关联分布，但本论文中的分析工作建立了统计减除方法在 ALICE 实验上的应用，当下次运行达到足够统计量时，我们可以很快采用该方法测量直接光子－强子关联分布并研究部分子碎裂函数和热密物质效应。

本论文的章节安排如下：在第一章中，将简单介绍标准模型的相关内容，包括最新发现的解释质量之源的希格斯玻色子、量子色动力学， 同时也给出了高

能重离子碰撞中格点 QCD 对相变的预言和 QCD 相图的相关内容。而在第二章中，我们将介绍与重离子碰撞相关的物理内容，包括相对论重离子碰撞的时空演化，碰撞中软、硬过程中的粒子产生及影响。 同时在这章中还总结了部分来自于 SPS，RHIC 和 LHC 能区表征重离子碰撞中形成了 QGP 热密物质相的特征信号。作为本论文工作的分析基础，我们将在第三章介绍 ALICE 实验探测器，ALICE 实验数据获取与分析的在线和离线系统。同时还将讨论与本工作物理分析相关的数据分析软件框架。 第四章里则阐述了两粒子关联的分析方法并总结了之前实验中测量到的强子－强子，中性π介子－强子以及直接光子－强子关联结果，这也是本论文工作物理分析的参考基础。而在接下的第五章到第七章，我们将对实验数据的选取，中性π介子－强子关联与直接光子－强子关联分析与处理过程以及测量结果进行详尽的讨论。其中在第五章中将介绍与本论文工作直接相关的数据事件、中心粒子团簇(cluster)及带电粒子径迹的选择标准。第六章中则详细讨论基于质心系能量$\sqrt{s_{NN}}$ = 2.76 TeV 的质子－质子和铅－铅碰撞数据的中性π介子鉴别及其触发的强子关联测量。利用孤立分析技术和统计减除方法提取质心系能量$\sqrt{s}$ =7 TeV 质子－质子碰撞数据中的直接光子－强子关联并测量部分子碎裂函数的分析细节将在第七章中给予详细的论述。最后第八章，我们将对本论文工作的分析方法与结果进行讨论和展望。

关键字：超相对论重离子碰撞，大型强子对撞机，大型重离子碰撞实验，夸克－胶子等离子体，热密介质效应，两粒子关联，中性π介子(π^0)，直接光子，部分子碎裂函数

Abstract

Since a long time ago, the ultimate constituents of matter have always puzzled the mankind and been researching. It began with the theory of *atomism* (indestructible atom) speculated by Democritus, a philosopher of ancient Greece, followed by the modern atomic theory proposed by John Dalton with the *law of multiple proportions* in 1803. In the early 20th century, the electron was discovered by J. J. Thomson through the measurement of *mass to charge ratio* in his explorations on the properties of cathode rays, and Ernest Rutherford theorized that atoms have their charge concentrated in a very small nucleus through his discovery and interpretation of *Rutherford scattering* with the gold foil experiment. With more experiments built for researching, more particles, such as proton, neutron and quark, are discovered in succession. All the discoveries let us clearly know that the atom consists of the nucleus and electrons, the nucleus is made up of protons and neutrons which are composed of fundamental particles, quarks and gluons.

Currently, it is widely known that the ultimate constitutes of the matter are three generation quarks, their anti-quarks and three leptons. These fundamental particles have strong, weak and electromagnetic interactions by mediating gluons, $W^{\pm}$ and Z^0 bosons, and photons. A famous theory, Standard Model(SM), established to describe the electromagnetic, weak, and strong nuclear interactions and the fundamental particles, is success in explaining a wide variety of experimental results. The strong force of quarks and gluons is described by a theory of Quantum Chromodynamics (QCD). Three significant features, *confinement*, *asymptotic freedom* and *chiral symmetry restoration*, reveal the main characteristics of QCD. The strong interaction increases or the coupling constant α_s describing the strong interaction strength becomes larger with the momentum transfer decreasing. Therefore, the quarks and gluons are confined in the hadrons in the normal world with low momentum transfers, known as *confinement*. The second feature is called *asymptotic freedom*. According to the asymptotic freedom, the coupling constant α_s becomes smaller and the interaction is perturbative with the momentum transfer increasing (equivalently at short distances). The third characteristic associated with QCD is *chiral symmetry restoration*. The chiral symmetry exists as an exact symmetry only when the mass parameter of a quark is strictly zero. At low energy region, Lattice QCD is a well-established non-perturbative approach to solving the quantum chromodynamics theory of quarks and gluons. According to the Lattice QCD prediction, a new matter, *Quark-Gluon Plasma* (QGP), which consists of decon-

fined quarks and gluons, is excepted to be created at extremely high temperature and/or high baryons density. More results demonstrate that the QGP matter may be created in the universe after a microsecond of the Big Bang due to the formed extremely high temperature or in the interior of the neutron stars with high baryons density. Therefore, it is great significant to search for the characteristic signatures of the QGP and research its properties for understanding the evolution and formation of the early stages of the universe. However, it is impossible to extract directly the signatures of the early stages of the universe due to its long time evolution and explore the interior of the neutron stars. So how to create the QGP matter under the normal laboratory conditions is a great challenge.

Ultra-relativistic heavy-ion collision experiment is considered as an available approach to producing the QGP phase. In the heavy-ion collisions, two Lorentz contracted nuclei approach to each other with velocities nearly equal to the velocity of light and have colliding. In the colliding instant, both contracted nuclei pass through each other in the region of geometrical overlap. Many processes of parton-parton hard scatterings occur in the overlap region, which result in depositing a large amount of energy in a limit volume. The energy density is so high that a new matter state consisting of defined quarks and gluons is created. Since 1960's, a series of heavy ion accelerators, such as Alternating Gradient Synchrotron (AGS), Super Proton Synchrotron (SPS) and Relativistic Heavy Ion Collider (RHIC), have been built to search for the QGP signatures and research its properties.

In European Organization for Nuclear Research (CERN), the current biggest accelerator, Large Hadron Collider (LHC), was designed at 1998 and run successfully at the end of 2009. As one of four experiments, A Large Ion Collider Experiment (ALICE), whose aim is to study the physics of the strongly interacting matter at extreme energy densities. The centre-of-mass energy of $\sqrt{s_{\rm NN}} = 2.76$ TeV of Pb+Pb collisions running in 2010 is about 14 higher than the highest energy of RHIC. Hence, it is excepted that the QGP created at LHC has longer lifetime and larger volume than at RHIC. This provides much better conditions for searching for the QGP and studying its properties. In the heavy-ion collisions, the formed QGP only exists in a short time and then fragment into a great variety of final hadrons. In this case, we can only study the QGP phase by different measurements from the final particles. Up to now, some main measurements which are considered as the signatures of the formation of the QGP are strangeness enhancement, suppression of J/ψ production, direct photons and thermal di-leptons, jet quenching, collective flow, and so on.

Two-particles correlation is considered as a powerful probe for understanding the

properties of the strongly interacting hot and dense medium. In such an analysis, a particle is chosen from higher p_{T} region and called the *trigger particle*, which is presumably from jet fragmentations. The so called *associated particles* from lower p_{T} region are always from the other fragmentation of the jet, or another production, such as collective flow. At RHIC and LHC, the measurements of the azimuthal angle distribution from two-particle correlations in A+A collisions show a strong suppression even disappeared at the high p_{T} and enhancement with double-peak at the low p_{T} on the away side, and "ridge" structure in pseudo-rapidity direction at the low p_{T} on the near side compared to pp collisions. All the measurements can be explained as the effects of the hot and dense medium, and imply the Quark-Gluon Plasma is indeed formed in the heavy-ion collisions. When the direct photon is selected as the trigger particle, the correlations probably tag the γ-jet events produced from the QCD Compton scattering process, $q+g \rightarrow q+\gamma$ and $q+\bar{q} \rightarrow g+\gamma$ annihilation process. In these processes, the photons momenta in the center-of-mass frame are approximately balanced by that of the recoil partons. The photons do not occur energy loss when going through the medium due to only electromagnetic interactions happen between photons and other particles because of the large mean free path of photons. The fragments of the recoil partons have rich information, such as the parton fragmentation function with the medium effects, due to the interactions of the recoil partons and medium.

In this thesis, the medium effects and the parton fragmentation function are measured by π^0-hadron correlations and direct photon-hadron correlations, where the π^0 and photons are detected by the electromagnetic calorimeters (EMCal) and the charged hadrons are reconstructed by the central barrel detector system. In the π^0-hadron correlations, the azimuthal angle distribution of the correlations and the per-trigger yield modification factor, $I_{\mathrm{AA}} = \frac{Y^{\mathrm{PbPb}}}{Y^{\mathrm{pp}}}$, on the near side and away side are measured in pp and Pb+Pb collisions at $\sqrt{s_{\mathrm{NN}}} = 2.76$ TeV. In central Pb+Pb collisions, an away side suppression from in-medium energy loss is observed ($I_{\mathrm{AA}} \approx 0.6$), which is from the effects of partons energy loss. Moreover, there is an enhancement above unity of ($I_{\mathrm{AA}} \approx 1.2$) on the near side which has not been observed with any significance at lower collision energies. The significant near side enhancement of I_{AA} in the p_{T} region observed shows that the near side parton is also subject to medium effects. I_{AA} is sensitive to (i) a change of the fragmentation function, (ii) a possible change of the quark/gluon jet ratio in the final state due to the different coupling to the medium, and (iii) a bias on the parton p_{T} spectrum after energy loss due to the trigger particle selection. In the direct photon-hadron

correlations, both isolation technique and statistical subtraction method are used to extract the direct photons and measure the azimuthal angle distribution of the correlations and the parton fragmentation function in pp at $\sqrt{s}$ = 7 TeV. The isolation technique used for the analysis is based on the physics that there is no particle or only a few particles around the leading order direct photons. The parton fragmentation function is measured and compared to the theory calculations at $8.0 < p_{\mathrm{T}}^{iso,\gamma} < 25.0$ GeV/c. The statistical subtraction method is based on the fact that all photons consist of direct photons and decay photons from hadrons decay. Since there is no enough statistics of pp collisions at $\sqrt{s}$ = 7 TeV, it is impossible to extract significant results with the statistical subtraction method. But the work in this thesis develops the method in ALICE data analysis, which can be used quickly for measuring the parton fragmentation function and studying the medium effects in the next running.

This thesis is organized as follows: Chapter 1 presents the Standard Model of the particle physics including the description of the Higgs boson and the Quantum Chromodynamics, the Lattice QCD predication and the QCD phase diagram. The space-time evolution of the heavy-ion collisions and some significant measurements for searching for the QGP phase from SPS, RHIC and LHC are summarized in Chapter 2. Chapter 3 gives an overview of the ALICE experiment and a description of the ALICE online and offline systems. The analysis framework for measuring the correlations is also presented shortly in this chapter. In Chapter 4, the analysis method of two-particle correlations is introduced as well as the measurements of the correlations with the triggers as charged hadrons, neutral pions and direct photons from RHIC and LHC. From Chapter 5 to 7, the selection criteria of the analysis data, analysis details of neutral pion-hadron correlations and direct photon-hadron correlations are discussed. Chapter 5 summarizes the selection criteria of data, clusters and tracks. The π^0 identification at EMCal and its trigger correlations are presented in Chapter 6. Chapter 7 deals with the analysis of direct photon-hadron correlations extracted from the pp collisions at $\sqrt{s}$= 7 TeV with the methods of the isolation and the statistical subtraction. At last, the discussion and outlook to the work in this thesis are addressed in Chapter 8.

Keywords: ultra-relativistic heavy-ion collisions, Quark-Gluon Plasma (QGP), Large Hadron Collider (LHC), A Large Ion Collider Experiment (ALICE), medium effects, two-particle correlations, neutral pion, direct photon, parton fragmentation function

Contents

List of Figures

List of Tables

Chapter 1

Fundamental theory

Since a long time ago, a great variety of questions about the world, such as *what are the ultimate constituents of matter? How do they interact with each other?*, has puzzled the mankind. Up to now, both theoretically and experimentally one can believe that all the matter consist of elementary particles and their interactions with *strong*, *weak*, *electromagnetic* and *gravitational* at different ranges and strengths. The latest experiment results at LHC demonstrated the Higgs boson, which explains why some particles have mass and others do not, *e.g.* the $W^{\pm}$ and Z^0 bosons are very massive, whereas the photon is massless, is indeed existence and has mass about 125 GeV/c^2.

This chapter will start with a brief overview of the elements of the Standard Model in Sec. 1.1. In Sec. 1.2, a theory describing the strong interaction of color quarks and color gluons, Quantum Chromodynamics (QCD), is introduced. This is followed by the description of the Quark-Gluon Plasma (QGP) consisting of deconfined quarks and gluons in Sec. 1.3.

1.1 Standard Model of particle physics

The Standard Model (SM) [1–3] of particle physics currently provides a theoretical description to the elementary particles constituting the matter as well as their interactions including the electromagnetic interactions, the weak and strong interactions (but not gravity). The theory was firstly set up by combining the electromagnetic and weak interactions by Sheldon Glashow in 1976 and then incorporating Higgs mechanism [4–7], which is believed to give rise to the masses of all the elementary particles, by Steven Weinberg and Abdus Salam in 1967.

In the SM, there are 61 elementary particles, as summarized in Tab. 1.1 and Fig. 1.1. According to the spin of physics, these elementary particles are mainly divided into two classes, fermions with spin $\frac{1}{2}$ and bosons with spin 1. The fermions consisting of 6 leptons, *electron* (e), *electron neutrino* (ν_e), *muon* (μ), *muon neutrino* (ν_μ), *tau* (τ), *tau neutrino* (ν_τ), and 6 quarks, *up* (u), *down* (d), *charm* (c), *strange* (c), *top* (t), *bottom* (b), which can be categorized into three generations shown in Fig. 1.1, respect the Pauli Exclusion Principle. For each quark (lepton), there is also an anti-quark (anti-lepton) with same mass, opposite electric charge and opposite baryon (lepton) number. Each (anti)quark has three color charge, red, blue and green, and carries an electric charge of $-\frac{1}{3}e$ or $\frac{2}{3}e$. Particles consisting of quarks are called hadrons, which divided into mesons and baryons. Mesons consist of quark-antiquark pair, such as $\pi^+(u\bar{d})$ and $\pi^-(\bar{u}d)$, while baryons are composed of three quarks, *e.g.* p (uud) and n (ddu). Recently, two independent groups, the BESIII Collaboration [9] and the Belle Collaboration [10], announced a new strange particle consisting of four quarks ($c\bar{c}\bar{d}u$), named $Z_c(3900)$, was discovered. The stable matter are composed of the first generation as the heavy quarks and lepton of higher gen-

Elementary particles	Types	Generations	Antiparticle	Colors	Total
Quarks	2	3	Pair	3	36
Leptons	2	3	Pair	None	12
Gluons	1	1	Own	8	8
W	1	1	Pair	None	2
Z	1	1	Own	None	1
Photon	1	1	Own	None	1
Higgs	1	1	Own	None	1
Total					61

Table 1.1: Elementary particles in the Standard Model.

Interaction	Carry boson(s)	Applies to
electromagnetic	photon γ	charged particles
strong	8 gluon g	quarks
weak	$W^\pm$ and Z^0	quarks and leptons

Table 1.2: Fundamental forces and their carries in the Standard Model [11].

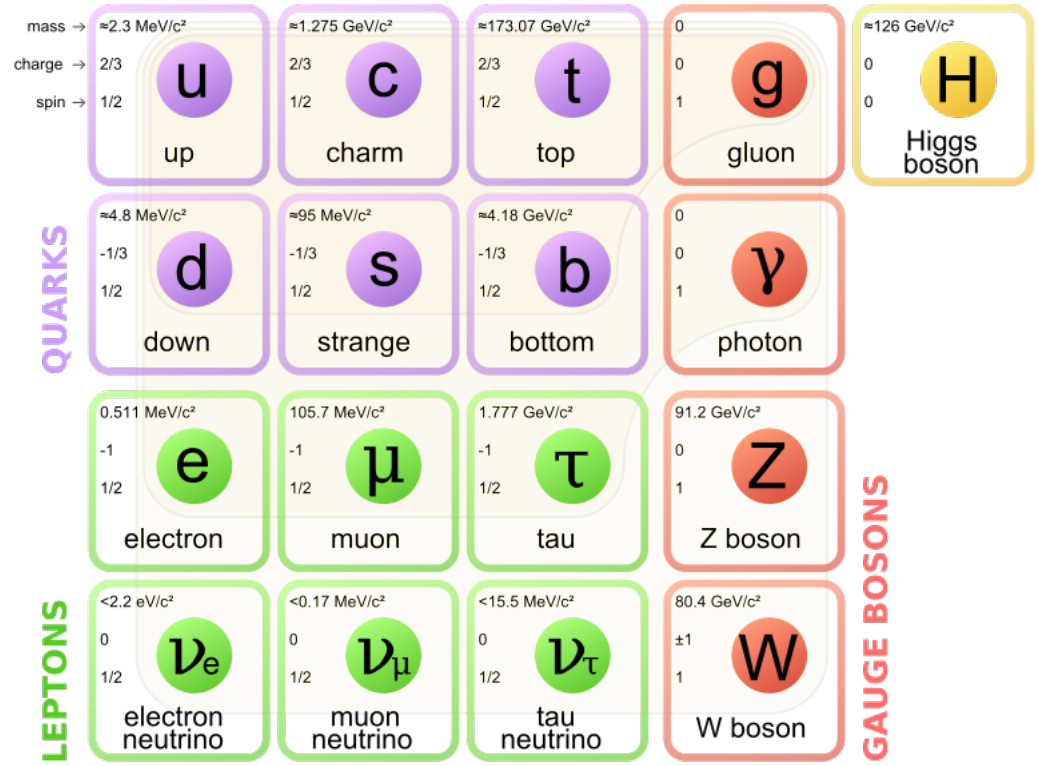

Figure 1.1: Standard Model elementary particles with three generations of matter, gauge bosons in the fourth column, and the Higgs boson in the fifth [8].

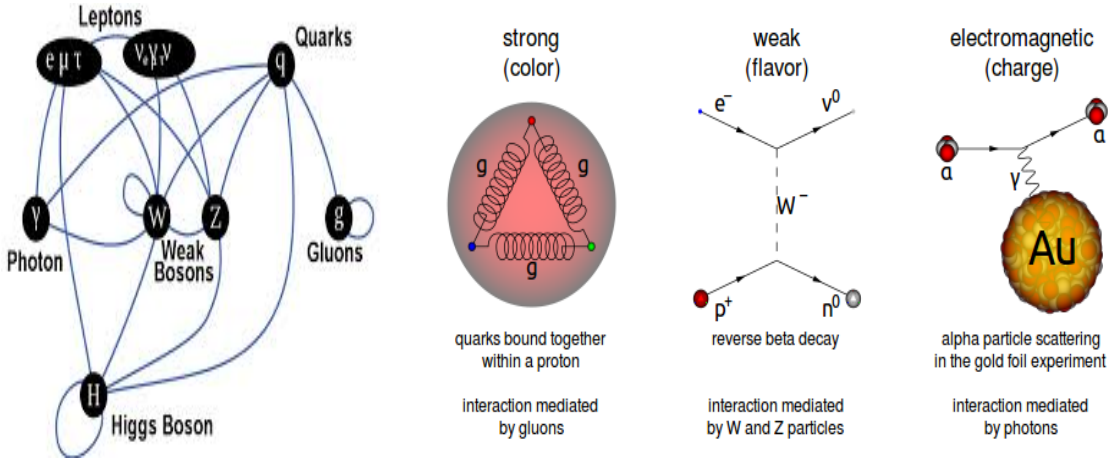

Figure 1.2: Summary of interactions between particles (first), and characterization of strong (second), weak (third) and electromagnetic (fourth) [8].

eration decay to the lighter ones immediately once created. The bosons, including photon (γ), gluon (g), $W^{\pm}$ and Z^0, are the carries of the electromagnetic, strong and weak fundamental interactions. The interactions and their carries are summarized in Tab. 1.2.

The Higgs boson was predicted to be an elementary particle by the Higgs mechanism with production modes shown in the left panel of Fig. 1.3. At LHC, The Higgs boson was firstly discovered by $H \to \gamma\gamma$ channel with mass $126.0 \pm 0.4(\text{stat}) \pm 0.4(\text{sys})$ GeV/c^2 at ATLAS [13] and $125.3 \pm 0.4(\text{stat}) \pm 0.5(\text{sys})$ GeV/c^2 at CMS [14], see the right panel in Fig. 1.3.

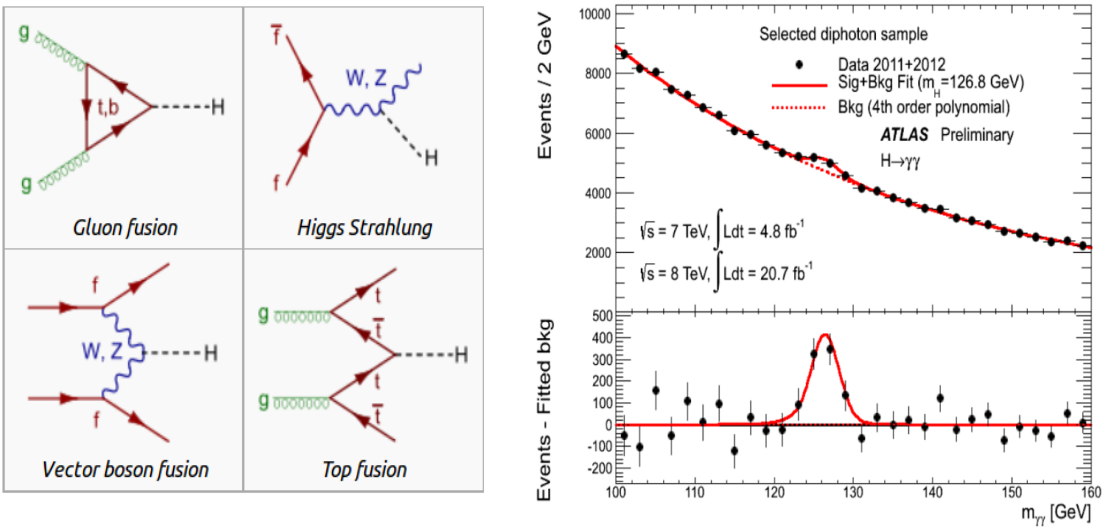

Figure 1.3: Feynman diagrams for Higgs production (left) [12] and invariant mass spectrum of two photons measured at the LHC [13].

1.2 Quantum Chromodynamics

Quantum Chromodynamics (QCD) is a theory for description of the strong interaction of color quarks and color gluons, the gluons as the quanta of the chromodynamic fild. It is analogous to the theory which describes the electromagnetic force, Quantum Electrodynamics (QED), with photons as the quanta of the Electrodynamic fild.

The Lagrangian of QCD is written as [15]:

$$\mathcal{L} = \sum_q \overline{\psi}_{q,a}(i\gamma^\mu \partial_\mu \delta_{ab} - g_s \gamma^\mu t^C_{ab} \mathcal{A}^C_\mu - m_a \delta_{ab})\psi_{q,b} - \frac{1}{4} F^A_{\mu\nu} F^{A,\mu\nu}. \tag{1.1}$$

where γ^μ is the Dirac γ-matrix which expresses the vector nature of the strong interaction with μ being a Lorentz vector index. $\psi_{q,a}$ are quark-field spinors for a quark of flavor q and mass m_q induced by the standard Higgs mechanism. The color-index, a, runs from $a = 1$ to $N_c = 3$ since the quark may be one of the three colors. The $\mathcal{A}_\mu^C$ correspond to the gluon fields with color-index C going from $C = 1$ to $N_c^2 - 1 = 8$ because of 8 types of gluons, and t_{ab}^C are the generators of the SU(3) group with eight 3×3 matrices, written as [16]:

$$\lambda^1 = \begin{pmatrix} 0 & 1 & 0 \\ 1 & 0 & 0 \\ 0 & 0 & 0 \end{pmatrix}, \lambda^2 = \begin{pmatrix} 0 & -i & 0 \\ i & 0 & 0 \\ 0 & 0 & 0 \end{pmatrix}, \lambda^3 = \begin{pmatrix} 1 & 0 & 0 \\ 0 & -1 & 0 \\ 0 & 0 & 0 \end{pmatrix}, \lambda^4 = \begin{pmatrix} 0 & 0 & 1 \\ 0 & 0 & 0 \\ 1 & 0 & 0 \end{pmatrix}$$

$$\lambda^5 = \begin{pmatrix} 0 & 0 & -i \\ 0 & 0 & 0 \\ i & 0 & 0 \end{pmatrix}, \lambda^6 = \begin{pmatrix} 0 & 0 & 0 \\ 0 & 0 & 1 \\ 0 & 1 & 0 \end{pmatrix}, \lambda^7 = \begin{pmatrix} 0 & 0 & 0 \\ 0 & 0 & -i \\ 0 & i & 0 \end{pmatrix}, \lambda^8 = \begin{pmatrix} \frac{1}{\sqrt{3}} & 0 & 1 \\ 0 & \frac{1}{\sqrt{3}} & 0 \\ 1 & 0 & \frac{-2}{\sqrt{3}} \end{pmatrix} \tag{1.2}$$

The field tensor $F_{\mu\nu}^A$ is expressed as:

$$F_{\mu\nu}^A = \partial_\mu \mathcal{A}_\nu^A - \partial_\nu \mathcal{A}_\mu^A - g_s f_{ABC} \mathcal{A}_\mu^B \mathcal{A}_\nu^C, \tag{1.3}$$

where the definition of SU(3) structure constants, f_{ABC}, are

$$[t^A, t^B] = i f_{ABC} t^C. \tag{1.4}$$

The useful color-algebra relations:

$$\begin{aligned} t_{ab}^A t_{bc}^A &= \delta_{ac} C_F \qquad (C_F \equiv \frac{N_c^2 - 1}{2N_c} = \frac{4}{3}), \\ f_{ACD} f_{BCD} &= \delta_{AB} C_A \qquad (C_A \equiv N_c = 3), \\ t_{ab}^A t_{ab}^B &= T_R \delta_{AB} \qquad\qquad T_R = 1/2. \end{aligned} \tag{1.5}$$

where C_F, C_A and T_R are the color-factor ("Casimir") associated with gluon emission from a quark, from a gluon, and a gluon to split to a $q\bar{q}$ pair, respectively.

The QCD coupling constant, $\alpha_s = \frac{g_s^2}{4\pi}$, which is analogous to $\alpha = 1/137$ in QED, describes the strong interaction strength depending on the momentum transfer Q, *i.e.* $\alpha_s \sim 0.1$ for 100 GeV-TeV range. In perturbative QCD (pQCD), α_s can be expressed as a function of an (unphysical) renormalization scale μ_R with [17]:

$$\begin{aligned} \mu_R^2 \frac{d\alpha_s}{d\mu_R^2} &= \beta(\alpha_s) \\ &= -b_0 \alpha_s^2 - b_1 \alpha_s^3 - b_2 \alpha_s^4 - \ldots \end{aligned} \tag{1.6}$$

where $b_0 = (11C_A - 4n_f T_R)/(12\pi) = (33 - 2n_f)/(12\pi)$ is referred to as the 1-loop beta function coefficient, the 2-loop coefficient is $b_1 = (17C_A - n_f T_R(10C_A + 6C_F))/(24\pi^2) = (153 - 19n_f)/(24\pi^2)$, and the 3-loop coefficient is $b_2 = (2857 - 5033n_f + 325n_f^2)/(128\pi^3)$. The negative sign in Eq. 1.6, combined with the fact that $b_0 > 0$ (for the number of quarks $n_f \leq 16$), gives a result which the QCD coupling effectively *decreases* with energy, called *asymptotic freedom*. One can consider only the b_0 term at an energy range where the number of flavors is constant, under the assumption $\mu_R^2 \simeq Q^2$, written as[18, 19]:

$$\alpha_s(Q^2) = \frac{1}{b_0 \ln(Q^2/\Lambda_{QCD}^2)} \tag{1.7}$$

where Λ_{QCD} is a constant of integration, corresponding to the non-perturbative scale of QCD. Currently, the measurements of the QCD coupling is presented as a function of the energy scale Q in Fig. 1.4, which demonstrates the agreement of measurements with the specific energy dependence of α_s predicted by QCD.

From Fig. 1.4, One can find a feature which reveals a main characteristic of QCD. With the momentum transfer increasing (equivalently at short distances), the coupling constant α_s becomes smaller. At α_s approaching zero, the quarks interact very weakly and can behave as if they are free. This feature of the strong interaction is so-called *asymptotic freedom*, or *deconfinement*. On the contrary, at low momentum transfers, the coupling constant α_s becomes larger and the perturbative approach is not valid anymore. In the normal world, the quarks and gluons are confined in the hadrons, known as *confinement*. The further explanation is given by the coupling strength between two interacting quarks which increases with the distance. The potential of the strong force between a $q\bar{q}$ pair as a function of distance r can be approximated by [21]:

$$V_s(r) = -\frac{4}{3}\frac{\alpha_s}{r} + \kappa r \tag{1.8}$$

where κ is the string tension and r is the distance between the two quarks. It concludes that the QCD potential between two quarks does not vanish for large distances r but grows linearly with r. The third characteristic associated with QCD is *chiral symmetry restoration*. The chiral symmetry exists as an exact symmetry only when the mass parameter of a quark is strictly zero. At high momentum transfers range, some quarks will have small mass and the chiral symmetry is said to be approximately restored. However, quarks inside hadrons are confined and have large dynamical masses. In this case, the chiral symmetry is considered to be broken (or hidden).

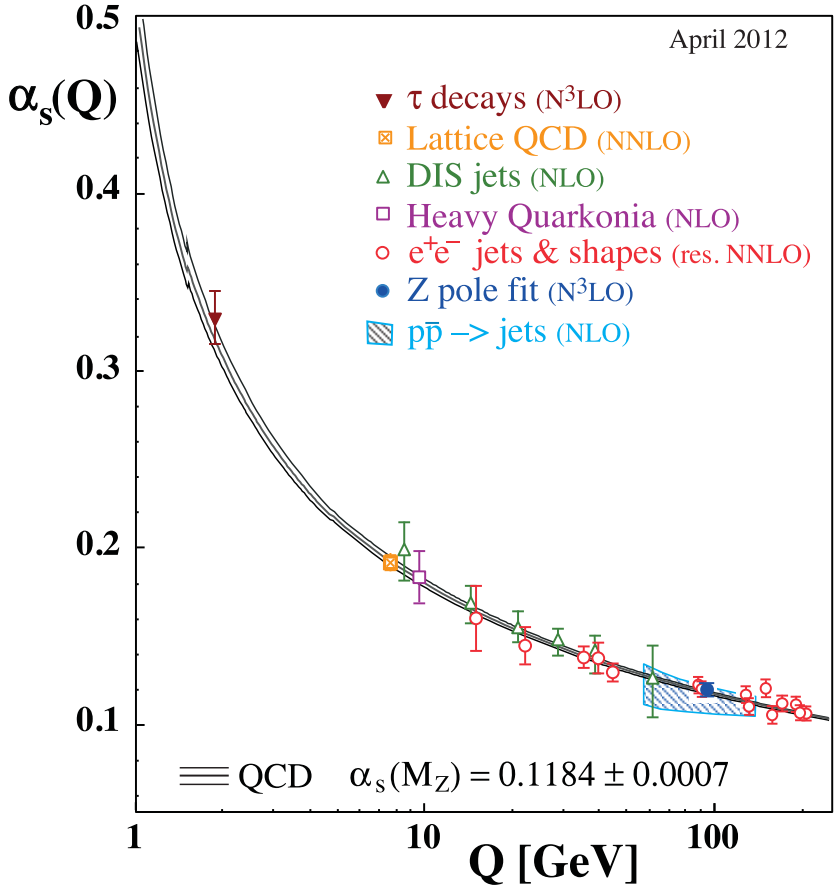

Figure 1.4: Summary of measurements of α_s as a function of the energy scale Q. The curves show the predictions from QCD at the average value of α_s between 4-loop approximation and 3-loop threshold matching heavy quark masses $M_c = 1.5$ GeV and $M_b = 4.7$ GeV. The α_s extracted from QCD perturbation are shown at next-to-leading order (NLO) (open triangles plussing squares), next-to-next-to leading order (NNLO) (open circles), next-to-NNLO (N^3LO) (Full symbols). The cross filled square is based on lattice QCD. The filled triangle at Q = 20 GeV (from DIS structure functions) is obtained from the original result which includes data in the energy range from Q = 2 to 170 GeV. The plot is taken from [20].

1.3 Quark-Gluon Plasma

To the ordinary matter in the world, they are made up of quarks and gluons, confined into hadrons by the strong interactions. As discussed in Sec. 1.2, the quarks and gluons is expected to be in a deconfined state based on the asymptotic property of QCD at extremely high temperatures and/or short distances. By analogy with classical plasma, the quarks and gluons deconfined state is called Quark-Gluon Plasma (QGP) [22]. After the discovery of the asymptotic freedom, One open question is about the properties of the transition from the hadron phase to the QGP phase.

1.3.1 Lattice QCD predictions

At low energy region, the increasing coupling constant requires the use of non-perturbative methods to study the properties of QCD. A new theory, Lattice gauge theory, was proposed by K. Wilson in 1974 [23] to solve the QCD theory of quarks and gluons on non-perturbative approach, well known as Lattice QCD. In lattice QCD, the QCD Lagrangian is described in Euclidean space-time lattice, where quark fields are located on the lattice sites and gauge fields are defined on the links between sites. Lattice QCD calculation provides quantitative information on the QCD phase transition between the hadron phase and the QGP phase. For massless quarks, a transition at baryonic potential $\mu_B = 0$ was obtained from the calculation, which is expected from the spontaneous breaking of the chiral symmetry in QCD. The estimated phase transition temperature, named critical temperature (T_c), and critical energy density would be $T_c \sim 170$ MeV and $\varepsilon = 0.7$ GeV/fm^3 [24], as shown in the left panel of Fig. 1.5. The QCD pressure can also approach the ideal QGP phase value at infinite temperature due to the asymptotic freedom of QCD. As shown in the right panel of Fig. 1.5, the pressure strongly reacts to changes in the number of degrees of freedom [25]. Both of calculations are based on $16^3 \times 4$ lattice and used the p4-improved staggered quark action with the Symanzik improved gauge [25]. A clear number of flavors dependence is observed for energy density and pressure, which becomes larger when going to larger number of degrees of freedom.

1.3.2 QCD phase diagram

Under different conditions such as temperatures and pressures, a physical system made up of many particles would appear different phases, *e.g.* water can be solid,

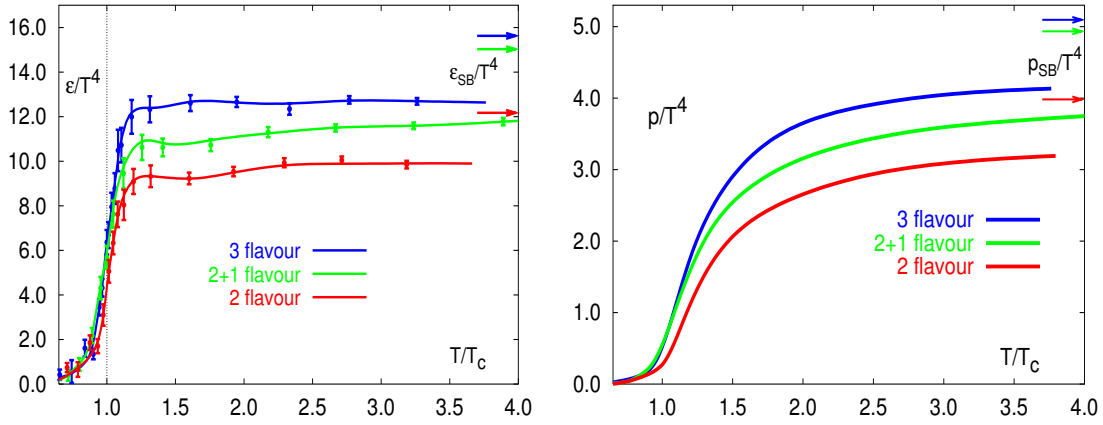

Figure 1.5: Left: Scaled energy density ε/T^4 as function of temperature T from lattice calculations. Right: Scaled pressure p/T^4 in QCD with different number of degrees of freedom as a function of temperature T. The calculations are carried out with 2 or 3 light flavors or 2 light and 1 heavy flavor (strange quark). The arrows are the Stefan-Boltzmann limit predictions corresponding to different number of flavors.

fluid, or gaseous. Analogously, the strong interacting matter would present different phases depending on the conditions of temperature and baryon chemical potential which is related to the density of baryons in the system, as shown in Fig. 1.6. Either experimentally or theoretically, the phase diagram is not well known. The names of the various phases including vacuum, hadron gas, nuclear matter, color superconductor and Quark-gluon plasma are shown in white words. The critical point and crossover are presented by a big point and dash lines, respectively. Some experiment regions also are shown in the phase diagram with yellow marks. Normal nuclear matter consist of neutrons and protons, such as a Pb nucleus, has low T and $\mu_B \sim 900$ MeV. The quarks and gluons are confined in neutrons and protons, generally said hadrons, as packed together in bags. However, under extreme conditions of high temperature or high baryon chemical potential (or both), quarks and gluons are set free due to the confinement breaking down. This is well known as the deconfinement of hadrons to the quark-gluon plasma. Deconfinement at large baryon chemical potential is considered to exist in the interior of neutron stars [26] and color superconductor [27], where the nuclear matter is strongly compressed to up to 10 times the normal nuclear density. Deconfinement by heating up nuclear matter can be achieved by colliding heavy nuclei at enormous energies, *i.e.* SPS, RHIC and LHC, at a critical temperature of $T_c \approx 170$ MeV. Along the first order phase transition line, the matter is shown with hadron gas (lower T) and quark-gluon plasma (higher T). The transition line is end at a point known as the QCD critical

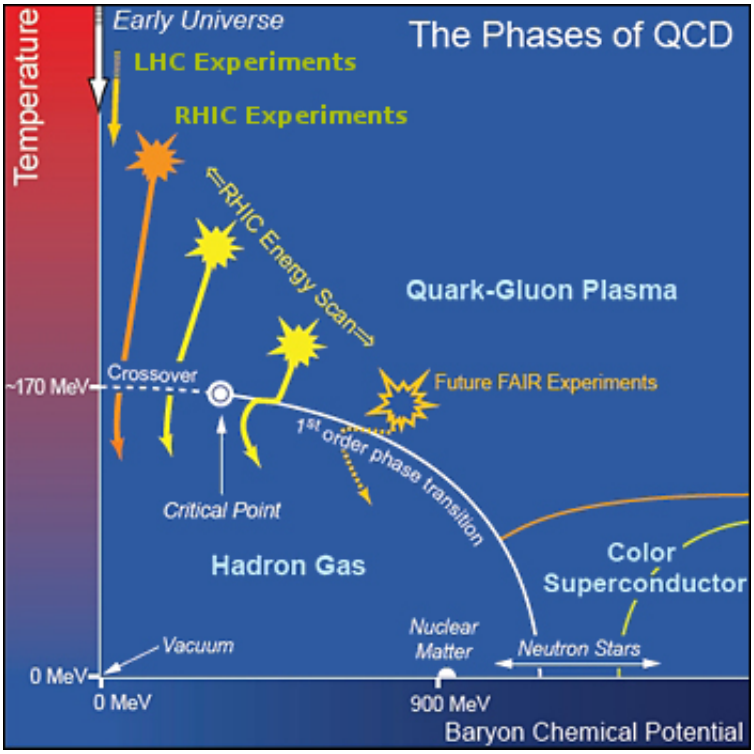

Figure 1.6: Schematic of the QCD phase diagram of nuclear matter in terms of the temperature (T) versus baryon chemical potential (μ_B). The solid lines show the phase boundaries for the indicated phases. The solid circle depicts the critical point where the sharp distinction between the hadronic gas and QGP phases ceases to exist. Possible trajectories for systems created in the QGP phase at different accelerator facilities are also presented.

point [28] where deconfinement occurs. To the point, both phases are distinct and the transition from one phase to the other is sharp. Meanwhile, both of them can co-exist and the transition from one to the other is a smooth crossover [29]. Locating the critical point both experimentally and theoretically is a great challenge. Current theoretical calculations are highly uncertain about the location of the critical point. At RHIC, a new running program has recently started to search for the critical point by energy scan using Au+Au collisions with energies between 5 GeV and 20 GeV, corresponding to μ_B values from about 100 MeV to 500 MeV. There is now considerable evidence that the universe began as a fireball, called "Big-Bang". It is believed that after the electro-weak transition ($t \sim 10^{-11}$ s and $E \sim 1$ TeV) the QCD phase transition happened at $t \sim 10^{-6}$ s. In other words, fractions of a second after the Big Bang the universe was filled with the free quarks and gluons. Therefore, studying the phase transitions of quark-gluon plasma also allows to understand the behavior of matter in the early universe.

Chapter 2

Heavy-ion physics

It is widely considered that the free quarks and gluons, referred to as strongly interacting matter or Quark-Gluon Plasma, exist in the universe after a microsecond after the Big Bang and the interior of neutron stars. Under controlled laboratory conditions, the Quark-Gluon Plasma may be created at extremely high temperatures and high densities by reactions of nucleus-nucleus pairs, usually named ultra-relativistic heavy-ion collisions. Since 1980's, many heavy-ion experiments have been developed to search for this matter and study its properties. For example, Alternating Gradient Synchrotron (AGS) at BNL (Brookhaven National Laboratory) with $\sqrt{s_{\rm NN}}$ = 5.4 GeV, Super Proton Synchrotron (SPS) at the European Organization for Nuclear Research (CERN) at $\sqrt{s_{\rm NN}}$ = 19.4 GeV, Relativistic Heavy Ion Collider (RHIC) at BNL with Au+Au collisions up to $\sqrt{s_{\rm NN}}$ = 200 GeV and currectly largest one, Large Hadron Collider (LHC) at CERN with Pb+Pb collisions energy $\sqrt{s_{\rm NN}}$ = 2.76 TeV.

In this chapter, an overview of the space-time evolution of ultra-relativistic heavy-ion collisions is summarized in Sec. 2.1. The particle production in ultra-relativistic heavy-ion collisions, including the effects from initial and final nuclear interactions, is briefly discussed in Sec. 2.2. Sec. 2.3 summarizes of the experiment probes for searching for and understanding the Quark-Gluon Plasma.

2.1 Ultra-relativistic heavy-ion collisions

2.1.1 Geometry of collisions

In the ultra-relativistic heavy-ion collisions, two highly Lorentz contracted nuclei (like "thin pancakes") approach each other with velocities nearly equal to the velocity

of light. Many nucleon-nucleon collisions are happened in the region of geometrical overlap, which are determined by the distance between the centers of the two colliding nucleus named *impact parameter* b as shown in Fig. 2.1. The impact parameter characterizes the *centrality* of the heavy-ion collisions. The corresponding nucleons

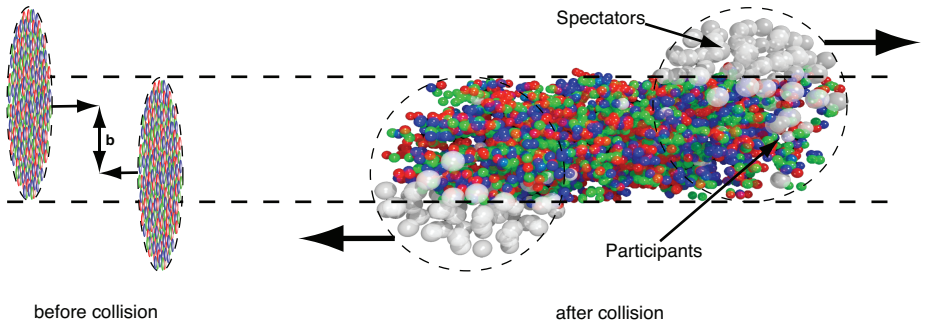

Figure 2.1: Schematic view of two colliding nuclei in the geometrical participant-spectator model. The distance between the centers of the two Lorentz contracted nuclei is the impact parameter $\vec{b}$.

in the overlap region are so-called *participants*, which consist of protons and neutrons taking part in the collision. While the nucleons outside the geometrical overlap are called *spectators*, which continue traveling almost unaffected. The participants interact with each other in the reaction zone, which lead to the formation of a hot and dense region, the fireball. The number of participating nucleons, N_{part}, is an important way of characterizing the heavy-ion collisions. It is also useful to know the number of binary nucleon-nucleon collisions, N_{call}. Both N_{part} and N_{call} can be calculated by a probabilistic model due to Glauber [30, 31] as presented in App.A.1.

2.1.2 Space-time evolution of collisions

A simple view of a ultra-relativistic nuclear collision including many various stages is presented in the top panel of Fig. 2.2. Sometimes it is useful to conceptualize such a collision in terms of a light cone diagram as shown in the bottom panel of Fig. 2.2. Here two Lorentz contracted nuclei approach each other with velocities nearly equal to the velocity of light and have colliding at $t = z = 0$. In the colliding instant, both contracted nuclei pass through each other in the region of geometrical overlap. Many processes of parton-parton hard scatterings occur in the overlap region, which result in depositing a large amount of energy in a limit volume. The energy density is so high that a new matter state consisting of defined quarks and gluons is formed, which is expected to happen in the early universe. The created new matter expands in the space-time going through different stages till a large

number of hadrons produced from partons fragmentation arrive at the detectors eventually. More illustration of the various forms of QCD matter intervening during the successive phases of the collisions is discussed briefly in the following.

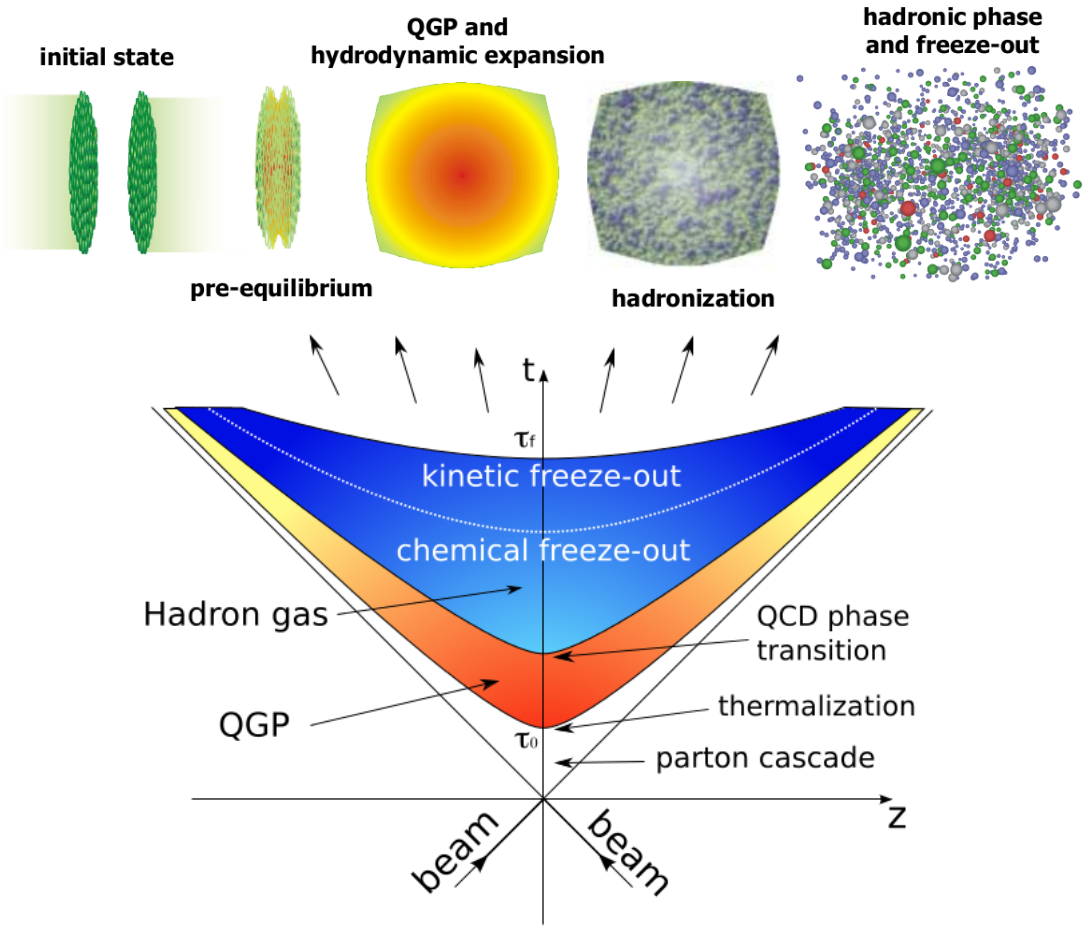

Figure 2.2: Top: Overview of the space-time evolution in a ultra-relativistic nuclear collision. Bottom: Schematic representation of the various stages of a heavy ion collision as a function of time t and the longitudinal coordinate z (the collision axis) [32, 33].

2.1.2.1 Initial state for collisions

Prior to the collision, in the center-of-mass frame, the accelerated projectile and target nuclei seem as two Lorentz-contracted "pancakes", with a longitudinal extent smaller by the Lorentz boost factor $\gamma = E/m \sim 100$ (E is the beam energy per nucleon, and m is the mass of nucleon) than the radial extent in the transverse plane. The Parton Distribution Functions (PDFs) in the nucleus, which govern the initial conditions of the evolution of the system, are modified by the Nuclear Initial

State Effects (or Cold Nuclear Effects). Two models, Glauber model and Color Glass Condensate (CGC) [34, 35], are commonly used to describe the initial state.

Glauber model:
The Glauber Model views the collision of two nuclei in terms of the individual interactions of the constituent nucleons. In all calculations of geometric parameters using a Glauber approach, two most important inputs are the nuclear charge densities measured in low-energy electron scattering experiments and the energy dependence of the inelastic nucleon-nucleon cross section. To a fixed impact parameter $\vec{b}$ heavy ion collision, the number of participants N_{part} and binary nucleon-nucleon collisions N_{coll} can be calculated as presented in Sec. 2.1.1. The PDFs in the nucleus, which are different from those in free protons and neutrons in the initial state effects, such as nuclear shadowing [36–40], initial state parton energy loss [41, 42]) and intrinsic transverse momentum (k_t) broadening or Cold Nuclear Effects [43], perform the initial conditions of the evolution system.

Color Glass Condensate:
Alternatively, the CGC takes saturation effects into account, given *e.g.* by the Kharzeev-Levin-Nardi (KLN) model [44, 45]. In this model, assuming two "pancakes" are mostly composed of gluons which carry a small fractions x_{Bj} (Bjorken-x) of the momentum of their parent nucleons ($x_{Bj} \ll 1$) due to the Lorenz contraction of the longitudinal size of the nucleus at high energy. However, the gluon density growth can not go on forever since it would lead to violation of unitarity for physical cross sections. The density is rapidly increasing with $1/x$ with carrying relatively large transverse momenta, written in Dokshitzer-Gribov-Lipatov-Altarelli-Parisi (DGLAP) [46, 47] formalism as:

$$xG(x, Q^2) \sim \exp[\sqrt{\alpha_s \log 1/x \log Q^2}] \tag{2.1}$$

A typical value for such a gluon in a Pb or Au nucleus is $k_\perp \simeq 2$ GeV for $x = 10^{-4}$. According to the Balitsky-Fadin-Kuraev-Lipatov (BFKL) evolution [48–50], the gluons with low x_{Bj} will overlap together and their density will saturate due to the finite nucleus volume, named *gluon saturation* [51]. The DGLAP and BFKL evolutions are shown in Fig. 2.3.

2.1.2.2 Fireball of collisions

The two nuclei collide with each other and the interactions start developing at the geometrical overlapping region. In the collision process, a fireball is created.

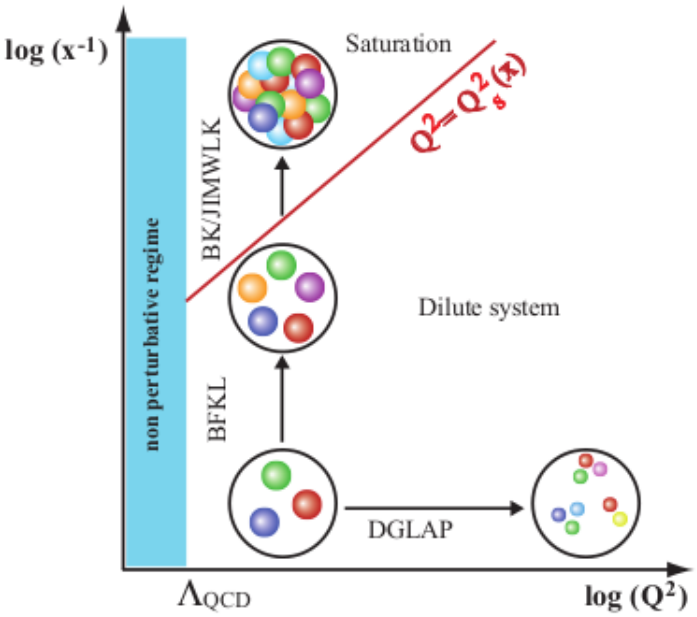

Figure 2.3: "Phase-diagram" for parton evolution in QCD in the CGC model. The straight line is the saturation line which separates the dense and dilute regimes [52].

A large amount of energy is deposited in the fireball of the two colliding nuclei, and is distributed among deconfined quarks and gluons that potentially form a equilibrated QGP when passing pre-equilibrium parton cascade stage firstly. The fireball keep expanding in space-time then going through a mixed phase with the QGP and hadrons till the eventually created particles freeze-out. More details about the fireball evolution to final state particles are presented as following:

- **Beam colliding**:
  At time $\tau = \sqrt{t^2 - z^2} = 0$, the two nuclei hit with each other. The nucleons of the colliding nuclei are resolved into their partons on the basis of the experimentally measured nucleon structure functions and the interactions start developing. The "hard" processes with large transferred momenta ($Q > 10$ GeV) occur fast (within $\tau < 1/Q$), which are responsible for the production of "hard particles", like (hadronic) jets, direct photons, dilepton pairs, heavy quarks, *etc.*

- **Pre-equilibrium**:
  At time $\tau < 1$ fm/c, parton-parton scattering predominantly occur in the space-time volume, and a large amount of energy is deposited which result in a new matter composed of deconfined quarks and gluons. While the matter is

currently still not in thermal equilibrium and perturbative QCD models can be used to describe the underlying dynamics as a cascade of freely colliding partons. The Parton Cascade Model (PCM) [53–55] is one of models to mainly describes the evolution of this stage of the collision based upon the Boltzmann equation, in order to estimate how fast partons belonging to incoming nucleons multiply and thermalize.

- **Chemical and thermal equilibrium**:
  After the short pre-equilibrium stage, the matter local equilibrium is achieved at the proper time τ_0. The system evolves to the law of hydrodynamics [56], which is established of thermal (but not necessarily chemical) equilibrium at partonic level. A special simplified hydrodynamics model of the collisions, the Bjorken longitudinal boost-invariant model, is commonly used to estimate the initial produced energy density in the collision by formula as [57, 58]:

$$\varepsilon \geq \frac{dE_{\mathrm{T}}/d\eta}{\tau_0 \pi R^2} = \frac{3}{2} < E_{\mathrm{T}}/N > \frac{dN_{ch}/d\eta}{\tau_0 \pi R^2} \tag{2.2}$$

  where τ_0 is the thermalization time, R is the radius of a nuclear, and $E_{\mathrm{T}}/N \sim 1$ GeV is the transverse energy per emitted particle. Until the interacting medium is thermalized, the hot and dense QCD matter consisting of quarks and gluons (QGP) is formed. The existence of this phase is well established via theoretical calculations on the lattice.

- **Hadronization and mixed phase**:
  The partonic matter keeps expanding and cooling down fast via strong interactions between quarks and gluons. Hadronization occurs when the (local) temperature becomes of the order of the critical temperature T_c for deconfinement, known from lattice QCD calculations as $T_c = 150 \div 180$ MeV. For larger times $10 \leqslant \tau \leqslant 20$ fm/c, this hadronic system is still relatively dense, so it still keeps collective expansion via hadron-hadron interactions to form *hadron gas*, whose temperature and density continue decrease with increasing time. A "mixed phase" is expected to exist between the QGP and hadron gas phases. In the mixed phase, the entropy density is transferred into fewer degrees of freedom, therefore, the system is prevented from a fast expansion.

- **Freeze-out**:
  Around time $\tau > 20$ fm/c, the hadrons stop interacting with each other after the system reaches a certain size and temperature, and the hadrons undergo

free streaming for the medium until they reach the detector. The memory of the QGP formation in the early stage of the collision is expected to be kept in their final distributions. Two types of freeze-out are appear in this stage. When inelastic collisions between constituents of the fireball do not occur any longer and the hadron abundances stop changing, including antibaryons, it is called as *chemical freeze-out* [59]. Subsequently, the elastic collisions also cease to happen in the fireball and the momenta of the hadrons can not undergo further change, this stage specifies the *kinetic freeze-out* or *thermal freeze-out* [59]. Both of the two freeze-outs are not indeed sharp occurrences for all hadronic species at the same time and different freeze-outs need to be considered for different particles.

2.2 Particle production

Many experment results show a fact that pions, the most abundant particles produced in a collision, have on average small transverse momenta, $p_T \sim 0.4\,\mathrm{GeV}/c$. [60]. The processes which lead to the production of such low-energetic pions are called *soft processes*. On the other hand, the processes producing the pions with large transverse momenta $p_\mathrm{T} > 1 - 2\ \mathrm{GeV}/c$ are called *hard processes*.

2.2.1 Soft processes

The soft processes are the bulk of the events taking place in heavy-ion collisions. Generally, particles in soft processes are produced by the decays of nucleons which are excited by soft collisions. Multiple soft collisions change only the excited states of the nucleons, which in turn produce particles the moment they leave the interaction region. This is why the multiplicity from soft processes is excepted to be scaled by the number of participants. The soft processes can not be described directly by perturbative QCD (pQCD). In this case, the strong coupling constant is large and the non-perturbative effects, which are very difficult to deal with, are important. The appropriate scaling of multiplicity of soft processes is postulated to be the number of participating nucleons N_part. QCD based phenomenological models, such as the *wounded nucleon model* [61] and *string model* [62], have been introduced by extrapolating the ideas developed for the hadron-hadron and hadron-nucleus interactions which correctly describe soft nucleon-nucleon collisions.

2.2.2 Hard processes

The hard processes involve large momenta transfers ($Q > 10$ GeV)connected with a small value of the strong coupling constant. Therefore, this process can be described successfully within the methods of pQCD. For the hard processes, the number of particles produced is assumed to scale with the number of binary collisions $N_{\rm coll}$. In this process, the inelastic hard scattering of the nucleons can be described by the pQCD in terms of the scattering of the pointlike partons (quarks or gluons) inside the nucleons. This eventually leads to the particles produced along the direction of the scattered partons, like a *jet*. The characteristic time and length scale of the parton-parton interaction is short compared to the soft processes between the bound partons in the initial state and to those of the fragmentation process of the scattered partons in the final state.

The hard inelastic cross section in nucleon-nucleon scattering is described in pQCD as the convolution of partonic reactions $ab \to cd$ with the parton distribution function (f) and the fragmentation function (D) as shown on Fig. 2.4. The produc-

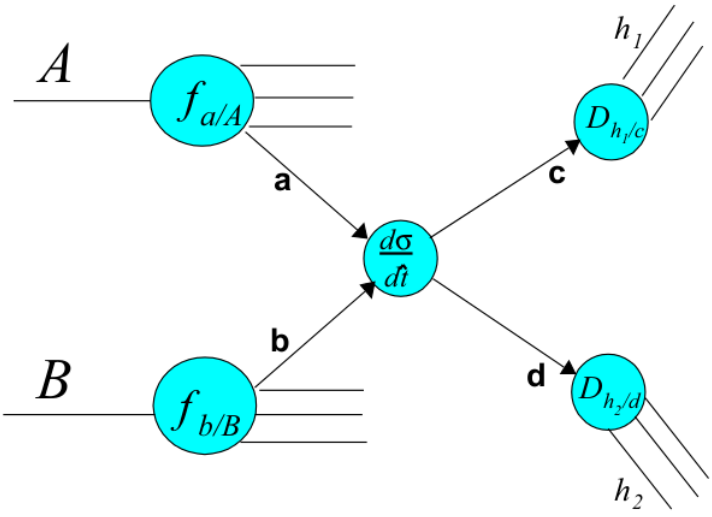

Figure 2.4: Diagram of calculation for the hard scattering process.

tion cross section of a given hadron h in a nucleus-nucleus collision A + B can be factorized as [63]:

$$E\frac{d^3\sigma^{hard}_{AB\to h}}{dp^3} = \sum_{a,b,c} f_{a/A}(x,Q^2) \otimes f_{b/B}(x,Q^2) \otimes \frac{d^3\sigma^{hard}_{ab\to cd}}{dp^3} \otimes D_{h/cd}(z_{cd},Q^2) \qquad (2.3)$$

where $f_{a/A}(x,Q^2)$ ($f_{b/B}(x,Q^2)$) is the PDFs of the initial parton "a" ("b") in the initial nucleus "A" ("B"), which depends only on the momentum transfer and the parton

fractional momentum x and can be determined *e.g.* in deep inelastic electron-nucleus reactions, $D_{h/cd}(z_{cd}, Q^2)$ is the non-perturbative Fragmentation Function (FF) of the scattered parton c (d) into the hadron h carrying a fraction $z = p^h/p^{c(d)}$ of the parton momentum, and $\frac{d^3\sigma^{hard}_{ab\to cd}}{dp^3}$ represents the parton-parton cross section. In the formula, only parton-parton scattering term, $\frac{d^3\sigma^{hard}_{ab\to cd}}{dp^3}$, is perturbatively computable, and other terms (PDFs and FF) are parameterizations based on the experimental data.

The PDFs are defined as the momentum distribution functions of the partons within the proton, which represent the probability densities to find a parton of flavor f carrying a fraction x of the hadron longitudinal momentum at a squared energy scale Q_2 ($= -q^2$). The PDFs are universally defined and independent of any specific physical process. Since PDFs can not be computed by the pQCD because of the inherent non-perturbative effect in a QCD binding state. The functions are obtained as parameterization by using measured nuclear structure function $F_2(x, Q^2)$ [64]. The proton structure function is measured by lepton Deep Inelastic Scattering (DIS) in many experiments. As an example, the parameterized PDFs are provided by the CTEQ group as shown in Fig. 2.5 [65].

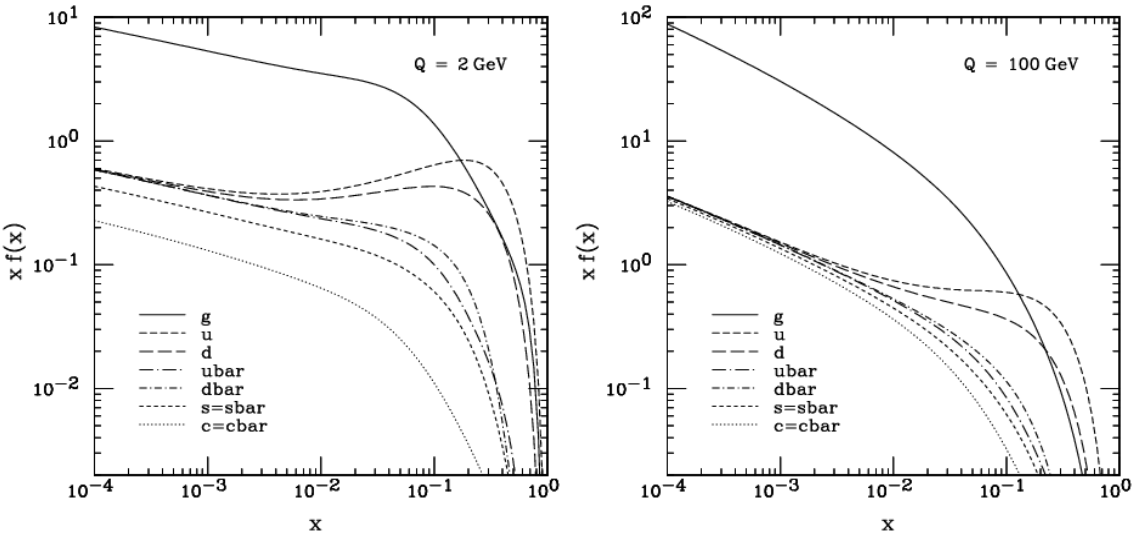

Figure 2.5: Parton distribution function from the CTEQ group as a function of x at $Q = 2$ GeV (left) and 100 GeV (right) [65].

The FFs represent a probability for a parton of flavor f to fragment into a particular hadron carrying a certain fraction of the parton's energy. The Fragmentation functions incorporate the long distance, non-perturbative physics of the hadronization process in which the observed hadrons are formed from final state partons of

the hard scattering process. They also can not be calculated in the perturbative QCD method. The FFs has been determined as a fraction with $z = p_{\mathrm{T}}^{h}/E_{T}^{parton}$ of the original parton in other processes, *e.g.* $e^{+}e^{-}$ and ep collisions, which are typically related to the transverse momentum of final state hadrons. As an example, the fragmentation functions of π^0 from different partons are shown in Fig. 2.6.

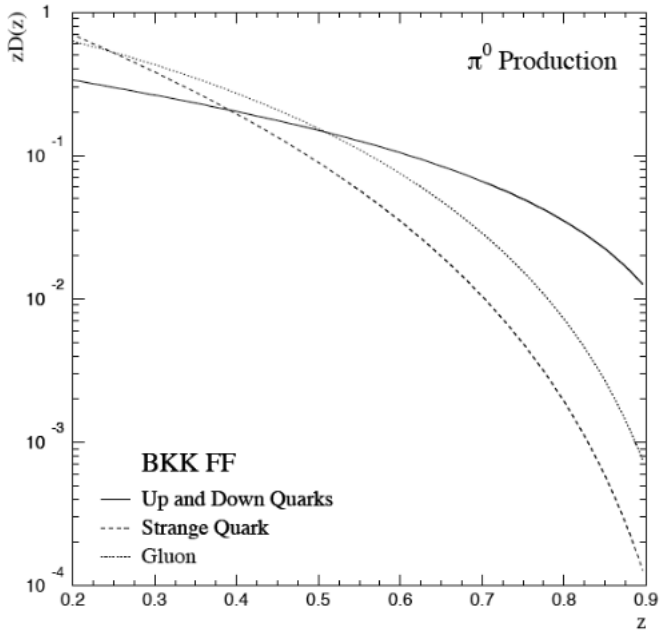

Figure 2.6: Fragmentation function of π^0 as a function of the momentum of fraction z of π^0. These fragmentation functions were evaluated at $Q^2 = 10$ GeV^2 [66].

The Leading Order (LO) and Next-to-Leading Order (NLO) pQCD calculations succeed in describing high-p_{T} particle production in high-energy nucleon-nucleon collisions [67]. Fig. 2.7 shows the π^0 spectra measured by ALICE in pp collisions at $\sqrt{s} = 0.9$ TeV and 7 TeV [68]. The π^0 production in pp collisions at $\sqrt{s} = 0.9$ TeV and 7 TeV is compared with NLO pQCD calculations using the PDF CTEQ6M5 and DSS π^0 [69], BKK π^0 [70] NLO fragmentation functions. The data and NLO predictions are compared via a ratio with the fit to the measured cross section. In the NLO calculations the factorization, renormalization and fragmentation scales are chosen to have the same value given by μ. State-of-the-art calculations describe the data at 0.9 TeV and 0.2 TeV [71], however this is not the case at 7 TeV, where the calculations overestimate the cross sections and exhibit a different slope compared to the data.

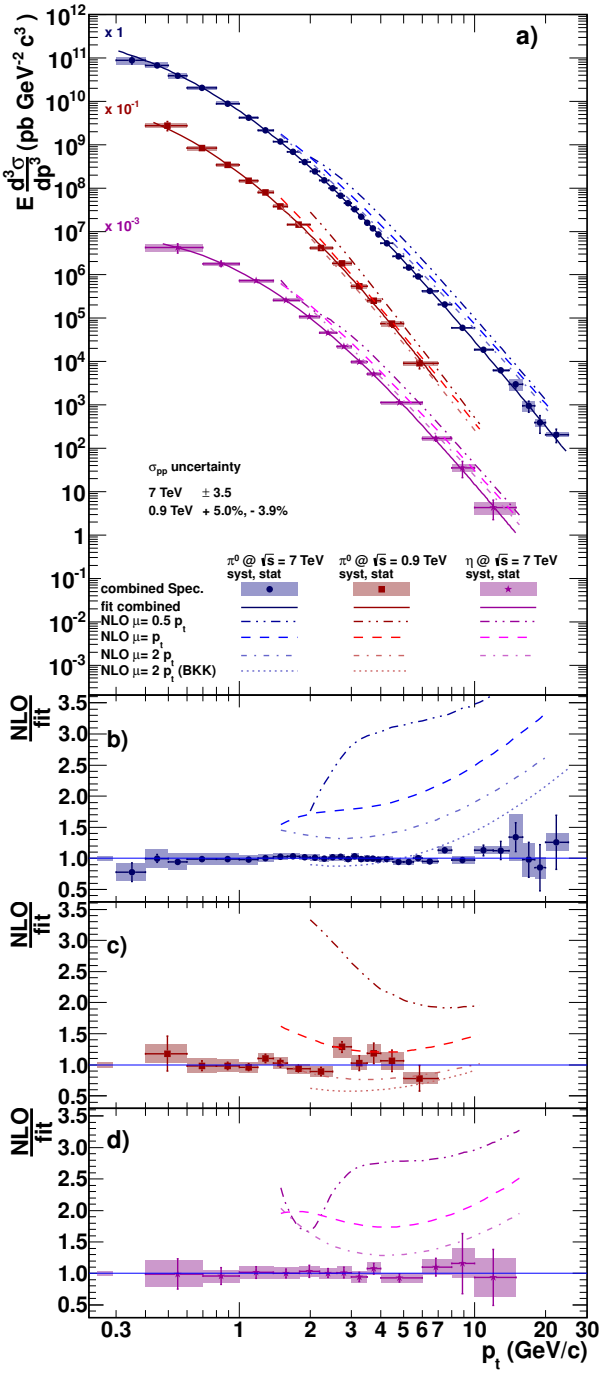

Figure 2.7: a) Differential invariant cross section of π^0 production in pp collisions at $\sqrt{s} = 7$ TeV (circles) and 0.9 TeV (squares) and of η meson production at $\sqrt{s} = 7$ TeV (stars). The lines and the boxes represent the statistical and systematic error of the combined measurement respectively. The uncertainty on the pp cross section is not included. NLO pQCD calculations using the CTEQ6M5 PDF and the DSS (AESS for η mesons) FF for three scales $\mu = 0.5\ p_{\mathrm{T}}$, $1\ p_{\mathrm{T}}$ and $2\ p_{\mathrm{T}}$ are shown. Dotted lines in panels b) and c) correspond to the ratios using the BKK FF. Ratio of the NLO calculations to the data parameterizations are shown in panels b), c) and d). The full boxes represent the uncertainty on the pp cross sections. [65].

2.2.3 Nuclear effects to particle production

Particles with large transverse momenta are predominantly produced with hard scattering process in parton-parton collisions as discussed above. In pp collisions, the produced partons in the hard scattering go to fragmentation directly in the QCD vacuum, which form particles concentrating upon the direction of motion of the primordial parton. In heavy-ion collisions, although the fundamental QCD parton-parton processes are the same as in nucleon-nucleon collisions, the initial state of the matter in a nucleus prior to the hard scattering can be significantly modified. The main initial state effects were presented shortly in Sec. 2.1.2.1, and some of them will be discussed in more details in the following section. The scattered partons may have to go through the hot and dense medium created in nucleus-nucleus collisions before they fragment into hadrons. Therefore, the production from hard scattering can probe matter produced in the early stage of the collisions. It is generally accepted that prior to hadronization, partons lose energy in the extremely hot and dense medium due to gluon radiation and multiple collisions discussed in the following. These phenomena are broadly known as "*jet quenching*"[72–74].

2.2.3.1 Effects of Cold Nuclear Matter

The effects of Cold Nuclear Matter [75] cause to enhance the particle production by multiple soft scattering, and/or make modification of the parton distribution functions in the initial state. Many mechanisms are introduced to describe these effects. For instance, followings are known as the initial state effects.

- **Cronin effect**:
  The Cronin effect was first observed in 1970's [76], featuring an enhancement of hadron production at intermediate p_{T} range in p+A relative to pp, when scaled by number of binary collisions. In p+A collisions, the hadron production cross section for a given p_{T} scales as:
  $$E\frac{d^3\sigma}{dp_{\mathrm{T}}^3}(p_{\mathrm{T}}, A) = E\frac{d^3\sigma}{dp_{\mathrm{T}}^3}(p_{\mathrm{T}}, 1)A^{\alpha} \tag{2.4}$$
  with $\alpha > 1$ for transverse momenta above about 2 GeV/c as shown in Fig. 2.8. Traditional explanations of the Cronin effect involve multiple soft scattering of incoming partons passing through the nucleus A prior to the hard scattering, which lead to an additional broadening at intermediate p_{T}. After the discovery of the Cronin effect, some theoretical models such as *soft hadronic rescattering models* [77] and the *colour dipole model* [78] were presented to explain it.

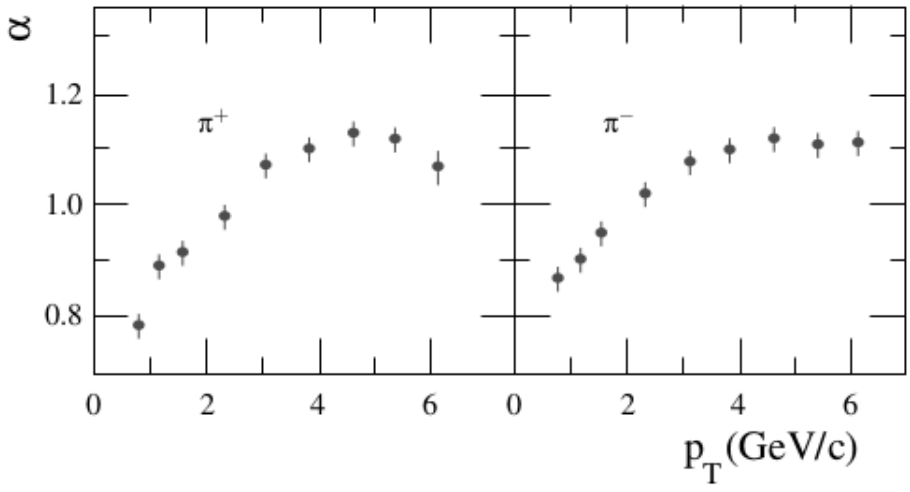

Figure 2.8: Transverse momentum dependence of the exponent α in Eq. 2.4. The nuclear enhancement for charged pion production was reported in [76].

- **Nuclear shadowing**:
  The modification of the parton distribution function in nuclei, can also have an effect on particle production. The measurements of the nuclear structure function $F_2^A(x, Q^2)$ by EMC group in DIS [79–81] indicate clearly that parton distributions of the bound protons are different from those of the free protons, $f_{i/A}(x, Q^2) \neq f_{i/p}(x, Q^2)$. The initial state nuclear effects are offten categorized as the ratio of the structure functions, written as:

$$R_i^A(x, Q^2) = \frac{f_{i/A}(x, Q^2)}{f_{i/p}(x, Q^2)} \tag{2.5}$$

  Fig. 2.9 shows a typical shape of the ratio $R_i^A(x, Q^2)$ of data for different nuclei [82]. According to this distribution shape, the nuclear effects in the ratio are usually divided into the following regions in Bjorken-x ($x \sim \frac{2p_{\mathrm{T}}}{\sqrt{s_{\mathrm{NN}}}}$ at mid-p_{T} rapidity region):

  - shadowing, a depletion $R_i^A(x, Q^2) < 1$ at $x \leq 0.1$;
  - anti-shadowing, an excess $R_i^A(x, Q^2) > 1$ at $0.1 < x \leq 0.3$;
  - EMC effect [83], a depletion $R_i^A(x, Q^2) < 1$ at $0.3 < x \leq 0.7$;
  - Fermi motion [84], an excess towards $x \to 1$ and beyond.

  Currently, there are two sets of nPDF available which are based on the global DGLAP fits to the data: (i) EKS98 [85, 86] and (ii) HKM [87].

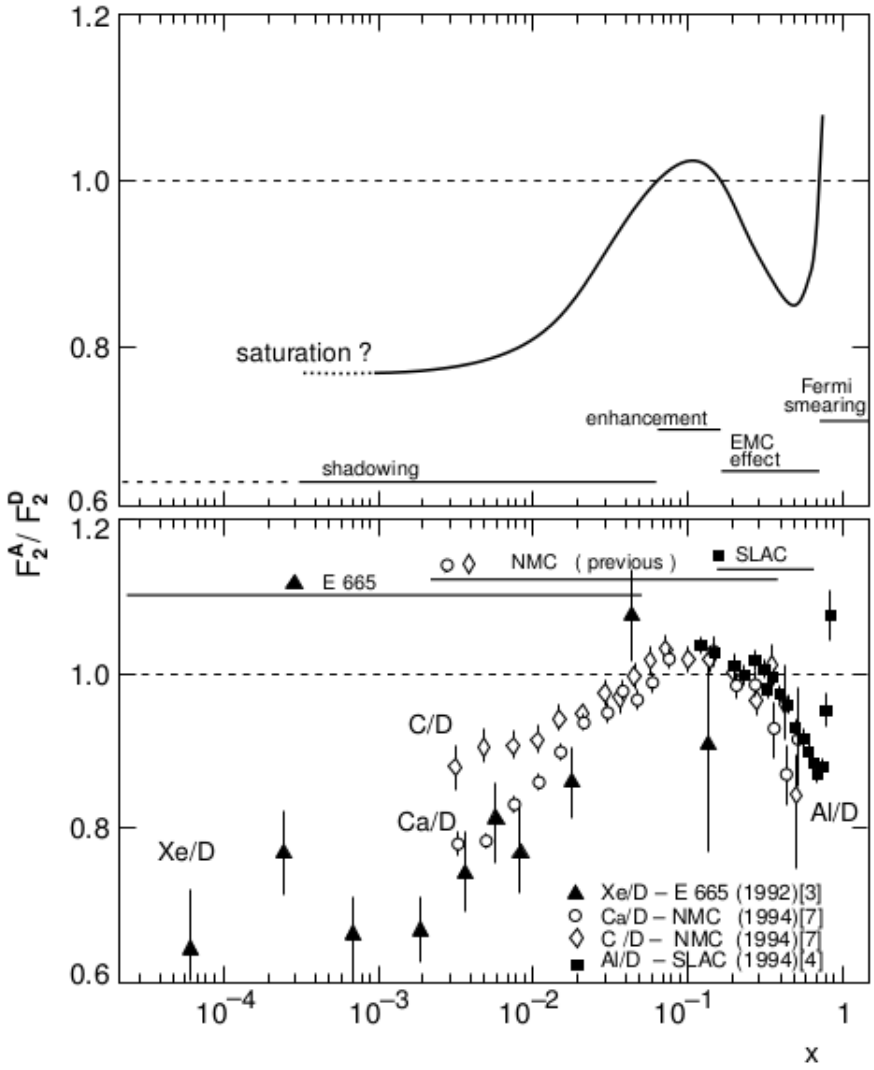

Figure 2.9: Phenomenological curve and some experimental data for the nuclear effect structure function, F_2^A/F_2^D, taken from [82].

2.2.3.2 Parton energy loss

In additional, final effects also have influence to the final particles production. In the nucleus-nucleus collisions, one of the generally known final effects, parton energy loss or jet quenching, gives influence to the final particle production by medium-modifications of partons fragmentation pattern and hadronization [88]. The explanation is that the partons created in the early stage of nucleus-nucleus collisions via hard scatterings go through the hot and dense medium formed in these collisions and loss a large fraction of their energy due to the interactions between partons inside the medium.

A first attempt to calculate the energy loss of a fast parton in the hot and dense QCD medium was made by J.D. Bjorken [72]. However, this calculation did not include the currently known dominant effect at high energies, namely, gluon radiation (gluon bremsstrahlung) energy loss [88, 89]. Recently, a new interaction mechanisms, collisional energy loss, is usually considered as the dominant mechanism especially at low energies. In a general way, the total energy loss of a parton going through the QCD medium is the sum of collisional and radiative term, written as:

$$\Delta E = \Delta E_{rad} + \Delta E_{coll} \tag{2.6}$$

where ΔE_{rad} is the gluon bremsstrahlung energy loss contribution via medium-induced multiple gluon emission, and ΔE_{coll} is the collision energy loss with the medium constituents. Their different processes can be indicated briefly with diagrams in Fig. 2.10.

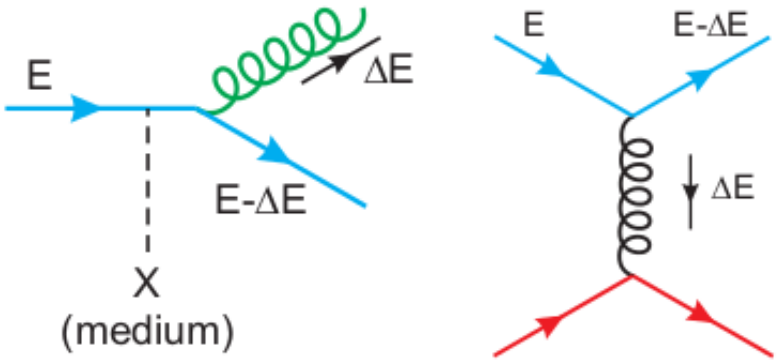

Figure 2.10: Diagrams for radiative (left) and collisional (right) energy losses of a quark of energy E traversing the quark-gluon medium.

- **Gluon radiation energy loss**:

  The fast partons lose their energy with gluon radiation energy loss through

inelastic scatterings within the medium dominantly at higher momentum. A simple diagram of this process is shown in the left panel of Fig. 2.10. More details is shown in Fig. 2.11. In a hard scattering, a initial created parton

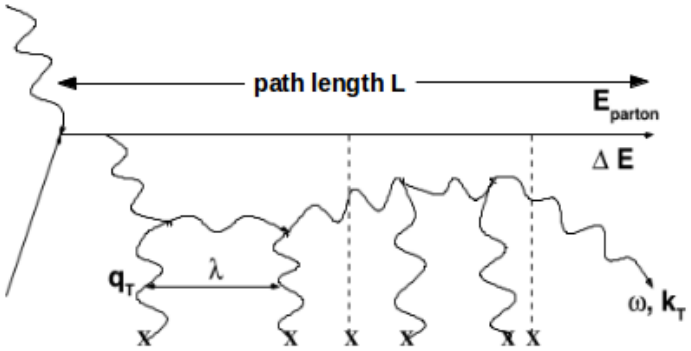

Figure 2.11: Typical gluon-radiation diagram, adapted from Ref. [90].

with energy E transversing the medium radiates of a gluon with energy ω with a probability proportional to L, the length of its path. Due to its non-abelian nature and its interaction with the medium the radiated gluon suffers multiple scattering with a mean free path λ. The number of scatterings with momentum transfer q_T that the radiated gluon undergoes until it eventually decoheres. Conveniently, the properties of the QCD medium are characterized by the so-called *transport coefficient*, $\hat{q}$, of the medium, which is defined as the average medium-induced transverse momentum squared transferred to the projectile per mean free path, written as:

$$\hat{q} = \frac{< q_T^2 >}{\lambda} \tag{2.7}$$

The determined radiated energy distribution $\omega\frac{dI}{d\omega}$ (or $\omega\frac{d^2I}{d\omega}dk_\perp$) is set by the characteristic energy ω_c as:

$$\omega_c = \frac{1}{2}\hat{q}L^2 \tag{2.8}$$

In the Baier-Dokshitzer-Mueller-Peigne-Schiff and Zakharov (BDMPS-Z) calculation [91, 92], the emitted gluon is allowed to exploit the full transverse phase space regardless of its energy. The number of coherent scattering centers, which act as a single source of gluon radiation: $N_{coh} = \frac{t_{coh}}{\lambda}$, where t_{coh} is the coherence/formation time, and $t_{coh} \simeq \frac{\omega}{k_\perp^2} \simeq \sqrt{\frac{\omega}{\hat{q}}}$. The average energy loss of the parton due to the gluon radiation with the gluon energy spectrum per

unit path length as [93, 94]:

$$\omega\frac{dI}{d\omega dz} \simeq \frac{1}{N_{coh}}\omega\frac{dI^{1scatt}}{d\omega dz} \simeq \frac{\alpha_s}{t_{coh}} \simeq \alpha_s\sqrt{\frac{\hat{q}}{\omega}} \tag{2.9}$$

However, physically the transverse momentum $k_\perp$ of the radiated gluon is kinematically bound to be smaller than its energy ω, This imposes a constraint on the emission probability via the dimensionless quantity

$$R = \omega_c L = \frac{1}{2}\hat{q}L^3 \tag{2.10}$$

first introduced as "density parameter" in Ref. [95]. The parameter R with w_c determines the radiated gluons energy distribution, $\omega\frac{dI}{d\omega}$, referred to as Baier-Dokshitzer-Mueller-Peigne-Schif-Zakharov and Salgado-Wiedeman (BDMPS-Z-SW), as shown in Fig. 2.12. In the limit $R \to \infty$, the energy distribution is

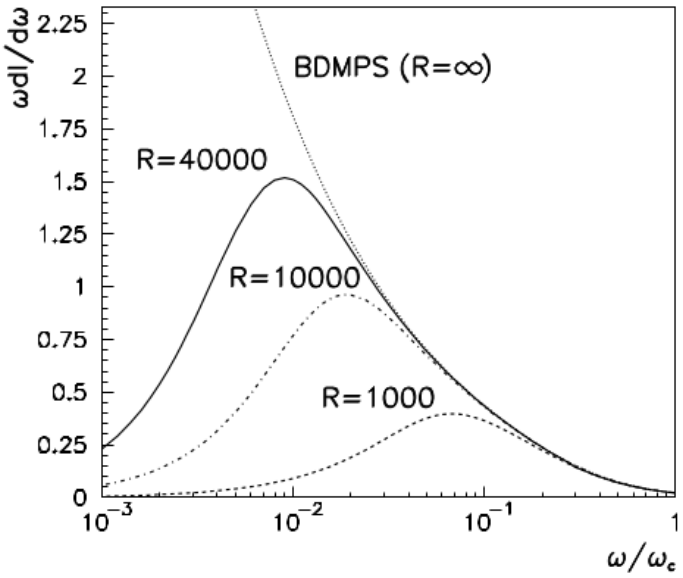

Figure 2.12: Medium-induced gluon energy distribution $\omega\frac{dI}{d\omega}$ in the multiple soft scattering approximation for different values of the kinematic constraint $R = \omega_c L$. The figure is taken from [94].

of the form [94]

$$\lim_{R\to\infty}\omega\frac{dI}{d\omega} \simeq \frac{2\alpha_s C_R}{\pi}\begin{cases}\sqrt{\frac{\omega_c}{2\omega}} & \text{for} \quad \omega < \omega_c \\ \frac{1}{12}(\frac{\omega_c}{\omega})^2 & \text{for} \quad \omega \geq \omega_c\end{cases} \tag{2.11}$$

where C_R is the QCD coupling factor or *Casimir factor* between the considered hard parton and the gluons in the medium. It is $C_F = 4/3$ to a quark and

$C_A = 3$ to a gluon. The average parton energy loss is the zeroth moment of this energy distribution, written as [94]

$$< \Delta E >_{R\to\infty} = \lim_{R\to\infty} \int_0^\infty d\omega \frac{dI}{d\omega} = \frac{\alpha_s C_R}{2}\omega_c \tag{2.12}$$

- **Collision energy loss**:
  The collision energy loss via elastic scatterings with the medium constituents dominates at low particle momentum as shown in the right panel of Fig. 2.10. The collisional energy loss in the QGP was originally calculated by Bjorken [72] and later improved by various authors [96–98]. The average energy loss in one scattering is:

$$< \Delta E^{1scatt} > \approx \frac{1}{\sigma T} \int_{m_D^2}^{t_{max}} t \frac{d\sigma}{dt} dt \tag{2.13}$$

  where $t = Q^2$ is the momentum transfer squared in a medium of temperature T; $m_D^2 \sim 4\pi\alpha_s T^2(1 + N_f/6)$ is the Debye screening mass squared; and $t_{max} = [s - (m_p + m_0)][s - (m_p - m_0)^2]/s$ is the maximum momentum transfer with $s = 2m_0E + m_0^2 + m_p^2$. In above equation, the $\frac{d\sigma}{dt}$ is as:

$$\frac{d\sigma}{dt} \approx C_i \frac{4\pi\alpha_s^2(t)}{t^2}, \quad \text{with } \alpha_s(t) = \frac{12\pi}{(33 - 2n_f)\ln(t/\Lambda_{QCD}^2)} \tag{2.14}$$

  where $C_i = 9/4, 1, \text{and} 4/9$ are the color factors for gg, gq and qq scattering respectively. Eventually, on can obtain [97]

  - Light-quark, gluon: $-\frac{dE_{coll}}{dl}|_{q,g} = \frac{1}{4}C_R\alpha_s(ET)m_D^2\ln(\frac{ET}{m_D^2})$
  - Heavy-quark: $-\frac{dE_{coll}}{dl}|_Q = -\frac{dE_{coll}}{dl}|_q - \frac{2}{9}C_R\pi T^2[\alpha_s(M^2\alpha_s(ET)\ln(\frac{ET}{M^2}))]$

  Due to the mass of heavy quarks, the gluon bremsstrahlung off a heavy quark differs from that of a massless parton in the nuclear medium. The radiation is suppressed smaller than the ratio of the quark mass M to its energy E at a angle of $\theta_0 = \frac{M}{E} = \frac{1}{\gamma}$ [99]. This effect, known as the *dead cone* [100, 101], results in a reduction of the total gluon radiation emitted off heavy-quarks.

For light flavor partons, the medium-induced gluon radiation has been shown to be more important than the collisional energy loss. However, for heavy quarks, the collisional energy loss is usually considered as the dominant mechanism especially at low energies due to the large masses of heavy quarks which suppress the phase space of gluon radiation [102]. However, at the LHC energies region, heavy quarks become ultra-relativistic as well and thus are expected to behave similarly as light partons for significantly considering the radiative energy loss corrections [103].

2.3 Signatures of the quark-gluon plasma

As it is widely known, it is impossible to directly observe the short lived ($\sim$ some fm/c) QGP phase. During the time when the QGP is created in the nucleus-nucleus collisions, final particles that arise from the interactions between the constituents of the matter can provide rich information concerning the state of the hot and dense matter. Meanwhile, one has to use models to deduce QGP properties from the measured particle distributions. The collective measurements in heavy-ion collisions need to be disentangled from the measurements already present in pp and/or p+A systems where it is considered no QGP creation. For this purpose, the same observables in A+A and pp (and/or p+A) collision systems are usually directly compared.

It is generally recognized that there is no single unique signature that allows an unequivocal identification of the QGP phase, and study the properties of QGP. A variety of observables have been measured which are proposed to be the reliable evidences of the he creation of a QGP. These observables mainly include three types, which are global observables, soft probes and hard probes:

- **Global observables**:
  The global observables describe the state and dynamical evolution of the bulk matter created in a heavy ion collision, and allow to study the global properties of the collision.

- **Soft probes**:
  The soft probes are these signatures produced in the later stage of the collisions. Even if they are produced during the hadronization stage, they keep indirect information on the properties of the phase transition and on the QGP. The probes mainly include momentum spectra, strangeness enhancement, elliptic flow, particle correlations and fluctuations.

- **Hard probes**:
  In the early stage of the collisions, the short-distance hard-scatterings produce "quasi-free" partons which fragment into the final partcles. The partons passing through the hot and dense QCD matter have energy loss via gluon bremsstrahlung and multiple scattering in the medium. The hard-scatterings cross sections can be theoretically calculated by the pQCD framework. Therefore, hard processes constitute experimentally- and theoretically-controlled

self-generated "tomographic" probes of the hot and dense medium. The hard probes mainly include jet quenching, production of quarkonium states (J/Ψ, Υ), thermal dileptons and photons.

In this sections, the main experimental observables of heavy-ion collisions probing the formation and properties of QGP are briefly discussed. Some observables measured in proton-proton collisions as a reference for nucleus-nucleus collisions are also presented shortly.

2.3.1 Global observables

The global observables describe the state and dynamical evolution of the bulk matter created in a heavy ion collision, and allow to study the global properties of the collision. The main global observables include multiplicity distributions, momentum distribution of identified particles and correlations between particles, *etc.*

Multiplicity distributions:
The multiplicity distributions of charged particles constrain the particle production mechanisms and be related to the initial energy density reached during the collisions. The initial energy density can be estimated with the help of a formula originally proposed by Bjorken [57] which relates the initial energy density ε to the transverse energy E_T, written as Eq. 2.2. At LHC energies, the measurement result implies

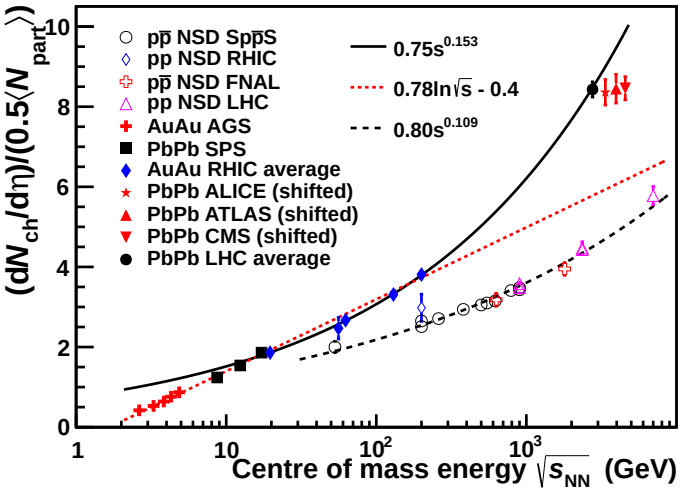

Figure 2.13: Charged particle pseudo-rapidity density $dN_{ch}/d\eta$ per colliding nucleon pair ($0.5N_{part}$)as a function of center of mass energy ($\sqrt{s_{\rm NN}}$) for pp and central nucleus-nucleus collisions. The black solid line is a power law with $s^{0.15}$ for the heavy-ion data, and the black dash line is for pp($p\bar{p}$) data with $s^{0.11}$.

that the initial energy density (at $\tau_0 = 1$ fm/c) is about 15 GeV/fm^3 [104], which is approximate three times higher than in Au+Au collisions at RHIC [105–108].

Since there are larger experimental acceptance of the detectors at LHC, the measured high multiplicity allows to obtain a very precise determination of the collision geometry in each event. Fig. 2.13 shows the charged particle multiplicity per participant pair [109–111], $dN_{ch}/d\eta/(0.5N_{part})$, at the LHC, compared to results from lower energies [112–114] at central A+A collisions. The measured multiplicity of heavy-ion collisions at LHC is significantly larger than those measured at lower energies at RHIC, but follows a power law with $s^{0.15}$. Also the pp measurements are well described by a power law, however with a less steep dependence on energy as $s^{0.11}$.

The centrality dependence of particle production is compared in Fig. 2.14 with the one measured at RHIC, which is normalized to the LHC result at $N_{part} = 350$ by scaling with a factor of 2.14. The result of LHC shown in the figure is the average

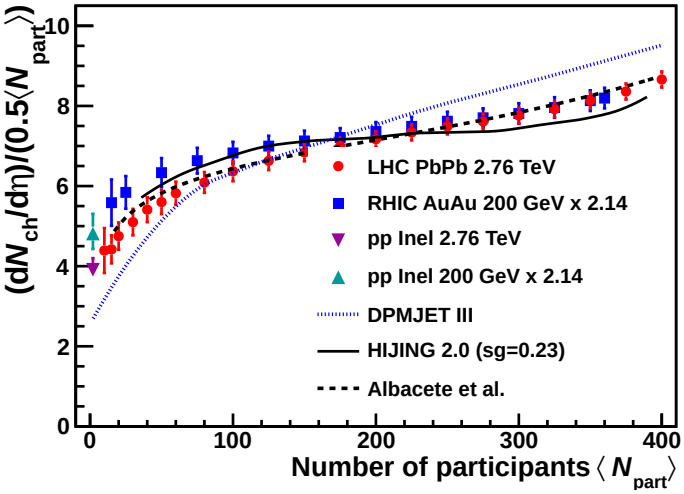

Figure 2.14: $dN_{ch}/d\eta$ per colliding nucleon pair as a function of the number of participating nucleons together with model predictions for Pb+Pb at $\sqrt{s_{\rm NN}}$=2.76 TeV.

value from the three LHC detectors [109–111], which are in excellent agreement with each other (within 1-2%). Compared to the averaged and scaled 200 GeV Au+Au data [112–114], it shows a similarity in the shape of both distributions. However, both distributions of the peripheral collisions extrapolate towards respective the measurements in pp inelastic collisions ($N_{part} = 2$) at $\sqrt{s} = 200$ GeV and 2.76 TeV, and they start to separate because of the different energy dependence which can be saw in Fig. 2.13.

Hanbury Brown-Twiss interferometry:

To obtain insight into the properties of the QGP created in heavy-ion collisions, it is important to extract the space-time characteristics of the emitting source. The measurement of two-particle correlations of identified particles at low relative momenta, widely known as Hanbury Brown-Twiss (HBT) interferometry or femtoscopy, allows us to characterize the size and lifetime information of the particle emitting source, created in heavy-ion collisions [115, 116]. The measurement of the HBT correlation are shown in Fig. 2.15 in central Pb+Pb collisions at $\sqrt{s_{\rm NN}} = 2.76$ TeV as a function of the charged particle density $dN_{ch}/d\eta$ [117], together with the measurements at lower energies [118–125]. The total freeze-out volume is given as the product of a ge-

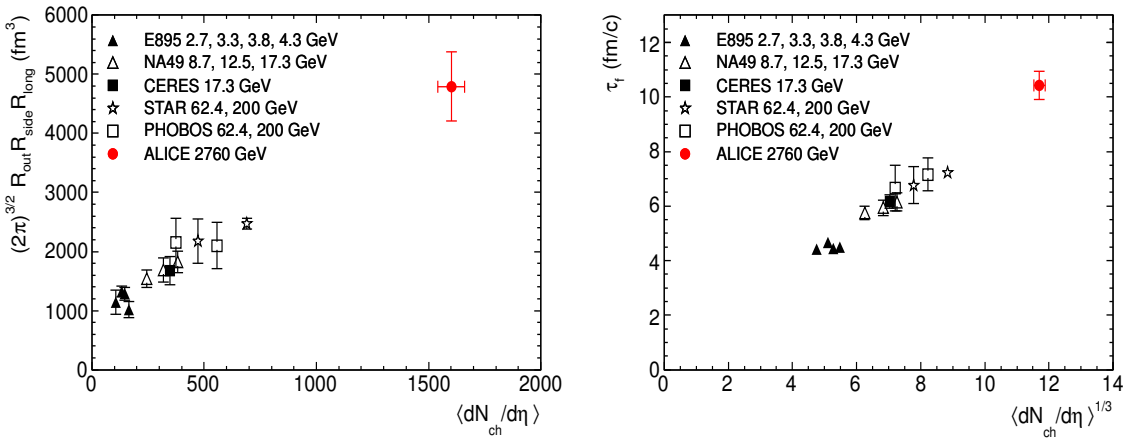

Figure 2.15: Left: Product of the three pion HBT radii at $k_T = 0.3$ GeV/c. Right: Decoupling time extracted from $R_{long}(k_T)$. The ALICE results (red filled dot) are compared to those obtained for central gold and lead collisions at lower energies at the AGS [118], SPS [119–121] and RHIC [122–124].

ometrical factor and the radii measured in three orthogonal directions (called R_{long}, R_{side} and R_{out}). The lifetime was estimated from the pair-momentum dependence of R_{long}. The systematics of the product of the three radii are shown in the left panel of Fig. 2.15. The product of the radii, which is connected to the volume of the homogeneity region, shows a linear dependence on the charged-particle pseudo-rapidity density and is two times larger at the LHC than at RHIC. The size of the homogeneity region is inversely proportional to the velocity gradient of the expanding system. The longitudinal velocity gradient in a high energy nuclear collision decreases with time as $1/\tau$ [126]. Therefore, the magnitude of R_{long} is proportional to the total duration of the longitudinal expansion. It was found the system lifetime is proportional to the cube root of the particle density and increases by about 30% to 10 fm/c in central Pb+Pb collisions collisions as shown in the right panel of the

Fig. 2.15.

2.3.2 Soft probes

The soft probes are these signatures produced in the later stage of the collisions. Even if they are produced during the hadronization stage, the soft parts of the produced spectra provide very powerful tools to characterize the collective properties of the nuclear collisions and eventually the properties of a new state of matter.

Anisotropic flow:
In Fig. 2.1, we show a schematic view of the fireball created at the early stage of the collisions. In the collision if the impact parameter is not zero, the initial overlapping region of the two nuclei is not azimuthally symmetric. In this case, the pressure gradients between the center of the overlapping region and its periphery in the collision vary with azimuth, and is stronger in the direction of the reaction plane defined by the impact parameter and the beam direction z than in the direction orthogonal to it, see Fig. 2.16. The initial coordinate-space anisotropy is converted

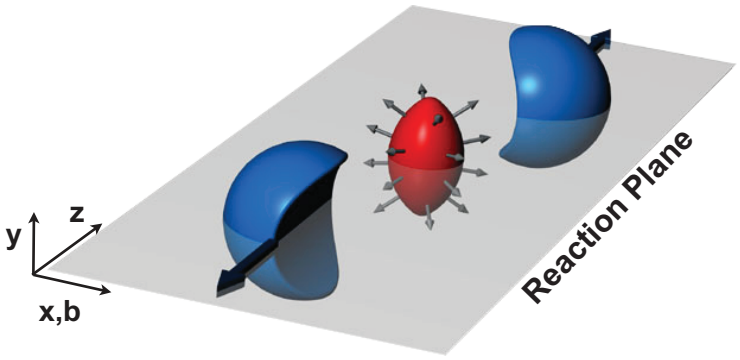

Figure 2.16: Almond-shaped interaction volume after a non-central collision of two nuclei, where z direction is the collision axis.

into a momentum-space anisotropy since the pressure gradient is not azimuthally symmetric, see Fig. 2.17. The spatial anisotropy is largest early in the evolution of the collision. However, with the fireball expanding it becomes more spherical, thus this driving force quenches itself. Therefore, the momentum anisotropy is particularly sensitive to the early stages of the system evolution [127]. Anisotropic particle distributions were first suggested in [128] as a signal of the collective flow in ultra-relativistic heavy-ion collisions. A convenient way of characterizing the various patterns of the anisotropic flow is to use a *Fourier expansion* of the invariant triple

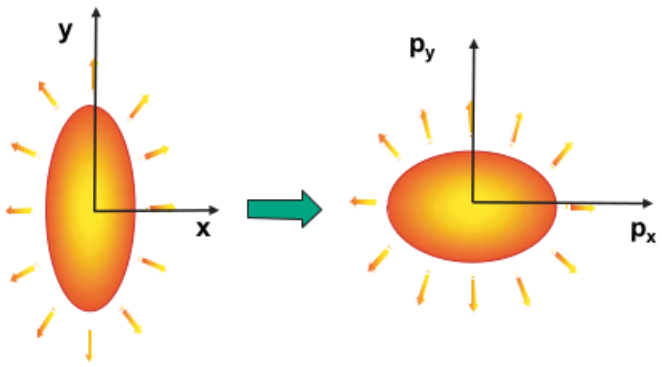

Figure 2.17: Coordinate-space anisotropy and momentum-space anisotropy.

differential distributions as [129]:

$$E\frac{d^3N}{d^3p} = \frac{1}{2\pi}\frac{d^2N}{p_{\mathrm{T}}dp_{\mathrm{T}}dy}(1+2\sum_{n=1}^{\infty}\upsilon_n\cos[n(\varphi-\Psi_R)]) \tag{2.15}$$

where E is the energy of the particle, p the momentum, p_{T} the transverse momentum, φ the azimuthal angle, y the rapidity, and Ψ_R the reaction plane angle. The $\upsilon_n = \langle\cos[n(\varphi-\psi_n)]\rangle$ is the n-th harmonic Fourier coefficient. The first order harmonics υ_1 and the second order harmonics υ_2 are usually called *directed flow* and *elliptic flow*, respectively. While the υ_3 is called *triangular flow*. The Elliptic flow depends on fundamental properties of the created matter, in particular the sound velocity and the shear viscosity. It has its origin in the amount of rescattering and in the spatial eccentricity of the collision zone. Detailed measurements of elliptic flow provide an experimental handle on the early information about the system.

An overview of the υ_2 measurements performed at RHIC can be found in [130–134]. The ALICE experiment has provided υ_2 measurement in Pb+Pb collisions at $\sqrt{s_{\mathrm{NN}}} = 2.76$ TeV [135]. Fig. 2.18a shows υ_2 as a function of p_{T} at centrality 40-50% obtained with different methods, To compare, STAR measurements [136, 137] at the same centrality from Au+Au collisions at $\sqrt{s_{\mathrm{NN}}} = 200$ GeV are indicated by the shaded area. The comparison indicates that the value of $\upsilon_2(p_{\mathrm{T}})$ does not change within uncertainties from $\sqrt{s_{\mathrm{NN}}} = 200$ GeV to 2.76 TeV.

The integrated elliptic flow measured in the 20-30% centrality class from ALICE [135] is compared to results from lower energies [138, 139] in Fig. 2.19. The comparison shows there is a continuous increase in the magnitude of the elliptic flow for this centrality region from RHIC to LHC energies. Compared to the elliptic flow measurements in Au+Au collisions at $\sqrt{s_{\mathrm{NN}}} = 200$ GeV, a factor about a 30% increasing is observed in the magnitude of υ_2 at $\sqrt{s_{\mathrm{NN}}} = 2.76$ TeV.

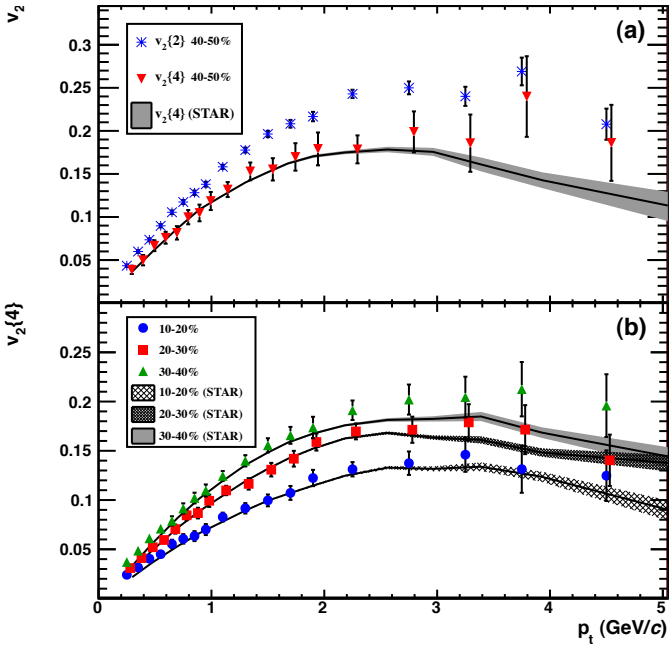

Figure 2.18: Measurements of charged particle v_2 as a function of p_T in Pb+Pb collisions at $\sqrt{s_{NN}} = 2.76$ TeV [135]. a) $v_2(p_T)$ for the centrality bin 40-50% from the 2- and 4-particle cumulant methods for this measurement and for Au+Au collisions at $\sqrt{s_{NN}} = 200$ GeV. b) $v_2 4(p_T)$ for various centralities compared to STAR measurements. The data points in the 20-30% centrality bin are shifted in p_T for visibility.

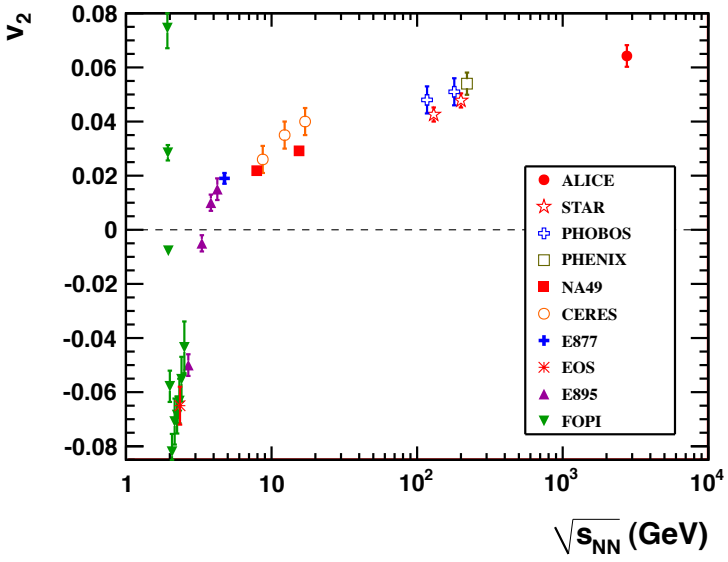

Figure 2.19: Integrated elliptic flow in Pb+Pb collisions at 20-30% centrality class at $\sqrt{s_{NN}} = 2.76$ TeV compared with results from lower energies taken at similar centralities [138, 139].

Elliptic flow of identified hadrons is sensitive to the hydrodynamical radial expansion of the medium. The identified particle (π, K, p, Ξ, Ω) $v_2(p_{\rm T})$ as a function of $p_{\rm T}$, together with theoretical prediction from ideal hydrodynamics [140], are shown in the left panel of Fig. 2.20 [141, 142]. The measurements indicate that v_2 has larger values for lower mass particles at $p_{\rm T} < 2$ GeV/c region. The hydrodynamical model describes the data very well for all particle species up to intermediate $p_{\rm T}$. The

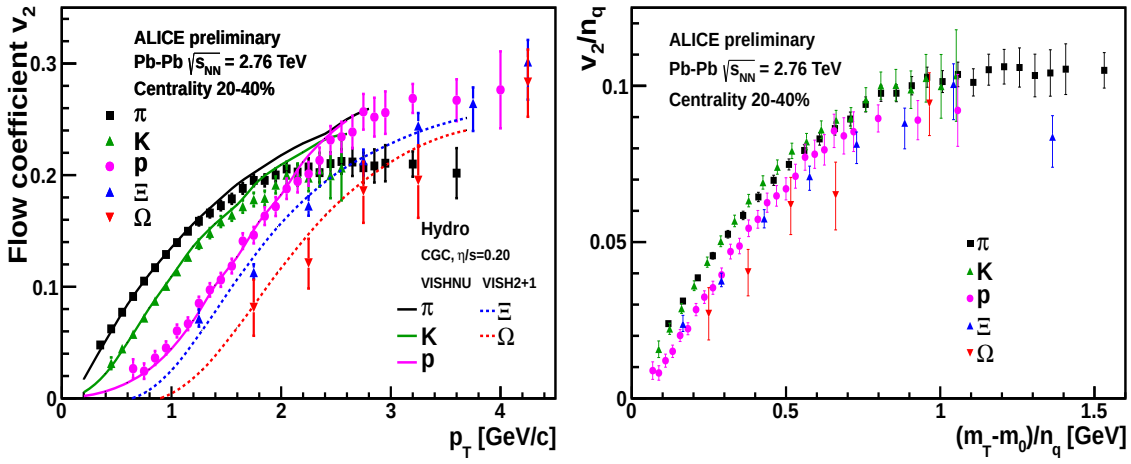

Figure 2.20: Left: Integrated elliptic flow at 2.76 TeV in Pb+Pb collision at 20-30% centrality class compared with results from lower energies taken at similar centralities [138, 139]. Right: Elliptic flow for mesons and baryons, scaled by the respective number of valence quarks n_q as a function of $(m_T - m_0)/n_q$.

mesons (π, K) are well agreement with the predicted flow below 1.5 GeV/c, however the baryons v_2 follows the hydrodynamical prediction curves, within the still large experimental errors, up to about 3 GeV/c. The different behaviour of mesons and baryons has been interpreted as a sign of *quark recombination* or *coalescence* [144–147]. A universal scaling for the flow of both mesons and baryons is observed in RHIC by measuring v_2/n_q as a function of $(m_T - m_0)/n_q$ [134], where n_q is the number of constituent quarks ($n_q = 2$ or 3) and $(m_T - m_0)$ is the transverse kinetic energy ($m_T = \sqrt{p^2 + m_0^2}$). The same measurement at ALICE is presented in the right panel of Fig. 2.20 [141, 142]. The measured results indicate that $(m_T - m_0)/n_q$ scaling of v_2 is at the level of $\pm 20\%$ for $p_{\rm T} > 3$ GeV/c in contrast to the observation at the top RHIC energy [143].

Strangeness enhancement:
The initial strangeness content of the colliding nuclei is very small and there is no net strangeness. In the collisions, the strange quark (s) and anti-quark ($\bar{s}$) are produced, which subsequently combine with other quarks and anti-quarks to form

strange particles, *e.g.* $K^+(u\bar{d})$, $\Sigma^+(uus)$. If the QGP is created after the nucleus-nucleus collisions, there would be many deconfined partons including gluons (g). It was proposed that strangeness production would be increased due to the formation of a QGP compared to that from a hadron gas [148]. The enhancement is thought from the high production rate of gluon fusion $gg \to s\bar{s}$ in an equilibrated gluon-rich plasma [148, 149]. During the hadronization, these (anti)strange quarks combine with other (anti)quarks which result in a significant increase of the strange particle production. Therefore, compared to pp collisions, the production strangeness is a significant signal to characterize the formation of the QGP phase.

The yield enhancement factor, $E(i)$, for a particle specie i is calculated using [150]:

$$E(i) = \frac{Y^{AA}(i)/N_{part}^{AA}}{\mathrm{Y^{NN}}(i)/N_{part}^{NN}} \tag{2.16}$$

where $Y^{AA}(i)$ and $Y^{NN}(i)$ are the yields of strange particles. N_{part}^{AA} and N_{part}^{NN} are the numbers of nucleon participants in nucleus-nucleus and nucleon-nucleon collisions, respectively. Fig. 2.21 shows the $E(i)$ distribution of strange particles, Ω^-, $\bar{\Omega}^+$, Ξ^-, $\bar{\Xi}^+$, Λ and $\bar{\Lambda}$, as a function of N_{part} from ALICE measurements [151]. The same measurements of RHIC can be found in [150]. It can be seen that there is an

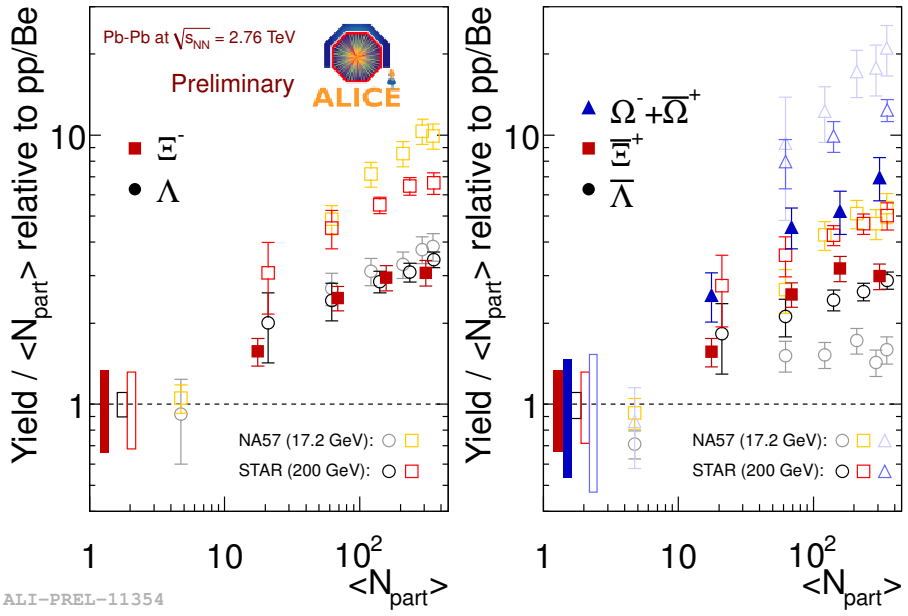

Figure 2.21: Strange particle production as a function of Npart for $\sqrt{s_{\mathrm{NN}}}$ = 0.017, 0.2, and 2.76 TeV collisions relative to pBe (NA57) and pp (STAR, ALICE).

enhancement in the yields over that expected from N_{part} scaling for all the particles presented.

2.3.3 Hard probes

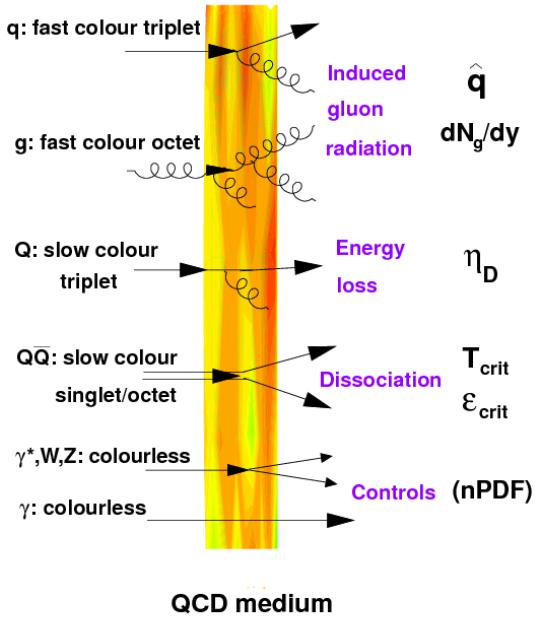

Figure 2.22: Tomography of QCD medium.

The hard scatterings produce "quasi-free" partons carrying large energy in the early time of the collisions. These partons passing through the hot and dense QCD matter have energy loss via gluon bremsstrahlung and multiple scattering in the medium. The final particles with large transverse momentum and/or mass, p_{T} , $m \geq Q_0 \gg \Lambda_{QCD}$, where $Q_0 = 1$ GeV and $\Lambda_{QCD} \approx 0.2$ GeV is the QCD scale, constitute valuable tools to study the "tomography" of the QGP [152], see Fig. 2.22 [178]. Some mainly observables of hard probes, such as jet quenching, production of quarkonium states (J/Ψ, Υ) and thermal dileptons and photons, are presented briefly in the following.

Jet quenching:

The initial energetic partons are produced by short-distance hard-scatterings at the early stage during the collisions. The partons have to go through the hot and dense QGP medium and are expected to interact with the medium and lose their energy. This parton energy loss is often referred to as "jet quenching". The fragmentation of the reduced-energy parton will yield fewer particles at high-p_{T} in the final state. That is to say the energy lost by a parton provides fundamental information on the thermodynamical and transport properties of the medium. A comparison of the final-state high-p_{T} particle yields in pp and A+A collisions will thus reveal the effect of jet-quenching.

Two main experimental techniques are available to explore the effect of jet-quenching. One is to measure inclusive single particle spectrum and make comparison with the measurement in pp collisions, which is called *nuclear modification factor*, R_{AA}, and defined as:

$$R_{AA}(p_{\mathrm{T}}) = \frac{d^2N_{AA}/dp_{\mathrm{T}}d\eta}{\langle T_{AA}\rangle d^2\sigma_{NN}/dp_{\mathrm{T}}d\eta} \tag{2.17}$$

where N_{AA} and σ_{NN} are the particle yield in nucleus-nucleus collisions and the

cross section in nucleon-nucleon collisions, respectively. T_{AA} is the nuclear overlap function, which can be obtained from the ratio of the number of binary nucleon-nucleon collisions, $\langle N_{coll} \rangle$, calculated from the Glauber model, and the inelastic nucleon-nucleon cross section. This measurement has been extensively studied at RHIC, and can be found in [105–108]. Instead of R_{AA} one can also approximate the centrality dependence by measuring R_{CP}, the ratio of central over peripheral events. The evolution of the nuclear modification factor with center-of-mass energy from SPS [153, 154] to RHIC [155, 156] to the LHC [157] is presented in Fig. 2.23. At LHC, the R_{AA} reaches a minimum value of 0.13 around 6-7 GeV/c in the 0-5% centrality. At higher-p_{T}, the value of R_{AA} rises and levels off above 40 GeV/c at a value of approximately 0.5. Besides charged hadrons, other types particle are selected

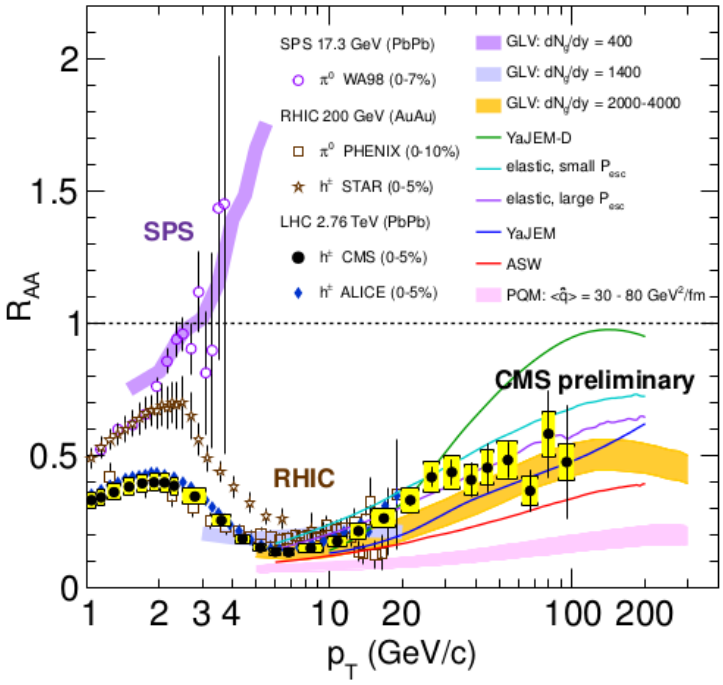

Figure 2.23: Measurements of the nuclear modification factor R_{AA} in central heavy-ion collisions at three different center-of-mass energies as a function of p_{T} for neutral pions and charged hadrons [153–157], compared to several theoretical predictions [159–162]. The error bars around the points are the statistical uncertainties, and the yellow boxes around the CMS points are the systematic uncertainties. The bands for several of the theoretical calculations represent their uncertainties. The plot is taken from [158].

to measure the nuclear suppression factor for distinguishing the exact mechanisms of energy loss. Measurements exist for identified π^0, K^0_S, Λ [163, 164], isolated photons [165], Z, W [166–169], D-mesons [164], jets [170], J/ψ [168, 171, 172], and Υ [172]. A summary of R_{AA} measurements for different particle species at the most

centrality is presented in Fig. 2.24.

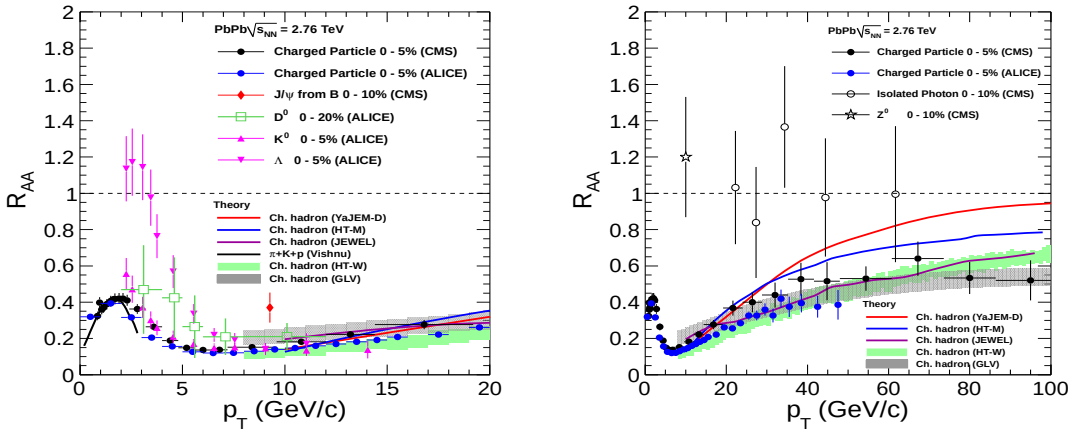

Figure 2.24: Nuclear modification factor R_{AA} as a function of p_{T} for a variety of particle species, together with theoretical predictions. Experimental error bars correspond to the total error (statistical and systematic errors added in quadrature). Left: Low momentum region $p_{\mathrm{T}} < 20$ GeV; Right: Entire momentum range measured at LHC. The curves show the results of various QCD-based models of parton energy loss [173–176]. More details can be found in [177].

The other approach is to reconstruct jets directly and compare jet yields in Pb+Pb with jet production in pp, as well as to measure jet-jet and jet-like particle energy and angular correlations [177]. Jets are formed by the fragmentation production from high-p_{T} partons as they pass through the created hot and dense matter. The energy of partons dissipation into the medium can be studied by measuring the asymmetry of dijets in nucleus-nucleus collisions as a function of centrality and/or by comparing to the same measurements from pp collisions. The asymmetry characterizes the dijet momentum balance (or imbalance) quantitatively, which is defined as [179]:

$$A_J = \frac{E_{T,1} - E_{T,2}}{E_{T,1} + E_{T,2}} \tag{2.18}$$

The $E_{T,1}$ and $E_{T,2}$ are the transverse energy of two back-to-back two jet, leading and subleading jet, respectively. The measurement from ATLAS is p_T instead of E_T [180]. The centrality dependence of dijet asymmetry A_J in Pb+Pb collisions from ATALS is shown in Fig. 2.25 and is compared with pp data and with fully-reconstructed HIJING+PYTHIA simulated events [179]. simulations. Similar with nuclear modification factor from single particle, the nuclear modification factors of jets, $R_{\mathrm{AA}}^{\mathrm{Jet}}$ and $R_{\mathrm{CP}}^{\mathrm{Jet}}$, are measured in ALICE [181] and ATLAS [182]. The ALICE measurements are shown in Fig. 2.26. As a reference, the spectrum from pp collisions at the same center-of-mass energy is estimated from the PYTHIA simulations. The

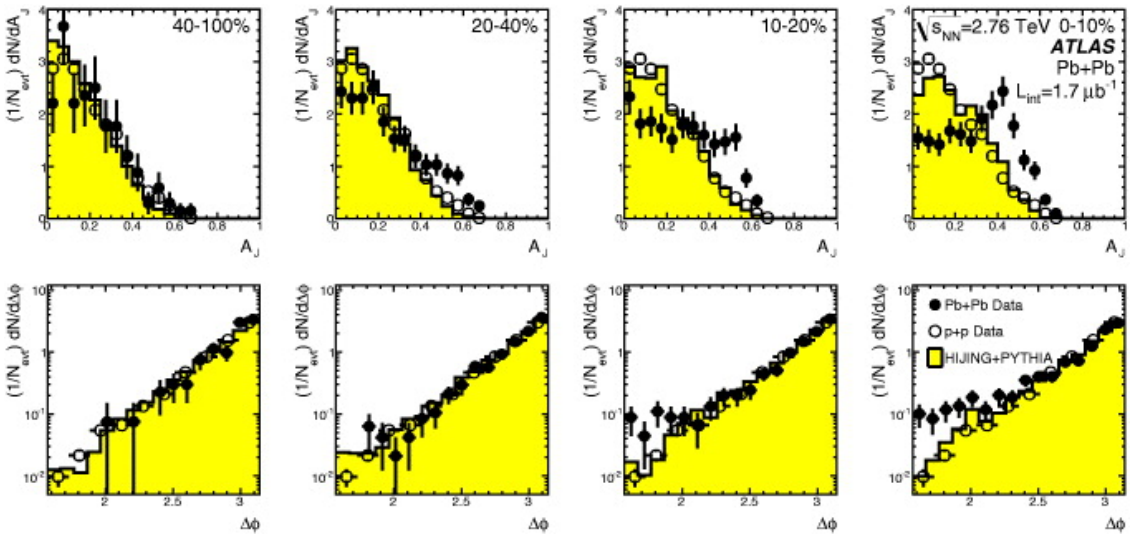

Figure 2.25: Top: Dijet asymmetry distributions for data (points) and unquenched HIJING with superimposed PYTHIA dijets (solid yellow histograms), as a function of collision centrality. Bottom: Distribution of $\Delta\varphi$, the azimuthal angle between the two jets, for data and HIJING+PYTHIA, also as a function of centrality. [179].

results for four centralities bins in R = 0.3 with *Anti*-k_T *algorithm* are shown. A strong nuclear suppression qualitatively and quantitatively similar to the R_{AA} of inclusive hadrons shown previous is observed in the most central collisions.

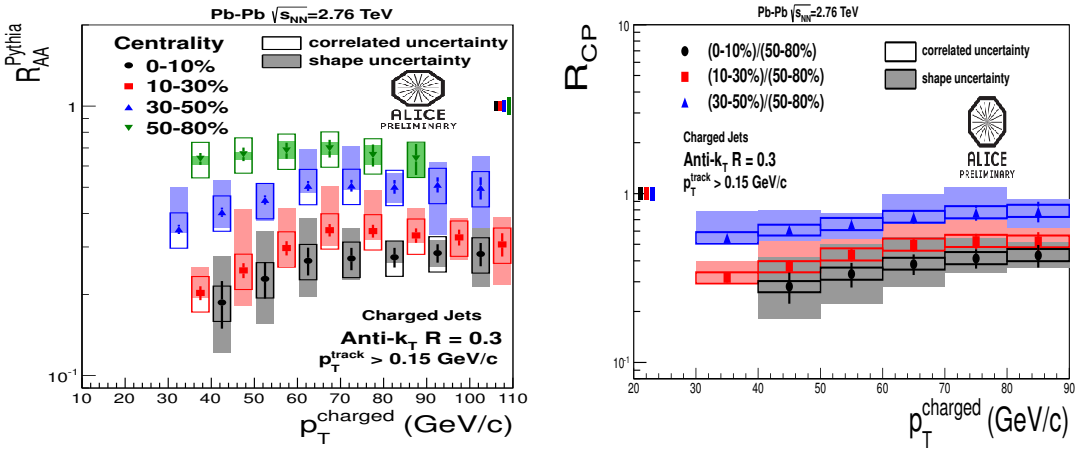

Figure 2.26: Left: Nuclear modification factor R_{AA} for jets reconstructed with radius R = 0.3, and PYTHIA Perugia0 simulation as the reference. Right: R_{CP} for jet radius R = 0.3 [181].

As mentioned previous, the jet-like hadron correlations, aslo called *two-particle correlations*, is a technique to characterize the jet quenching. In such an analysis, a particle is chosen from a p_{T} region and called the *trigger particle*. The so called *associated particles* from another p_{T} region are correlated to the trigger particle

where $p_{\mathrm{T}}^{\mathrm{assoc}} < p_{\mathrm{T}}^{\mathrm{trig}}$ generally. The associated per-trigger yield is measured as a function of the azimuthal angle difference $\Delta\varphi = \varphi_{\mathrm{trig}} - \varphi_{\mathrm{assoc}}$ and pseudo-rapidity difference $\Delta\eta = \eta_{\mathrm{trig}} - \eta_{\mathrm{assoc}}$:

$$Y(\Delta\varphi, \Delta\eta) = \frac{1}{N_{\mathrm{trig}}} \frac{dN_{\mathrm{assoc}}}{d\Delta\varphi d\Delta\eta} \tag{2.19}$$

where N_{assoc} is the number of particles associated to a number of trigger particles N_{trig}. This quantity is measured for different ranges of $p_{\mathrm{T}}^{\mathrm{trig}}$ and $p_{\mathrm{T}}^{\mathrm{assoc}}$. Generally, in the two-particle correlations, the azimuthal angle distribution at $\Delta\varphi \sim 0$ and $\Delta\varphi \sim \pi$ are named *near side* and *away side*, respectively. Fig. 2.27 shows a typical di-hadron correlations measurements from RHIC [183]. The di-hadron correlations

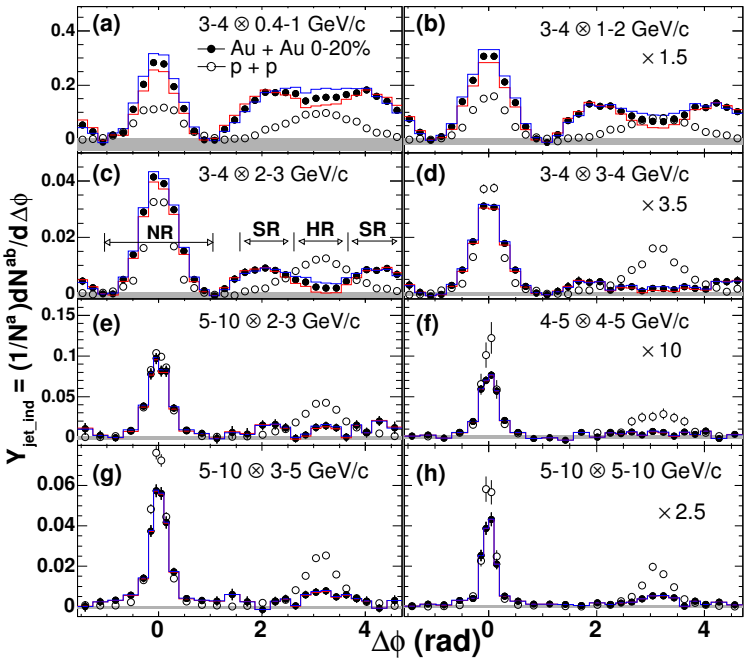

Figure 2.27: Per-trigger yield versus $\Delta\varphi$ for various trigger and associated p_{T} ($p_{\mathrm{T}}^{\mathrm{trig}} \otimes p_{\mathrm{T}}^{\mathrm{assoc}}$) in pp and 0-20% Au+Au collisions. Solid histograms (shaded bands) indicate elliptic flow (ZYAM) uncertainties. [183].

in Au+Au reactions at RHIC show several striking features, mainly summarized in following:

- The away-side azimuthal peak at $\Delta\varphi \sim \pi$ shows strong suppression (even disappeared) with increasing centrality for hadrons with $p_{\mathrm{T}}^{\mathrm{assoc}} > 2$ GeV/c.
- The vanishing of the away-side peak is accompanied with an enhanced production of lower p_{T} hadrons ($p_{\mathrm{T}}^{\mathrm{assoc}} < 2$ GeV/c) with a characteristic double-

peak structure at $\Delta\varphi \sim \pi \pm 1.1 - 1.3$. Different mechanisms have been proposed to explain the phenomenon, such as the medium-induced gluon radiation [184, 185], the Mach-cone wave formed by the passing partons in the QGP [186, 187], the path-length-dependent jet energy loss [188, 189], the Cerenkov radiation from the jet [190], the strong parton cascade [191], and triangular flow [192], *etc.*

- The away-side suppressed peak reappears when both p_{T} of trigger and associated particles go to high, shown in the *g* and *h* panels. This has been interpered that the selected jets in the correlations are produced in the surface of the fireball, and the parton in the opposite direction of the trigger particle passing through a short length in the medium has lost a significant amount of its energy but survived to undergo fragmentation in the vacuum.

- A large broadening ("ridge") was observed on the near-side in pseudo-rapidity direction at Au+Au collisions, and no in d+Au collisions [193], see Fig. 2.28. Some models try to explain this phenomenon. *e.g*, triangular flow [192], and radiated gluons broadened by *longitudinal flow* [194], or by *QCD magnetic fields* [195], or by *Anisotropic plasma* [196], *medium heating* and *recombination model* [197], *radial flow* and *trigger bias* [198], *momentum kick model* [199], *etc.*

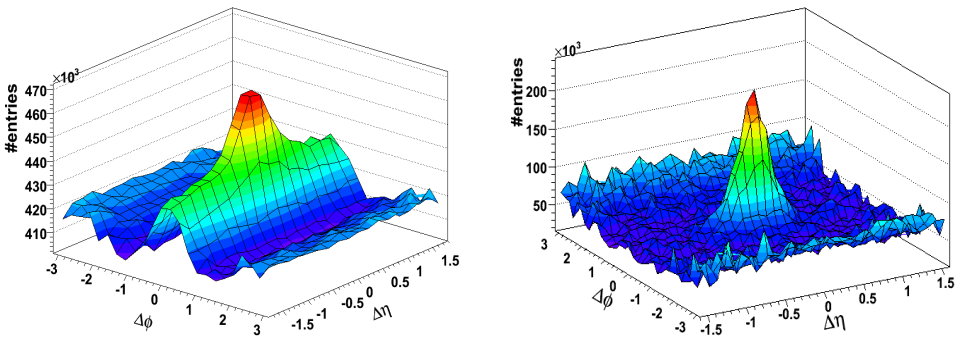

Figure 2.28: "Ridge" structure was observed in the Au+Au collisions (left), and not shown in d+Au collisions (right) [193].

Quarkonium states:

Heavy quarkonia, charmonium (J/ψ, ψ, χ_c, *etc.*) and bottomonium (Υ(1S, 2S, 3S), χ_b, *etc.*), containing at least one heavy quark (c or b) are important probes of the

QGP phase [200]. The heavy quarks are produced in the beginning of the collisions and interact with the medium and can be slowed down. Furthermore, they are however not completely thermalized due to their large masses. Compared to in pp collisions, the quarkonia are predicted to have suppression in heavy-ion collisions, which is considered as a consequence of deconfinment ("melting") in the QGP [201]. The suppression is predicted to occur above the critical temperature of the medium (T_c) and depends on the $Q\bar{Q}$ binding energy. Of course, the initial state effects presented at Sec. 2.2.3.1 are further possible changes to the quarkonium production in heavy-ion collisions [202, 203].

In the past decades, the charmonium studies in heavy-ion collisions have been measured at SPS [204] and RHIC [205]. At LHC energies, the measurement of quarkonia production suppression [171, 172] for both J/ψ and Υ is shown in Fig. 2.29. At the LHC another effect, namely regeneration, due to the high density of $c\bar{c}$ pairs was predicted, and in fact explains why the J/ψ is less suppressed for LHC than for RHIC in Fig. 2.29.

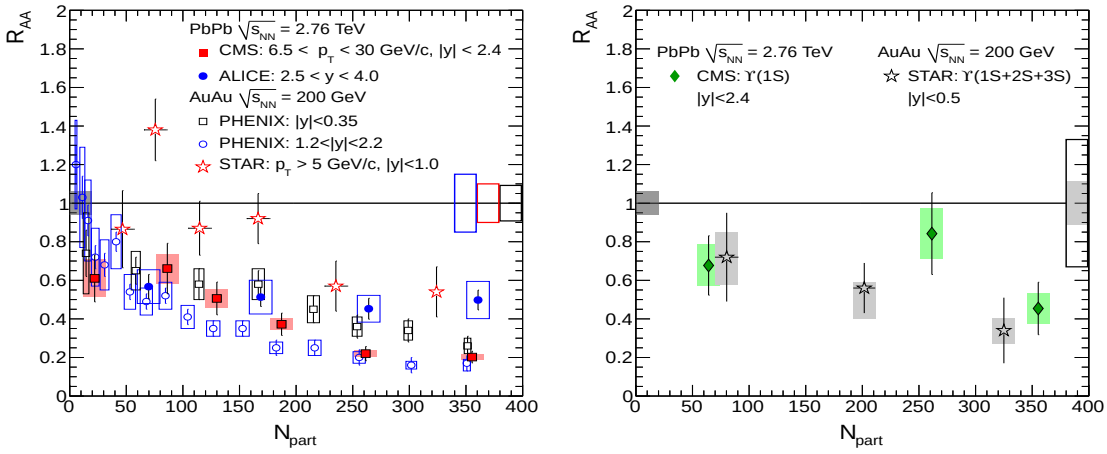

Figure 2.29: Nuclear modification factor R_{AA} as a function of centrality for J/ψ (left) and Υ (right) at LHC, together with the measurements from RHIC [206–208].

Thermal dileptons and photons:

Thermal dileptons and photons produced during the entire space-time evolution of the system belong to electromagnetic probes to investigate the thermodynamical state of the early stages of collisions. These electromagnetic probes interact with medium or other particles only electromagnetically, and their mean free path is considerably larger than the size of the collision volume, therefore they are considered as the ideal probes. Thermal dileptons are directly related to chiral restoration, and the photons are a control/complementary probe of the partonic phase in heavy-ion

collisions because of without strong interactions with the partons in the QGP. The dilepton production is mainly from annihilation of quark and antiquark ($q\bar{q} \rightarrow \gamma^* \rightarrow l^+l^-$). The left panel of Fig. 2.30 shows a schematic view of the dilepton e^+e^- pair mass distribution. At the leading order, the production processes of photons are Compton scattering ($qg \rightarrow \gamma q$) and annihilation ($q\bar{q} \rightarrow \gamma g$). More processes of photons are shown in the right panel of Fig 2.30.

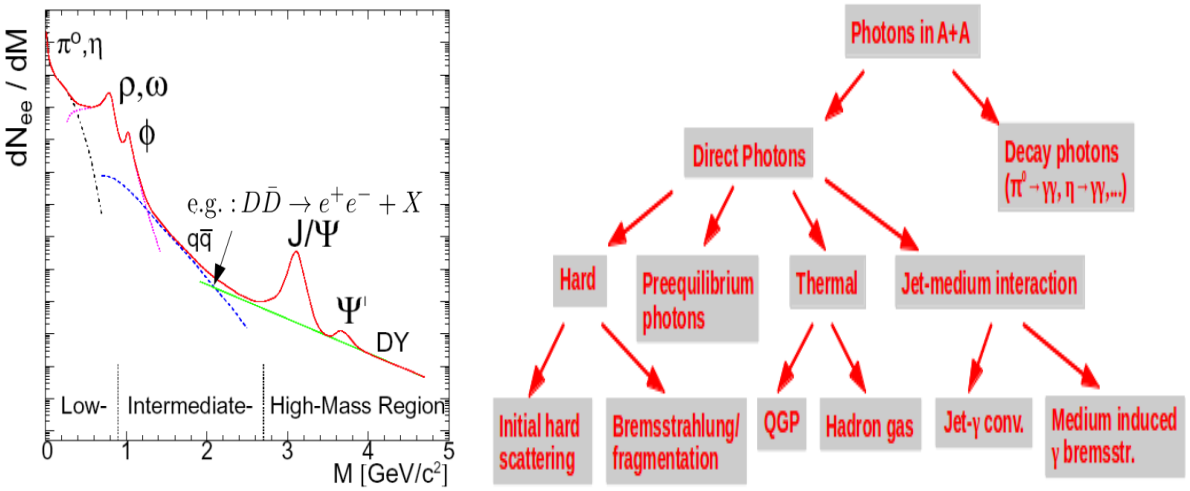

Figure 2.30: Left: Schematic view of the dilepton e^+e^- pair mass distribution. Right: Photon sources in nucleus-nucleus collisions.

The dileptons in low mass region was measured by the CERES collaboration [209], which show a strong enhancement at invariant masses of about 400 MeV for SPS-energy S+Au heavy-ion collisions as compared to proton-proton as well as proton-nucleus collisions. At RHIC, the enhancement of dileptons at low-mass was also measured [210] and shown in Fig. 2.31. The left panel of the figure shows that the low-mass enhancement is concentrated in the first two centrality classes, 0-10% and 10-20%. When go to more peripheral collisions, the enhancement diminishes. The right panel shows the measurements by quantifying the centrality dependence of the enhancement in the mass region $0.15 < m_{ee} < 0.75$ GeV/c^2 and $0 < m_{ee} < 0.1$ GeV/c^2 scaled by the number of participating nucleon pairs ($N_{part}/2$).

The direct photons was firstly measured in ultra-relativistic heavy-ion reactions in WA98 experiment in central Pb+Pb collisions at $\sqrt{s_{\rm NN}} = 17.2$ GeV [211]. In the jet quenching, the nuclear modification factor of hadrons shows a strong suppression at high-$p_{\rm T}$. Simiar measurements, the nuclear modification factor of direct photons, were analyzed at RHIC [212] and LHC [213] as shown in Fig. 2.32. At RHIC, the nuclear modification factor R_{AA} of direct photon was found to be consistent with

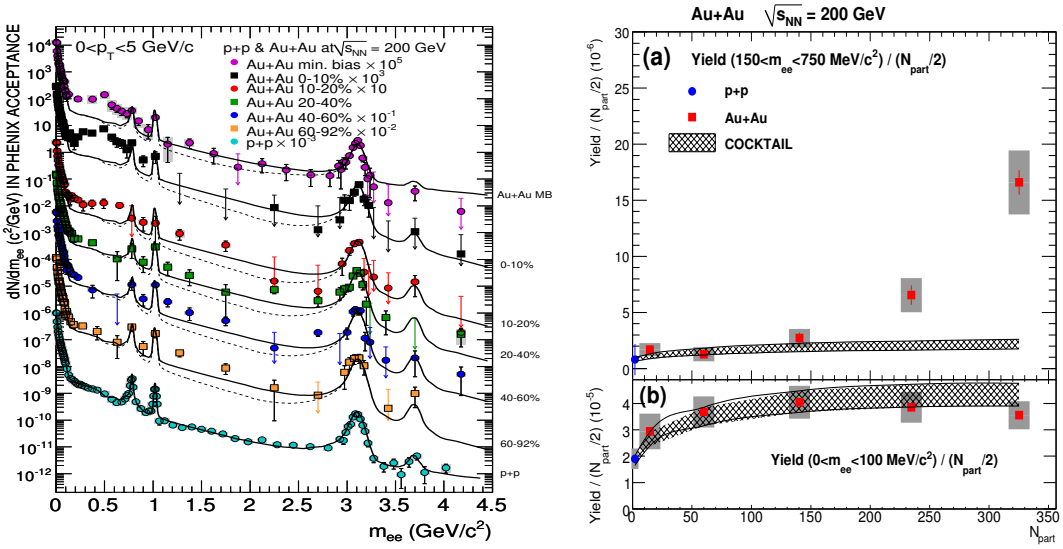

Figure 2.31: Left: Invariant mass spectrum of e^+e^- pairs at $0 < p_T < 5$ GeV/c compared to expectations from the model of hadron decays for pp and for different Au + Au centrality classes. Right: Dielectron yield per participating nucleon pair ($N_{part}/2$) as function of N_{part} for two different mass ranges (a: $0.15 < m_{ee} < 0.75$ GeV/c^2, b: $0 < m_{ee} < 0.1$ GeV/c^2) compared to the expected yield from the hadron decay model.

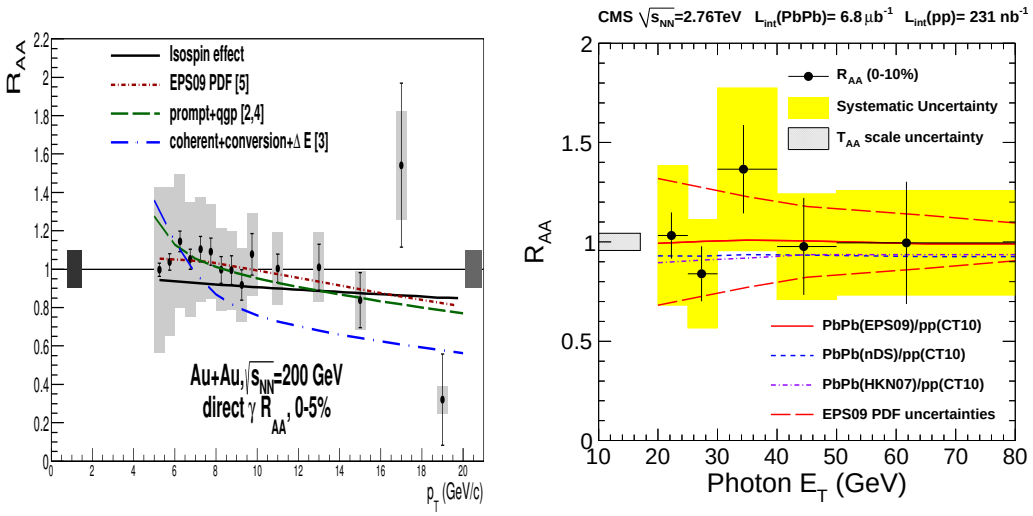

Figure 2.32: Left: Nuclear modification factor of direct photons for 0-5% most central events in Au+Au Collisions at 200 GeV, compared with theoretical calculations [214–217] for different scenarios. Right: Nuclear modification factor of isolated photons as a function of the photon E_T measured in the 0-10% most central Pb+Pb collisions at 2.76 TeV.

unity for all centralities over the entire measured p_{T} range [212]. The R_{AA} of direct photons is compared to theoretical calculations that predict modifications of the direct photon yield due to initial state and final state effects [214–217]. The comparison indicates that the data is consistent with a scenario where the hard scattered photons are produced taking account of the isospin effect and modifications of the nuclear PDFs and then simply traverse the matter unaffected [212]. The leading order direct photons are produced from Compton scattering and Annihilation processes, therefore a new analysis method, isolation technique, can be use to extract these direct photons. At LHC, the isolated photon production was measured and the nuclear modification factor of isolated photon as a function of transverse energy E_T [213]. More measurements of direct photons, such as enhanced production of direct photons [218], direct photon flow [219], can be found in the corresponding to references.

Chapter 3

ALICE Experiment at LHC

A Large Ion Collider Experiment (ALICE) [220] is one of the seven experiments at the Large Hadron Collider (LHC) located at CERN, which is designed as a dedicated heavy-ion detector to mainly explore the properties of strongly interacting matter created at extremly high energy densities and temperatures in ultra-relativistic heavy-ion collisions. It enables to investigate hadrons, electrons, photons and muons produced in heavy-ion collisions up to a high particle multiplicity environment expected at the LHC. Meanwhile, ALICE also operates in proton-proton and proton-nucleus collisions in order to obtain the required reference for QGP analysis and investigate open issues in elementary particle physics, such as the quarkonium production mechanism.

In this chapter, the main features of the LHC, CERN accelerator complex and main research purposes of each experiment are presented in Sec. 3.1. Sec. 3.2 shows more detail descriptions of the ALICE detector. The online system and offline projects in data processing chain and framework used at ALICE, including data simulation and reconstruction, is also described briefly in Sec. 3.3.

3.1 Large Hadron Collider

The LHC located at CERN laboratory is the world's highest-energy particle collider and dedicated to the pursuit of fundamental science, which is based in the northwest suburbs of Geneva on the border between Switzerland and France. It lies in a circular tunnel spanning about 27 km in circumference, at a depth ranging from 50 to 175 m beneath the earth's surface. The large accelerator follows the Large

Electron Positron[1] (LEP) collide [222] tunnel geometry, which contains two adjacent parallel beamlines (beam pipes) kept at ultra-high vacuum. Inside the beamlines, two particle beams travel in opposite directions at close to the speed of light before they are made to collide at four main points (P1, P2, P5 and P8) in the LHC, see Fig. 3.1. The CERN accelerator complex [223], shown in Fig. 3.2, is a succession of machines that accelerate particles to increasingly higher energies. Each accelerator injects the beam into the next one, which takes over to push the beam to a higher energy to nearly the speed of light. As an example, a relationship between kinetic energy and speed of a proton in the CERN accelerators can be found at in Tab. 3.1.

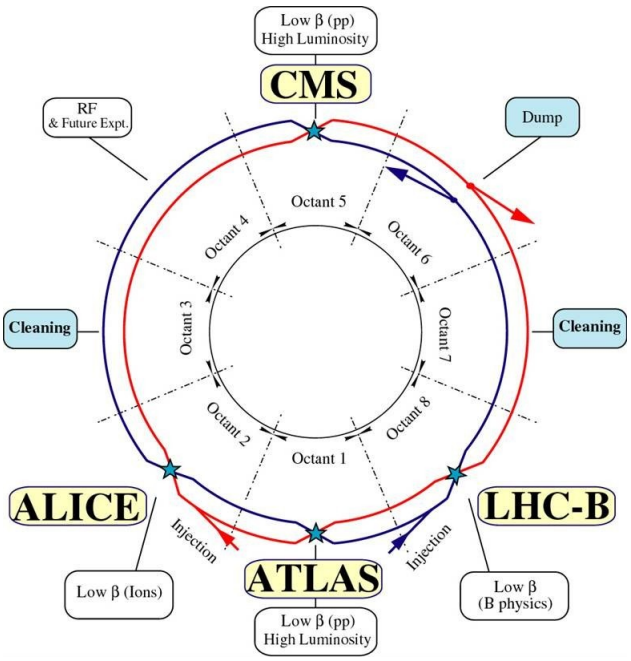

Figure 3.1: Layout of the LHC sectors and the interaction points for the four experiments. The two hadron beams, going in clockwise (Beam 1) and anticlockwise (Beam 2) directions, are shown in red and blue [222].

In pp, p+Pb and Pb+Pb collisions, protons or lead ions are accelerated through the CERN accelerator complex as following processes [223–225]:

- protons acceleration
  - Hydrogen atoms are taken from a bottle containing hydrogen. Protons are obtained by stripping orbiting electrons from hydrogen atoms in using an electric field.

[1]The Large Electron Positron collider was a particle accelerator built at CERN, which operated from 1989 to 2000 with the maximum center-of-mass energy 209 GeV [221].

Kinetic energy of a proton	Speed (%c)	Accelerator
50 MeV	31.4	Linac 2
1.4 GeV	91.6	PS Booster
25 GeV	99.93	PS
450 GeV	99.9998	SPS
7 TeV	99.9999991	LHC

Table 3.1: Relationship between kinetic energy and speed of a proton in the CERN machines. The rest mass of the proton is 0.938 GeV/c^2 [224].

  - The protons are injected into the PS Booster (PSB) at an energy of 50 MeV from the Linear accelerator2 (Linac2), and are accelerated to 1.4 GeV.
  - The protons are fed into the Proton Synchrotron (PS) where they accelerated to 25 GeV, are then transferred to the Super Proton Synchrotron (SPS) where they are accelerated to 450 GeV.
  - Finally, the protons are sent to the LHC rings where they are accelerated for 20 minutes to their maximum energy of 7 TeV. Currently, the protons are accelerated to maximal 4 TeV before colliding in the LHC.

- lead ions acceleration

  - Lead ions are produced from a highly purified lead sample heated to a temperature of around 500°C. This allows a small number of lead atoms to vaporize.
  - The lead vapour is ionized by an electron current, and formed many different charge states with a maximum around Pb^{29+}.
  - The Pb^{29+} ions are injected into the Linear accelerator (Linac3) and accelerated to 4.2 MeV per nucleon before going through a carbon foil, which strips off most of the remaining electrons to Pb^{54+}.
  - The Pb^{54+} ions are filled into the Low Energy Ion Ring (LEIR) where these ions are accumulated and accelerated to 72 MeV per nucleon, then transferred to the PS.
  - The PS accelerates the ions to 5.9 GeV per nucleon and sends them to the SPS. Before arriving at the SPS, the accelerated ions are fully stripped to Pb^{82+} by passing though a second foil.

– The ions are accelerated once more to 177 GeV per nucleon in the SPS, and then sent to the LHC. In the LHC, the lead ions can be accelerated to maximal energy per nucleon of 2.76 TeV. Currently, the ions are accelerated to maximal 1.38 TeV before colliding in the LHC.

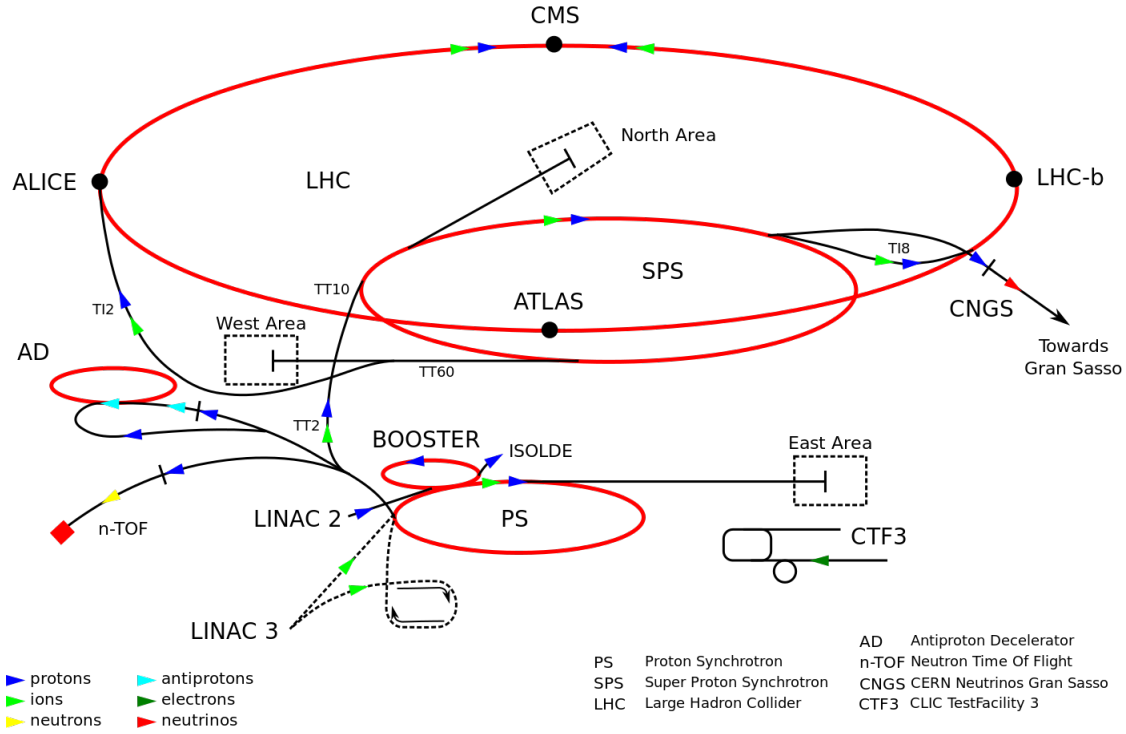

Figure 3.2: Overview of the CERN accelerator complex [224].

Since running in proton-proton collisions at $\sqrt{s} = 0.9$ TeV, the LHC has performed subsequently proton-proton collisions at center-of-mass energies $\sqrt{s} = 2.36$, 2.76, 7.0 and 8.0 TeV, lead-lead collisions at center-of-mass energy $\sqrt{s_{\rm NN}} = 2.76$ TeV and proton-lead collisions at center-of-mass energy $\sqrt{s_{\rm NN}} = 5.02$ TeV in around 3.5 years. Up to now, the achieved center-of-mass energy in pp collisions by the LHC is around 4 times higher than the former highest running at proton-antiproton collisions with $\sqrt{s} = 1.96$ TeV in the Tevatron [226] at the Fermi National Accelerator Laboratory (Fermilab). In heavy-ion collisions, the LHC runs Pb+Pb collisions at $\sqrt{s_{\rm NN}} = 2.76$ TeV, which is about 14 times higher than the Au+Au collisions at $\sqrt{s_{\rm NN}} = 200$ GeV in the RHIC [227] located at BNL. The ultimate anticipated center-of-mass energy is up to 14 TeV in pp collisions with an unprecedented luminosity of 10^{34} cm^{-2}s^{-1}, and up to $\sqrt{s_{\rm NN}} = 5.5$ TeV in Pb+Pb collisions with a peak luminosity of 10^{27} cm^{-2}s^{-1}.

The LHC mainly consists of seven experiments: ALICE, A Toroidal LHC Apparatus (ATLAS) [228], Compact Muon Solenoid (CMS) [229], Large Hadron Collider beauty (LHCb) [230], TOTal Elastic and diffractive cross section Measurement (TOTEM) [231], Large Hadron Collider forward (LHCf) [232] and Monopole and Exotics Detector At the LHC (MoEDAL) [233]. ALICE, ATLAS, CMS and LHCb are installed in the four collision points of the LHC beams. TOTEM and LHCf are the smallest experiments in the LHC, which are installed close to the CMS interaction point and near the ATLAS, respectively. MoEDAL is built at the same cavern with LHCb in 2010. A brief introduction about the main physics aims of each experiment is presented as follows [223, 224]:

- **ALICE**
  The ALICE experiment is mainly dedicated to the heavy-ion collisions for investigate the properties of the QGP created under conditions of very high temperatures and densities. Such a state of matter probably existed just a microseconds after the Big Bang, before particles such as protons and neutrons were formed. It also plays a significant role in searching particle physics in proton-proton collisions.

- **ATLAS and CMS**
  The ATLAS and CMS experiments are two general-purpose experiments designed to cover a wide range of physics. The main aims of them are to search for the Higgs boson[2], extra dimensions, and particles that constitute dark matter such as particles predicted by the supersymmetric extension of the standard model (SUSY) [235]. Meanwhile, heavy-ion collisions and the understanding of the QGP are also in the scope of the two experiments facilities. Although both of the experiments have a similar research program, they use different technical setups and designs in order to complement each other and give the possibility of cross checks and reassurance in case of discoveries.

- **LHCb**
  The LHCb experiment specializes in the study of the slight asymmetry between matter and antimatter present in interactions of B-particles (particles containing the b quark). Understanding it should prove invaluable in answering the question: "Why is our universe made of the matter we observe?"

[2]The Higgs boson is an elementary particle initially theorized in 1964 [4–7] and tentatively confirmed to exist on 14 March, 2013 [234]

- **TOTEM**
  The TOTEM experiment studies forward particles to focus on physics which is not accessible to the general-purpose experiments. It measures the effective size or "cross-section" of the proton at the LHC. Furthermore, this experiment accurately monitors the luminosity of the LHC.

- **LHCf**
  The LHCf experiment studies particles generated in the "forward" region by proton collisions in the LHC, and uses these particles as a source to simulate cosmic rays in laboratory conditions and understand the origin of ultra-high-energy cosmic rays.

- **MoEDAL**
  The MoEDAL experiment is built to directly search for the Magnetic Monopole (MM) or dyon and other highly ionizing Stable (or pseudo-Stable) Massive particles (SMPs).

3.2 ALICE detector overview

As mentioned previous, the ALICE was built as general-purpose detector for exploring the properties of QGP which is created in the ultra-relativistic heavy-ion collisions. It is also used to take the data with proton beams at the LHC energies to collect reference analysis for the heavy-ion programmes and to address several QCD topics for which ALICE is complementary to the other LHC detectors. The detector has been built by a collaboration including currently over 1000 physicists and engineers from 138 institutes in 36 countries, which is located at the Intersection Point (IP) 2 of the LHC machine, and around 80 m underground at Saint-Genis-Pouilly, France. Fig. 3.3 shows the schematic layout of ALICE detector. The detector setup consists of three parts including a central barrel detector system, several forward detectors and a muon spectrometer [236, 237].

- **Central barrel detector system**
  The central barrel system covers the pseudo-rapidity range $-0.9 < \eta < 0.9$ (polar angles $45° < \theta < 135°$) over the full azimuth, and measures and identifies charged hadrons, electrons and photons. It is embedded in a large solenoid magnet with an internal length of 12 m and a radius of 5 m and a field of 0.5 T [238]. From the collision point to the outside, the installed sub-detectors

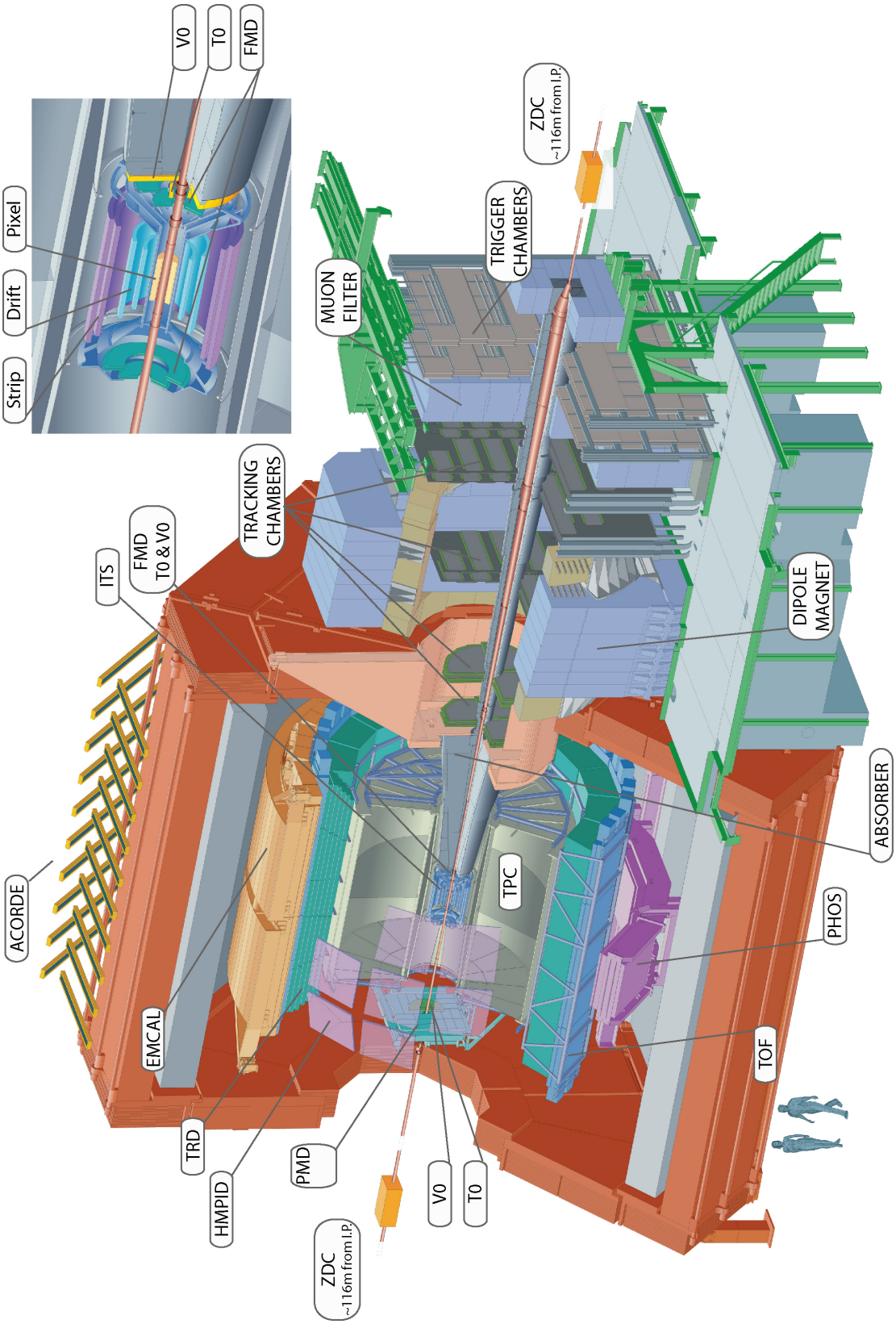

Figure 3.3: ALICE schematic layout.

of the central barrel system are: the Inner Tracking System (ITS) [242] made up of six layers of high resolution Silicon Pixel Detector (SPD), Silicon Drift Detector (SDD) and Silicon Strip Detector (SSD), the cylindrical tracking detector Time Projection Chamber (TPC) [243], the electron identification detector Transition Radiation Detector (TRD) [244], the particle identification array Time-Of-Flight (TOF) [245], the ring imaging Cherenkov detector, High Momentum Particle Identification Detector (HMPID) [246] for high-momentum particles identification, and two electromagnetic calorimeters[3], the Electro-Magnetic Calorimeter (EMCal) [247] made of Pb-scintillators for full jet measurement and the high-density crystals PHOton Spectrometer (PHOS) [248] for the photon and neutral mesons detection. These sub-detectors configuration in frontal view is shown in Fig. 3.4. They allow to reconstruct primary vertex, track charged particles over a wide range of transverse momenta (150 MeV/c $\sim$ 100 GeV/c) and identify charged hadrons, electrons and photons.

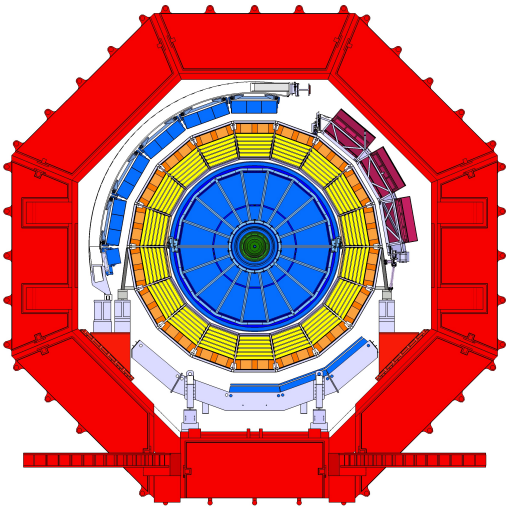

Figure 3.4: Cross-sectional overview of Central barrel detector system. It includes ITS, TPC, TRD, TOF, Cherenkov detector HMPID and two electromagnetic calorimeters EMCal and PHOS. The new installed DCal does not be shown, which is close to PHOS.

An array of plastic scintillators, ALICE COsmic Ray DEtector (ACORDE), placed above the solenoid magnet, is built to trigger on cosmic rays events for calibration and alignment.

[3]A third calorimeters, Di-jet Calorimeters (DCal) [239] was installed closely to PHOS during the LHC shutdown in 2013-2014 [240] for the di-jet measurement.

- **Forward detectors**

  Several smaller detectors, the Zero Degree Calorimeter (ZDC) [249], the Photon Multiplicity Detector (PMD) [250], the Forward Multiplicity Detector (FMD) [251], the fast timing and triggering detector T0 [251] and the collision multiplicity (centrality in Pb+Pb) triggering detector VZERO [251] at forward and backward pseudo-rapidity regions. They are built for global event characteristics, *e.g.*, multiplicity measurement, centrality determination and event plane reconstruction in heavy-ion collisions, and triggering.

- **Muon spectrometer**

  The muon spectrometer [252] consists of a complex arrangement of absorbers, a large dipole magnet with a 3 Tm field, 10 planes of tracking, and 4 planes of Resistive Plate Chambers (RCP) used for triggering chambers. It is designed to detect and identify muons in the pseudo-rapidity range of $-4 < \eta < -2.5$ for the measurement of heavy-quark vector-mesons resonances, open heavy flavour semi-muonic decays, and low mass resonances (ρ, ω and φ) *etc.*

An overview of the pseudo-rapidity η coverage of the ALICE system is shown in Fig. 3.5 and Tab. 3.2.

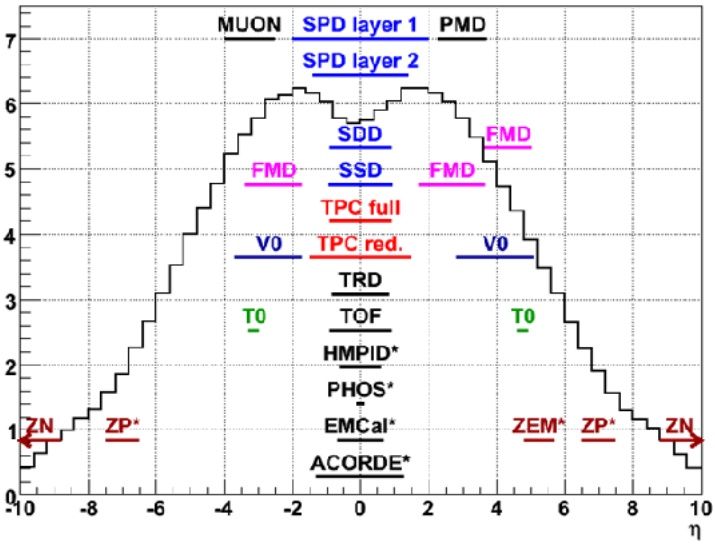

Figure 3.5: Overview of the pseudo-rapidity acceptance of ALICE sub-detectors [241].

In the following sections, the detectors which have been used in the presented data analysis, ITS, TPC, VZERO and EMCal, are described in more details. A little description is also given briefly to the other detectors.

Detector	Acceptance (η, φ)	Position (m)	Dimension (m^2)	Channels
Central barrel detector system				
ITS layer 1,2 (SPD)	± 2, ± 1.4	0.039, 0.076	0.21	9.8 M
ITS layer 3,4 (SDD)	± 0.9, ± 0.9	0.150, 0.239	1.31	133 000
ITS layer 5,6 (SSD)	± 0.97, ± 0.97	0.380, 0.430	5.0	2.6 M
TPC	± 0.9 at $r = 2.8$ m ± 1.5 at $r = 1.4$ m	0.848, 2.466	readout 32.5 m^2 Vol. 90 m^3	557 568
TRD	± 0.84	2.90, 3.68	716	1.2 M
TOF	± 0.9	3.78	141	157 248
HMPID	± 0.6, $1.2° < \varphi < 58.8°$	5.0	11	161 280
PHOS	± 0.12, $220° < \varphi < 320°$	4.6	8.6	17 920
EMCal	± 0.7, $80° < \varphi < 187°$	4.36	44	12 672
ACORDE	± 1.3, $-60° < \varphi < 60°$	8.5	43	120
Forward detectors				
ZDC:ZN	$\lvert\eta\rvert < 8.8$	± 116	2×0.0049	10
ZDC:ZP	$6.5 < \lvert\eta\rvert < 7.5$	± 116	2×0.027	10
ZDC:ZEM	$4.8 < \eta < 5.7$ $-16° < \varphi < 16°$ and $164° < \varphi < 169°$	7.25	2×0.027	10
PMD	$2.3 < \eta < 3.5$	3.64	2.59	2 221 184
FMD disc 1	$3.62 < \eta < 5.03$	inner: 3.2	0.266	51 200
FMD disc 2	$1.7 < \eta < 3.68$	inner: 3.2		
FMD disc 3	$-3.4 < \eta < -1.7$	outer: 0.752 inner: -0.628 outer: -0.752		
V0A	$2.8 < \eta < 5.1$	3.4	0.548	32
V0C	$-3.7 < \eta < -1.7$	-0.897	0.315	32
T0A	$4.61 < \eta < 4.92$	3.75	0.0038	12
T0C	$-3.28 < \eta < -2.97$	0.727	0.0038	12
Muon spectrometer				
Tracking station 1	$-4 < \eta < -2.5$	-5.36	4.7	1.08 M
Tracking station 2		-6.86	7.9	
Tracking station 3		-9.83	14.4	
Tracking station 4		-12.92	26.5	
Tracking station 5		-14.22	41.8	
Trigger station 1		-16.12	64.6	21 000
Trigger station 2		-17.12	73.1	

Table 3.2: Summary of the ALICE experiment sub-detectors [236].

3.2.1 Central barrel detector system

3.2.1.1 Inner Tracking System

The Inner Tracking System (ITS) [242] is placed closely to the interaction point, which is made up of three different silicon detectors (SPD, SDD, SSD) with two layers (each silicon has two layers) around the beam pipe at radii between 4 cm and 44 cm. It covers roughly the pseudo-rapidity region of $|\eta| < 0.9$ and full azimuthal coverage for all vertices located within $\pm 1\sigma_z$ length of the beam-beam interaction diamond (± 5.3 cm along the beam direction) (see Fig. 3.6). The number, position and segmentation of the ITS layers, as well as the detector technologies, have been optimized for efficient track finding in the high multiplicity environment and high resolution on track impact-parameter.

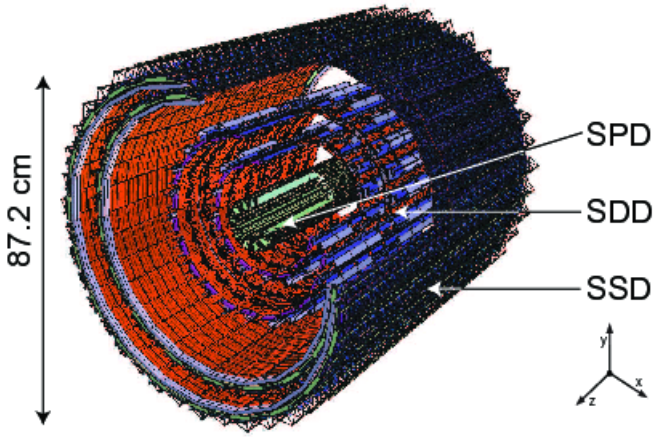

Figure 3.6: Schematic view of the ITS. It consists of three silicon detectors, SPD, SDD and SSD, with each having two layers.

The first two layers of the ITS constitute the Silicon Pixel Detector (SPD), which are located at an average distance of 3.9 cm and 7.6 cm from the beam axis, respectively. The SPD is based on hybrid silicon pixels, consisting of a two-dimensional matrix (sensor ladder) of reverse-biased silicon detector diodes bump-bonded to readout chips. It plays an important role in determination of the position of the primary vertex, measurement of the impact parameter of secondary tracks from the weak decays of strange, charm and beauty particles. Furthermore, the most inner layer has a more extended coverage ($|\eta| < 1.75$) which provides a broad rapidity coverage range for charged particle multiplicity measurements of $-3.4 < \eta < 5.1$ together with the FMD, and contributes to the minimum bias trigger and the tracklet reconstruction. The outer radius is designed for the necessity to match tracks with

TPC.

The two intermediate layers of ITS, Silicon Drift Detector (SDD), sit at the average radius of 14.9 cm and 23.8 cm, where the charged particle density is expected to reach up to 7 cm^{-2}. The SDD has very good multi-track capability and provides two out of the four dE/dx samples needed for the ITS particle identification.

The outer two layers consist of double-sided silicon micro-strip, which are positioned at 38 and 43 cm, called Silicon Strip Detector (SSD). The SSD is crucial for the connection of tracks from the ITS to the TPC and provides dE/dx information to assist particle identification for low-momentum particles. A summary parameter information on the six silicon detector layers of the ITS can be found in Tab. 3.3 [242]

Layer	Radius (cm)	$\pm z$ (cm)	$\|\eta\|$	$\sigma_{r\varphi}$ (μm)	σ_z (μm)
1 (SPD 1)	3.9	14.1	1.98	0.266	100
2 (SPD 2)	7.6	14.1	0.9		
3 (SDD 1)	14.9	22.1	0.9	35	25
4 (SDD 2)	23.8	29.7	0.9		
5 (SSD 1)	38.0	443.1	0.9	20	830
6 (SSD 2)	43.0	48.9	0.98		

Table 3.3: A summary parameter information on the six silicon detector layers of the ITS [236, 242].

The general design considerations of ITS are:

- localize the primary vertex positions with a resolution better than 100 μm.
- reconstruct the secondary vertices from the decays of hyperons, D and B mesons.
- track and identify charged particles with transverse momentum below 100 MeV/c.
- improve the resolution of momentum and angle of charged particles reconstructed by the TPC and reconstruct particles traversing dead regions of the TPC.

Some ITS performance results are introduced in the following. The measurement impact parameter resolution in ITS is presented in Fig. 3.7.

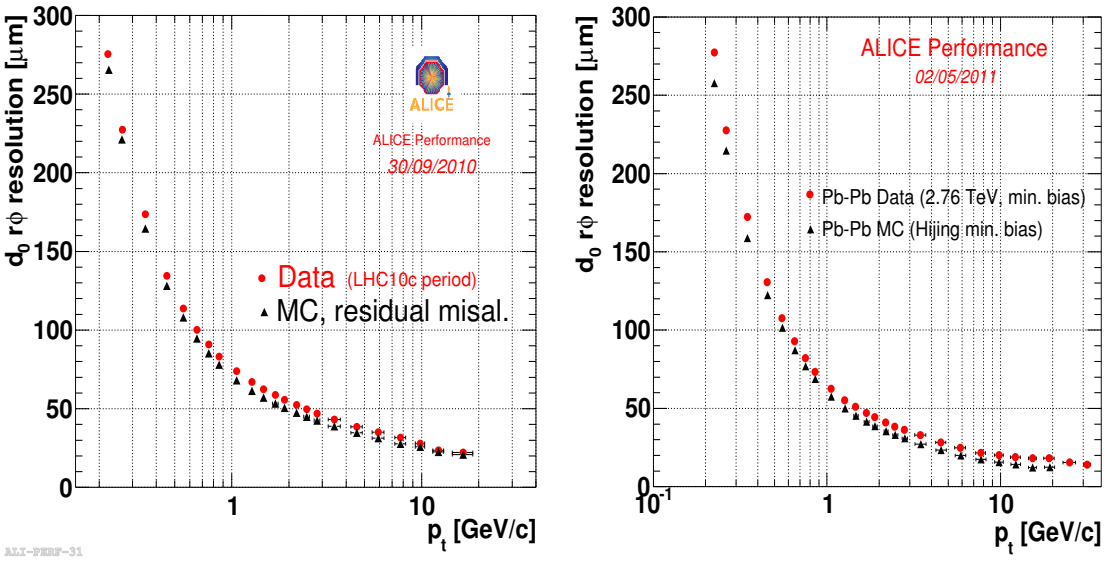

Figure 3.7: Impact parameter resolution of ITS+TPC tracks for proton-proton [253] (left) and lead-lead collisions [254](right). Data (red) has been compared with Monte-Carlo simulations (boxes) with residual misalignment has been introduced

The ITS is able to identify particles with two methods: reconstruction only with the ITS (called *ITS standalone*) and reconstruction using the ITS and TPC together. In both of the reconstructions, the dE/dx is measured in the SDD and the SSD. The standalone tracking extends the momentum range to lower p_{T} than the measurement in the TPC, while the combined tracking in ITS and TPC provides a better momentum resolution. Fig. 3.8 shows the measurement of dE/dx for the sample of ITS standalone tracks along with the PHOBOS parametrization of the most probable value [255] as function of momentum in pp collisions at $\sqrt{s} = 7$ TeV and Pb+Pb collisions at $\sqrt{s_{\mathrm{NN}}} = 2.76$ TeV.

3.2.1.2 Time Projection Chamber

The Time Projection Chamber (TPC) [243] is a cylinder shape surrounding the ITS, which has an inner radius of 85 cm determined by the maximum acceptable hit density (0.1 cm^2) and an outer radius of 250 cm chosen in order to have an average particle path length in the chamber sufficient to get a dE/dx resolution better than 10%. The total active length in the z direction is about 500 cm, which allows the acceptance in the pseudo-rapidity range of $-0.9 < \eta < 0.9$ as shown in Fig. 3.9. The detector is made of a large cylindrical field cage, filled with 88 m^3 of Ne/CO_2 (90%/10%), which has been optimized for the drift velocity, low electron diffusion,

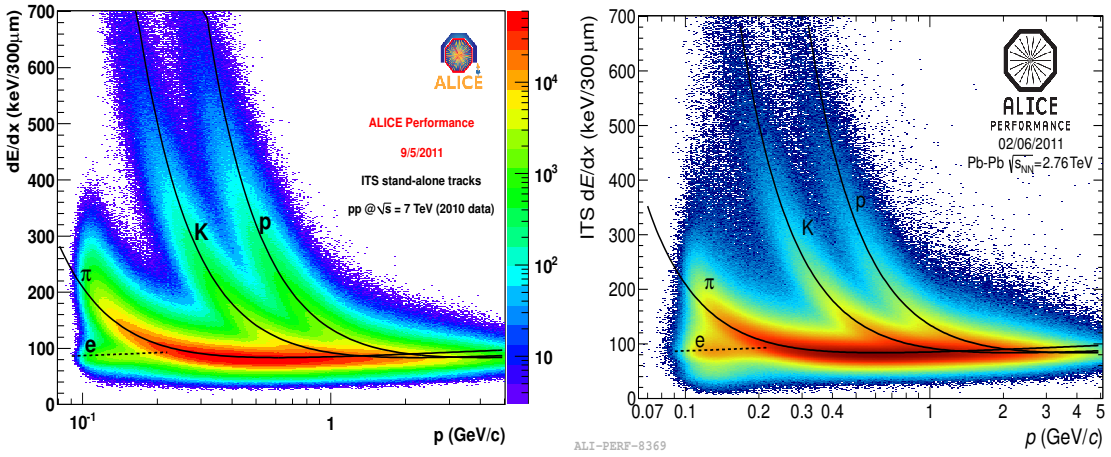

Figure 3.8: Specific energy-loss signal dE/dx vs. momentum in pp collisions at $\sqrt{s} = 7$ TeV (left) and in Pb+Pb collisions at $\sqrt{s_{\rm NN}} = 2.76$ TeV (right) for ITS standalone tracks measured with the ITS. The continuous curves represent the Bethe-Bloch parametrization, the dashed curves the asymmetric bands used in the PID procedure.

a low radiation length and hence low multiple scattering, small space-charge effect, and aging properties. Because of the gas mixture used in the TPC, the field cage is operated at very high-voltage gradients, of about 400 V/cm, with a high voltage of 100 kV at the central electrode which results in a maximum drift time of about 90 μs. This time is the limiting factor for the maximum luminosity which the ALICE can handle. The readout chambers instrument the two end-caps of the TPC cylinder with an overall active area of 32.5 m^2. The chambers are multi-wire proportional chambers with cathode pad readout. For the design of ITS the maximal expected multiplicity, $dN_{ch}/dy = 8000$, was used which results in 20000 charged primary and secondary tracks in the TPC.

The TPC is the main tracking detector of the ALICE central barrel together with the other central barrel detectors, ITS, TRD, and TOF, which provides charged-particle momentum measurements, particle identification through dE/dx measurement, and vertex determination with sufficient momentum resolution, two-track separation and dE/dx resolution for studies of hadronic and leptonic signals. The TPC is capable of detecting tracks of charged particles with transverse momenta from 0.1 GeV/c up to 100 GeV/c, with a transverse momentum resolution in central Pb+Pb collisions, of about 1% for $p_{\rm T} < 5$ GeV/c, 3% for $p_{\rm T} < 10$ GeV/c and 6% for particles at $p_{\rm T} < 20$ GeV/c. While the higher transverse momenta resolution is worsen, for instance in interval $60 < p_{\rm T} < 80$ GeV/c, it is about 25% in central Pb+Pb collisions shown in Fig. 3.10. Both in central Pb+Pb collisions and pp colli-

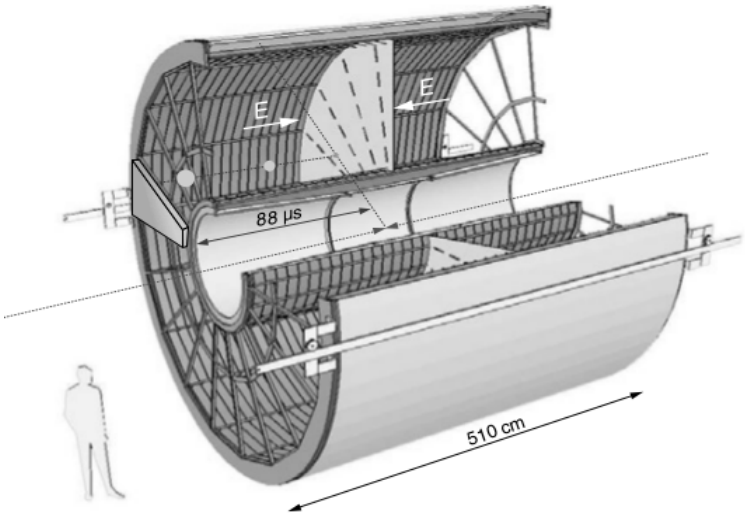

Figure 3.9: Schematic view of the TPC. It has a cylinder shape with the inner radius of 85 cm and the outer radius of 250 cm in in the pseudo-rapidity $-0.9 < \eta < 0.9$.

sions, the track finding efficiency of TPC saturates at about 90% for $p_{\mathrm{T}} > 1$ GeV/c. Moreover, TPC is also used as a centrality estimator with a resolution of about 0.5% centrality bin width in the most central collisions. Fig. 3.11 shows the Glauber fit track multiplicity in TPC. Finally, The TPC identifies particles via the specific energy loss in the gas: up to 159 samples can be measured. A truncated mean, utilizing only 60% of the available samples, is employed. It provides identification particles from the low-momentum region up to few tens of GeV/c, in combination with ITS, TRD and TOF. The dE/dx measurement in the TPC with global tracks in pp collisions is shown in the left panel of Fig. 3.12 and Pb+Pb collisions in the right panel of this figure.

3.2.1.3 Transition Radiation Detector

The Transition Radiation Detector (TRD) [244] covers the active length of 7 m in longitudinal direction at pseudo-rapidity $-0.84 < \eta < 0.84$ and full azimuth with radial position of $2.90 < r < 3.68$ m shown in Fig. 3.13. It consists of 540 individual readout detector modules, which are arranged into 18 super modules each containing 30 readout chambers arranged in five stacks along z and six layers in radius. The readout chambers are filled with gas mixture Xe/CO_2 (85%/15%), in which ionizing radiation produces electrons. The particles pass through the radiator, the generator of the Transition Radiation (TR), and then enter the conversion and drift region of the readout chamber. This passing procedure is shown in Fig. 3.14 in rz-direction.

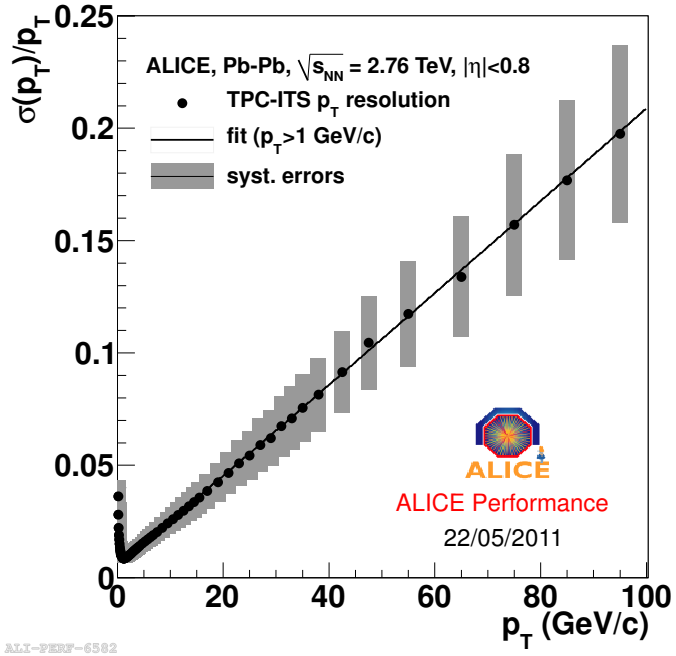

Figure 3.10: Track transverse momenta resolution dependence of p_{T} for TPC+ITS combined tracking.

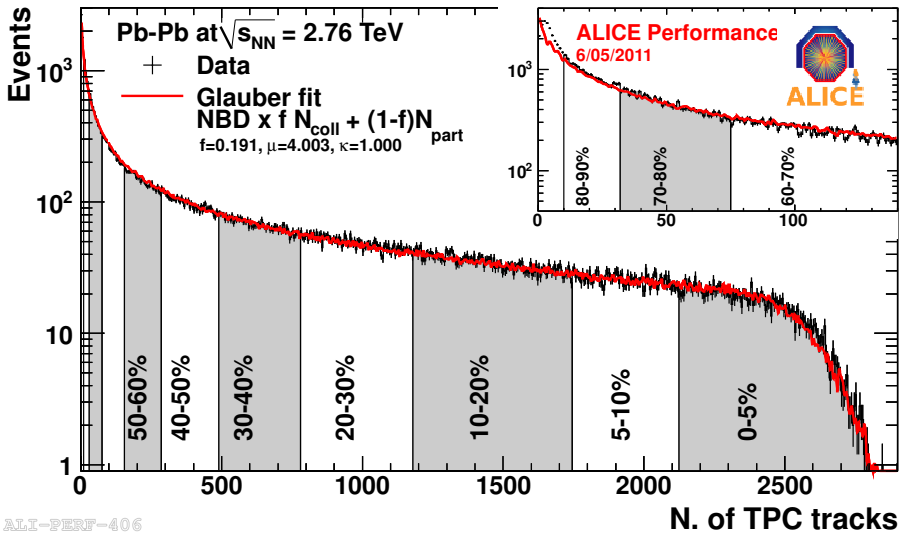

Figure 3.11: Distribution of the track multiplicity in the TPC. The distribution is fitted with the NBD-Glauber fit shown as a red line.

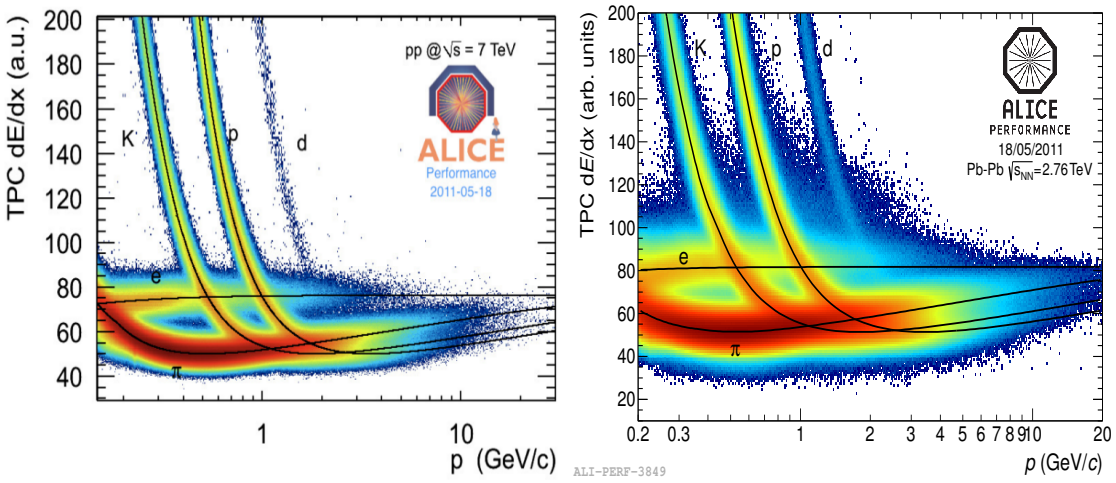

Figure 3.12: dE/dx measured in the TPC in pp collisions (left) and Pb+Pb collisions (right). The continuous curves represent the Bethe-Bloch parametrization.

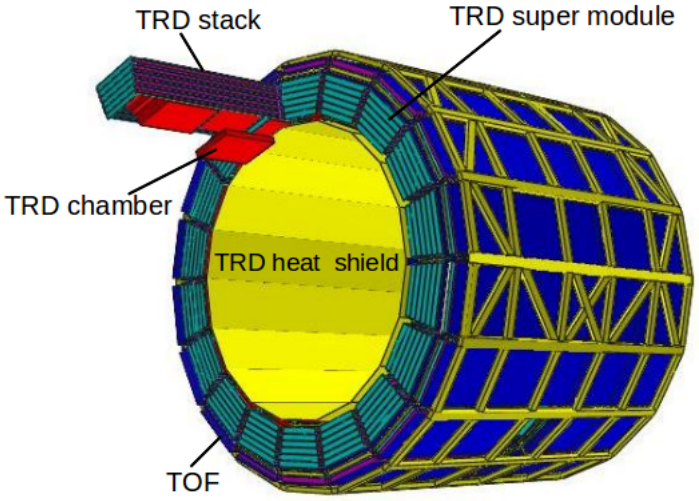

Figure 3.13: Schematic drawing of the TRD layout in the ALICE space frame. There are 18 super modules each containing 30 readout chambers (red). On the outside the TRD is surrounded by the Time-Of-Flight (TOF) system (dark blue). On the inside the heat shield (yellow) towards the TPC is shown.

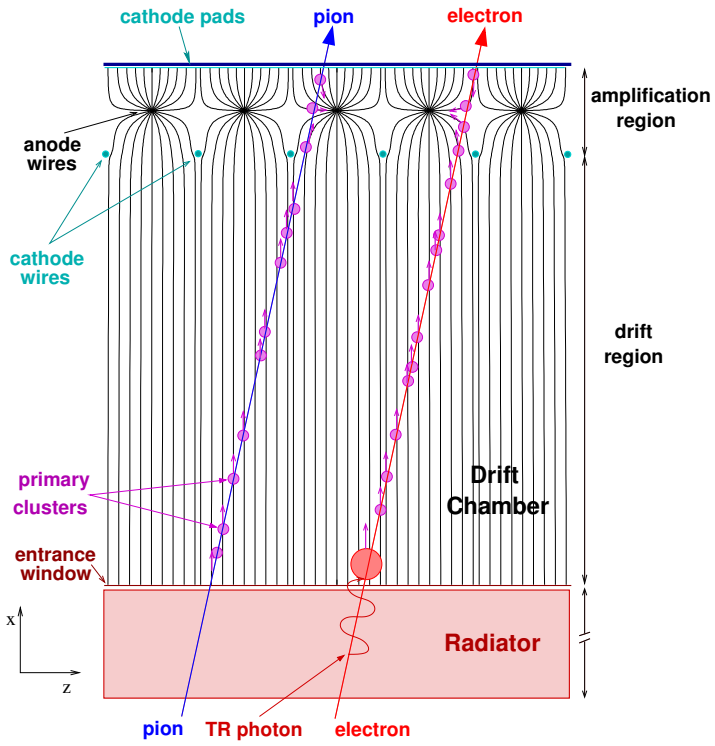

Figure 3.14: Schematic cross-sectional view of a detector module in rz-direction. It shows the charge deposit from an inclined track which is used for momentum reconstruction.

The TRD is built to provide electron identification in the central barrel for momenta larger than 1 GeV/c, where the pion rejection capability has a factor of 100. To below 1 GeV/c, the electrons can be identified via specific measurement of energy loss in the TPC. In conjunction with information from the ITS and the TPC, it provides the necessary electron identification capability to measure the production of light and heavy vector mesons as well as the continuum in the di-electron channel in pp and Pb+Pb collisions.

3.2.1.4 Time-Of-Flight

The Time-Of-Flight (TOF) detector [245] is a large area array that covers the central pseudo-rapidity region ($|\eta| < 0.9$) and full azimuth. The detector is a cylindrical shape with with an inner and outer radius of 3.70 m and 3.99 m, which has a modular structure corresponding to 18 sectors in the azimuthal angle. And each of these sectors is divided into 5 modules in the longitudinal direction along the beam axis. Fig. 3.15 shows the layout of the TOF detector. All the modules contain a total of 1638 Multigap Resistive Plate Chamber (MRPC) strips, which cover an area of 160 m^2 with 157248 readout channels (pads).

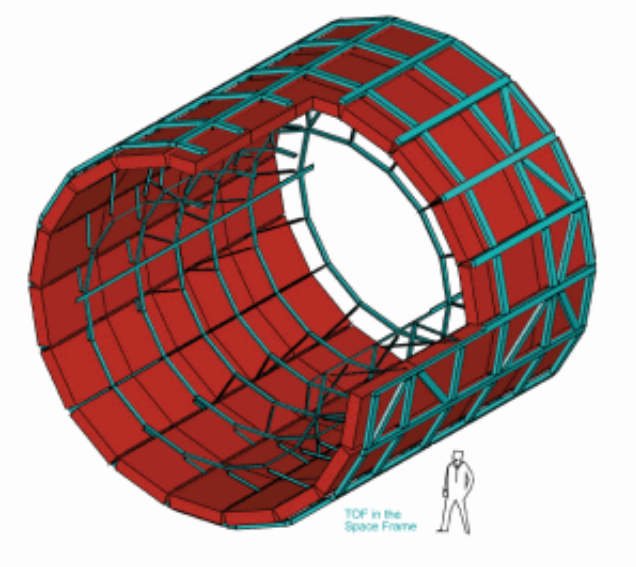

Figure 3.15: Time-Of-Flight (TOF) detector layout: modular structure.

The TOF MRPC shown in Fig. 3.16 is an ionization chamber filled with a gas mixture of 90% $C_2F_4H_2$, 5% C_4H_{10} and 5% SF_6, which has a sandwich structure of resistive plate and gas layer. A charged particle going through the gas gives rise to an avalanche of electrons, which in turn induce a signal on the read-out pads. The particle mass, m, is calculated by combining the track momentum, p, passing length, L, and the measured time t of a particle traveling from the interaction vertex to the TOF detector as:

$$m = p\sqrt{(\frac{ct}{L})^2 - 1} \tag{3.1}$$

The TOF is designed to identify charged particles in the intermediate momentum range, from 0.2 to 2.5 GeV/c for pions and kaons, up to 4 GeV/c for protons, with a π/K and K/p separation better than 3σ [256, 257]. Coupling with the ITS and TPC for track and vertex reconstruction and for dE/dx measurements in the low-momentum range, it provides event-by-event identification of large samples of pions, kaons, and protons. The particle identification capabilities of the TOF detector is presented in Fig. 3.17.

3.2.1.5 High-Momentum Particle Identification

The High-Momentum Particle Identificaton Detector (HMPID) [246] covers 5 m in radial position corresponding to pseudo-rapidity $-0.6 < \eta < 0.6$ and azimuth range $12° < \varphi < 58.8°$, which consists of seven identical proximity-focusing Ring

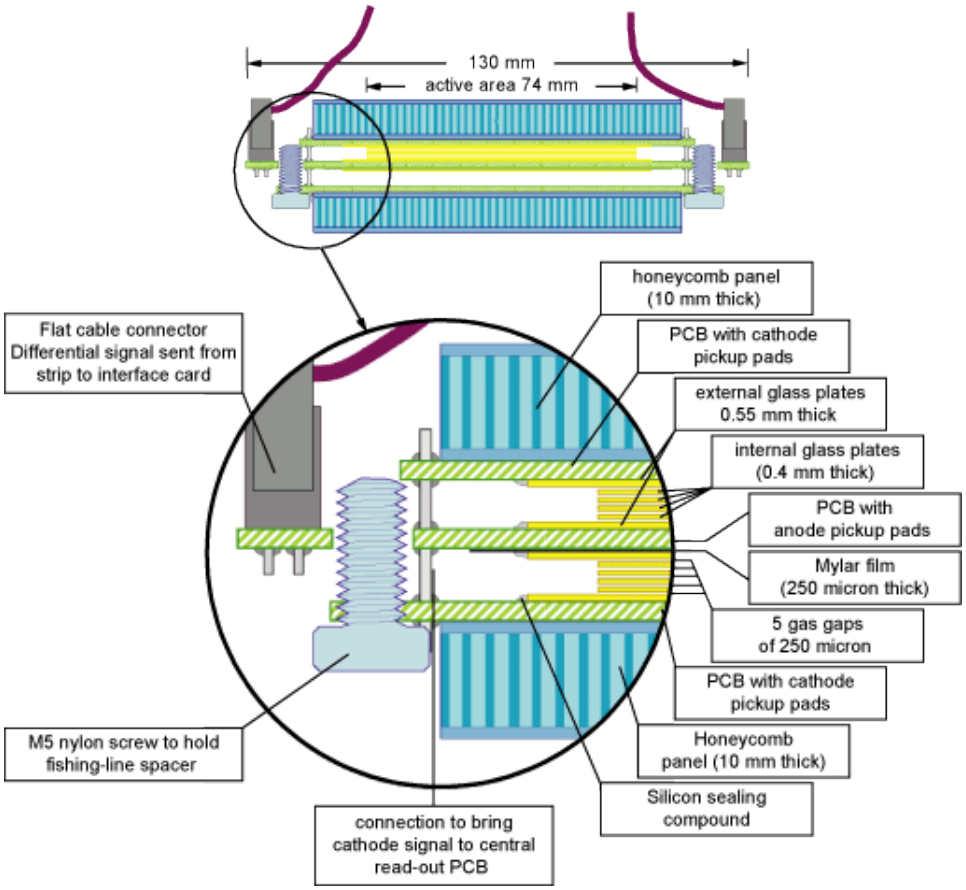

Figure 3.16: Schematic diagram of the TOF double-stack MRPC units.

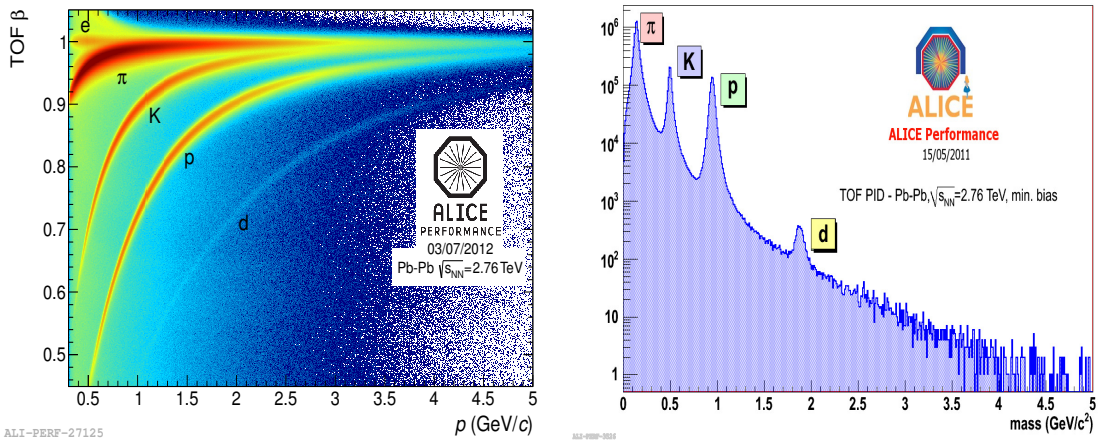

Figure 3.17: TOF particle identificaiton capability performance in Pb+Pb collisions. The left panel shows the TOF β bands as a function of the momentum (p) for e, π, K, p and d. The right panel gives the mass spectra of different species clearly.

Imaging Cherenkov Counter (RICH) modules of about $1.5 \times 1.5\text{m}^2$ each. The modules are placed on an independent support cradle and mounted at the two o'clock position of the ALICE space frame as shown in Fig. 3.18. Each HMPID module is

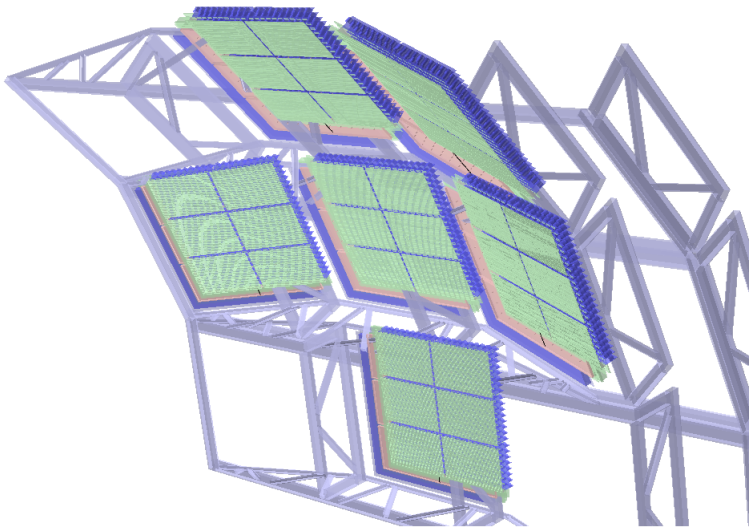

Figure 3.18: View of the seven modules of the HMPID mounted on the cradle.

equipped with three radiator vessels made of NEOCERAM, providing 15 mm radiator thickness. Cherenkov photons, emitted by a fast charged particle going through the radiator are detected by a photon counter, which exploits the novel technology of a thin layer of CsI deposited onto the pad cathode of a Multi-Wire Pad Chamber. The HMPID is dedicated to measurements of identified hadrons at $p_{\text{T}} > 1$ GeV/c, which enhances the PID capability of charged hadrons identification beyond the momentum interval for which the particle identification can not be performed through energy-loss in ITS, TPC and TOF. The detector is optimized to extend the useful range for π/K and K/p discrimination, on a track-by-track basis, up to 3 GeV/c and 5 GeV/c, respectively. The separation (n-σ) for π/K and K/p as a function of transverse momentum in HMPID is shown in Fig. 3.19. The Cherenkov angle as a function of transverse momentum in different particles is presented in Fig. 3.20 in pp and Pb+Pb collisions.

3.2.1.6 PHOton Spectrometer

The PHOton Spectrometer (PHOS) [248] is built as a single-arm high-resolution high-granularity electromagnetic spectrometer consisting of a highly segmented electromagnetic calorimeter, which is placed at the bottom of the ALICE setup at a distance of 460 cm from the collision vertex and covers in pseudo-rapidity, $-0.12 <$

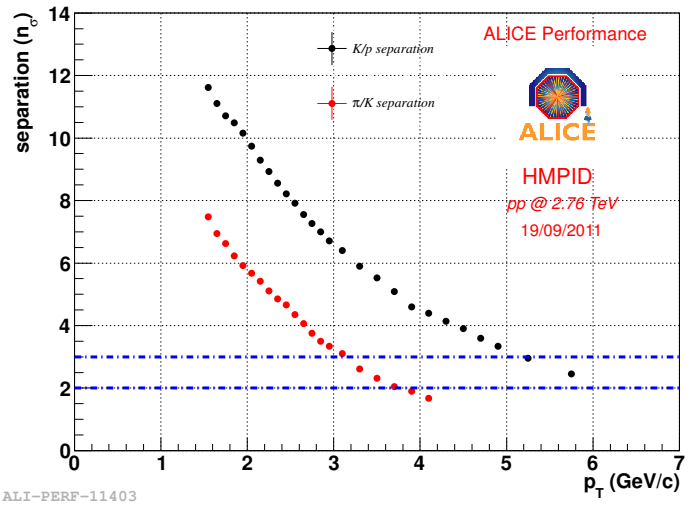

Figure 3.19: Separation (n-σ) for π/K and K/p as a function of transverse momentum.

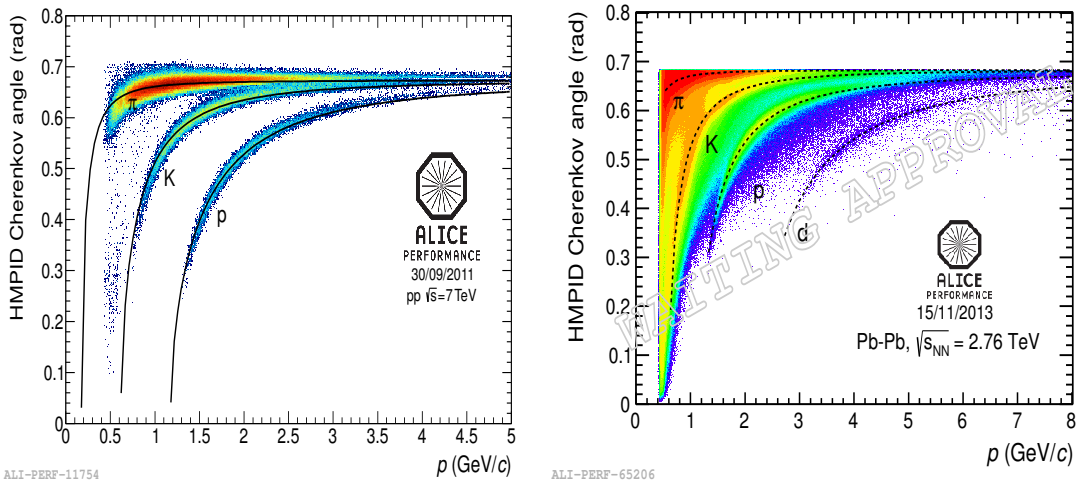

Figure 3.20: Cherenkov angle as a function of track transverse momentum in pp collisions (left) and Pb+Pb collisions (right).

$\eta < 0.12$, and 100° in azimuthal angle with five modules (three modules are installed up to now). Each PHOS module is segmented into 3584 detection cells arranged in 56 rows of 64 cells. The detection cell consists of a $22 \times 22 \times 180$ mm lead-tungstate crystal, $PbWO_4$ (PWO), coupled to a 5×5 mm Avalanche Photo-Diode (APD) followed by a low-noise preamplifier [258], see the left panel of Fig. 3.21. The PWO crystal is designed with this geometry corresponding to $20X_0$ radiation length in the longitudinal direction, which is known as its characteristics of the fast signal and the small Moliere radius of about 2 cm. The right pannel of Fig. 3.21 shows the obtained energy resolution as a function of photon energy together with previous results from the prototypes [258, 259] and a fitting result by following formula:

$$\frac{\sigma}{E\ (\mathrm{GeV})} = \sqrt{\frac{0.018}{E} \oplus \frac{0.033}{\sqrt{E}} \oplus 0.011} \tag{3.2}$$

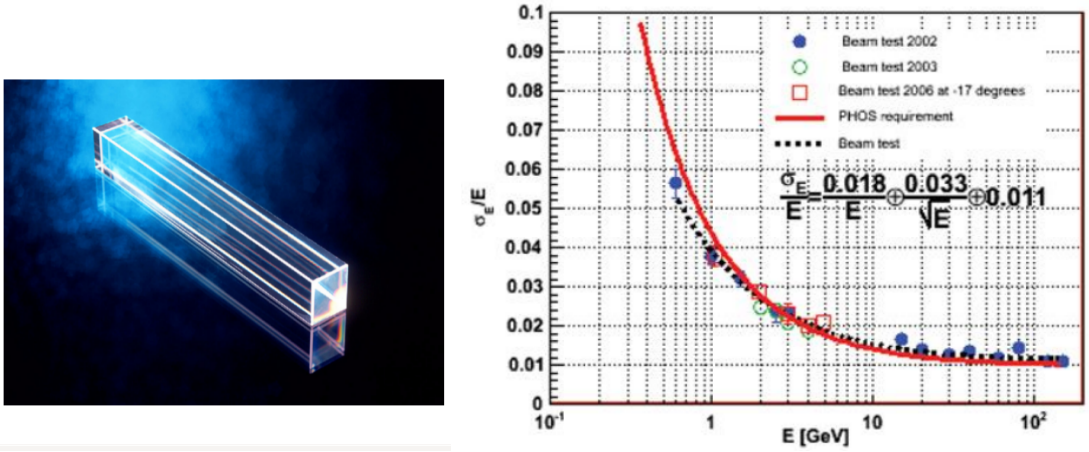

Figure 3.21: Left: $PbWO_4$ crystal inset into PHOS module. Right: Energy resolution measured in 2006 for first PHOS module together with the measured resolution for prototypes. All results can be described by a single fitting as shown in a dotted line.

The PHOS provides unique coverage of the following physics topics:

- thermal and dynamical parameters of the initial phase of the collision, in particular the initial temperature, via direct single photons and di-photons
- jet-quenching as a probe of deconfinment, studied via high-p_{T} π^0
- signals of chiral-symmetry restoration

A performance of invariant mass spectrum of PHOS cluster pairs after combinatorial background subtraction in centrality 0-10% in Pb+Pb collisions at $\sqrt{s_{\mathrm{NN}}} =$ 2.76 TeV is shown in Fig. 3.22.

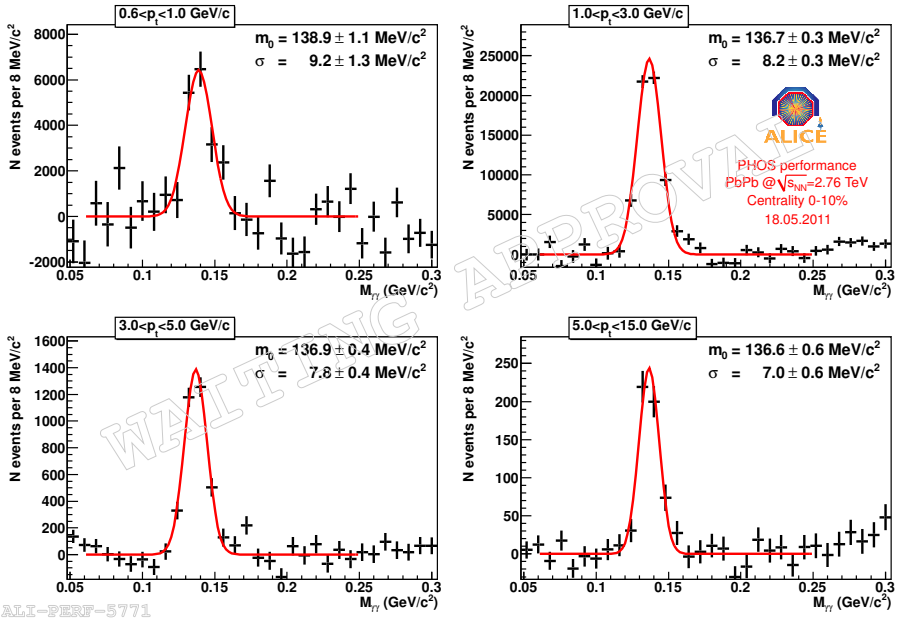

Figure 3.22: Invariant mass spectrum of PHOS cluster pairs in centrality 0-10% after combinatorial background subtraction. The π^0 peak is fitted by a Gaussian function, the mean mass and the σ are shown.

3.2.1.7 Electromagnetic Calorimeter

The ElectroMagnetic Calorimeter (EMCal) [247] is a layered Pb-scintillator sampling calorimeter with a longitudinal pitch of 1.44 mm Pb and 1.76 mm scintillator with longitudinal wavelength shifting fiber light collection. It occupies a cylindrical geometry adjacent to the ALICE magnet coil at a radius of 450 cm from the interaction point, covering a length $\sim$ 700 cm with the pseudo-rapidity $|\eta| < 0.7$ and azimuth of 107°. The EMCal detector is positioned to provide partial back-to-back coverage with the PHOS calorimeter. The detector Super Modules, the basic structural units of the calorimeter, can be seen in Fig. 3.23. There are 10 full size and 2 one-third size Super Modules in the full detector acceptance. The full size modules span $\Delta\eta = 0.7$ and $\Delta\varphi = 20°$, whereas the 1/3 modules span a smaller azimuthal range of $\Delta\varphi = 7°$. A full-sized Super Module is assembled from $12 \times 24 = 288$ modules. Each one-third size Super Module is assembled from $4 \times 24 = 96$ modules. Each module comprises four independent detection channels/towers giving a total of 1152 towers per full sized Super Module, each of which is approximately projective in η and φ to the collision vertex. More physical characteristics of the EMCal are summarized in Tab. 3.4

The EMCal is focused mostly at measurement of photons from hard jets, which

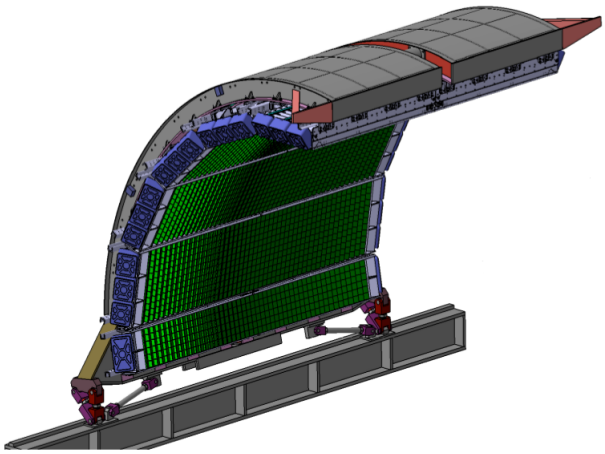

Figure 3.23: Array of EMCal Super Modules shown in their installed positions on the support structure.

Quantity	Value
Tower Size (at $\eta = 0$)	$\sim 6.0\times \sim 6.0 \times 24.6$cm (active)
Towser Size	$\Delta\varphi \times \Delta\eta = 0.0143 \times 0.0143$
Sampling Ratio	1.44 mm Pb/1.76 mm Scintillator
Number of Layers	77
Effective Radiation Length X_0	12.3 mm
Effective Moliere Radius R_M	3.20 cm
Effective Density	5.68g/cm^2
Sampling Fraction	10.5
Number of Radiation Lengths	20.1
Number of Towers	12,288
Number of Modules	3072
Number of Super Module	10 full size, 2 one-third size
Weight of Super Module	$\sim$ 7.7 metric tons (full size)
Total Coverage	$\Delta\varphi = 107°$, $-0.7 < \eta < 0.7$

Table 3.4: EMCal physical parameters.

reduces the bias of jet quenching studies and improve jet energy resolution coupled with ALICE tracking detectors. Fig. 3.24 shows the inclusive differential full jet cross section obtained with R = 0.2 compared to a pQCD calculation at NLO and a PYTHIA8 prediction [260]. It also improves the ability of ALICE to neutral mesons

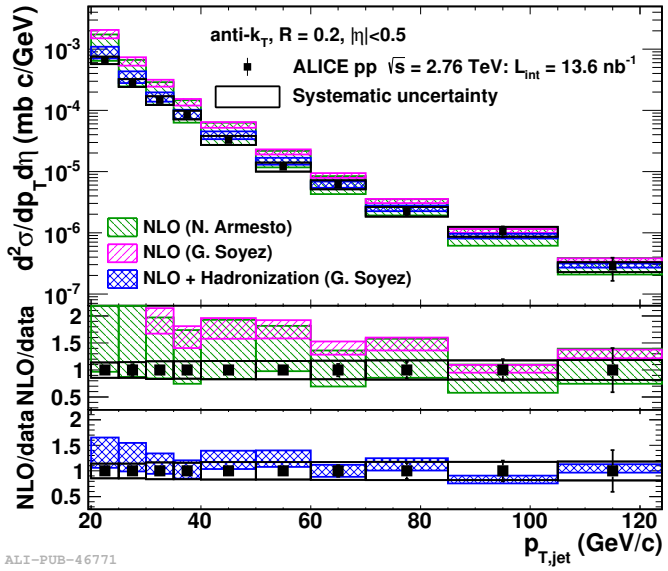

Figure 3.24: Upper panel: Inclusive differential jet cross sections for R=0.2. Vertical bars show the statistical error, while boxes show the systematic uncertainty. The bands show the NLO pQCD calculations. Lower panels: Ratio of NLO pQCD calculations to data. Data points are placed at the center of each bin.

and high momentum photons in a larger acceptance compared to the PHOS detector. Discrimination of γ and π^0 using EM shower shape characteristics is possible in the EMCal up to $p_{\mathrm{T}} \sim 30$ GeV/c. While additional techniques, isolation cuts, can be used for photon (direct photon) measurements to higher p_{T}. The measurement of heavy flavor production at high-p_{T} provides unique observables of jet quenching. At high-p_{T}, semi-leptonic decay channels (branching ratio $\sim$ 10% for both B and D mesons) are favorable for heavy flavor measurements because they can be triggered, but also require good hadron rejection. The ALICE has extensive capabilities for electron measurements at $p_{\mathrm{T}} > 10$ GeV/c and provides both an efficient and fast trigger and sufficient hadron rejection via the EMCal. Secondary vertex provides additional discrimination, and ALICE with the EMCal can measure b-jet production in Pb+Pb collisions up to $E_{\mathrm{T}} \sim 80$ GeV [247].

Furthermore, the EMCal provides collecting data trigger system with the goal for enhancing the kinematic reach of recorded data for hard probes such as high-p_{T} π^0, γ, electrons and jets, within the overall trigger rate and bandwidth constraints

of ALICE. The ALICE Trigger System consists of two independent components: a Central Trigger Processor (CTP) providing the trigger decision logic, generating triggers for the readout detectors and a Trigger Distribution Network delivering these triggers to the detectors. The earliest trigger decision (Level 0 or L0) is issued 1.2 μs after the interaction, L1 is issued at 6.5 μs, and L2 is issued at 88 μs. The rejection of L0 triggers is provided by L1 and L2 decisions. In terms of EMCal event rejection the following relevant trigger observables have been implemented: neutral cluster trigger and jet trigger

- **Neutral cluster trigger**
  The cluster trigger searches for high-p_{T} showers from γ (π^0, η,...) and electrons. The L0 algorithm identifies the shower energy above threshold in the local region of a Trigger Region Unit (TRU). The energy is summed over a sliding window of 4×4 towers and compared to a threshold above noise. The left panel of Fig. 3.25 shows the ratio of distributions EMCal/MB, which measures the rejection factor of the EMCal trigger. Uniform trigger efficiency is observed above $\sim$ 5 GeV, with a rejection factor of $\sim$ 1000 [261]. This value corresponds closely to the online rejection factor during data-taking. The right panel of Fig. 3.25 shows the EMCal-L0 trigger efficiency for EMCal clusters calculated via simulation with comparison to data of pp collisions at $\sqrt{s} = 2.76$ TeV. The trigger efficiency is extracted by making the ratio of the energy distribution of clusters containing valid trigger bit in triggered events to the energy distribution of all the clusters in the MB events. Then the efficiency curve from data is scaled to match the simulation curve above 5 GeV.

- **Jet trigger**
  The jet trigger that is efficient and unbiased requires integration over a phase space region larger than that subtended by a single TRU, which decision at L1 is evaluated using a "patch" trigger. A single patch is made up of a number of adjacent $n \times n$ towers.

An absolute energy calibration of the test beam data was obtained from the known incident electron energy using an iterative procedure. The energy resolution obtained at the different positions was combined and the average values as a function of the incident beam momentum are displayed in Fig. 3.26. The simulation data points and a fit to the energy resolution as a function of the incident energy are also

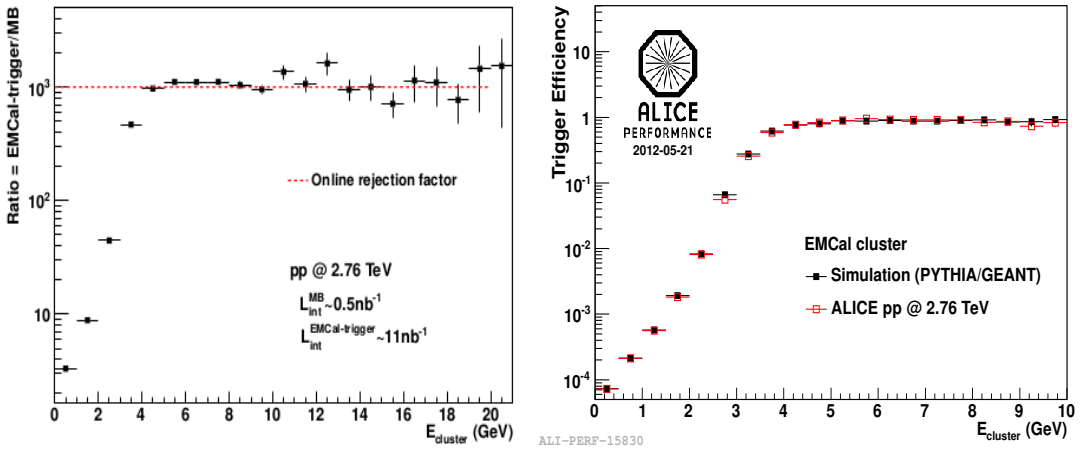

Figure 3.25: Left: Ratio of the distributions EMCal/MB. The horizontal dashed red line is drawn at 1000, indicating the online rejection factor. Right: EMCal-L0 trigger efficiency for EMCal clusters calculated via simulation with comparison to data of pp collisions at $\sqrt{s} = 2.76$ TeV.

shown in Fig. 3.26. The fitting is done by following formula:

$$\frac{\sigma}{E\ (\mathrm{GeV})} = \sqrt{(\frac{a}{E})^2 + \frac{b}{E} + (c)^2} \tag{3.3}$$

where the coefficients of a, b and c are 0.0435, 0.0973 and 0.0163, respectively.

The linearity of the energy response was investigated in conjunction with the energy resolution. Fig. 3.27 displays the average ratio of the reconstructed and incident beam energy as a function of the incident beam energy obtained by combining the measurements at different detector positions. The simulation result is shown in the same plot with red points. The fits to the test beam data and simulation data are shown by formula:

$$\frac{E_{rec}}{E_{true}} = a_1 \times (\frac{1}{(1 + a_2 \times e^{\frac{-E}{a_3}}} \times \frac{1}{1 + a_4 \times e^{\frac{E-a_5}{a_6}}}) \tag{3.4}$$

where coefficients of a_1, a_2, a_3, a_4, a_5 and a_6 are 0.977, 0.183, 0.664, 0.131, 163.460 and 24.689 to data fitting, and are 0.981, 0.114, 1.002, 0.0967, 219.381, 63.16 to simulation fitting.

The position resolution of the EMCal was investigated by tge test beam data using the incident beam location projected from the tracking information from the MWPCs. The distribution of energies in the towers of the cluster is used to calculate the cluster position in x and y. The x and y position resolution as a function of incident momentum for electrons and a fit with 1.5 $mm + 5.3\ mm/\sqrt{E}$ are shown

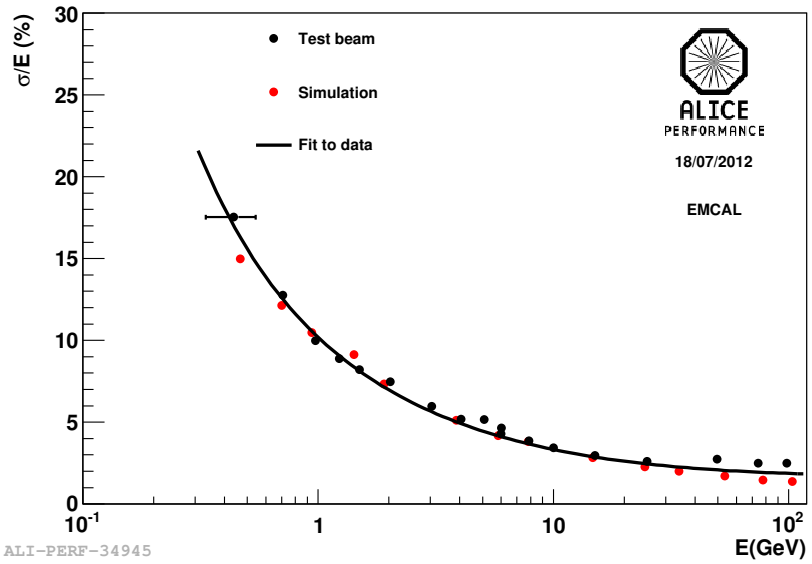

Figure 3.26: EMCal energy resolution from 2010 electron test beam measurements (black) and simulation data (red). The curve is the fit result of test beam data.

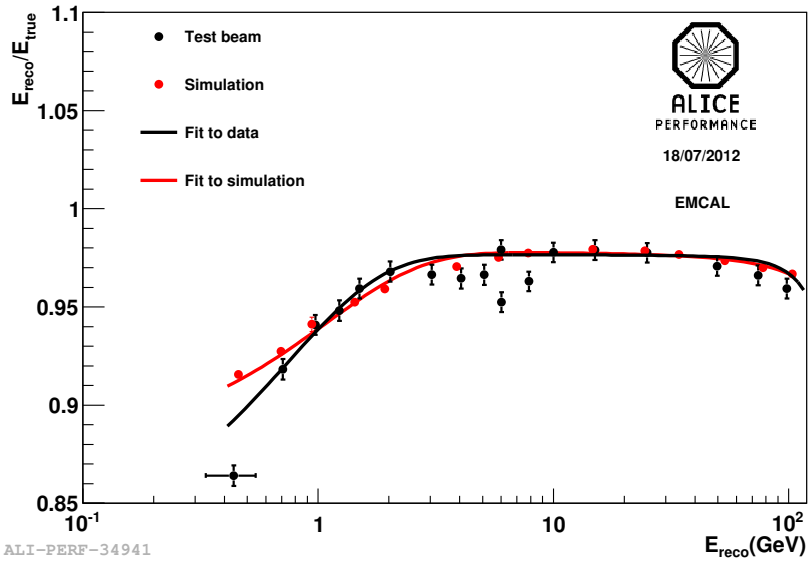

Figure 3.27: Energy non linearity in EMCal, comparison of test beam data with electrons (black) with simulation (red). The curves are the fit results.

in Fig. 3.28. As expected, no significant difference between the x and y position is observed.

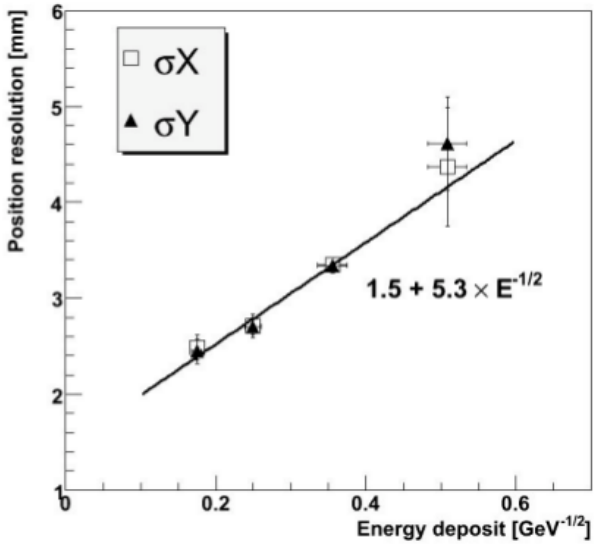

Figure 3.28: Dependence of the position resolution as a function of $1/\sqrt{E}$ (GeV) for electrons. The curve shows the best fit result. Taken from [247].

A performance of invariant mass spectrum of EMCal cluster pairs with and without background subtraction in pp collisions at $\sqrt{s} = 7$ TeV with minimum bis trigger is shown in Fig. 3.29.

3.2.2 Forward detectors

3.2.2.1 Zero Degree Calorimeters

There are two Zero Degree Calorimeters (ZDCs) [249] which are located at 114 m either side of the IP. Each ZDC set consists of two hadron calorimeters: one for spectator neutrons (ZN, $7.04 \times 7.04 \times 100$ cm^3) placed at zero degrees relative to the LHC axis, and one for spectator protons (ZP, $12 \times 22.4 \times 150$ cm^3) placed externally to the outgoing beam pipe on the side where positive particles are deflected. The ZDC project includes electromagnetic calorimeter (ZEM)) with dimensions $7 \times 7 \times 21$ cm^3 at ~ 7 m from IP covering rapidity range $4.8 < \eta < 5.7$ only on one side to improve the centrality trigger. It is made of lead and quartz fibres and designed to measure the energy of particles emitted at forward rapidities, essentially photons generated from π^0 decays event by event. The ZDC provides a centrality estimation and trigger in Pb+Pb collisions by measuring the energy carried in the forward direction by non-interacting (spectator) nucleons.

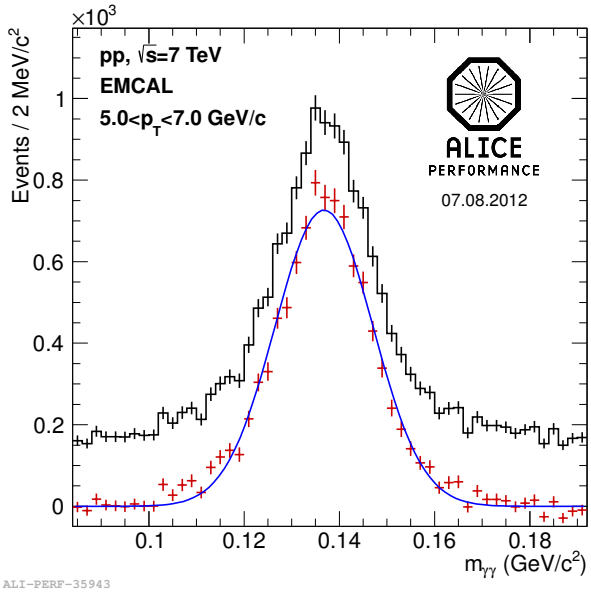

Figure 3.29: Two-photon invariant mass spectrum in pp collisions at $\sqrt{s} = 7$ TeV with minimum bias trigger at $5 < E < 7$ GeV in EMCAL.

3.2.2.2 Photon Multiplicity Detector

The Photon Multiplicity Detector (PMD) [250] is installed at 360 cm from the IP, on the opposite side of the forward muon spectrometer, covering the pseudo-rapidity $2.3 < \eta < 3.5$ and full azimuth. The PMD consists of two identical planes of detectors with a $3X_0$ thick lead converter in between them and made up of four supermodules with six identical unit modules in each. The unit modules are separated among themselves by a thin 100 μm kapton strip supported on a 0.3 mm thick FR4 sheet for rigidity. The detector is designed to measure the multiplicity and spatial $(\eta - \varphi)$ distribution of photons on an event-by-event basis in the forward region of ALICE.

3.2.2.3 Forward Multiplicity Detector

The Forward Multiplicity Detector (FMD) [251] is a silicon strip detector of modest segmentation, placed around the beam pipe with psedo-rapidity coverage of $-3.4 < \eta < -1.7$ and $1.7 < \eta < 5.0$, see Fig. 3.30. It consists of five rings FMD1i, FMD2i, FMD2o, FMD3i and FMD3o located at $z = 340$ cm, 83.4 cm, 75.2 cm, -62.8 cm and -75.2 cm with different psedo-rapidity range shown in Fig. 3.31. The rings consists of two types with 10 (for the inner rings, FMD1i, FMD2i, and FMD3i) or 20 (for the outer rings FMD2o, FMD3o) hexagonal silicon sensors in azimuthal

angle, respectively. Each sensor is azimuthal segmented into 2 sectors, and each sector is segmented into strips at constant radii. The segmentation is made up of a total of 51200 silicon strip channels. The FMD is designed to study multiplicity

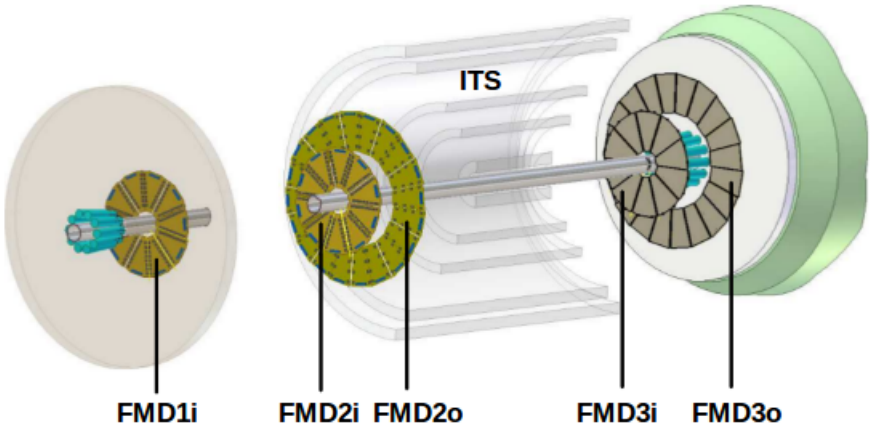

Figure 3.30: Layout of the FMD five rings in the ALICE experiment.

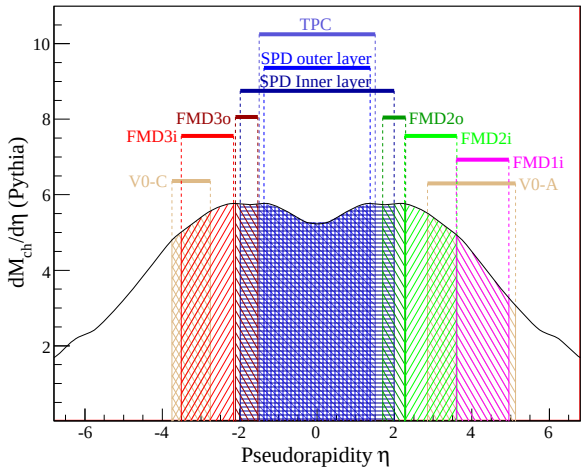

Figure 3.31: Continuous pseudo-rapidity coverage provided by the FMD five rings together with the SPD [262].

fluctuations on an event-by-event basis and flow in the considered pseudo-rapidity range. It provides early charged particle multiplicity distributions for all collision types in the psedo-rapidity range $-3.4 < \eta < 5.1$ together with the pixel system of the ITS. The detector is also able to reconstruct event plane with fine resolution based on the benefit of its many segment in φ direction.

3.2.2.4 T0

The T0 [251] detector is built with two arrays of Cherenkov counters, 12 counters for each array. The two arrays are asymmetrically placed at 72.7 cm (T0-C, muon spectrometer side) and 375 cm (T0-A, PMD side) from the interaction vertex with the pseudo-rapidity coverage range $-3.28 < \eta < -2.97$ and $4.61 < \eta < 4.92$ shown in Fig. 3.32, respectively. It is designed to perform the following functions:

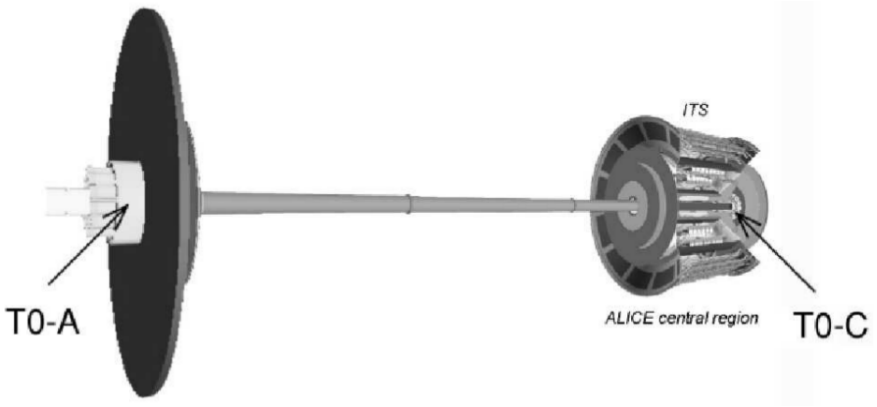

Figure 3.32: Position of the T0 detector arrays inside ALICE.

- To give a start signal with good time resolution for the TOF detector particle identification system in ALICE. The signal corresponds to the real time of the collision (plus a fixed time delay) and is independent on the position of the vertex.
- To measure the vertex position with a precision ±1.5 cm for each interaction and provide a L0 trigger when the position is within the preset values.
- To provide an early (prior to the L0 trigger) "wake-up" trigger to the TRD.
- To measure the particle multiplicity and generate one of the three possible trigger signals: $\mathrm{T0_{min-bias}}$, $\mathrm{T0_{semi-central}}$, or $\mathrm{T0_{central}}$.

3.2.2.5 VZERO

The VZERO [251] is a small-angle detector consisting of two arrays of scintillator counters placed at two sides of the ALICE interaction region. The two counters have the pseudo-rapidity coverage $2.8 < \eta < 5.1$ (VZERO-A) and $-3.7 < \eta < -1.7$ (VZERO-C) overlapping partly with the FMD acceptance shown in Fig. 3.33. The V0-A device is located on the positive z-direction at a distance of about 340 cm from

the interaction point. The V0-C device is placed at the negative z-direction along the absorber nose at 90 cm from the interaction point. Both of V0-A and V0-C are segmented into 32 elementary counters distributed in four rings. Each ring covers 0.4-0.6 unit of pseudo-rapidity.

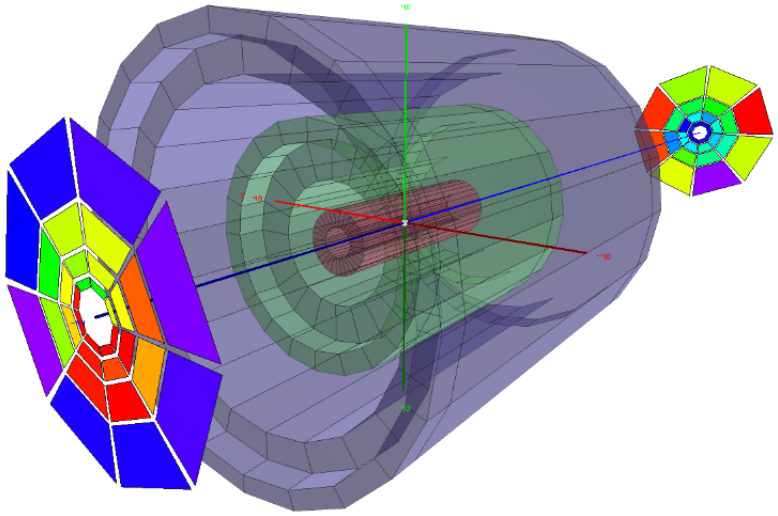

Figure 3.33: Layout of VERO-A and VZERO-C in the ALICE experiment.

The VZERO detector has multiple roles as:

- a minimum bias trigger for the central barrel detectors.
- two centrality triggers in Pb+Pb collisions.
- a centrality indicator.
- a control of the luminosity.
- a validation signal for the muon trigger to filter background in pp mode.

Fig. 3.34 shows the distribution of VZERO amplitudes for all events triggered with the $3-out-of-3$ (signals in VZERO-A and VZERO-C and at least 2 chips hit in the outer layer of the SPD) trigger after removing the beam background.

3.2.3 Muon spectrometer

The muon spectrometer is built to detect muons in the polar angular range $2-9°$. This interval, a compromise between acceptance and detector cost, corresponds to the pseudo-rapidity range of $-4.0 < \eta < -2.5$. The spectrometer consists of five

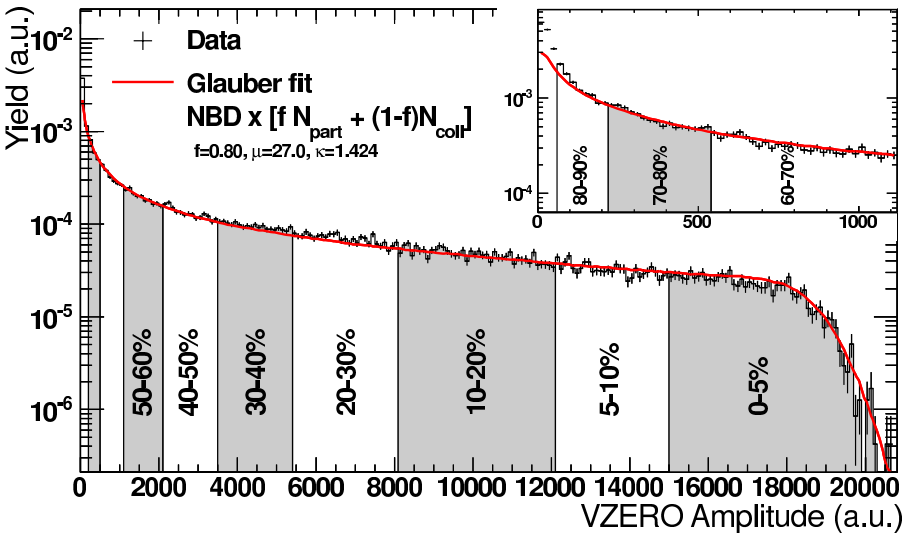

Figure 3.34: Distribution of the sum of amplitudes in the VZERO scintillators. The distribution is fitted with the NBD-Glauber fit shown as a line. The inset shows a zoom of the most peripheral region [263].

components which are, a passive front absorber absorbing hadrons and photons, a high-granularity tracking system, a large dipole magnet, a passive muon filter wall and an inner beam shield protecting the chambers from particles and secondaries produced at large rapidities, see Fig. 3.35 and 3.3. The ALICE forward muon

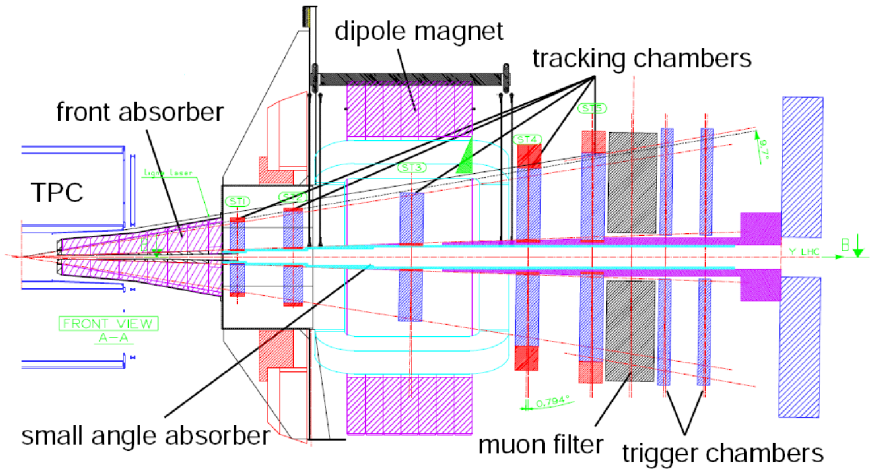

Figure 3.35: Layout of the ALICE muon spectrometer.

spectrometer is designed to study the complete spectrum of heavy quarkonia (J/ψ, ψ', Υ, Υ', Υ'') via their decay in the $\mu^+\mu^-$ channel. Meanwhile, $W\pm$ and Z_0 can be also measured with the muon spectrometer.

3.3 ALICE online system and offline project

In this section, the ALICE online system, which includes the Trigger system (TRG), the Data Acquisition system (DAQ), the High Level Trigger (HLT), and the Experiment and Detector Control Systems (ECS and DCS), is briefly described firstly. Subsequently, the ALICE offline project including AliRoot analysis, especial analysis framework to this thesis work and ALICE Grid, is presented.

3.3.1 ALICE online system

The ALICE online systems, namely, the Trigger system (TRG), the Data Acquisition system (DAQ), the High Level Trigger system (HLT), and the Detector Control System (DCS) interface to each other through a controls layer: the so-called Experiment Control System (ECS).

3.3.1.1 Trigger System

The ALICE Trigger System (TRG) [236, 264] is designed to select events displaying a variety of different features at rates which is able to be scaled down to suit physics requirements. It operates with interaction rates for nucleus-nucleus, proton-nucleus and proton-proton collisions at rates between about 8 kHz and 300 kHz. The Central Trigger Processor (CTP) is the main block of the ALICE trigger electronics, which receives and aligns up to 60 trigger inputs parallelly from the trigger detectors, and then processes these triggers information for each cluster and generates the result of this processing. There are three different hardware trigger levels (L0, L1 and L2) with latencies from 1.2 microseconds to 100 microseconds. The L0 trigger signal reaches detectors at 1.2 μs from interaction, which includes 800 ns input to CTP, made decision by CTP with 100 ns and delivered to detectors up to 300 ns. The L1 trigger signal is sent at 6.5 μs which includes 6.1 μs input to CTP and made decision by CTP with 100 ns. To L2 trigger signal, it is delivered to detectors with 105 μs from interaction. After these trigger signals sent to CTP, they are combined by logical operations inside a FPGA[4] to form the different physics triggers (*e.g.* minimum-bias, central collision, high-pt jet). Outputs from the CTP go to the Local Trigger Units (LTUs) of each sub-detector, where they are further processed according to the different detector needs and finally sent back to the detector Front-End Electronics (FEE). The LTU serves as an interface between the

[4]FPGA: Field-Programmable Gate Array, more details can be find in Wikipedia: FPGA.

CTP and the sub-detector readout electronics, and is able to run in a stand-alone mode of operation where the LTU fully emulates the CTP protocol.

3.3.1.2 Data Acquisition system

In ALICE, a variety of physics observables are investigated by using different beam conditions. In this environment, a large number of trigger classes is used to select and characterize the collision events. These trigger classes belong to two broad categories depending on whether they are frequent(*e.g.*, central, semi-central and minimum-bias) or rare (dimuon and dielectron). The task of the ALICE Data AcQuisition (DAQ) [236, 264] system, combined with the ALICE Trigger and High-Level Trigger (HLT) systems, is to select interesting physics events, to provide an efficient access to these events for the execution of high-level trigger algorithms and finally to archive the data to permanent data storage for later analysis. In a word, the ALICE DAQ handles the data flow from the sub-detector electronics to the archiving on tape shown in Fig. 3.36. Furthermore, The DAQ system also includes software packages for raw data integrity and system performance monitoring and overall control of the DAQ system. The detectors receive the trigger signals and the associated information from the CTP, through a dedicated LTU interfaced to a Timing, Trigger and Control (TTC) system. The Front-End Read-Out (FERO) electronics of the detectors is interfaced to the ALICE-standard Detector Data Links (DDL). The same standard protocol is used to inject data produced from the detectors (event fragments) on the DDL. In the DQA system, The event fragments are read out from the optical DDL and reassembled into sub-events by the Local Data Concentrators (LDCs), which are then transferred to the Global Data Collectors (GDCs), in charge of performing the event building network. The Event Destination Manager (EDM) broadcasts information about the availability of the GDCs to all LDCs. All the sub-events are received by the same GDC, and assembled into a full event. The assembled event is then archived over the storage network as data files of a fixed size to the Transient Data Storage (TDS) consisting of storage arrays connected to the storage network. The data files are then read by the TDS movers (TDSM) over the storage network and exported to the computing center where they are recorded to the Permanent Data Storage (PDS). Each uninterrupted data collecting period is called a run, ranging from few minutes to many hours, with the same hardware and software configuration. During a run period, all GDCs produce a sequence of such files which are registered in the ALICE Grid software

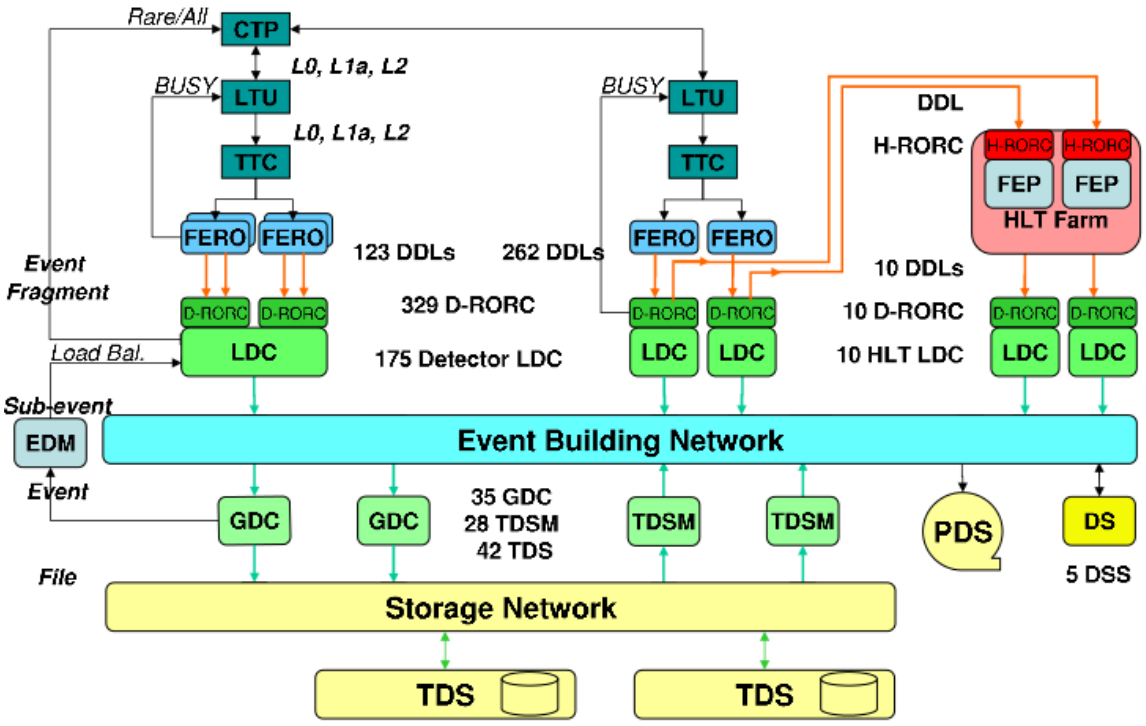

CTP: Central Trigger Processor
DA: Detector Algorithm
DDL: Detector Data Link
DQM: Data Quality Monitoring
D-RORC: Detector Read Out Receiver Card
DSS: DAQ Service Server
EDM: Event Distribution Manager
FERO: Front End Read Out electronics
FEP: Front End Processor
GDC: Global Data Collector
HLT: High-Level Trigger
H-RORC: HLT Read Out Receiver Card
LDC: Local Data Concentrator
LTU: Local Trigger Unit
PDS: Permanent Data Storage
TDSM: Transient Data Storage Manager
TTC: Timing, Trigger and Control

Figure 3.36: Overall architecture of the ALICE DAQ and the interface to the HLT system [236, 265].

(AliEn) [266].

3.3.1.3 High-Level Trigger

The ALICE High-Level Trigger (HLT) [236, 264, 267] is a dedicated real-time system for online event reconstruction and triggering. It is designed to combine and process the full information from all major ALICE sub-detectors in a large computer cluster. Its main goal is to reduce the raw data volume read from the detectors by an order of magnitude, and to fit within the available data acquisition bandwidth while preserving the physics information of interest. This is achieved by a combination of different techniques which require a detailed online event reconstruction:

- **Trigger**:
  selecting interesting events based on detailed online analysis of its physics observables.

- **Selection**:
  selecting the Regions of Interests (interesting part of single events).

- **Compression**:
  reducing the event size by advanced data compression without any loss of the contained physics.

Fig. 3.37 shows six architectural layers of the HLT. The HLT system physically comprises a large computing cluster built mostly from commodity components. The main production cluster has 205 individual machines used for computation, which are divided into 117 Front End Processor (FEP) machines, 84 Compute Nodes (CN) and 4 portal machines. At the layer 1, the raw data from all ALICE sub-detectors are received over these channels and fed into the HLT compute farm via 454 DDLs. When going to the layer 2, the first processing performs basic calibration and extracts hits and clusters, which is achieved in part with hardware coprocessors and therefore simultaneously with the receiving of the data. The event for each detector is reconstructed individually at the layer 3. At the Layer 4, the processed and calibrated information of all detectors is combined and the whole event is reconstructed. The reconstructed physics observables is use to perform the selection of events or regions of interest by layer 5 based on run specific physics selection criteria. The selected data is further subjected to complex data compression algorithms.

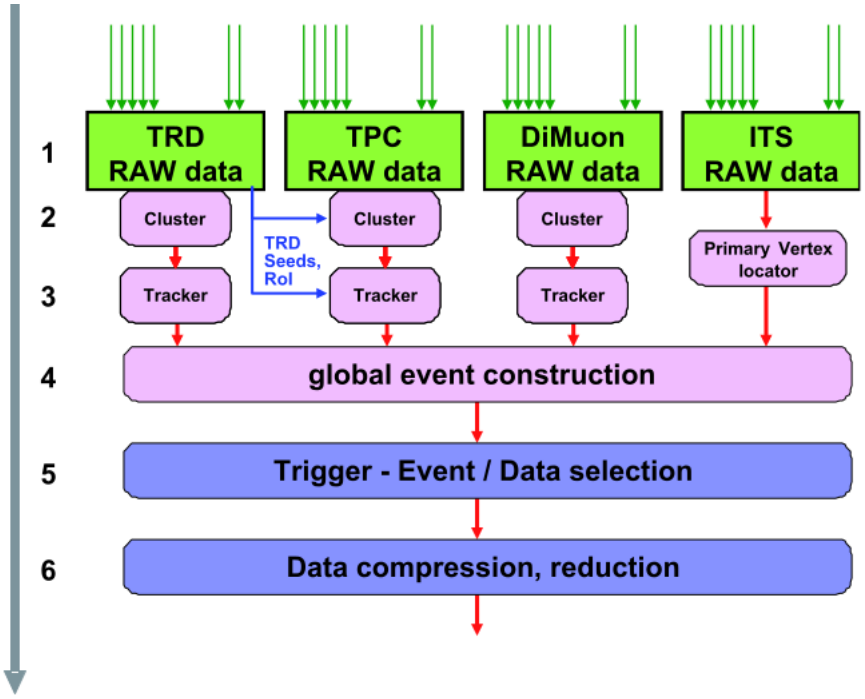

Figure 3.37: Schematic diagram of the six architectural layers of the HLT [236].

3.3.1.4 Detector Control System

The ALICE Control System (DCS) [264] performs to ensure a safe and correct operation of the ALICE experiment. It provides remote control and monitoring of all experimental equipment in such a way that the ALICE experiment can be operated from a single workplace through a unique set of operator interface panels. The optimal operational conditions are provided vis the system in order to keep high quality in the data taking by the experiment.

The hardware architecture of the control system consists of three layers shown in Fig. 3.38. The first layer is supervisory layer, which provides the user interfaces to the operators and connect to disk servers with a number of PCs' supports. The supervisory level will interface, mainly through a LAN, to the control layer. The control layer collects and processes information from the lowest (field) layer via field buses or the Local Area Network and forward them to the supervisor. The third layer, field layer, contains all field devices (*e.g.* power supplies), sensors and actuators. To the software architecture, it is built as a tree-like structure representing the structure of sub-detectors, their sub-systems and devices. The basic building blocks for the entire hierarchical control system are two types of nodes, Control Units (that model the behaviour and interactions between components) and Device Units (that

drive the equipment to which they correspond).

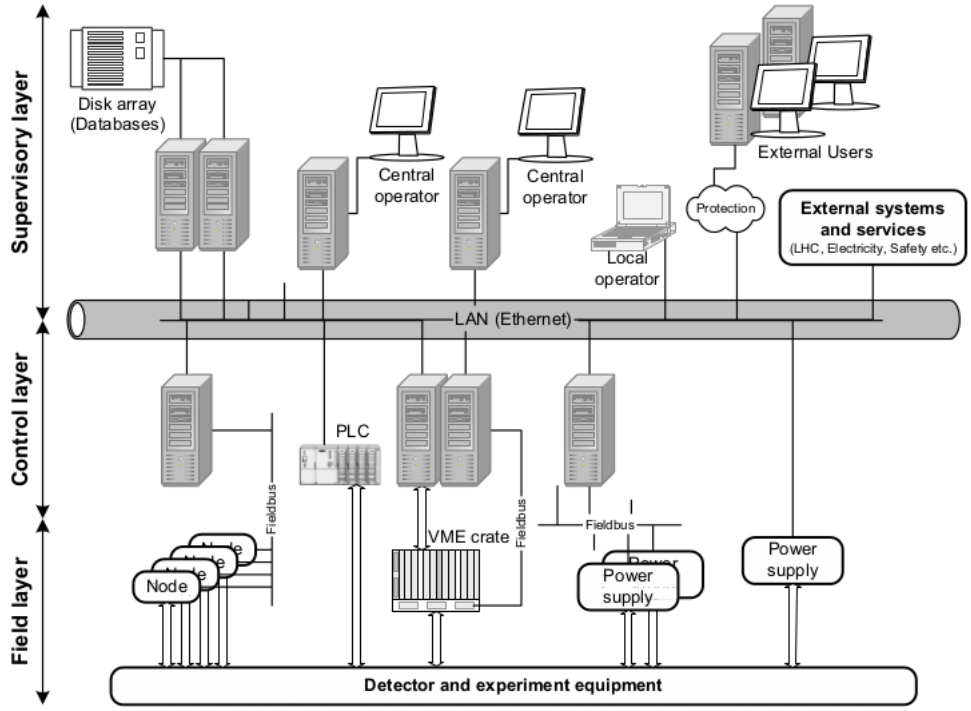

Figure 3.38: Hardware architecture of the DCS in the ALICE experiment [264].

3.3.1.5 Experiment Control System

The Experiment Control System (ECS) [264] is logically a part of the ALICE control system, which is responsible for the coordination and synchronization of the online systems involved (DAQ, TRG, HLT, and DCS) and the LHC machines as shown in Fig. 3.40. The role of the ECS mainly includes the following. On the one

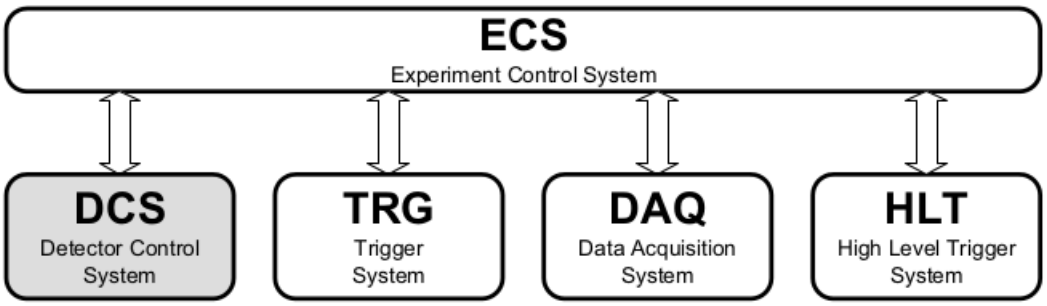

Figure 3.39: Interface of ECS with other online system in the ALICE experiment [264].

hand, it provides the operators with a unified view of the experiment and a central

point from where to steer the experiment operations. On the other hand, it also permits independent concurrent activities on parts of the experiment by different operators at the detector level. At last, it has to coordinate the operations of the control systems active on each detector: the trigger control, the detector control, the DAQ run control and the High-Level Trigger control.

Fig. 3.40 illustrates the architecture of the ECS. The database is the heart of the system, where all the resources are described. The Experiment Control Agent (ECA) is a utility that facilitates the manipulation of the database. Resources are allocated by the Partition Control Agent (PCA), which creates an environment in which only allocated resources are seen by the online systems. The major components of

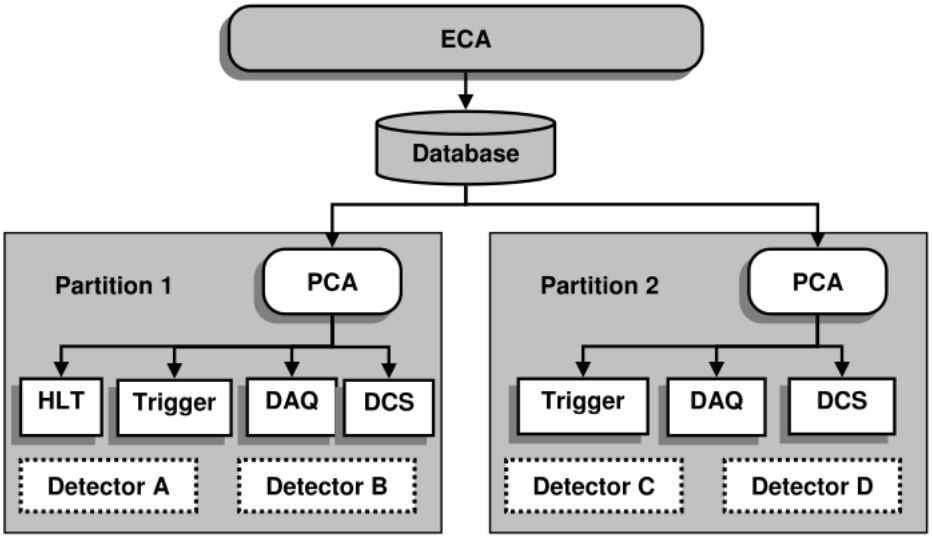

Figure 3.40: Architecture of the ECS in the ALICE experiment [264].

the system include Finite State Machines (FSM), PCA, The Database and Human Interface. The FSM provides an intuitive way of representing the behavioural model of a real object, therefore they constitute the ideal paradigm for the implementation of the ECS, and also provides a natural communication model, based on the control of objects located in remote Activity Domains. The PCA controlling each partition is a process performing its task through FSMs and implemented using the FSM package SMI++. The database holds the list of all the resources and their characteristics. The operators can interact with the ECS by means of human-interface processes. These processes have a passive role: they establish a connection with one of the ECS agents (ECA or PCA), display on the screen the information that the agent makes available to them, and forward to the agent the commands required by the operator.

3.3.2 ALICE offline project

The ALICE offline project is a complex environment for development and operation of the data processing framework. The tasks of the offline project mainly includes simulation, reconstruction, calibration, alignment, visualization and analysis. In this section, Two main parts of the offlie environment, AliRoot framework and ALICE computing grid, are introduced.

3.3.2.1 ALICEROOT framework

The ALICE offline framework, AliRoot [237, 268, 269], was started to develop in 1998, at a time when computing was facing a huge challenging task in high-energy physics. The AliRoot is entirely based on Object Oriented technology (C++) for programming and complemented by the AliEn system which gives access to the computing grid. It is developed from the ROOT [270] which provides an environment for the development of software packages for event generation, detector simulation, event reconstruction, data acquisition and a complete data analysis framework. The final objective of the AliRoot offline framework is to reconstruct and analyze the physics data coming from Monte-Carlo simulation and real collisions data in ALICE experiment. It also was used to perform simulation studies for the Technical Design Reports of all ALICE detectors and optimize their design during the initial stage of ALICE experiment.

The AliRoot framework is schematically shown in Fig. 3.41. The STEER module as the core in this framework provides steering, run management, interface classes and base classes. The codes for simulation and reconstruction from the different detectors are independent. The response of different detector simulation is performed via different transport packages like GEANT3 [271], GEANT4 [272] and FLUKA [273]. In the EVGEN module, it contains some hadronic collisions event Monte-Carlo generators like, PYTHIA [274], HIJING [275], etc. The ROOT capabilities are extended by providing an ALICE Environment (AliEn) specific implementation to allow ALICE users a transparent access to datasets on the Grid.

In ALICE, the data processing of AliRoot framework is shown in Fig. 3.42 [237]. Associated with real particle collisions, simulated collisions are generated via simulation programs by Monte-Carlo event generators and detector response simulation packages. The data produced by the event generators contains the full information about the generated particles (PID, momentum, charge, *etc*), and then is transported to detectors where the detector response is simulated with the transport

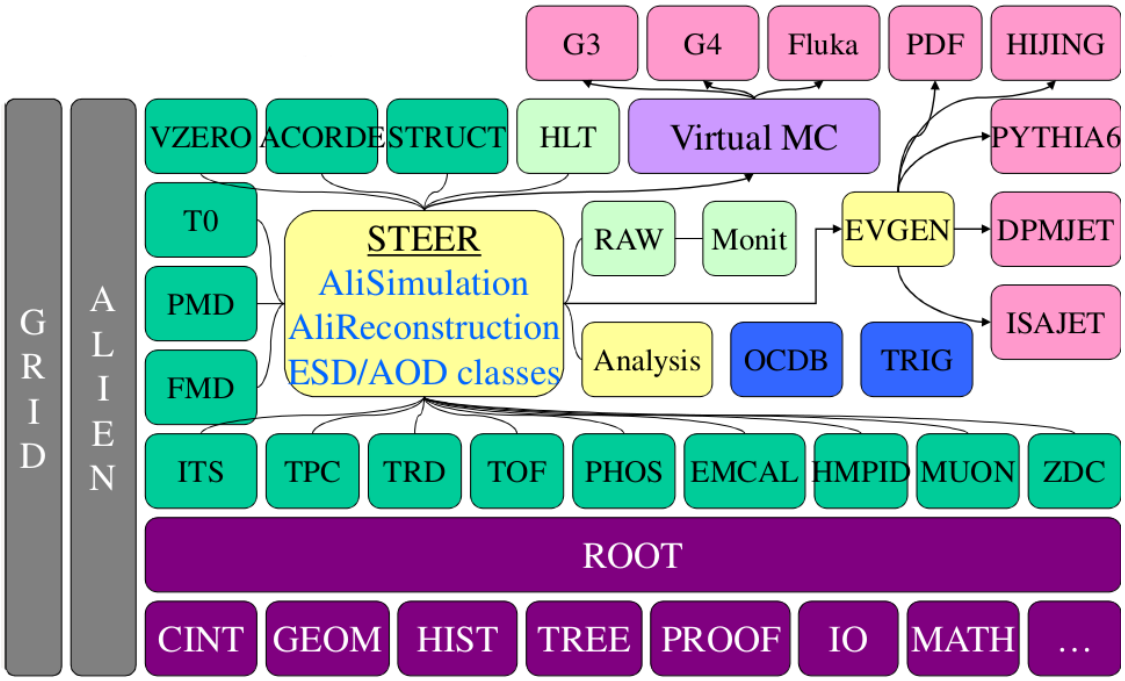

Figure 3.41: Schematic view of the AliRoot offline framework [268].

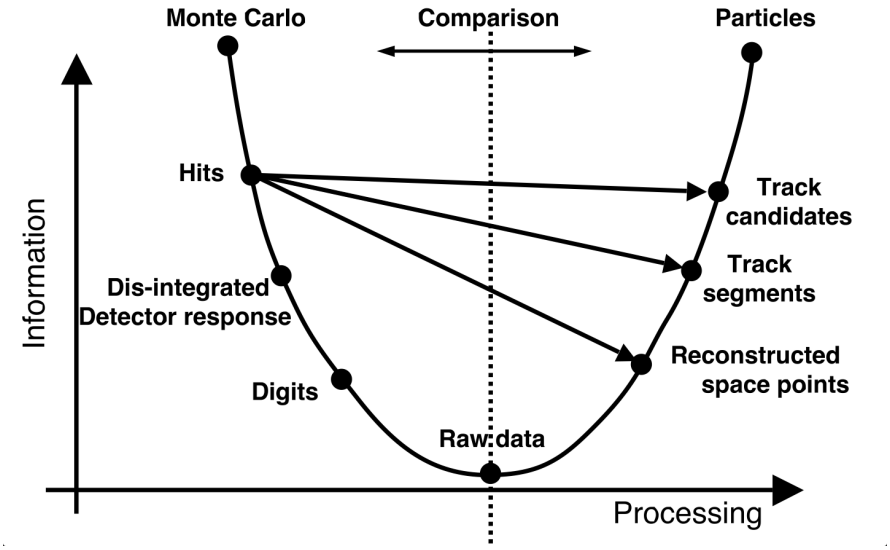

Figure 3.42: Data Processing Framework in AliRoot [237].

packates. The transport package transports the generated particles through the set of detectors, and produces *hits*. The hits are energy deposition at a given point and time, which are transformed into *digits* by taking into account the detector response and associated electronics response. In the transport procedure, each original and new particle from interactions is traced up till the moment when it leaves the full ALICE detector volume or its energy drops below a predesignated threshold. Finally, *raw data* are produced when the digits from simulated events are stored in the specific hardware format of each detector. The reconstruction and analysis chains can be activated from the raw data produced point.

In the reconstruction chain, full information of the particles trajectory and mass starting are reconstructed by the reconstruction algorithms. For example, a local reconstruction of clusters is performed in each detector firstly, then vertexes and tracks are reconstructed and particles types are identified. In order to evaluate the software and detector performance, the simulated events are processed through the whole cycle, and the reconstructed particles are eventually compared to the Monte-Carlo generated ones. The final output of the reconstruction stored in the Event Summary Data (ESD) which is a root file containing all the information needed during the physics analysis, as follows [268]:

- fields to identify the event such as run number, event number, trigger word, version of the reconstruction, etc.;
- reconstructed ZDC energies and number of participant;
- primary vertex;
- T0 estimation of the primary vertex;
- array of ESD tracks;
- arrays of HLT tracks both from the conformal mapping and from the Hough transform reconstruction;
- array of MUON tracks;
- array of PMD tracks;
- arrays of reconstructed V0 vertexes, cascade decays and kinks;
- indexes of the information from PHOS and EMCAL detectors in the array of the ESD tracks.

From the Monte-Carlo simulation to the ESD data, the procedure can be shown in Fig. 3.43. Compared to the simulation, in the real data, the similar chain is presented in this figure, which includes the online system introduced in Sec. 3.3.1.

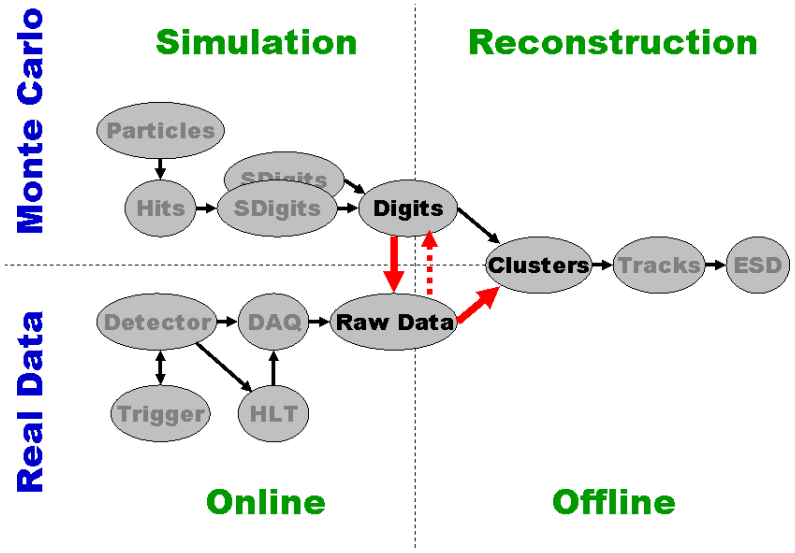

Figure 3.43: Simulation and reconstruction framework in AliRoot [268].

In the ALICE computing model, the analysis activity starts from the ESD, whose size is about one order of magnitude lower than the corresponding raw data. From the ESD data, some filters are performed through a train of "analysis tasks" required by the analyzers (the physics working groups in the ALICE collaboration) who are interested in specific physics. In this case, the ESD data is filtered to result in the creation of Analysis Object Data (AOD) files, which also contain all the informations needed for a specific analysis and can be more easily handled by the users. The typical analysis to calculation the physics quantities of interest requires processing of selected sets of events, and then looping over all the selected events. Usually, in each event, a set of loops over the reconstructed entities such as tracks, neutral clusters, etc, is needed to select the signal candidates by applying a number of criteria (cuts). The selection criteria is usual estimated via simulation data analysis to achive optimization. The analysis results obtained after using the criteria are raw, and need to be corrected with many detector correction factors, *e.g.*, trigger efficiency, reconstruction efficiency, geometrical acceptance, etc. The last part to achive the physics quantity usually involves quite complex mathematical treatment, and sophisticated statistical tools, *e.g.*, statistical errors, systematic errors, *etc.*

3.3.2.2 ALICE Grid

To the present and foreseen real and simulated data, the enormous computing resources required to process the data coming from the ALICE experiment isof such magnitude that it is not feasible to concentrate it in a single computing center. Therefore, in order to utilize the computing centers located at worldwide for solving this problem, the Grid Middleware was developed in the ALICE experiment, which allows for efficient, seamless, and democratic access to worldwide-distributed heterogeneous computing and storage resources distributed at the HEP computing facilities of the institutes and universities participating in the experiment. The technical side of the decentralized offline computing scenario has been formalized in the so-called MONARC model [276] schematically shown in Fig. 3.44. All real data

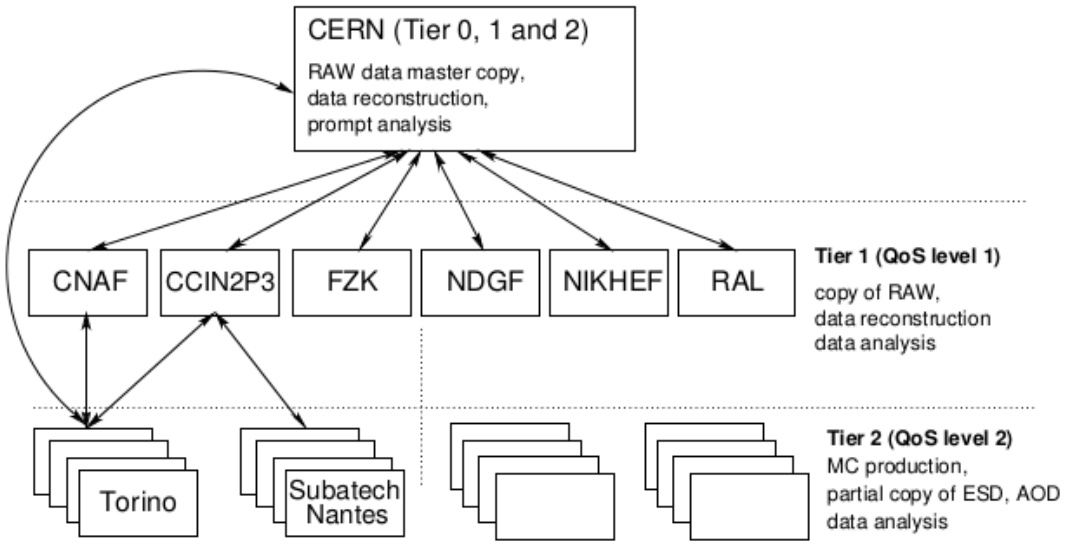

Figure 3.44: Schematic view of the ALICE offline computing tasks in the framework of the tiered MONARC model [269].

originate from CERN, with a very large computing center called Tier 0. Tier 1s are the major large regional computing centers which provide a safe data storage on high reliably storage media and perform the bulk of the organized processing of the data. Tier 2s are smaller centers which are logically clustered around the Tier 1's. The major role of Tier-2's is simulation and end-user analysis. The MONARC model also foresees Tier 3s which are university departmental computing centers and Tier 4s that are user workstations. Generally, the raw data from the experiment is stored at CERN (Tier 0), and the Tier 1 centers share the reconstruction to the ESD level. The Tier 1s also participate subsequent data reduction to the Analysis

Object Data (AOD) level, analysis and Monte-Carlo production with Tier 2s. While the Tier 2s also perform Monte-Carlo and end-user analysis. Presently, the ALICE grid is composed of over 90 sites scattered all over the world (mainly, Africa, Asia, Europe, North and South America), involving 5 Tier 0 centers, 5 Tier 1 centers and more than 80 Tier 2 centers [277] shown in Fig. 3.45

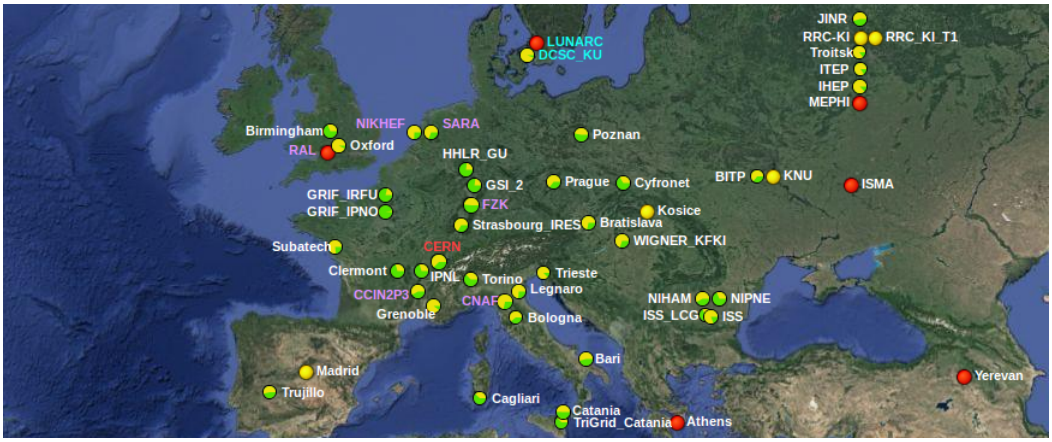

Figure 3.45: Part of ALICE Grid sites spotted in the worldwide [277].

The ALICE developed in year 2000 an interface to the Grid with Alice Environment (AliEn) [278, 279]. The AliEn has been developed to offer the ALICE user community a transparent access to computing resources distributed worldwide through a single interface as AliEn User Interface (UI). The AliEn components are mainly as following:

- File catalogue with meta-data capabilities.
- Data management tools for data transfers and storage.
- Authentication and authorization
- Workload management system.
- Interfaces to other Grid implementations.
- ROOT interface.
- Monitoring.

3.3.2.3 Neutral trigger correlations analysis framework

Analysis is the final operation performed on the data and the user finally destined to extract interesting physics information. In the ALICE Computing Model, the analysis starts from the ESD produced during the reconstruction step. The AOD is produced with a very general analysis filter named *AliAnalysisTaskESDfilter* from the ESD (more filters can be done according to the user own for specific physics analysis from ESD or AOD). Further analysis passes can start from condensed AODs. The overview of the analysis chain in AliRoot can be found in Fig. 3.46.

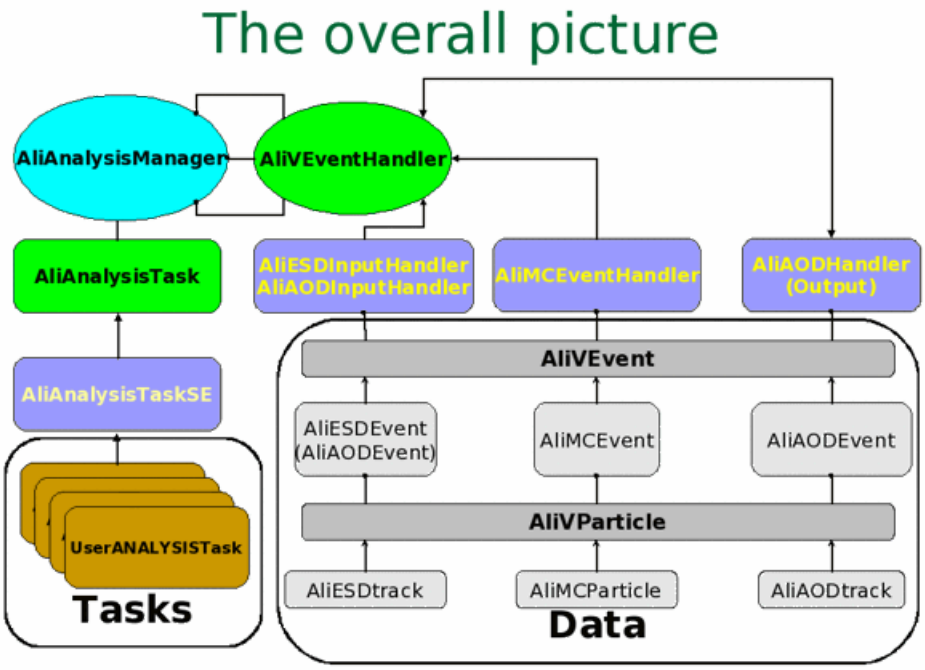

Figure 3.46: Schematic view of analysis framework starting from ESD and AOD data in AliRoot [268].

The neutral trigger correlations in this work are analyzed with tasks located in two sub-directories in AliRoot:

- PWG/CaloTrackCorrBase
- PWGGA/CaloTrackCorrelations

In PWGGGA/CaloTrackCorrelations/macros, the analysis macros to launch the analysis can be found. The framework is rather flexible and allows to analyze correlations between trigger particles, γ, π^0, η and associated particles, tracks (charged hadrons).

The analysis includes the following steps:

- **Event, cluster and track filtering**: Events are selected depending on the vertexes, centralities and other criteria tracks and calorimeter clusters are filtered based on the cuts required by the analyzer. The filtering is done in the class *AliCaloTrackReader*.

- **Particle identification**: Looping over the clusters or tracks in their array, this selects the particles needed in the analysis with the corresponding PID criteria to the clusters or tracks. The particle with PID is put into a new array which will be the list of possible triggers for the correlations, or the invariant mass analysis for neutral mesons analysis. In our analysis, the triggers includingγ, π^0 and η are identified via two different classes as:

  - γ **with** *AliAnaPhoton*: This class loops over all clusters in an array with the photon identification criteria, such as track matching, cluster timing, cluster shower shape cuts, etc to select the photon candidates for correlation or neutral mesons analysis.

  - π^0 (η) **with** *AliAnaPi0EbE*: This class can perform different kind of neutral meson selections event-by-event.

    * **Shower shape and splitting**: Clusters with large shower shape long axis are likely to be produced together by two photons from one neutral meson decay. They can be split and if the invariant mass of the new split two clusters is close to the one of the neutral meson, then the cluster is selected.

    * **Invariant mass in calorimeter**: Two clusters in the calorimeter falling in a given mass window are selected. The side bands around the peak are checked to address the background.

- **Correlation with tracks (charged hadrons)**: This is done in class *AliAnaParticleHadronCorrelation*. The azimuthal correlations of the trigger particles with tracks and other available measurements are stored in histograms. The same is done for the event mixing (in case it is needed).

Chapter 4

Two-particle azimuthal correlations

Many experimental and theoretical studies of the QGP have been obtained from the study of hadron jets, the fragmentation products of high transverse momentum (p_{T}) partons [105–108, 280]. It is generally accepted that prior to hadronization, partons lose energy in the extremely hot and dense medium due to the gluon radiation and the multiple collisions. These phenomena are broadly known as "jet quenching" [72–74]. A strong di-jet energy asymmetry for leading jet transverse momenta above 100 GeV/c has been reported [179, 180]. At low transverse momenta ($p_{\mathrm{T,\ jet}} < 50$ GeV/c), background fluctuations due to the underlying event dominate [281] and event-by-event jet reconstruction becomes difficult. Two-particle correlations allow the study of medium effects on the jet fragmentation without the need for jet reconstruction. A brief introduction about the measurements of two-particle correlations is presented in Sec. 2.3.3. In this chapter, more details about two-particle correlations, including di-charged hadron correlations, π^0-charged hadrons and γ-hadron correlations, are summarized.

4.1 Two-particle correlation analysis method

The p_{T} dependence of the correlation is studied by measuring triggered correlations. In such an analysis, a particle is chosen from a p_{T} region and called the *trigger particle*. The so called *associated particles* from another p_{T} region are correlated to the trigger particle where $p_{\mathrm{T}}^{\mathrm{assoc}} < p_{\mathrm{T}}^{\mathrm{trig}}$. The associated per-trigger yield is measured as a function of the azimuthal angle difference $\Delta\varphi = \varphi_{\mathrm{trig}} - \varphi_{\mathrm{assoc}}$ and pseudo-rapidity difference $\Delta\eta = \eta_{\mathrm{trig}} - \eta_{\mathrm{assoc}}$:

$$Y(\Delta\varphi, \Delta\eta) = \frac{1}{N_{\rm trig}} \frac{dN^2_{\rm assoc}}{d\Delta\varphi d\Delta\eta} \tag{4.1}$$

where $N_{\rm assoc}$ is the number of particles associated to a number of trigger particles $N_{\rm trig}$. This quantity is measured for different ranges of $p_{\rm T}^{\rm trig}$ and $p_{\rm T}^{\rm assoc}$. A typical schematic view of di-jet events and two particles azimuthal angle correlations are shown in Fig. 4.1.

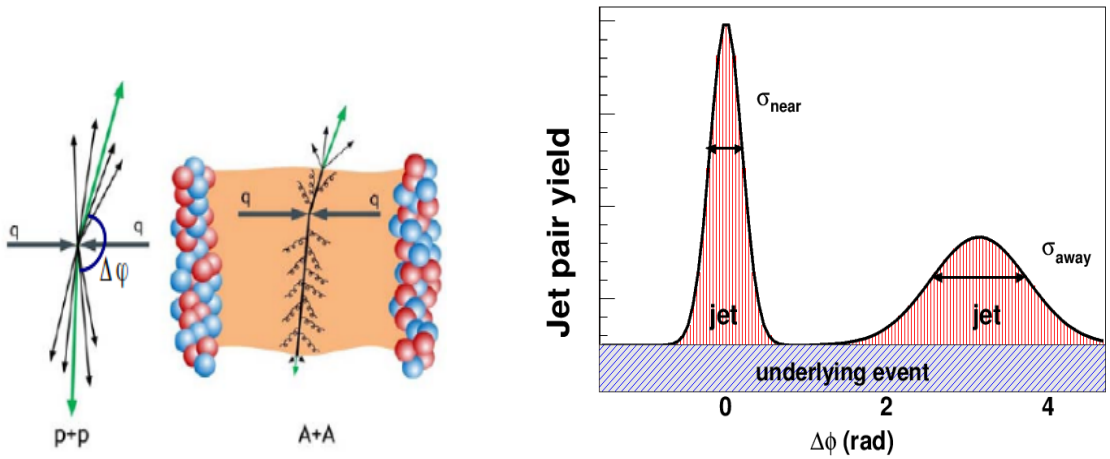

Figure 4.1: Left: Schematic view of di-jet production in pp and A+A collisions. Right: Cartoon of two-particle azimuthal angle correlations distribution in $\Delta\varphi$ in pp collisions. It has two peaks corresponding to near side ($\Delta\varphi \sim 0$) and away side ($\Delta\varphi \sim \pi$) jet, and a flat component representing the underlying event pairs.

To obtain the fully corrected per-trigger associated primary particle yield, two steps are performed on the raw correlations. Firstly, detector acceptance effects are assessed by using a mixed-event technique: the differential yield defined in Eq. 4.1 is also constructed for pairs where the trigger and the associated particle come from different events with similar centrality (or multiplicity in pp) and z-vertex position. The angular correlation constructed from particles within the same event and mixed events are shown in the left and right panel in Fig. 4.2. The acceptance corrected distribution can be obtained from the ratio of pair distributions from the same and mixed events with a proper normalization factor, as written as:

$$C(\Delta\varphi, \Delta\eta) = \frac{d^2N^{\rm raw}(\Delta\varphi, \Delta\eta)}{d\Delta\varphi d\Delta\eta} = \frac{1}{N_{\rm trig}} \frac{d^2N^{\rm same}/d\Delta\varphi d\Delta\eta}{d^2N^{\rm mixed}/d\Delta\varphi d\Delta\eta} \cdot \alpha \tag{4.2}$$

where the normalization factor α is chosen to normalize the background distribution such that it is unity for pairs at $\Delta\varphi = \Delta\eta \approx 0$. If one only focuses on the distribution of $\frac{1}{N_{\rm trig}} \frac{dN}{d\Delta\varphi}$, the factor $\alpha = \frac{dN^{\rm mixed}}{d\Delta\varphi}|_{\Delta\varphi=0}$ is selected. Secondly, tracking efficiency and

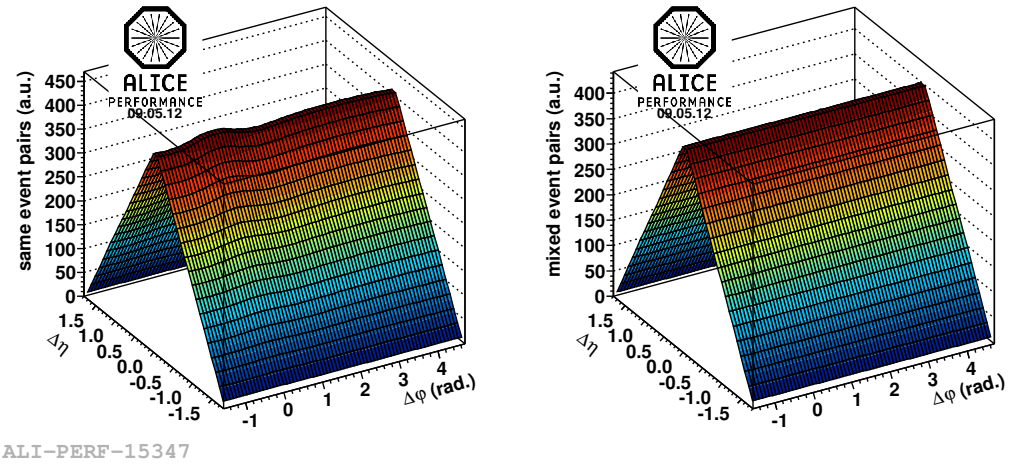

Figure 4.2: Correlation constructed from pairs of particles from the same events (left panel) and the mixed events (middle panel) [282].

track contamination from secondary particles are used to correct the correlation function.

In nucleus-nucleus collisions, multiple processes, such as jets, mini-jets, resonance decays and anisotropic flow, have contributions to the two-particle correlations. To obtain the jet-like correlations, one needs to subtract other sources, so-called background, contributed to the correlations. Among these background sources, anisotropic flow is dominant. Generally, the jet-like correlations noted by $J(\Delta\varphi)$ are obtained as:

$$J(\Delta\varphi) = C(\Delta\varphi) - B(\Delta\varphi) \tag{4.3}$$

where $B(\Delta\varphi)$ is the background contribution term estimated by anisotropic flow. According to the expression of anisotropic flow in Sec. 2.3.2. When one only takes into account the main flow contribution, elliptic flow, the jet correlations term is written as:

$$J(\Delta\varphi) = C(\Delta\varphi) - b_0(1 + 2\langle v_2^{trig} v_2^{assoc}\rangle \cos(2\Delta\varphi)) \tag{4.4}$$

where v_2^{trig} and v_2^{assoc} are the elliptic flow coefficients of trigger particles and associated particles, respectively, b_0 is the background scaled factor, which is generally determined by a pedestal subtraction employing the zero-yield-at-minimum (ZYAM) method.

4.2 Di-hadron correlations

Many significant measurements of di-hadron correlations from previous experiments were obtained and presented in the Jet quenching summary of Sec. 2.3.3. A little more measurements from ALICE are discussed in the following.

4.2.1 Near-side jet shape

A typical per-trigger yield is shown in the left panel of Fig. 4.3. At low-p_{T}, per-trigger yield includes a sizable contribution from collective flow with a strong modulation in $\Delta\varphi$ but independent of $\Delta\eta$. For isolating jet-like correlations to study the shape of the near-side jet peak, the flow contributions are determined in the long-range correlation region at $1 < |\Delta\eta| < 1.6$ and subtracted from the short-range correlation region at $|\Delta\eta| < 1$. This prescription called the η-gap method provides a measurement independent of the flow strength. The middle panel of Fig. 4.3 shows the projection to azimuthal $\Delta\varphi$ in $1 < |\Delta\eta| < 1.6$ (red) and $|\Delta\eta| < 1$ (black). The difference between the two distributions in the near-side is the signal to be searched. The away-side peak is removed by construction in this procedure. Hence, the away-side region can not be studied with this method. The right panel of Fig. 4.3 shows the subtracted per-trigger yield distribution in $\Delta\varphi$ and $\Delta\eta$ with $4 < p_{\mathrm{T}}^{\mathrm{trig}} < 8$ GeV/c and $1 < p_{\mathrm{T}}^{\mathrm{assoc}} < 2$ GeV/c in most central Pb+Pb collisions.

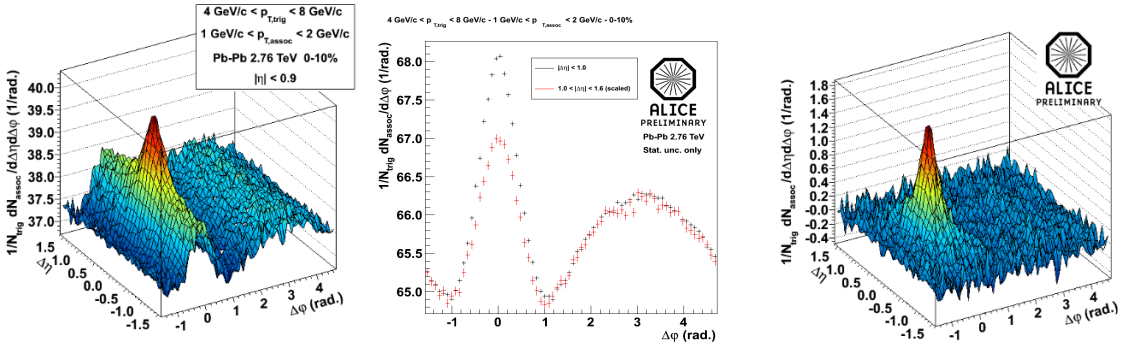

Figure 4.3: Left: Per-trigger yield; middle: Per-trigger yield projection to $\Delta\varphi$ in $1 < |\Delta\eta| < 1.6$ (red) and $|\Delta\eta| < 1$ (black); right: Per-trigger yield subtracted flow contributions. Shown is at trigger $4 < p_{\mathrm{T}}^{\mathrm{trig}} < 8$ GeV/c, associated $1 < p_{\mathrm{T}}^{\mathrm{assoc}} < 2$ GeV/c in most central Pb+Pb collisions [282].

In order to quantify the near-side peak shape, the peak is fitted with a sum of two 2D Gaussians with the center at $\Delta\varphi = \Delta\eta = 0$. The fit parameters are used

to calculate the *rms* (equal to the square root of the variance, σ, for distributions centered at 0) in $\Delta\varphi$ and $\Delta\eta$ direction ($\sigma_{\Delta\varphi}$, $\sigma_{\Delta\eta}$). Fig. 4.4 presents the centrality dependence of $\sigma_{\Delta\varphi}$ and $\sigma_{\Delta\eta}$ together with reference results from pp collisions in five different bins of $p_{\mathrm{T}}^{\mathrm{trig}}$ and $p_{\mathrm{T}}^{\mathrm{assoc}}$. The results indicate that the $\sigma_{\Delta\varphi}$ is independent of centrality within the errors, and decreases with increasing $p_{\mathrm{T}}^{\mathrm{trig}}$ and $p_{\mathrm{T}}^{\mathrm{assoc}}$, whereas the $\sigma_{\Delta\eta}$ has a significant increase of moving from pp to central collisions and also decreases with higher $p_{\mathrm{T}}^{\mathrm{trig}}$ and $p_{\mathrm{T}}^{\mathrm{assoc}}$. More details about this analysis can be found in [282, 283].

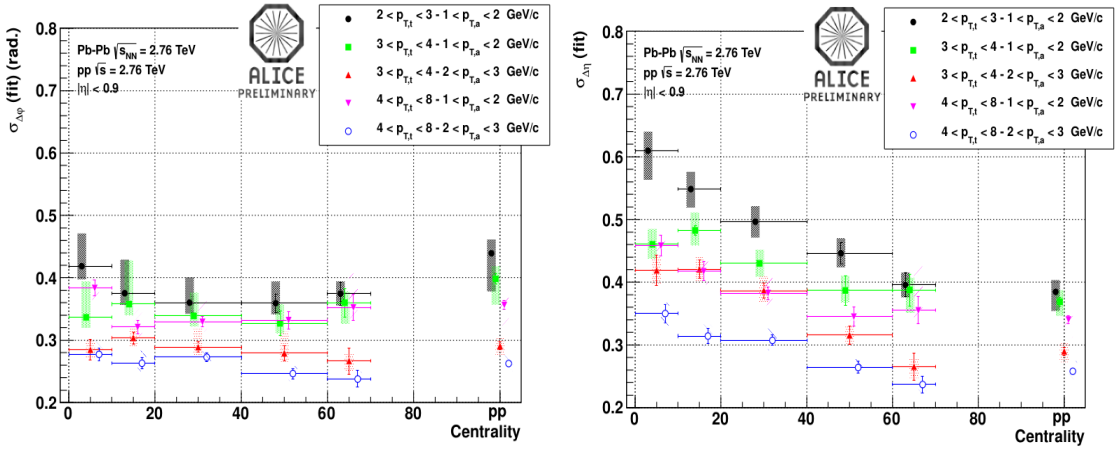

Figure 4.4: Centrality dependence of $\sigma_{\Delta\varphi}$ (left) and $\sigma_{\Delta\eta}$ (right) in five different $p_{\mathrm{T}}^{\mathrm{trig}}$ and $p_{\mathrm{T}}^{\mathrm{assoc}}$ p_{T} bins.

4.2.2 Modification of the jet-particle yield

At higher p_{T} ($p_{\mathrm{T}}^{\mathrm{trig}} > 8$ GeV/c, $p_{\mathrm{T}}^{\mathrm{assoc}} > 3$ GeV/c) where collective effects are small and jet-like correlations dominate, the medium modification of the jet-particle yield has been studied by calculating ratios of yields on the near-side and away-side. In order to remove uncorrelated background from the yield, a pedestal value is determined by a constant fitting the region close to the minimum of the $\Delta\varphi$ distribution ($\Delta\varphi \approx \pm\frac{\pi}{2}$) where uncorrelated background is dominated. A background shape considering the elliptic flow parameter v_2 is also analyzed. For a given p_{T} bin, the v_2 background is calculated as $2\langle v_{2,\mathrm{trig}}\rangle\langle v_{2,\mathrm{assoc}}\rangle \cos 2\Delta\varphi$. The v_2 values are taken from an independent measurement [284]. The η-gap method, described in Sec. 4.2.1, is also used to remove the contributions from $\Delta\eta$-independent correlations on the near-side of the per-trigger yield. Subsequent to the background subtraction, the near-side and away-side yields are integrated within $|\Delta\varphi| < 0.7$ and $|\Delta\varphi - \pi| < 0.7$, respectively.

The modification of the jet-particle yield is calculated by the ratio of the per-trigger yield in Pb+Pb to pp collisions ($I_{\rm AA}$) and the yield in central to peripheral in Pb+Pb collisions ($I_{\rm CP}$) with $I_{\rm AA} = Y_{\rm Pb+Pb}/Y_{\rm pp}$ and $I_{\rm CP} = Y^{\rm Pb+Pb}_{\rm central}/Y^{\rm Pb+Pb}_{\rm peripheral}$, respectively. The top panel in Fig. 4.5 presents the yield modification factor $I_{\rm AA}$ for central and peripheral Pb+Pb collisions using the three background subtraction schemes as discussed. The main significant difference is in the lowest $p_{\rm T}^{\rm assoc}$ interval that confirms the small bias due to flow anisotropies in this $p_{\rm T}$ region. In central collisions, an away-side suppression from in-medium energy loss is observed ($I_{\rm AA} \approx 0.6$). Moreover, there is an enhancement above unity of ($I_{\rm AA} \approx 1.2$) on the near-side which has not been observed with any significance at lower collision energies [285]. In peripheral collisions, both near-side and away-side are consistent with unity. Furthermore, the bottom panel in Fig. 4.5 shows the ratio of the yield

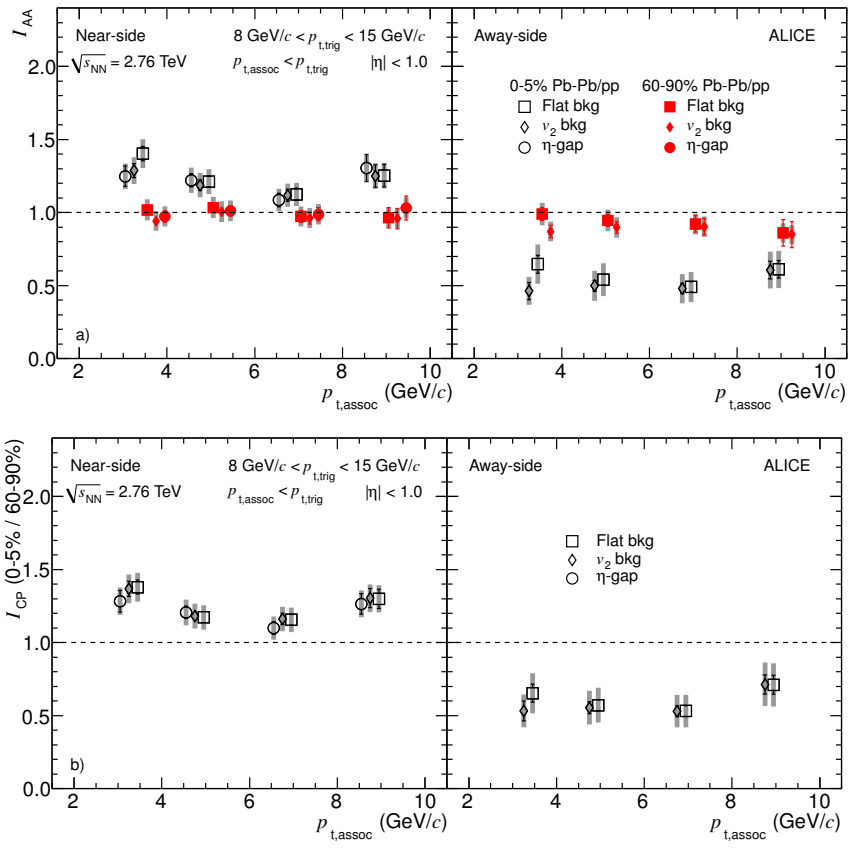

Figure 4.5: $I_{\rm AA}$ (top panel) for central (open black symbols) and peripheral (filled red symbols) collisions , and $I_{\rm CP}$ (bottom panel). Different background subtraction schemes, a flat pedestal (squares), v_2 subtraction (diamonds) and η-gap subtraction (circles, only near-side) are presented [286, 287].

in central and peripheral collisions, $I_{\rm CP}$. The result of $I_{\rm CP}$ is consistent with $I_{\rm AA}$

in central collisions with respect to the near-side enhancement and the away-side suppression.

A significant near-side enhancement of $I_{\rm AA}$ and $I_{\rm CP}$ in the $p_{\rm T}$ region observed shows that the near-side parton is also subject to medium effects. $I_{\rm AA}$ is sensitive to (i) a change of the fragmentation function, (ii) a possible change of the quark/gluon jet ratio in the final state due to the different coupling to the medium, and (iii) a bias on the parton $p_{\rm T}$ spectrum after energy loss due to the trigger particle selection. More details about this analysis can be found in [286, 287].

4.3 Neutral pion-hadron correlations

In this section, the measurement of π^0-hadron correlations at RHIC is introduced. The similar measurement at ALICE is a main constituent of my work included in this thesis. The π^0-hadron correlations is not only an important step to achieve the direct photon-hadron correlation, but also a powerful tool to study the properties of the hot and dense medium. Generally, the trigger, neutral pion, is identified in each event through $\pi^0 \to 2\gamma$ channel. Two photons are paired by satisfying a minimum energy threshold cut and requiring the reconstructed invariant mass around the π^0 PDG mass (ideal mass, ~ 135 MeV/c^2) peak.

Fig. 4.6 shows the measurements of per-trigger jet pair yields in pp and 0-20% in Au+Au collisions at $\sqrt{s_{\rm NN}} = 200$ GeV [288]. On the near side, the yield widths in central Au+Au are comparable to pp in all selected $p_{\rm T}^{\rm trig}$ and $p_{\rm T}^{\rm assoc}$ ranges, and the yields are slightly enhanced at low-$p_{\rm T}$ in both collisions. On the away side, a non-Gaussian and strong broadening distribution compared to pp was qualitatively observed at low $p_{\rm T}^{\rm trig}$ and $p_{\rm T}^{\rm assoc}$ in the Au+Au collisions. In contrast, the yield shows a strong suppression at high $p_{\rm T}^{\rm trig}$ and high $p_{\rm T}^{\rm assoc}$ with the shape consistent with in pp collisions. The measured azimuthal angle distrubitons of π^0-hadron correlations are similar with di-hadron correlations introduced in Sec. 2.3.3.

In addition, the modification of the per-trigger yield of associated particles, $I_{\rm AA} = \frac{Y^{AA}(p_{\rm T}^{\rm trig},\, p_{\rm T}^{\rm assoc})}{Y^{pp}(p_{\rm T}^{\rm trig},\, p_{\rm T}^{\rm assoc})}$, was measured in two different regions on the away side. The measurement results are presented in Fig. 4.7 [288]. On the away side, the modification facotor $I_{\rm AA}$ distribution for $p_{\rm T}^{\rm trig} > 7$ GeV/c tends to fall with $p_{\rm T}^{\rm assoc}$ until $p_{\rm T}^{\rm assoc} \approx 2-3$ GeV/c. While a roughly constant distribution is show at above $p_{\rm T}^{\rm assoc} = 3$ GeV/c. Compared to π^0 $R_{\rm AA}$, the modification factor values is consistently higher than $R_{\rm AA}$ results at $p_{\rm T} > 5$ GeV/c. Two theoretical calculations, ACHNS [290] and ZOWW [291], are presented to compare with the measurements.

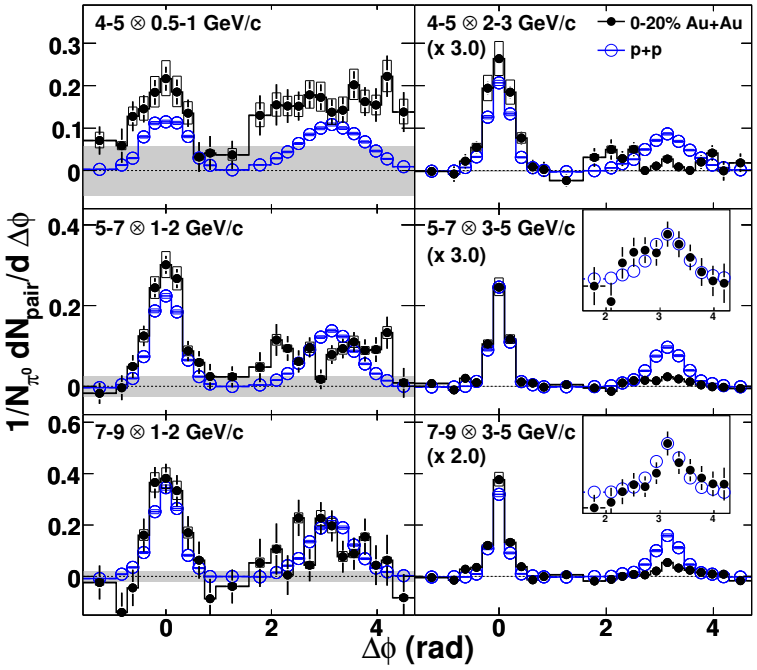

Figure 4.6: Per-trigger of π^0 trigger correlations as a function of $\Delta\varphi$ in Au+Au (solid symbols) and p+p (open symbols) collisions. The systematic uncertainties in Au+Au collisions include point-to-point correlated background level (gray bands) and modulation (open boxes) uncertainties.

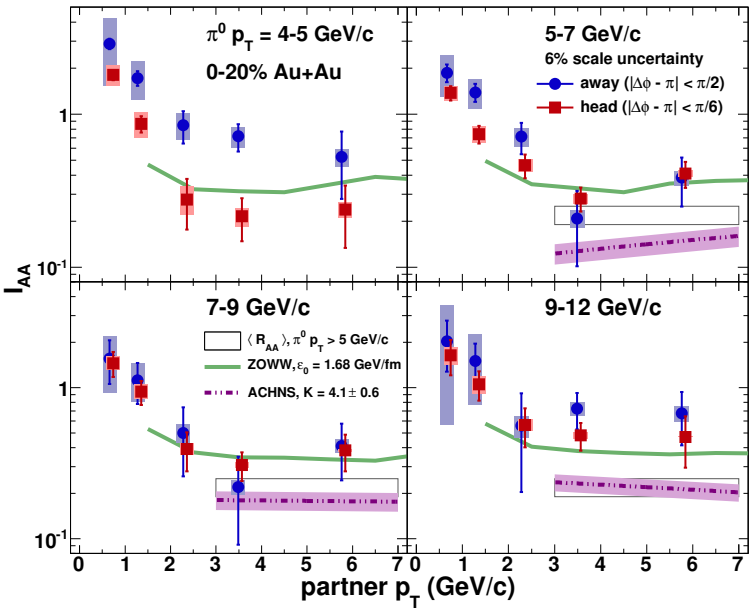

Figure 4.7: Away side modification factor $I_{\rm AA}$ in a narrow "head" region $|\Delta\varphi - \pi| < \pi/6$ (solid squares) and the entire away side region $|\Delta\varphi - \pi| < \pi/2$ (solid circles) in π^0-hadron correlations. Two theoretical predictions are also shown for the head region. For comparison, π^0 R_{AA} [289] bands are presented at $p_{\rm T} > 5$ GeV/c.

The ZOWW calculation, which utilizes a simple spherical nuclear geometry, predicts $I_{\mathrm{AA}} > R_{\mathrm{AA}}$ in well agreement with the measurements.

4.4 Direct photon-hadron correlations

A typical two-particle correlation, direct photon-hadron correlation, offers two major advantages as compared to di-jet measurements because of the nature of the photon. First of all, in contrast to partons, photons do not carry color charge and hence do not interact strongly when traversing the medium [292]. Secondly, the direct photon production at leading-order (LO) in pp and A+A collisions is dominated by the QCD Compton scattering process, $q+g \rightarrow q+\gamma$ and $q+\bar{q} \rightarrow g+\gamma$ annihilation process, and the photon momentum in the center-of-mass frame is approximately balanced by that of the recoil parton when considering the initial transverse momentum, k_{T}, of the colliding partons inside the nucleons. In nucleus-nucleus collisions, the direct photon contributions from next-to-leading-order (NLO) processes, such as fragmentation photons and thermal photons, are expected to be small ($\approx 10\%$) at high-p_{T} [293]. For these reasons, direct photon-hadron correlations have been considered as a "golden channel" for studying the properties of parton energy loss including parton fragmentation function without the need of the jet reconstruction [294, 295]. Furthermore, significant measurements about parton energy loss in the medium by isolated photon-jet correlations at CMS are presented in [296].

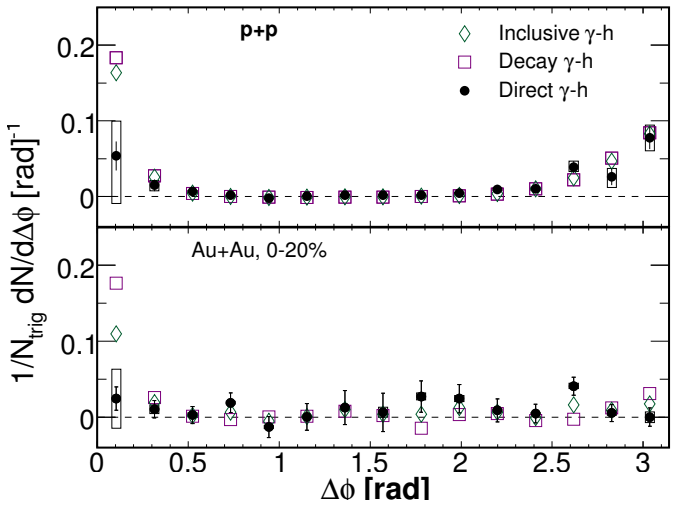

Figure 4.8: Azimuthal angle correlation distributions with trigger inclusive (open diamond), decay (open square) and direct photon (full circle) in pp (top) and in Au+Au at 0-20% collisions (bottom), taken from [297].

At RHIC, a so-called *statistical subtraction method* is mainly used to determine the direct photon-hadron correlations by subtracting the decay photon-hadron correlations from the inclusive photon-hadron correlations. The method can be expressed by a formula as [298]:

$$Y_{\rm dir} = \frac{R_\gamma Y_{\rm inc} - Y_{\rm dec}}{R_\gamma - 1} \tag{4.5}$$

where $Y_{\rm inc}$ and $Y_{\rm dec}$ are inclusive photon-hadron correlation yield and decay photon-hadron correlation yield, respectively, R_γ is the ratio of inclusive photons to decay photons, which implies the direct photon signal existence if $R_\gamma > 1$. In order to measure the decay photon-hadron correlations contribution, meason (main π^0 and η) trigger correlations are constructed firstly. More details about this method can be found in [298] and Chap. 7. Typical measurements of the azimuthal angle correlations from the three trigger particles are shown in Fig. 4.8 [298].

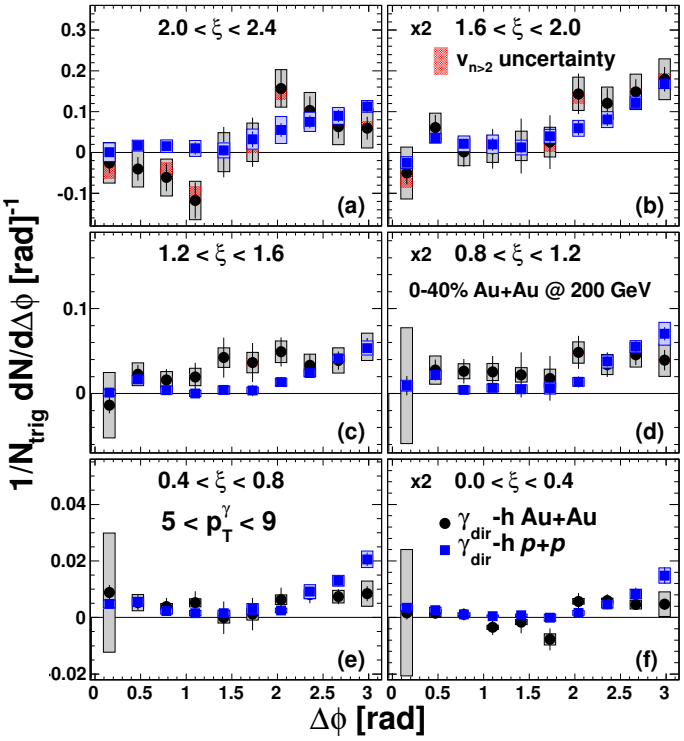

Figure 4.9: Azimuthal angle correlation distributions of direct γ-hadron for (a) $2.0 < \xi < 2.4$, (b) $1.6 < \xi < 2.0$, (c) $1.2 < \xi < 1.6$, (d) $0.8 < \xi < 1.2$, (e) $0.4 < \xi < 0.8$, and (f) $0.0 < \xi < 0.4$ in Au+Au collisions at 0-40% (circles) and pp reference (squares), taken from [297].

The jet fragmentation function, $D(z)$, is determined as a function of $z_T = \frac{p_{\rm T}^{h^\pm}}{p_{\rm T}^{\gamma}}$ where $p_{\rm T}^{h^\pm}$ and $p_{\rm T}^{\gamma}$ are the transverse momenta of associated hadrons and trigger photons, respectively. To focus on the measurement at low z_T region, the fragmentation function can be expressed as a function of the variable, $\xi = \ln(\frac{1}{z_T})$. Fig. 4.9

presents the azimuthal angle correlation distributions of direct photon-hadron correlations in Au+Au collisions at 0-40% centrality, as well as comparison with the measurement in pp collisions [297]. On the near side, the associated hadron yields considering systematic uncertainties in Au+Au collisions show an integrated yield consistent with zero. On the away side, the yields shows some extent suppression in Au+Au collisions comparing the correlations with pp collisions. To further quantify the suppression, the fragmentation function as a function of ξ are measured in full away side region $|\Delta\varphi - \pi| < \pi/2$, as shown in Fig. 4.10. The measurements indicate

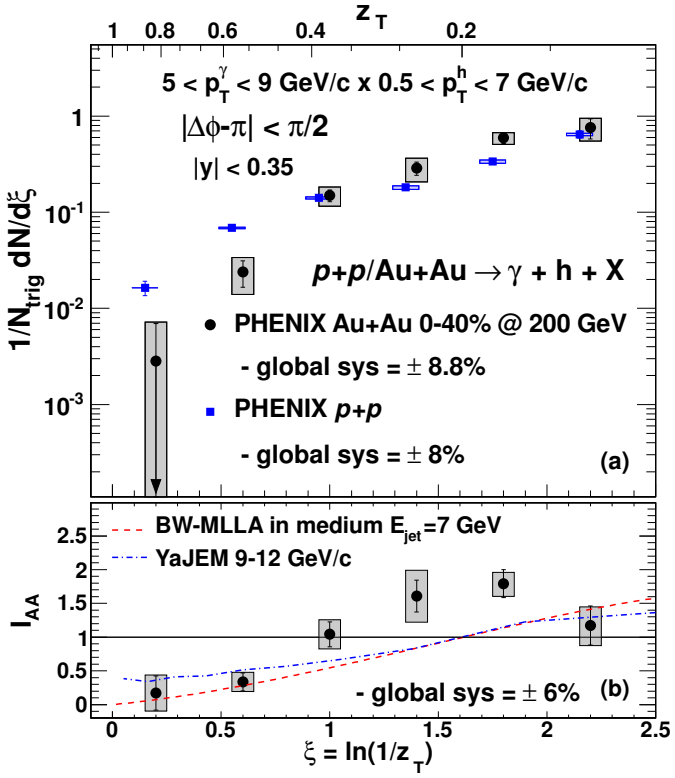

Figure 4.10: Top: Per-trigger yield as a function of ξ in Au+Au collisions at 0-40% (circles) and pp collisions (squares). Bottom: Modification factor, $I_{\rm AA}$, the ratio of fragmentation function in Au+Au collisions to in pp collisions, compared to two theoretical calculations from BW-MLLA [299] (dashed line) and YaJEM-DE [300] (dot-dashed curve). The plot is taken from [297].

all away side jet fragments show a strong suppression at low ξ (high-$p_{\rm T}$) due to parton energy loss in Au+Au collisions, and enhancement with the increasing of ξ (low-$p_{\rm T}$). The enhancement is due to the lost low energy being redistributed and fragmenting lower momenta final particles. More details about the direct γ-hadron correlations from RHIC can be found in [297, 298].

Chapter 5

Data, event, calorimeter cluster and track selection

In this chapter, the data, event, cluster and track selections used in the data analysis are presented. Sec. 5.1.1 describes the used data sets and simulation productions of pp collisions at $\sqrt{s}$ = 2.76 and 7 TeV, and Pb+Pb collisions at $\sqrt{s_{\rm NN}}$ = 2.76 TeV. The analyzed events selections including event trigger, event vertex are briefly discussed in Sec. 5.2. The description of cluster and track selections for correlations analysis are summarized in Sec. 5.3.

5.1 Data and Monte-Carlo production selection

5.1.1 Data production selection

In this work, the analysis is performed based on two pp collisions data samples recorded at the center-of-mass energies of $\sqrt{s}$ = 2.76 and 7.0 TeV, and one Pb+Pb collisions data at $\sqrt{s_{\rm NN}}$ = 2.76 TeV. The analyzed data is based on the collision events which are recorded by the ALICE online system described in Sec: 3.3.1 firstly, and quality assurance analysis train (QA-train) in the ALICE offline analysis framework. The summary of the classification of data can be found at ALICE Run Condition Table (RTC) [301] hosted by the MonALISA framework. From the classification information, the collected data can be selected by the physics analysis groups depending on the specific analysis requirements. All the selected runs have global data quality flag "1" in the RCT. The analysis results from the QA-train allows to classify the data sets in terms of the performance each sub-detector separately. The data samples considered in the analysis are:

- **pp data**

  In pp collisions, two data samples at $\sqrt{s}$ = 2.76 and 7.0 TeV are used in this work. At $\sqrt{s}$ = 2.76 TeV, The data has been collected in March 2011 and belongs to the ALICE data taking period LHC11a. In LHC11a period, due to a misbehaving LED trigger board, one quarter of the super module 3 is flashed by LED events 0.1% of the time, for runs 146858, 146859 and 146860. To remove such events, it is found a selection criteria based on the calorimeter activity: if there are more than 35 (21) cells in EMCal (Min Bias) triggered events with energy larger than 100 MeV, the event is skipped. Results from the pass 4 AOD113 reconstruction in period LHC11a are used to extract the physics observables in the analysis. At $\sqrt{s}$ = 7 TeV, The data has been collected in 2011 and belongs to the production of pass1 AOD106. Those analyzed data runs had almost full EMCal and TPC acceptance and are marked with quality flag "1" in the RCT as good runs.

- **Pb+Pb data**

  The Pb+Pb collision events at $\sqrt{s_{\rm NN}}$ = 2.76 TeV, which are selected in the analysis, are collected in 2011 and belongs to the ALICE data taking period LHC11h. Those analyzed data runs from LHC11h pass2 data AOD115 had almost full EMCal and TPC acceptance and are marked with quality flag "1" in the RCT as good runs.

5.1.2 Monte-Carlo production selection

Monte-Carlo data including full detector simulation and reconstruction are used to determine the detector performance. The detector performances include the trigger efficiency, vertex reconstruction efficiency, tracking efficiency as well as the track contamination from secondary particles after quality track selection cuts. These performance factors are analyzed for corrections of data raw results. Simulations are anchored to real data runs which define what kind of detector configuration and beam vertex condition is used. In order to increase the statistics of the high-$p_{\rm T}$ particles, simulations are produced for different intervals in the exchanged momentum in the $2 \rightarrow 2$ processes, which is called $p_{\rm T}^{\rm hard}$.

The selected simulation productions in pp and Pb+Pb are summarized as following:

- **pp simulation**

– Production LHC12a15a: Pythia6 pp collisions at $\sqrt{s}$ = 2.76 TeV in 11 p_{T}-hard bins. The production is anchored to run 146805 from period LHC11a. About 11 millions jet-jet events per p_{T}-hard bins weighted by the cross section are analyzed. The weight factor is calculated as:

$$w_{p_{\mathrm{T}}}^{\mathrm{hard}i} = \frac{\sigma_{p_{\mathrm{T}}}^{\mathrm{hard}i}}{N_{\mathrm{trials}}} \tag{5.1}$$

where $\sigma_{p_{\mathrm{T}}}^{\mathrm{hard}i}$ is the average cross section in each $p_{\mathrm{T}}^{\mathrm{hard}}$ bin where the total number of generated events N_{trials}.

– Production LHC12f1a: Pythia8 pp collisions at $\sqrt{s}$ = 2.76 TeV. About 22 millions jet-jet events are anchored to period LHC11a.

– Production LHC12f1b: Phojet pp collisions at $\sqrt{s}$ = 2.76 TeV. About 20 millions jet-jet events are anchored to period LHC11a.

– Production LHC12f2a: PYTHIA pp collisions at $\sqrt{s}$ = 7 TeV in 10 p_{T}-hard bins. The production triggered by π^0 with $p_{\mathrm{T}} > 5$ GeV/c in the EMCal acceptance is anchored to run 159582 to LHC11d period. About 0.7 millions jet-jet events per p_{T}-hard bins weighted by the scaled cross section with Eq. 5.1 are analyzed.

– Production LHC12a15f: PYTHIA pp collisions at $\sqrt{s}$ = 7 TeV. The production is anchored to 159582 to LHC11d period. About 11 millions jet-jet events per p_{T}-hard bins weighted by the scaled cross section with Eq. 5.1 are analyzed.

- **Pb+Pb simulation**

– Production LHC12a17a_fix: HIJING Pb+Pb collisions, 0-10% centrality, with added signals, among them high

– Production LHC12a17e_fix: HIJING Pb+Pb collisions, 10-50% centrality, with added signals, among them high energy π^0 and η, flat p_{T} distribution from 1 to 50 GeV/c particles generated in the ALICE acceptance ($0 < \varphi < 360$ °, $|\mathrm{y}| < 1.2$). About 0.14 millions events are analyzed.

– Production LHC12a17f_fix: HIJING Pb+Pb collisions, 50-90% centrality, with added signals, among them high energy π^0 and η, flat p_{T} distribution from 1 to 50 GeV/c particles generated in the ALICE acceptance ($0 < \varphi < 360°$, $|\mathrm{y}| < 1.2$). About 0.14 M events are analyzed.

5.2 Event selection

The event sample used in the analysis is composed of events with at least one track with a transverse momentum of $p_{\mathrm{T}} > 0.15$ GeV/c in the acceptance regions of the ITS and the TPC of $|\eta| < 0.8$ and one cluster in EMCal acceptance selected by the Minimum Bias, EMCal and central trigger. In addition, the events have to contain exactly one reconstructed vertex of good quality.

5.2.1 Trigger selection

In pp collisions analysis, two types of triggers, Minimum Bias and EMCal trigger, are used to select the events. While one more trigger, central trigger, is used in Pb+Pb collisions.

The definition of each trigger is summarized in the following:

- Minimum Bias (MB) trigger: At least one charged particle needs to be detected in either the SPD or in one of the two VZERO detectors VZERO-A and VZERO-C in coincidence with signals from the two BPTX beam pick-up counters.

- EMCal trigger: At least one cluster with energy above a threshold value at EMCal.

- Central trigger: The selected collision of Pb+Pb should be with centrality of at 0-10%.

5.2.2 Vertex and centrality selection

In ALICE, the reconstruction of the primary-vertex position is done by using the information provided by the SPD, the two innermost layers of the ITS. The quality of the vertex is ensured by the requirement that at least one track is used to reconstruct the vertex. Furthermore, the analyzed events are selected from longitudinal vertex position within $|z_{\mathrm{vertex}}| < 10$ cm with respect to the nominal interaction point at $z = 0$ cm along the z-axis. The reconstructed vertex positions in z-direction for the 3 different center-of-mass energies are presented in Fig. 5.1.

For the analysis of Pb+Pb collisions, it is important to determine the impact parameter of the two colliding nuclei, usually called the reaction *centrality*. Two

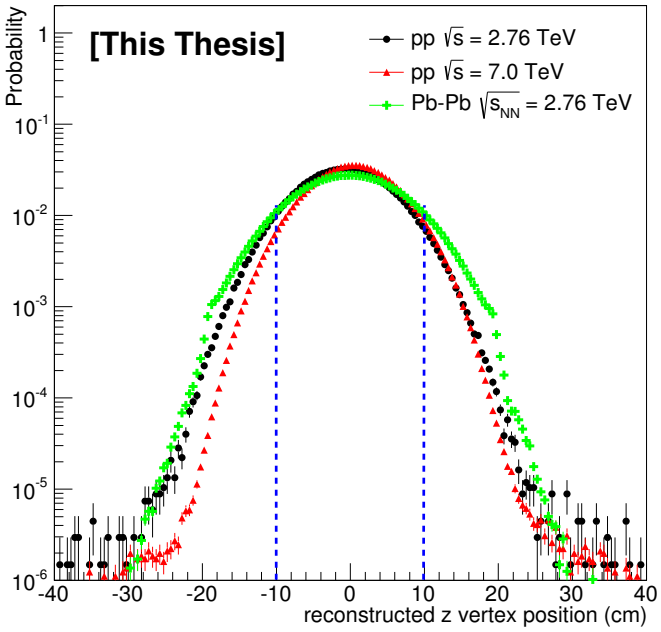

Figure 5.1: Longitudinal reconstructed vertex position measured in pp at $\sqrt{s} = 2.76$ (black) and 7.0 TeV (red), and Pb+Pb collisions at $\sqrt{s_{\rm NN}} = 2.76$ TeV (green).

experimental observables related to the collision geometry are the average charged-particle multiplicity N_{ch} and the energy carried by particles close to the beam direction and deposited in ZDC, called the *zero-degree energy* $E_{\rm ZDC}$. The average charged-particle multiplicity is assumed to decrease monotonically with the increasing of the impact parameter. The energy deposited in the ZDC, $E_{\rm ZDC}$, is directly related to the number of spectator nucleons $N_{spe} = 2A - N_{\rm part}$. The centrality is usually expressed as a percentage of the total nuclear interaction cross section σ. The centrality percentile c of an A+A collision with an impact parameter b is defined by integrating the impact parameter distribution $d\sigma/db'$ as [263]:

$$c = \frac{\int_0^b {\rm d}\sigma/{\rm db}'\,{\rm db}'}{\int_0^\infty {\rm d}\sigma/{\rm db}'\,{\rm db}'} = \frac{1}{\sigma_{AA}} \int_0^b \frac{{\rm d}\sigma}{{\rm db}'}\,{\rm db}'. \tag{5.2}$$

In ALICE, the centrality is defined as the percentile of the hadronic cross section corresponding to a particle multiplicity above a given threshold (N_{ch}^{THR}) or an energy deposited in the ZDC below a given value (E_{ZDC}^{THR}) in the ZDC energy distribution ${\rm d}\sigma/{\rm dE}'_{\rm ZDC}$

$$c \approx \frac{1}{\sigma_{AA}} \int_{N_{ch}^{THR}}^{\infty} \frac{{\rm d}\sigma}{{\rm d}N'_{\rm ch}}\,{\rm d}N'_{\rm ch} \approx \frac{1}{\sigma_{\rm AA}} \int_0^{E_{ZDC}^{THR}} \frac{{\rm d}\sigma}{{\rm d}E'_{\rm ZDC}}\,{\rm d}E'_{\rm ZDC}. \tag{5.3}$$

The procedure can be simplified by replacing the cross section with the number of observed events, corrected for the trigger efficiency. The total Pb+Pb cross section

is calculated as $\sigma_{\mathrm{PbPb}} = N_{\mathrm{evt}}(N_{coll} \geq 1)/N_{\mathrm{evt}}(N_{coll} \geq 0) \times \pi b^2_{\mathrm{max}}$, *i.e.* the geometrical value corrected by the fraction of events with at least one nucleon-nucleon collision. The measurement is $\sigma_{\mathrm{PbPb}} = (7.7 \pm 0.1(stat.)^{+0.6}_{-0.5}(syst.))$b [302].

The centrality measurement result from charged particle multiplicity method (measured by various detectors, with different rapidity coverage, such as the VZERO, the SPD, and the TPC) can be found in Fig. 3.11 from TPC and 3.34 from VZERO. The second method uses the ZDC, which measures the nucleon spectators directly, as well as the correlation to the ZEM energy in order to resolve the ambiguity due to nuclear fragmentation. The centrality is obtained from linear functions that fit the contours of the classes defined by the VZERO, in the ZDC-ZEM plane. The measurement result can be saw in Fig. 5.2.

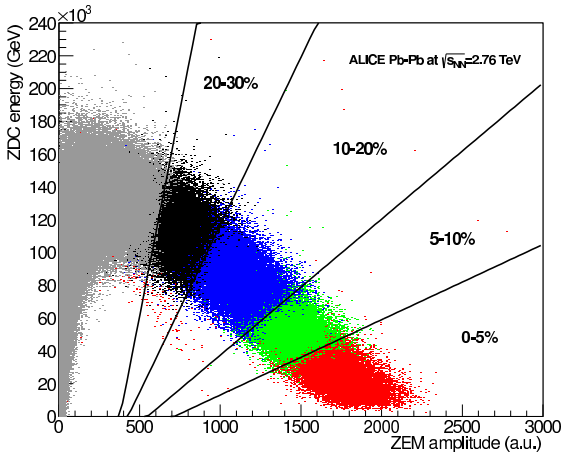

Figure 5.2: Spectator energy deposited in the ZDC calorimeters as a function of ZEM amplitude. The same correlation is shown for different centrality classes (5%, 10%, 20% and 30%) obtained by selecting specific VZERO amplitudes. The lines are a fit to the boundaries of the centrality classes with linear functions, where only the slope is fitted and the offset point is fixed [302].

In this analysis, the Pb+Pb data sample is divided into two classes of centrality intervals at central 0-10% and peripheral 60-90%. A sample of centrality distribution in MB, EMCal L0 gamma and central trigger events is shown in Fig. 5.3. After the event physical selection combining the vertex cut, about 34 millions Minimum Bias and/or 0.6 millions EMCal L0 triggered pp collision events at $\sqrt{s}$ = 2.76 TeV, about 10 millions EMCal triggered pp collision events at $\sqrt{s}$ = 7.0 TeV in LHC11c (6.5 millions events) and LHC11d (3.5 millions events) are analyzed. To Pb+Pb collisions, about 15 millions at 0-10% events, 0.5 millions EMCal L0 gamma trigger events and 0.2 millions peripheral (60-90%) with EMCal L0 gamma trigger events are used in this analysis.

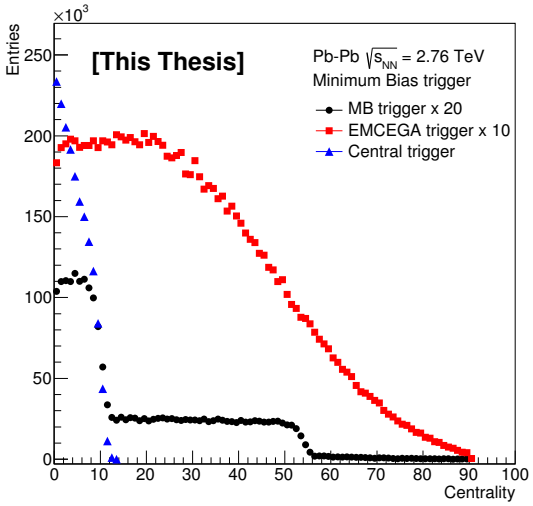

Figure 5.3: Centrality distribution for the Minimum Bias, EMCal L0 gamma and central trigger events used in this analysis.

5.3 Calorimeter cluster and track selection

In the two-particle correlation analysis, the trigger particles are neutral particles which are reconstructed in the EMCal detector, while the associated particles are tracks that are reconstructed by the ITS and TPC detectors. In this section, the reconstruction and main selection criteria of calorimeter clusters and tracks are presented briefly.

5.3.1 Calorimeter clusters

5.3.1.1 Clusterization

In the EMCal, a calorimeter cluster is an aggregate of calorimeter towers/cells. The clusterization method chosen defines what cells belong to a cluster. Clusters represent ideally the energy a given particle deposited in the calorimeter, particularly for photons, electrons or π^0 whose decay products produce a single cluster. There are several clusterization methods available for EMCal, the clusterization method selected is relevant for the identification methods described later. Detailed information on the clusterizers used for the EMCal are given in the following:

- **V1 clusterization**
  Start the clusters selecting a seed cell with energy above a given threshold E_{seed}. Then, it aggregates to the cluster all cells with common side to the

seed tower if their energy is above E_{min}. It continues aggregating towers with common side to the already aggregated ones if their energy is still larger than E_{min}. A cell cannot belong to more than one cluster. This cluster algorithm is the default clusterizer in pp collisions.

- **V2 clusterization**
  Similar to V1 clusterization but before aggregating a cell to the cluster, it checks if the energy of the cell to be aggregated is smaller than the energy of the cell that belongs already to the cluster and is neighbor with common side. If the energy is larger, the cell is not added to this cluster and the clusterization stops. This cluster algorithm is the default clusterizer in Pb+Pb and p+Pb collisions.

- **$N \times M$ clusterization**
  If there is a cell with energy over E_{seed}, it aggregates the N or M cells in η or φ direction around the seed tower. This clusterizer was used in the Pb+Pb 2010 data reconstruction with 3×3 clusters. Like V2 and V1+unfolding it naturally splits merged showers, but there can be clusters larger than $N \times M$, in such case part of the deposited energy is lost.

- **V1+unfolding clusterization**
  Similar to V2 method, it splits the V1 clusters into several sub-clusters but it allows the possibility that a cell is present in 2 clusters. One cell can have contributions from several showers, due to the fact that close particles in space will have their electromagnetic showers overlapping. Basically, the V1+unfolding forms as many clusters as there are local maxima cells in the cluster, cells more energetic with respect the surrounding cells (see below), and studies the shower energy profile of the sub-clusters, assigning to each one a fraction of the cell energy, according to this profile. For the same reasons as for V2, this clusterization is also not suitable for our analysis at least up to clusters with energy of the order of 20 GeV.

Fig. 5.4 show schematically how the different clusterization methods work.

The main parameters in all clusterization methods are E_{seed} and E_{min} and the cell time window. The default cuts in the reconstruction passes are:

- $E_{\text{seed}} = 100$ MeV.
- $E_{\text{min}} = 50$ MeV.

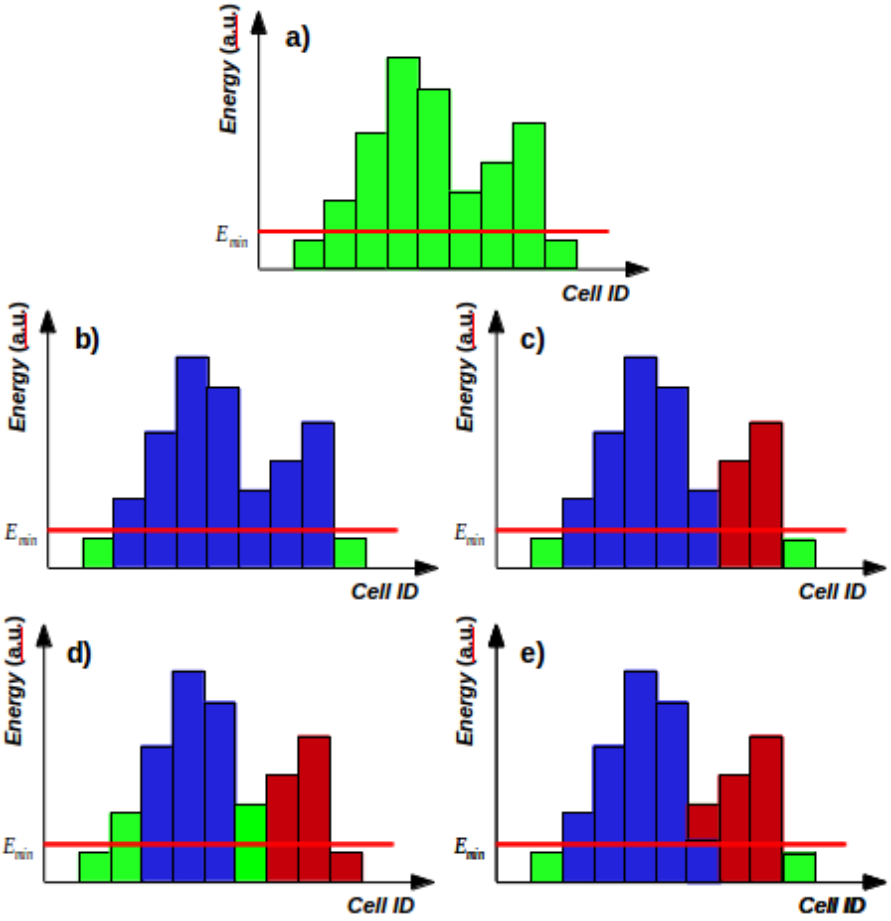

Figure 5.4: Comparison of different algorithms of clusterization. Boxes represent energy in cells. Eth is the clusteriza- tion threshold defined in the text as Emin (minimum cell energy of the cells in the cluster). a) Energy in cells before clusterization marked by green color. b) Result of V1 clusterizer. There is one big cluster made of cells in blue color. Green cells are below threshold and not associated to the cluster. c) Result of V2 clusterizer. There are two clusters made of blue and orange cells. Green cells are below threshold and not associated to any cluster. d) Result of NxN clusterizer (3x3). There are two clusters made of blue and orange cells. Green cells are not associated to any cluster. e) Result of V1+unfolding clusterizer. There are two clusters made of blue and orange cells. One cell is associated to two clusters and its energy is shared. Green cells are below threshold and not associated to any cluster. Taken from [303].

- $425 < t < 825\ ns$. Note that this is the time of the cluster before re-calibration which was not available during the reconstruction. This large value is due to cable lengths among other factors, note for comparison that photons arrive to the calorimeter at about 15 ns after their production.

In Pb+Pb collisions, with the default cuts, the V1 clusterizer creates too large clusters, specially in central collisions. In this analysis, for Pb+b collisions, reclusterization is done during the analysis using the V1 clusterizer but increasing the thresholds to $E_{\text{seed}} = 300$ MeV and $E_{\text{min}} = 150$ MeV, in order to avoid the creation of too large clusters with contributions from too many particles. The E_{min} cut will bias the cluster energy and π^0 peak mass position but its effect can be quantified with the simulation.

In our analysis, all the clusters are reclusterized with new clusterization parameters shown above in V1 and V2 clusterizations. Besides the three parameters, some corrections are applied over those clusters, compared to what is produced in the reconstruction pass. In the data, some recalibration procedures are applied since the needed correction factors are available in Offline Analysis Data Base (OADB), which include the time calibration the temperature dependent energy calibration corrections, the energy calibration, bad channels map and the non linearity correction. The non linearity correction is different for the data and the simulation.

In the reconstructed cluster, two performances, shower shape parameters and Number of Local Maxima (NLM), play important roles in the selection of photon-like and merged π^0-like cluster, which are introduced in the following.

- **Shower shape parameters**:
  The shower shape of a cluster shown in Fig. 5.5 can be described by an ellipsoidal parametrization by the axis of the shower surface ellipse [237, 247]. The shower surface is defined by the intersection of the cone containing the shower with the front plane of the calorimeter. This surface can be represented by a covariance matrix with four terms representing the average cluster position in η and φ direction in the calorimeter plane, weighted logarithmically by the cell energy [304]. The diagonalization of the covariance matrix gives as eigen-values the shower surface ellipse axis λ_0 (long axis) and λ_1(short axis). The calculation of such parameters is computed in the code with the following equations:

$$\lambda_0^2 = 0.5(\delta_{\varphi\varphi} + \delta_{\eta\eta}) + \sqrt{0.25(\delta\delta_{\varphi\varphi} - \delta_{\eta\eta})^2 + \delta_{\varphi\eta}^2} \tag{5.4}$$

$$\lambda_1^2 = 0.5(\delta_{\varphi\varphi} + \delta_{\eta\eta}) - \sqrt{0.25(\delta_{\varphi\varphi} - \delta_{\eta\eta})^2 + \delta_{\varphi\eta}^2} \tag{5.5}$$

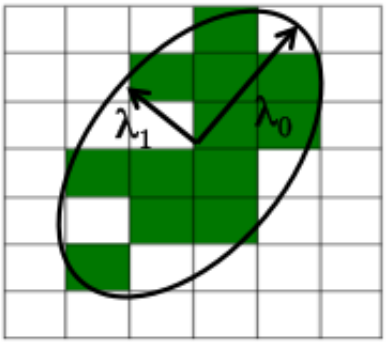

Figure 5.5: Schematic of the shower shape of a calorimeter cluster.

where $\delta_{\varphi\varphi}$, $\delta_{\eta\eta}$ and $\delta_{\varphi\eta}$ are weighted coefficients by the cell energy:

$$\delta_{\alpha\beta} = \sum_i \frac{w_i \alpha_i \beta_i}{w_{tot}} - \sum_i \frac{w_i \alpha_i}{w_{tot}} \sum_i \frac{w_i \beta_i}{w_{tot}} \tag{5.6}$$

$$w_i = \max(0, w_0 + ln(\frac{E_i}{E_{cluster}})) \tag{5.7}$$

$$w_{tot} = \sum_i w_i \tag{5.8}$$

In this analysis, only the V1 and V2 clusterizations are used. Fig. 5.6 shows the λ_0^2 distribution of a cluster in V1 and V2 clusterization. According to the special distribution of λ_0^2, this parameter is used as the main cut to distinguish photon clusters and other source clusters.

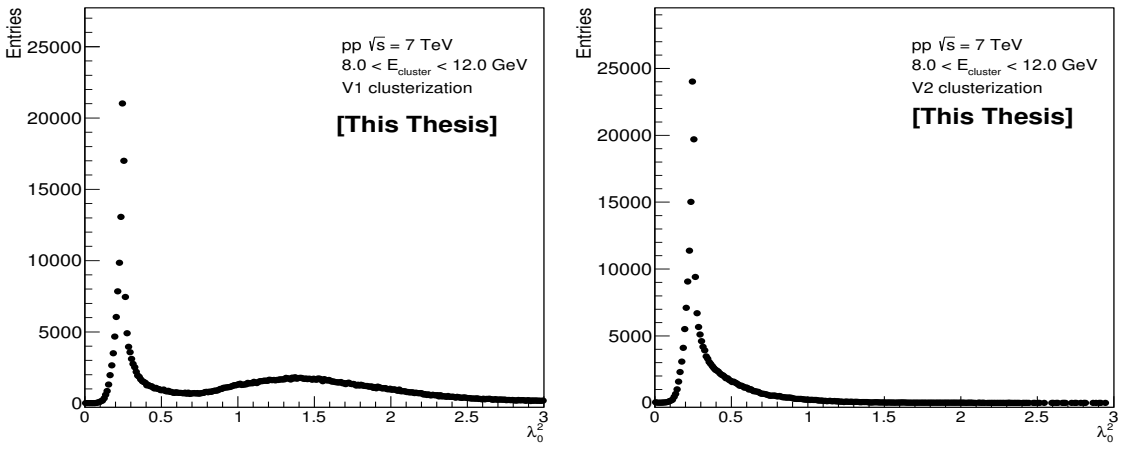

Figure 5.6: Cluster shower shape long axis λ_0^2 distribution in pp collision at $\sqrt{s} = 7$ TeV.

- **Number of Local Maxima**:
  A local maxima cell inside the cluster is defined as a cell with higher a certain energy threshold ΔE_{seed} than its adjacent cells, written as:

$$E(\text{Local Max candidate}) - \text{E(adjacent cell)} > \Delta\text{E}_{\text{seed}} \tag{5.9}$$

  In this analysis, $\Delta E_{\text{seed}} = 30$ MeV was used, which likes an energy threshold $\Delta E_{\text{seed}} = 100$ MeV for pp and 200 MeV for Pb+Pb used in the EMCal reconstruction code for the unfolding procedure. The Number of Local Maxima, is used in the analysis to select the clusters, since the shape of the shower depends on this number. With the V1 clusterization, photon clusters can have only NLM = 1 unless they suffered previously a conversion in the material in front of EMCal or have a random contribution from other particles. While π^0 clusters have NLM = 2 at low energy and NLM = 1 at higher energy (decrease of opening angle when increasing the energy). The reason of more than two maxima can be that other particles are close to the two decay photons or that at least one of the photons converted in the material in front of the calorimeter, producing at least two separated e^+e^- particles, or some spurious noise in the calorimeter. Fig. 5.7 is an example of the energy deposition in a cluster of a possible photon-cluster with one local maximum and for possible π^0-clusters with several local maxima.

5.3.1.2 Cluster cuts

Before going to correlation analysis, the clusters sample needs to be cleaned from pile-up, bad channels, charged particles signal etc. and correct them from decalibration or non linearity effects. The main selection cuts are listed below, but the time cut, exotic clusters cut and track-matching veto are explained in more detail in Appendix B:

- **Energy:**
  $E_{\text{cluster}} > 0.3$ GeV in pp and 0.5 GeV in Pb+Pb.

- **Distance to border:**
  Cell with highest energy in cluster must be 1 cell away from border of the calorimeter.

- **Number of Cells:**
  Clusters must contain at least 2 cells.

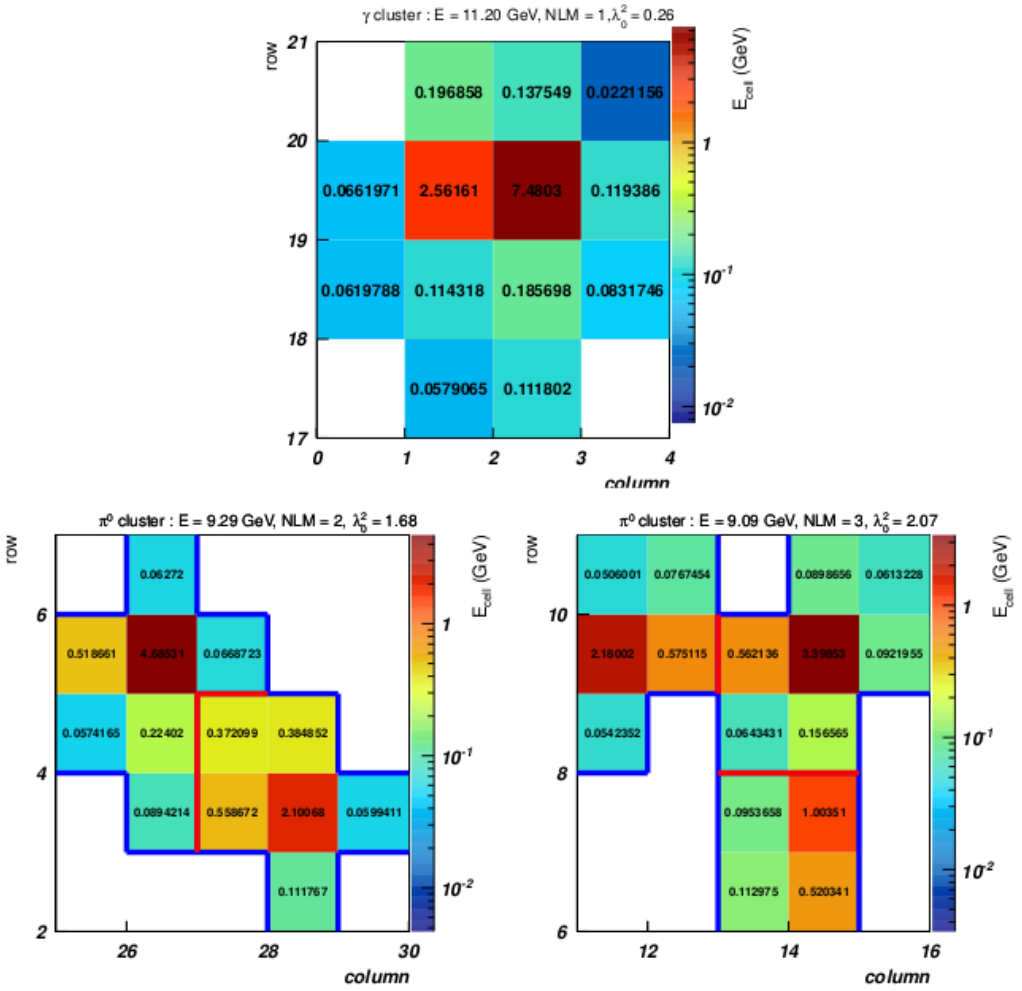

Figure 5.7: Examples of V1 clusters measured in real data, pp collisions $\sqrt{s} = 7$ TeV, coming likely from a photon (upper), and a π^0 (bottom left and right) for different Number of Local Maxima. The squares represent the cells energy, being the y and x axis the position in the super-module. The thick lines (blue and red) in the π^0 plots represent the sub-clusters that a V2 clusterizer would do. The red line is the border of glued cells that would contribute to two sub-clusters in case of using V1+unfolding method but with the proper fraction of energy in each cluster. Taken from [305].

- **Bad channel:**
  Removal of clusters containing a bad channel. Besides, clusters for which the distance of the highest energy cell to the closed bad channel is smaller than 2 cells are removed.

- **Clusters time cut:**
  The cluster time is the time of the cell with highest energy in the cluster. It is not calibrated during the reconstruction. At the analysis level, a recalibration procedure has been implemented allowing to improve the time cell resolution and recenter the time distribution around 0 ns. The cluster time with and without recalibration are shown in Fig. 5.8. After time calibration,

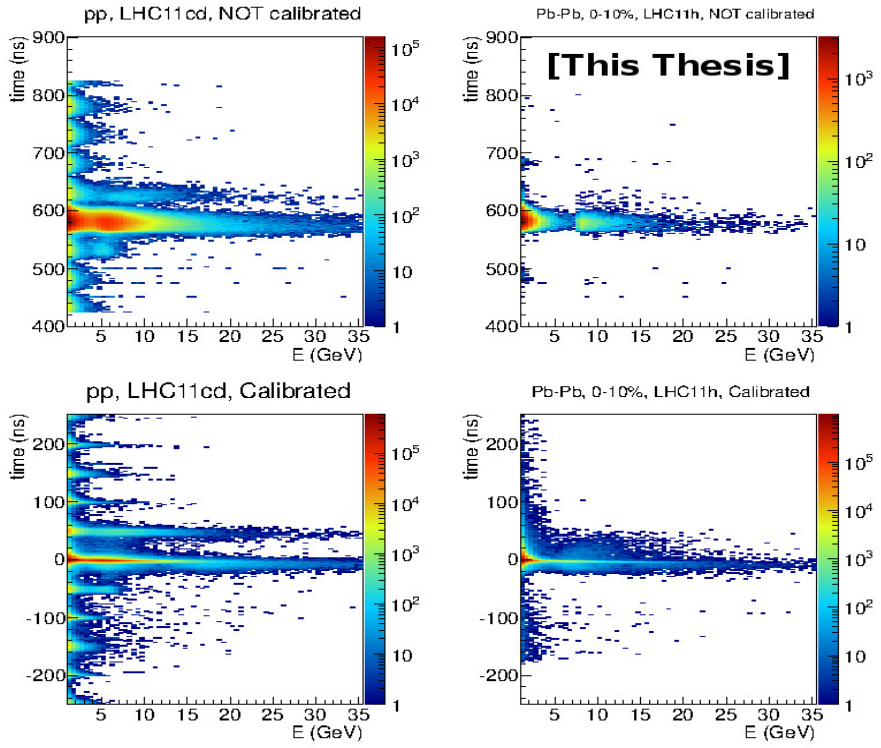

Figure 5.8: Cluster time distribution with and without time recalibration in pp at $\sqrt{s}$ = 7 TeV and Pb+Pb in 0-10% at $\sqrt{s_{\rm NN}}$ = 2.76 TeV, taken from [305].

only clusters with time at $-25 < t < 20$ ns are selected.

- **Exotic clusters:**
  In EMCal, there is a little fraction of clusters with large energy but small number of towers, called exotic clusters. These clusters may be generated by slow neutrons/anti-neutrons interactions with the calorimeter avalanches

photo-diodes (APD), specially on EMCal triggered events. Accurate simulation of this process is not possible, so such clusters need to be fully removed in the analysis. The rejection criterion to define such clusters is based on the value for for each cluster of the quantity

$$F_{\text{cross}} = 1 - \frac{E_{\text{cross}}}{E_{\text{cell}}^{\text{max}}} \tag{5.10}$$

where $E_{\text{cell}}^{\text{max}}$ is the energy of the most energetic cell in a cluster and E_{cross} is the summed energies of the three or four cells in the same cluster that share an edge with the $E_{\text{cell}}^{\text{max}}$ cell. When $F_{\text{cross}} > 97\%$, most of the exotic clusters can be removed in high efficiency. Fig. 5.9 shows the number of cell per cluster as a function of the cluster energy before (left) and after (right) applying the rejection criterion. Exotic clusters appear as a band corresponding to a small number of cells in a cluster, which almost disappears after applying the cut. To improve low energetic exotic clusters rejection efficiency (less sensitive to the F_{cross} cut), a selection on the λ_0^2 parameter, which characterize the cluster shape, is also applied: $\lambda_0^2 > 0.1$.

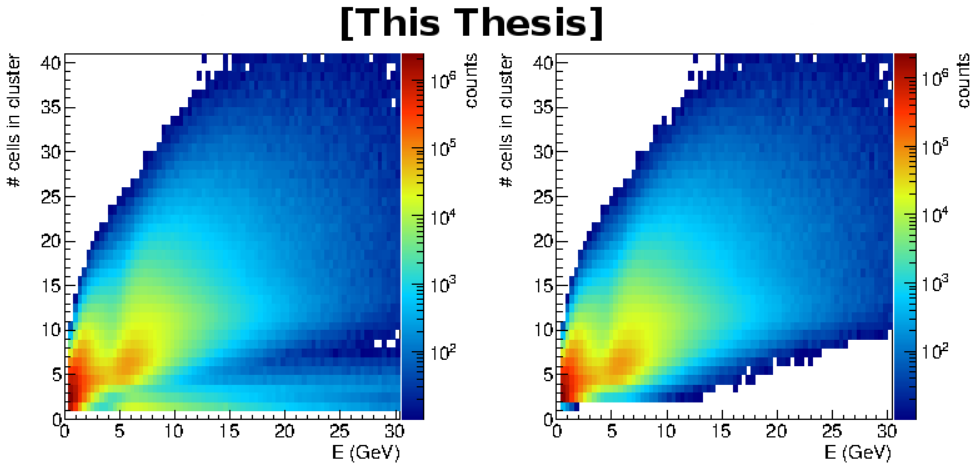

Figure 5.9: Number of towers by cluster as a function of the energy before (left) and after (right) using the rejection criterion, taken from [306].

- **Cluster-Track Matching:**
  Clusters originated by charged hadrons or electrons (positrons) are matched by the tracks projected to the calorimeter surface. This matching in φ and η is not exact due to the magnetic field interactions to the tracks, especially to the low momenta tracks. The residual distributions for matched track-cluster pairs in $\Delta\varphi = \Delta\varphi_{cluster} - \Delta\varphi_{track}$ and $\Delta\eta = \Delta\eta_{cluster} - \Delta\eta_{trck}$ are shown in

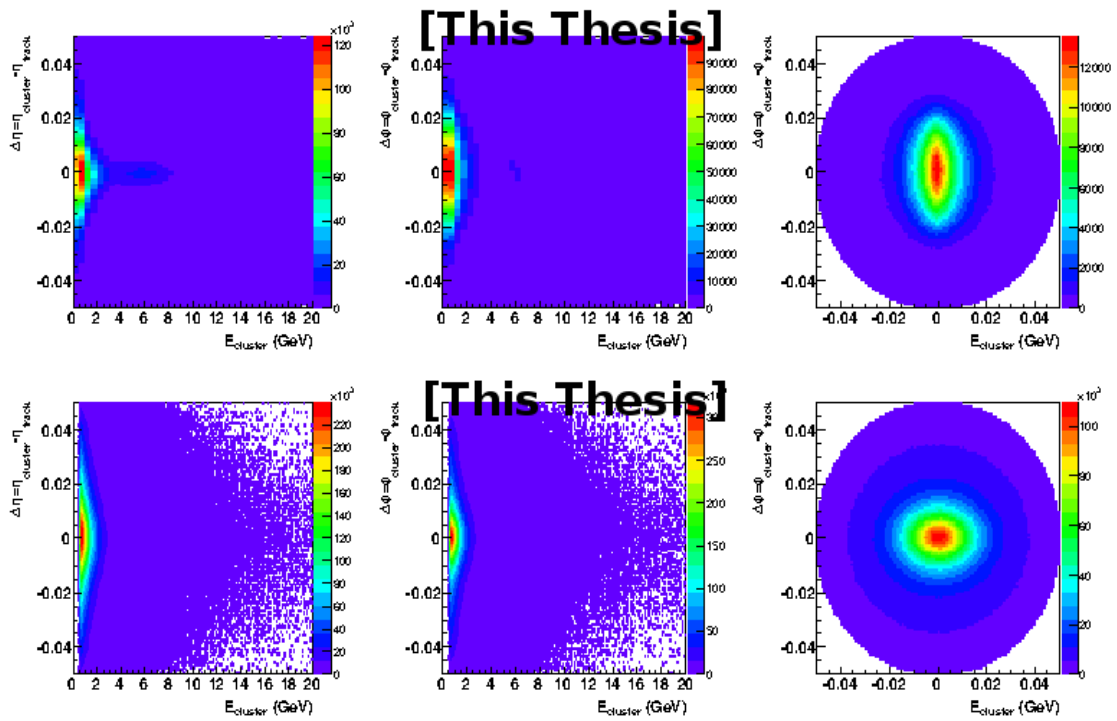

Figure 5.10: Residual distributions for matched track-cluster pairs in $\Delta\varphi$ and $\Delta\eta$ as a function of cluster energy and $\Delta\varphi$ versus $\Delta\eta$ in pp collisions data at $\sqrt{s} = 7$ TeV from LHC11d period (upper) and Pb+Pb in 0-10% at $\sqrt{s_{\rm NN}} = 2.76$ TeV from LHC11h.

Fig. 5.10. To remove these track matching cluster, the cuts of $\Delta\eta \leq 0.025$ and $\Delta\varphi \leq 0.03$ in pp, and $\Delta\eta \leq 0.03$ and $\Delta\varphi \leq 0.035$ in Pb+Pb events are used. One more cut, shower shape long axis λ_0^2, is used differently in the photon clusters and π^0 clusters selection. To photon clusters, the cut $0.1 < \lambda_0^2 < 0.27$ is used. While to π^0 clusters, the cut is a little complex, which is dependent on the cluster energy, see more details in 6.2.1.

Fig. 5.11 shows the cluster distribution as φ vs η in pp with EMCal L0 trigger (left) and Pb+Pb at Central trigger (right).

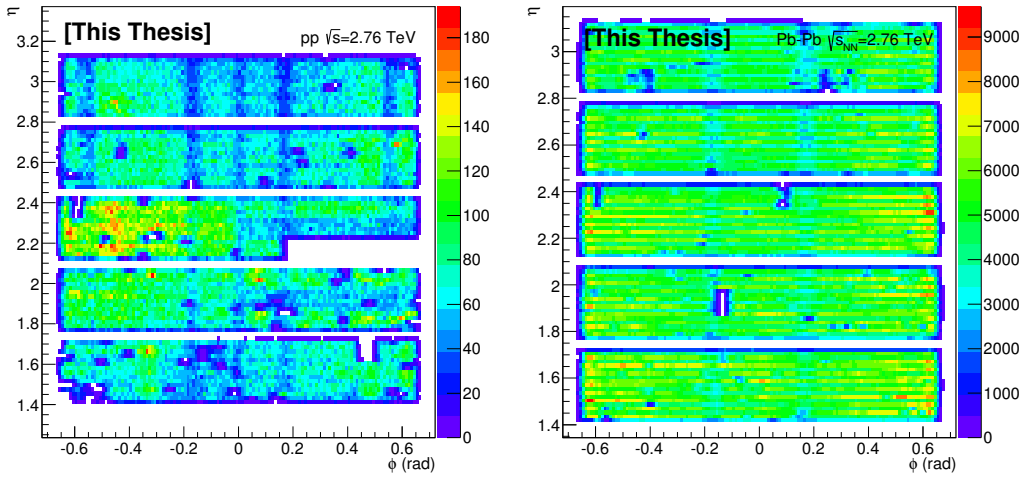

Figure 5.11: Cluster distribution as φ vs η in pp with EMCal L0 trigger (left) and Pb+Pb with Central trigger (right).

5.3.2 Tracks

5.3.2.1 Tracking strategy

The tracking strategy stats from the track seeds at the outer radius of TPC where the track density is minimal. Due to the small number of clusters to a selected seed, the precision of its parameters is not enough to safely extrapolate it outwards to the other detectors, *e.g.* TRD, TOF, HMPID and PHOS. In this case, the tracking stays within the TPC and proceeds towards the inner radius of the TPC and new clusters are assigned to it, using the Kalman-filter procedure, thus improving the track precision. When all of the seeds are extrapolated to the inner limit of the TPC, the tracking in the ITS stats. In the ITS these tracks are propagated towards the primary vertex. On the way to the primary vertex, the tracks are collected

additional, precisely reconstructed ITS clusters, which which results in improving the precision of the track parameters.

After all the seeds from the TPC are assigned their clusters in the ITS, a new tracking procedure is stated. In this procedure, the tracks which are not found in the TPC due to p_{T} cut-off, dead zones between the TPC sectors, etc, are recovered. Subsequently, the tracking is restarted from the primary vertex back to the outer layer of the ITS and then repeated towards the outer radius of the TPC. At this point the precision of the track parameters is good enough to allow the extrapolation of the tracks to the outer detectors. Finally, all the tracks are refitted with the Kalman filter backwards to the primary vertex [256].

5.3.2.2 Track cuts

Some parts of the SPD were switched off during many run periods, inefficient regions for common track reconstruction are apparent. In order to ensure uniform distributions in the η and φ direction, in the analysis an approach of *hybrid tracks* is used, whose selection cuts are defined as:

- global tracks with SPD hit(s) and an ITS refit
- global tracks without ITS refit, constrained to the primary vertex (only for 2010 data and LHC11a pp data)

The second and third selection are constrained to the primary vertex of the collision, in order to improve the p_{T} resolution in spite of a missing hit in the SPD or failing the refit in the ITS. These track selection are classified two approaches which are *global* and *complementary* tracks, which are summarized to 2010 data and LHC11a pp data in Tab. 5.1. To other 2011 pp and Pb+Pb data, the hybrid track selection settings are summarized in Tab. 5.2

Fig. 5.12 shows the azimuthal distribution of the global and complementary of hybrid tracks. In addition, the sum of the hybrid tracks, which shows a uniform azimuthal distribution, is also be presented in the figure. Fig. 5.13 shows the track distribution as φ vs η in pp with EMCal L0 trigger (left) and Pb+Pb with kCentral trigger (right). It shows no holes in TPC acceptance, excess of particles in EMCAL region due to trigger.

Track cuts	Setting value	Comments
Global tracks		
SetMinNClustersTPCPtDep	70 + 30/20 $\cdot p_{\mathrm{T}}$, 20	linear rise from 70 ($p_{\mathrm{T}} = 0$) to 100 ($p_{\mathrm{T}} = 20$ GeV/c), 100 for $p_{\mathrm{T}} > 20$ GeV/c
SetMaxChi2PerClusterTPC	4	Maximum χ^2 per TPC cluster in the first iteration
SetRequireTPCStandAlone	kTRUE	Enable cut on TPC clusters in the first iteration
SetAcceptKinkDaughters	kFALSE	Reject tracks with kink
SetRequireTPCRefit	kTRUE	Require TPC refit
SetMaxFractionSharedTPCClusters	0.4	Maximum fraction of shared TPC clusters
SetRequireITSRefit	kTRUE	Require ITS refit
SetMaxDCAToVertexXY	2.4	Maximum Distance of Closest Approach (DCA) to the main vertex in transverse
SetMaxDCAToVertexZ	3.2	Maximum DCA in longitudinal
SetDCAToVertex2D	kTRUE	Cut on the quadratic sum of DCA in XY- and Z-direction
SetMaxChi2PerClusterITS	36	Maximum χ^2 per ITS cluster
SetMaxChi2TPCConstrainedGlobal	36	Maximum χ^2 between global and TPC constrained tracks
SetRequireSigmaToVertex	kFALSE	No sigma cut to vertex
SetEtaRange	-0.9, 0.9	Pseudorapidity cut
SetPtRange	0.15, 1e15	Minimum $p_{\mathrm{T}} = 0.15$ GeV/c
w/o SPD hit		
SetClusterRequirementITS	AliESDtrackCuts::kSPD, AliESDtrackCuts::kAny	Require at least one hit in SPD
w/o ITS refit		
SetRequireITSRefit	kTRUE	Require ITS refit

Table 5.1: Summary of the hybrid track cuts setting in 2010 data and LHC11a pp data.

Track cuts	Setting value	Comments
Global tracks		
SetMinNClustersTPC	50	Minimum number of clusters in TPC
SetMaxChi2PerClusterTPC	4	Maximum χ^2 per TPC cluster in the first iteration in the first iteration
SetAcceptKinkDaughters	kFALSE	Reject tracks with kink
SetRequireTPCRefit	kTRUE	Require TPC refit shared TPC clusters
SetRequireITSRefit	kTRUE	Require ITS refit
SetMaxDCAToVertexXY	2.4	Maximum Distance of Closest Approach (DCA) to the main vertex in transverse
SetMaxDCAToVertexZ	3.2	Maximum DCA in longitudinal
SetDCAToVertex2D	kTRUE	Cut on the quadratic sum of DCA in XY- and Z-direction
SetMaxChi2PerClusterITS	36	Maximum χ^2 per ITS cluster
SetMaxChi2TPCConstrainedGlobal	36	Maximum χ^2 between global and TPC constrained tracks
SetRequireSigmaToVertex	kFALSE	No sigma cut to vertex
w/ SPD		
SetClusterRequirementITS	AliESDtrackCuts::kSPD, AliESDtrackCuts::kAny	Require at least one hit in SPD
w/o SPD hit		
SetClusterRequirementITS	AliESDtrackCuts::kSPD AliESDtrackCuts::kNone	without hits in SPD

Table 5.2: Summary of the hybrid track cuts setting in 2011 data except LHC11a pp data.

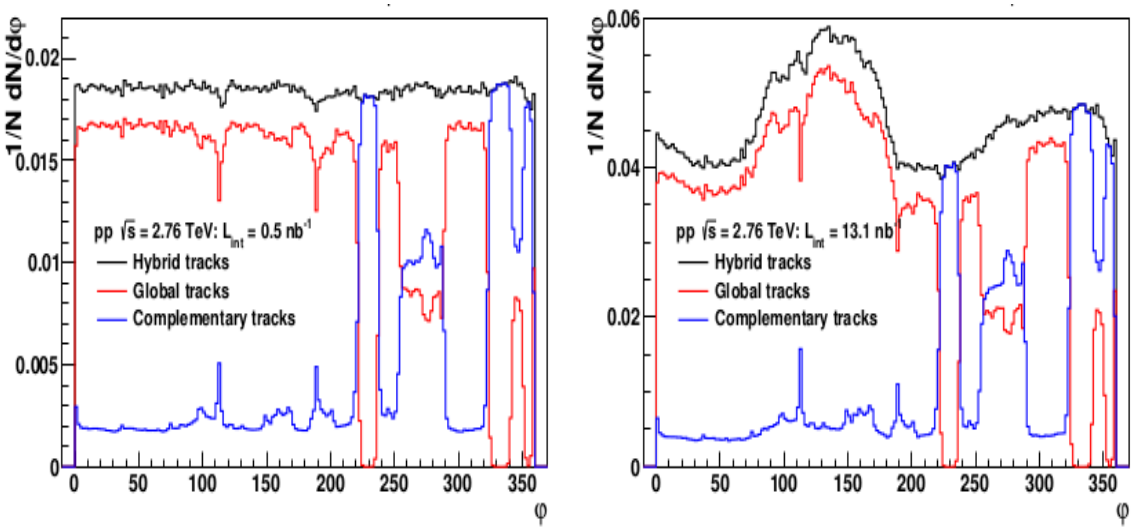

Figure 5.12: $\Delta\varphi$ distribution of two track classes of Hybrid tracks with $p_{\mathrm{T}} > 0.15$ GeV/c in MB (left) and EMCal L0 triggered (right) in pp at $\sqrt{s} = 2.76$ TeV. The hybrid track, which is the sum of the global (blue) and complementary (red) distributions, is seen to be uniform. The plots are taken from [261].

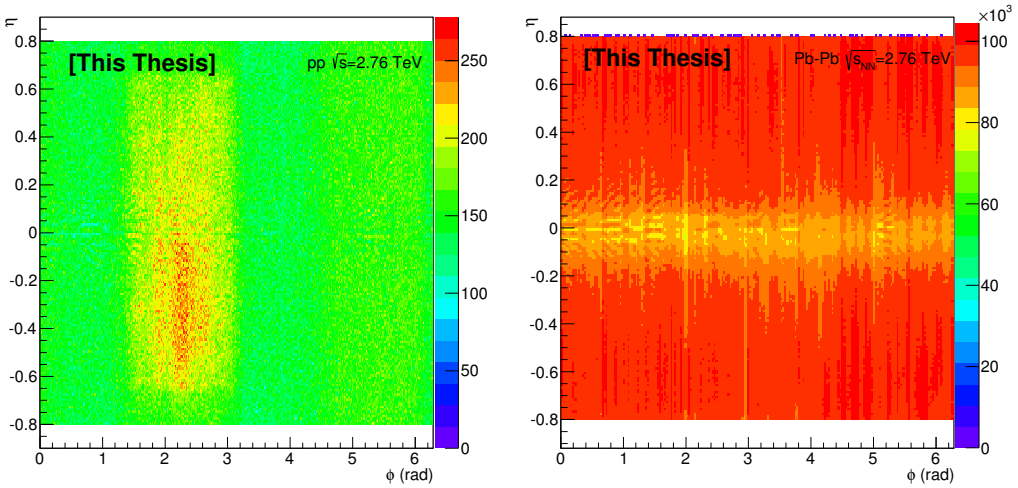

Figure 5.13: Track distribution as φ vs η in pp with EMCal L0 trigger (left) and Pb+Pb with kCentral trigger (right).

Chapter 6

Neutral pion-hadron correlations

The π^0-hadron correlations analysis consists in studying the relative azimuthal and transverse momentum distributions of charged particles associated to a high-p_{T} π^0 selected as a trigger particle. The two main observables, azimuthal angle correlation $\Delta\varphi = \varphi^{\mathrm{trig}} - \varphi^{\mathrm{assoc}}$ and charged hadrons yield as a function of their p_{T}, are measured to study the properties of medium. Especially, the per-trigger yield modification factors, $I_{\mathrm{AA}}(p_{\mathrm{T}}^{\pi^0}, p_{\mathrm{T}}^{h^{\pm}}) = \frac{Y^{\mathrm{PbPb}}(p_{\mathrm{T}}^{\pi^0}, p_{\mathrm{T}}^{h^{\pm}})}{Y^{\mathrm{pp}}(p_{\mathrm{T}}^{\pi^0}, p_{\mathrm{T}}^{h^{\pm}})}$ and $I_{\mathrm{CP}} = \frac{Y^{\mathrm{PbPb}}_{\mathrm{central}}(p_{\mathrm{T}}^{\pi^0}, p_{\mathrm{T}}^{h^{\pm}})}{Y^{\mathrm{PbPb}}_{\mathrm{peripheral}}(p_{\mathrm{T}}^{\pi^0}, p_{\mathrm{T}}^{h^{\pm}})}$, are analyzed like in [288], [286]. The π^0-hadron correlations analysis is an important step to measure direct photon-hadron correlations.

This chapter presents the measurements of π^0-hadron correlations in pp and Pb+Pb at $\sqrt{s_{\mathrm{NN}}} = 2.76$ TeV. The trigger particle, π^0, is measured with the EMCal detector with cluster splitting method (more details about π^0 reconstruction with this method can be found in [305]) in EMCal trigger data samples. The associated particles, charged hadrons, are measured with TPC+ITS (no PID performed on the charged hadrons). The π^0-hadron correlations analysis strategy at ALICE is introduced in Sec. 6.1. Sec. 6.2 describes π^0 identification via cluster splitting method at EMCal. Further steps of the analysis, such as azimuthal correlations and integrated yield of charged associated hadrons extraction, raw results correction and systematic uncertainties estimation are presented in Sec. 6.3, Sec. 6.4 and Sec. 6.5, respectively. The final results, including azimuthal angle distribution, integrated per-trigger yield of associated hadrons, modification factors of I_{AA} and I_{CP}, are presented in Sec. 6.6.

6.1 π^0-hadron correlation analysis strategy

In Sec. 4.1 and 4.3, the π^0-hadron correlations analysis strategy was introduced briefly. A little more description of the π^0-hadron correlations analysis procedure at ALICE is as following:

- The trigger particle, π^0, is reconstructed at EMCal. The opening angle of decay photons from π^0 becomes smaller with increasing π^0 energy due to the Lorentz boost. In the EMCal, when the energy of the π^0 is larger than 5-6 GeV, the two photons start to be close, and their two electromagnetic showers overlap in the calorimeter cells. Therefore, a new identification π^0 technique, cluster splitting method, is used in this analysis.

- The associated particles are charged hadrons, which are reconstructed by the ITS and TPC without identification analysis.

- The correlations between π^0 and charged particles are constructed in azimuthal angle difference $\Delta\varphi = \varphi^{\rm trig} - \varphi^{\rm assoc}$ and pseudo-rapidity difference $\Delta\eta = \eta^{\rm trig} - \eta^{\rm assoc}$ defined as Eq. 4.1. A schematic overview of the construction is shown in Fig. 6.1.

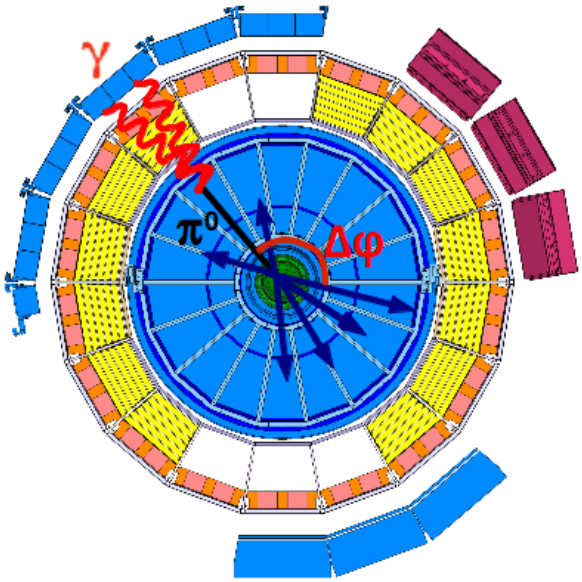

Figure 6.1: A schematic overview of the construction of π^0-hadron correlations with the electromagnetic calorimeter (EMCal) and the tracking system (ITS and TPC).

- Two observables, azimuthal angle correlation $\Delta\varphi = \varphi^{\mathrm{trig}} - \varphi^{\mathrm{assoc}}$ and per-trigger yield of charged hadrons as a function of their p_{T}, are measured with uncorrelated background subtraction.

- Same measurements are operated in the simulation production corresponding to the analyzed data in order to extract the correction factors for data.

- Finally, some main used analysis cuts of π^0 and charged hadron are changed for estimation the their systematic uncertainties.

6.2 Neutral pion identification

Generally, π^0 can be reconstructed via $\pi^0 \to \gamma\gamma$, $\pi^0 \to \gamma e^+e^-$ and $\pi^0 \to e^+e^-e^+e^-$ decay channels. In this analysis, the channel $\pi^0 \to \gamma\gamma$ is used to identify the π^0 according to the invariant mass of two photons calculated as:

$$M_{\gamma_1\gamma_2} = \sqrt{2E_1E_2(1-\cos\theta_{12})} \tag{6.1}$$

where the E_1 and E_2 are the energy of two decay photons, and θ_{12} is the relative angle between the photons in the laboratory frame. In this section, the π^0 identification at EMCal via cluster splitting method and invariant mass of two calorimeter clusters from splitting is presented in details.

6.2.1 π^0 identification via cluster splitting

The opening angle of decay photons from neutral mesons becomes smaller with increasing neutral mesons energy due to the Lorentz boost. In the EMCal, when the energy of the π^0 (η) is larger than 5-6 GeV ($\sim$ 22 GeV), the two photons start to be close, and their two electromagnetic showers overlap in the calorimeter cells. In Fig. 6.2, the fraction of **V1** clusters that are generated by one or two photons is shown for single π^0 simulated with a flat energy distribution. It indicates that the cluster from two photons overlapping is dominant at π^0 energy above 8 GeV in EMCal; Based on the performance of clusters in EMCal as shown in Fig. 6.2, two ways can be used to identify π^0:

- **Invariant mass**: Combine photon clusters in the event and select the pairs with an invariant mass close to the π^0 mass, within a mass window. The combinatorial background under the peak will be more or less strong depending

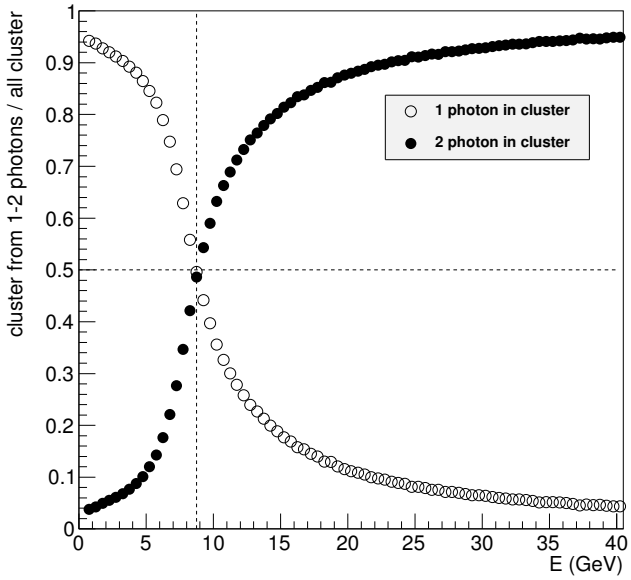

Figure 6.2: Fraction of clusters generated by the electromagnetic shower of two π^0 decay photons (filled points) or a single π^0 decay photon (open points) in a simulation of single π^0 (flat energy distribution from 1 to 50 GeV) over EMCal. The discontinuous lines are added to guide the eye to the region where the merged and non merged clusters have similar proportion. The figure is taken from [305].

the energy of the meson. To subtract this combinatorial background contribution, one can do a Polynomial+Gaussian fit where the Polynomial represents the background. For the invariant mass technique, the **V2** and V1-unfold clusterization is more suitable.

- **Cluster splitting**: For merged photon clusters, the λ_0^2 value is generally larger than that for single photons. Therefore, we select on clusters with large λ_0^2 defined in Eq. 6.2. and consider them for further analysis as explained below. The **V1** clusterizer is more suited for the cluster splitting method.

Further cluster selection cuts for splitting identification π^0 and the splitting technique details based on **V1** clusterization are presented as follows:

- As discussed pervious, two electromagnetic showers formed by two decay photons from a high-p_{T} π^0 would overlap in the calorimeter cells, which are clusterized one cluster via V1 clusterization algorithm. Generally, the overlapping becomes stronger with the increasing of π^0 transverse momentum, which performs clearly on the shower shape long axis λ_0^2 of the cluster as shown in Fig. 6.3. Accroding to the cluster shower shape λ_0^2 versus its energy distri-

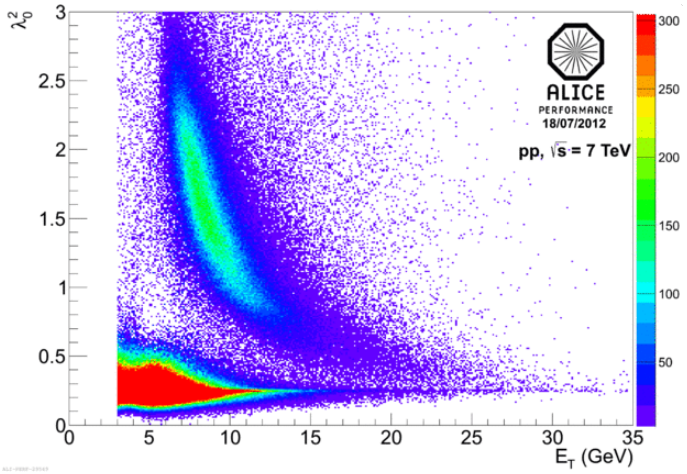

Figure 6.3: Cluster shower shape long axis λ_0^2 versus cluster energy E distribution. Two clear regions can be seen. Bbottom one is mainly formed by photon and upper one is mainly generated by π^0.

bution, a Band Criterion on the λ_0^2, $\lambda_{0,min}^2 < \lambda_0^2 < \lambda_{0,max}^2$, is used to select π^0 cluster with more probability, where the $\lambda_{0,min}^2$ and $\lambda_{0,max}^2$ are expressed as [305]:

$$\lambda_{0,min/max}^2(E) = e^{a+b\times E} + c + d \times E + e/E \tag{6.2}$$

The parameters of $\lambda_{0,min}^2$ and $\lambda_{0,max}^2$ in the formula can be found in Tab. 6.1. A limit value of $\lambda_{0,min}^2 = 0.3$ to cluster energy above 13.6 GeV at NLM=1

	a	b	c	d	e
NLM = 1 Min	2.135	-0.245	0	0	0
NLM = 2 Min	6.021	-0.866	0.733	-0.00966	0
NLM = 1, Max	0.0662	-0.0201	-0.0955	1.86×10^{-3}	9.91
NLM = 2, Max	0.353	-0.0264	-0.524	5.59×10^{-3}	21.9

Table 6.1: Parameters for $\lambda_{0,min/max}^2(E)$ of Eq. 6.2 [305].

and above 45 GeV at NLM=2. The λ_0^2 selection performances on cluster with NLM=1 and NLM=2 in pp at $\sqrt{s} = 7$ TeV are shown in the left and righ panel of Fig. 6.4, respectively.

- Select cluster which has one or two local maxima. Meanwhile the number of cells in a cluster schould be larger than 6 in pp collisions and 4 in Pb+Pb collisions.

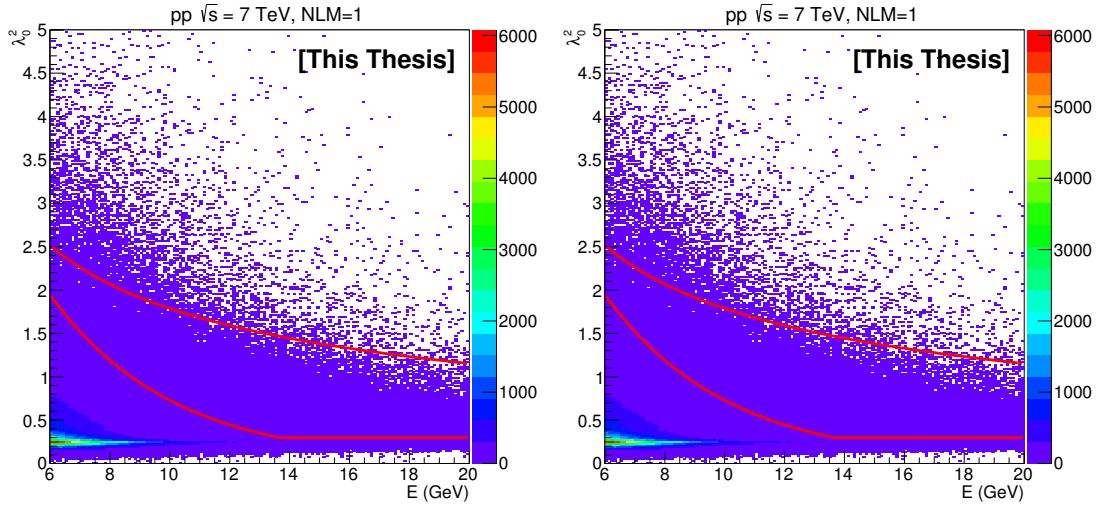

Figure 6.4: Cluster shower shape long axis λ_0^2 versus cluster energy E distribution at NLM=1 (left) and NLM=2 (right). Two red lines are obtained from the Eq. 6.2 with parameters at Tab. 6.1. The clusters between the two lines are selected as the input cluster for splitting method.

- Split the cluster in two new sub-clusters with the two highest local maxima cells and aggregate all the cells around them with 3×3 clusters clusterization. If a cell belongs to two clusters in 3, the cell energy, E_{cell}, is split assigning to each cluster with a fraction of the two local maxim cell energy $F_i \times E_{\text{cell}}$ given by $F_i = E_i^{LocalMax}/E_{cluster}$, where i indicates the first or second local maxima cell, E_i^{LocalMax} is the energy of the local maxima cell and $E_{cluster}$ is the original cluster energy. This is not a full unfolding but a good enough estimate of the energy distribution between clusters;

- Obtain the two newly formed clusters and calculate their invariant mass.

In Fig. 6.5 for pp and Pb+Pb at different centralities, invariant mass distributions from splitting clusters are shown. From the figure, a clear mass peak can be seen close to the PDG mass (0.135 GeV/c^2) of π^0, and the invariant mass distributions at more energy intervals are shown in App. A.2. After analysis the mass peak position and width in NLM=1 and NLM=2 clusters, we conclude that a good mass window to select the clusters as a candidate of merged π^0 is $M(E)-3\sigma < M_{\gamma\gamma} < M(E)+3\sigma(E)$. The $M(E)$ and $\sigma(E)$ are obtained from the fitting of mean and width extracted from the invariant mass at different energy intervals via the Gaussian function as shown in Fig. 6.6 for pp collisions and Fig. 6.7 for Pb+Pb collisions [305], which are expressed by formula as:

$$M(E), \sigma(E) = a + b \times E \tag{6.3}$$

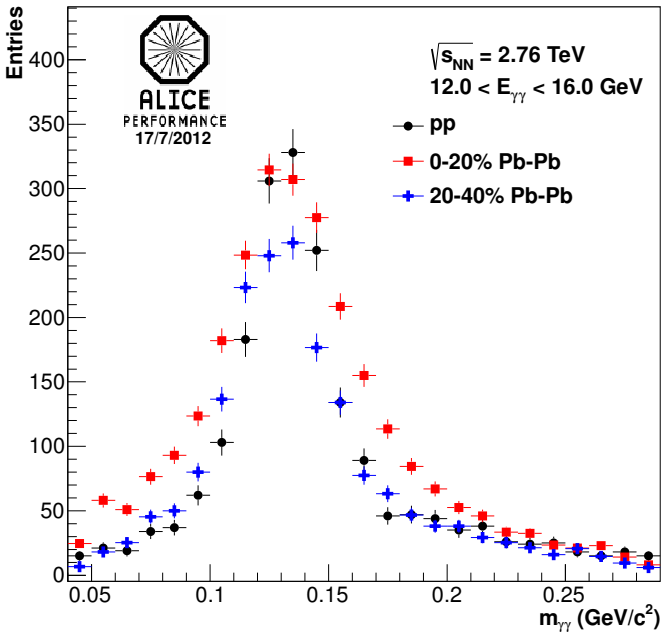

Figure 6.5: Performance plots for the distributions of splitting mass in pp and Pb+Pb different centralities in clusters energy $12.0 < E < 16.0$ GeV/c.

The parameters of $M(E)$ and $\sigma(E)$ in the above formula can be found in Tab. 6.2.

By the cluster splitting technique, a cluster with large λ_0^2 is identified as a π^0 candidate. However several sources can give the large λ_0^2 and may be mis-identified as π^0:

- conversion photons that produce the EM shower earlier,
- several particles from a jet produced nearby,
- in heavy-ion collisions the underlying event from overlapping particles,
- decay of different meson types (π^0 , η, ...).

The π^0 identification purity is defined as the ratio of identified real π^0 clusters to all identified π^0 clusters. The purity in pp estimated with Pythia is shown in Fig. 6.8 left. It is about 90% above 10 GeV/c. The purity in 0-10% Pb+Pb estimated with HIJING is shown in Fig. 6.8 right. At GeV it is about 80%, slightly rising to about 90% at above 20 GeV/c. The π^0 identification efficiency is defined as the ratio of identified real π^0 clusters to all input π^0 where both decay photons are in the

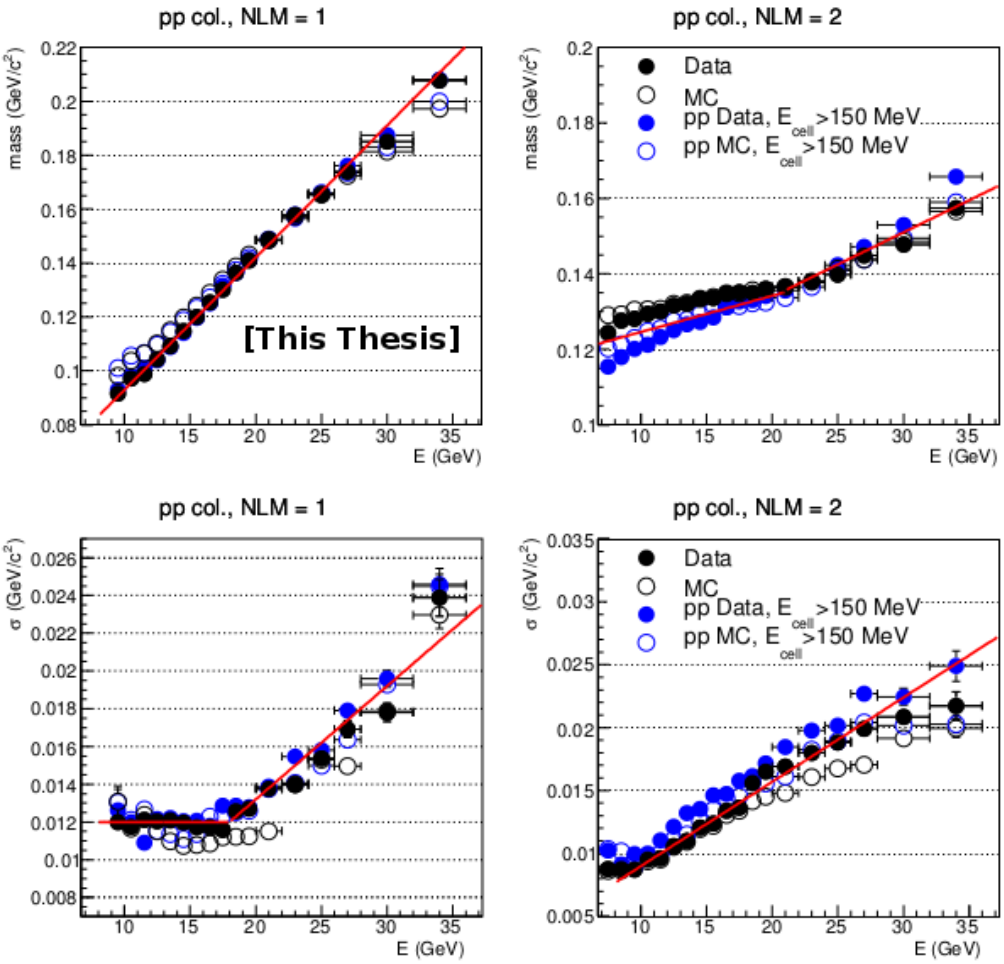

Figure 6.6: Mean mass (upper) and width (lower) of split sub-clusters invariant mass distribution versus cluster energy for different values of NLM=1 (left) and NLM=2 (right) in pp data (filled circles) and MC production (open circles) at $\sqrt{s} = 7$ TeV. As a comparison, the blue markers which represent the analysis of the same data but with the Pb+Pb clusterization settings. The red lines is the fitting results of single π^0 simulation analysis. More details can be seen in [305].

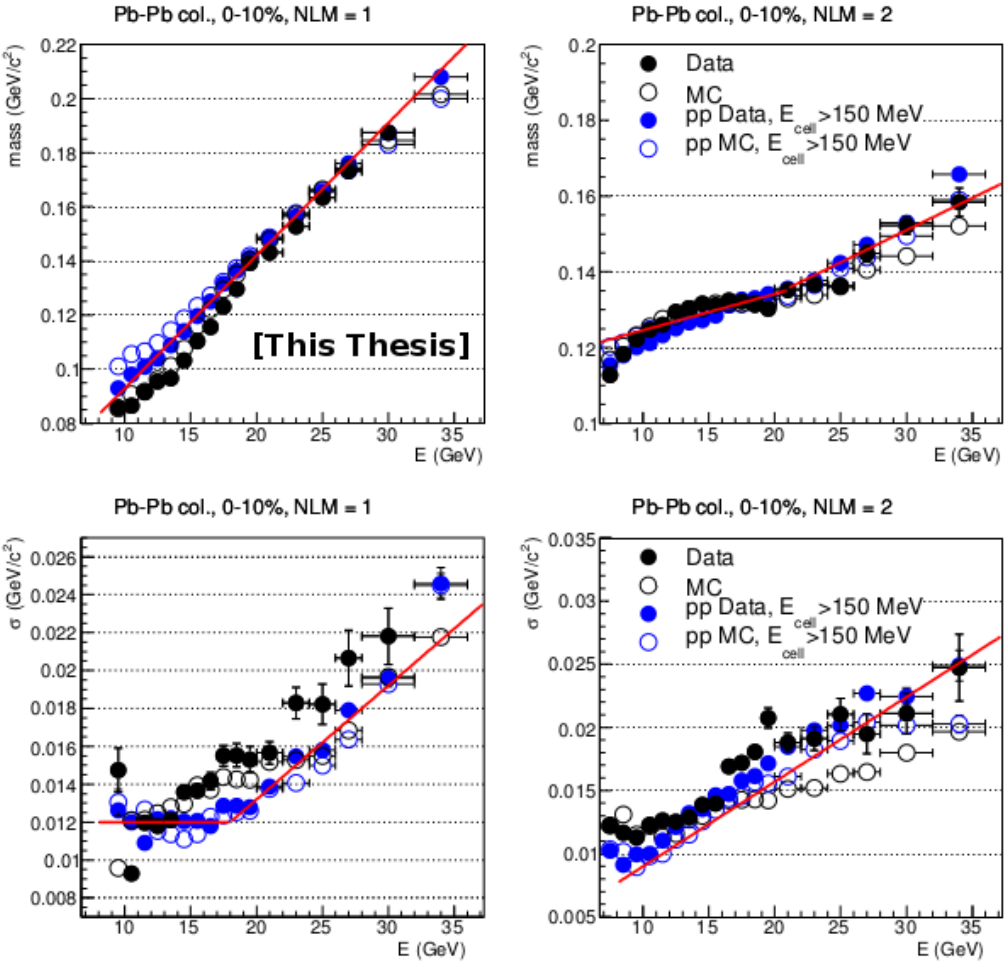

Figure 6.7: Mean mass (upper) and width (lower) of split sub-clusters invariant mass distribution versus cluster energy for different values of NLM=1 (left) and NLM=2 (right) in Pb+Pb data (filled circles) and MC production (open circles) in 0-10% at $\sqrt{s_{\rm NN}}$ = 2.76 TeV. As a comparison, the blue markers which represent the analysis of the same data but with the pp clusterization settings. The red lines is the fitting results of single π^0 simulation analysis. More details can be seen in [305].

Functions	NLM	E range(GeV)	a	b
M(E)	1	12-50	0.044	0.0049
M(E)	2	6-21	0.115	0.00096
M(E)	2	21-50	0.10	0.0017
$\sigma(E)$	1	12-19	0.012	0
$\sigma(E)$	1	19-50	0.0012	0.0006
$\sigma(E)$	2	6-10	0.009	0
$\sigma(E)$	2	10-50	0.023	0.00067

Table 6.2: Parameters for mass and width evolution of Eq. 6.3 for pp clusterization settings. Same parameters are used in Pb+Pb collisions [305].

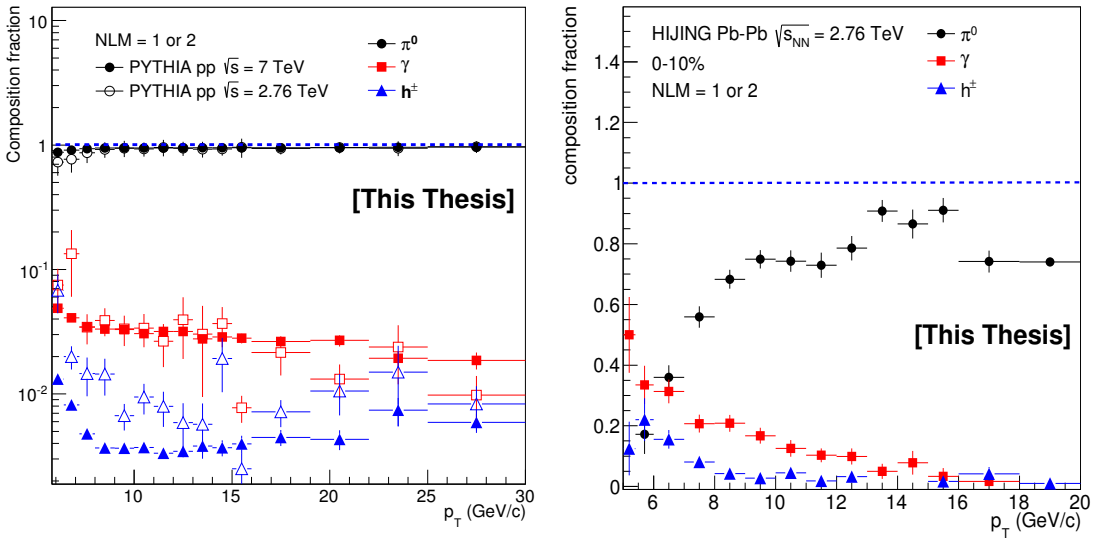

Figure 6.8: Ratio of clusters identified as π^0 but in reality being produced by a π^0 (2 merged γ, black circles), a single γ (red squares) or hadrons (blue triangles), over all the clusters identified as π^0. The left is for production LHC12a15a Pythia jet-jet simulation in pp at $\sqrt{s}$ = 2.76 TeV, and LHC12f2a Pythia jet-jet simulation in pp at $\sqrt{s}$ = 7 TeV. The right is extracted from LHC12a17d_fix simulation with only HIJING production for Pb+Pb at 0-10% at $\sqrt{s_{\rm NN}}$ = 2.76 TeV.

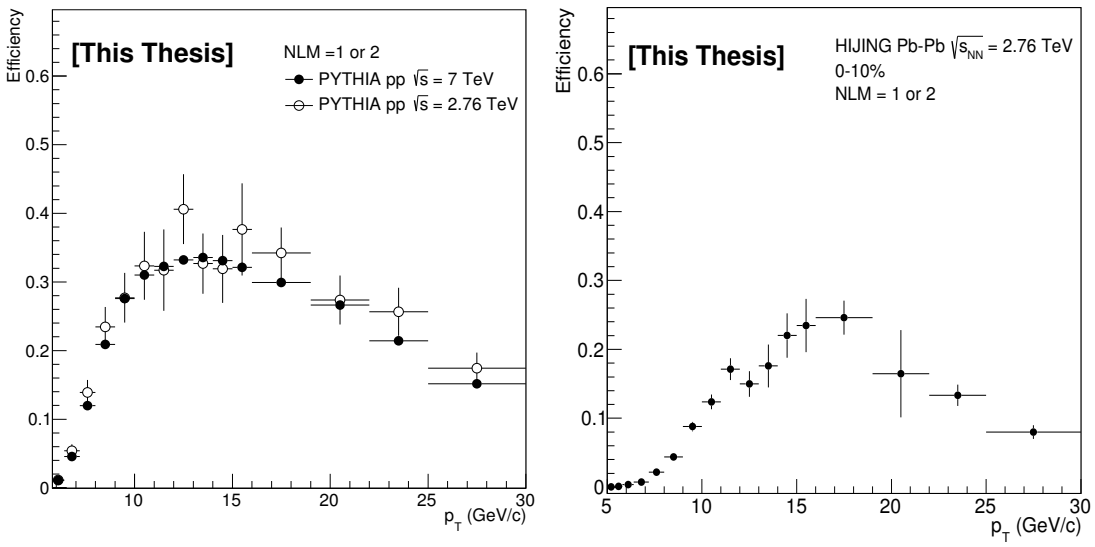

Figure 6.9: π^0 reconstruction efficiency with cluster splitting method in pp at $\sqrt{s} = 2.76$ TeV and $\sqrt{s} = 7$ TeV (left), and Pb+Pb 0-10% at $\sqrt{s_{\rm NN}} = 2.76$ TeV (right).

EMCal acceptance. The efficiency results are shown in Fig. 6.9 for pp (left) and 0-10% Pb+Pb (right) estimated using PYTHIA and HIJING simulations.

6.2.2 Changed cuts for systematic uncertainty

In Sec. 5.3.2 and 5.3.1, the default analysis cuts to tracks and clusters are presented. According to the introduction of π^0 identification in this section, in order to estimate the systematic uncertainties of some main cuts, some cuts are changed in the uncertainty analysis. Tab. 6.3 shows the main changed cuts for uncertainty analysis. The obtained raw results with changed cuts are corrected by the MC analysis correction factors in new cuts.

collision \ cut source		cluster shower shape long axis λ_0^2	π^0 candidate $M_{\gamma\gamma}$ window (GeV/c^2)	Track selection
pp	standard	Band criterion	$\|M_{\gamma\gamma}\| < \text{Mean} + 3\sigma$	Hybrid track cuts
	changed	$0.3 < \lambda_0^2 < 5$	$\|M_{\gamma\gamma}\| < \text{Mean} + 2.5\sigma$	TPC-Only track cuts
Pb+Pb	standard	Band criterion	$\|M_{\gamma\gamma}\| < \text{Mean} + 3\sigma$	Hybrid track cuts
	changed	$0.3 < \lambda_0^2 < 5$	$\|M_{\gamma\gamma}\| < \text{Mean} + 2.5\sigma$	TPC-Only track cuts

Table 6.3: Summary of some main changed cuts for systematic uncertainty estimation in pp and Pb+Pb data analysis.

6.3 Per-trigger correlated yields

The associated per-trigger yield as a function of the azimuthal angle difference $\Delta\varphi = \varphi^{\text{trig}} - \varphi^{\text{assoc}}$ and pseudo-rapidity difference $\Delta\eta = \eta^{\text{trig}} - \eta^{\text{assoc}}$ is defined as Eq. 4.1. For the analysis with pp and Pb+Pb collisions data at $\sqrt{s_{\text{NN}}} = 2.76$ TeV with π^0 triggers, the triggered $p_{\text{T}}^{\text{trig}}$ range [8.0-12.0] GeV/c and [12.0-16.0] GeV/c are selected for azimuthal correlations measurements. The trigger particle is within the EMCal acceptance $\Delta\varphi < 100^{\text{o}}$ and $\Delta\eta < 0.7$. The associated particles, charged hadrons, are grouped in the following $p_{\text{T}}^{\text{assoc}}$ bins: [0.5-1.0], [1.0-2.0], [2.0-4.0], [4.0-6.0], [6.0-10.0] GeV/c. The analysis is done by filling two kinds of histograms:

- $N_{\text{trig}}(p_{\text{T}}^{\text{trig}})$: number of trigger particles as a function of their $p_{\text{T}}^{\text{trig}}$.
- $N_{\text{assoc}}(p_{\text{T}}^{\text{trig}}, p_{\text{T}}^{\text{assoc}}, \Delta\varphi, \Delta\eta)$: number of associated particles to a number of trigger particles N_{trig}.

The per-trigger yield is measured for different ranges of trigger $p_{\text{T}}^{\text{trig}}$ and associated transverse momentum $p_{\text{T}}^{\text{assoc}}$ and in bins of centrality. Similar histograms are filled for the mixed event, where we compare the trigger particle with charged hadrons different events but with similar global properties, defined in the next subsection.

6.3.1 Event mixing

The event mixing may be useful to correct for detector acceptance or performance (missing or misbehaving TPC sectors) and analysis cuts effects. When the analysis done on EMCal triggered events, such events cannot be used to construct the mixed event pool due to the limited EMCal acceptance and the trigger, which make most of the time the selected associated particles close to the trigger particle in the calorimeter. Fig. 6.10 shows the same event and mixed event correlations with candidate π^0 trigger p_{T} at $8.0 < p_{\text{T}}^{\text{trig}} < 16.0$ GeV/c and associated charged hadrons p_{T}at $1.0 < p_{\text{T}}^{\text{assoc}} < 5.0$ GeV/c in pp at $\sqrt{s} = 2.76$ TeV. The left plot presents the same and mixed events from EMCal triggered events. We observe the correlation on the near side in the mixed event (and even on the away side) due to the explained EMCal trigger bias even though we should have a flat distribution since in the used data sample as the TPC acceptance was uniform. The right one shows the same events from EMCal trigger, while mixed events from MB trigger showing a no bias and flat distribution. So in this analysis, the MB trigger events are used to construct the mixed event pool.

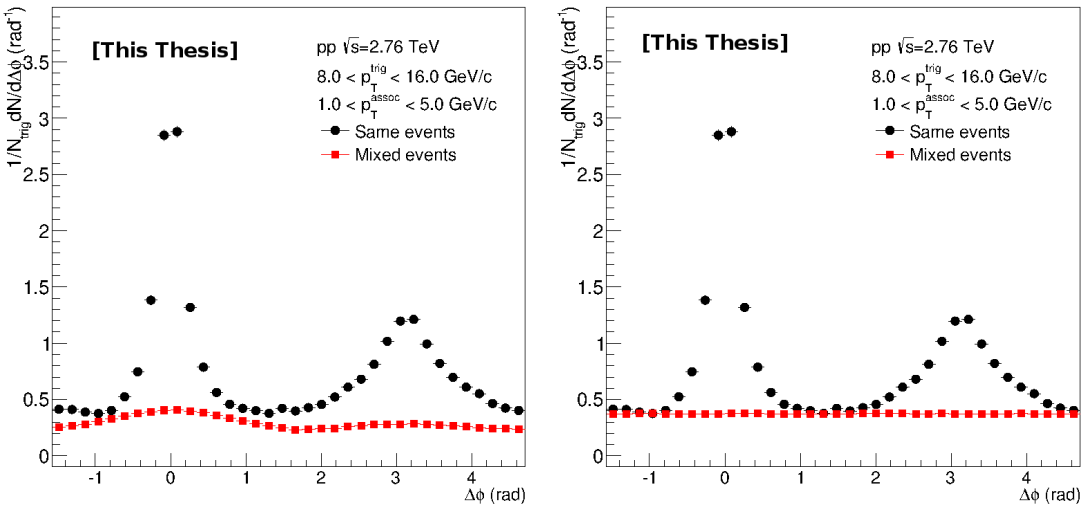

Figure 6.10: Same event and mixed event correlations with photon trigger transverse momentum of $8.0 < p_{\mathrm{T}}^{\mathrm{trig}} < 16.0$ GeV/c, associated charged hadrons transverse momentum at $1.0 < p_{\mathrm{T}}^{\mathrm{assoc}} < 5.0$ GeV/c. Mixed event pool is constructed with EMCal L0 triggered events (left), MB trigger events (right), respectively.

The pool of events must be filled with non biased events, AliVEvent::kMB. The created pool with MB events in different bins, which depends on the collision types:

- **pp collisions**:
  - 100 events in the pool.
  - z vertex bin 2 centimeter bin, 10 bins from -10 to 10 cm.
  - Track multiplicity, 9 bins on multiplicity of hybrid tracks being :[0-5], [5-10], [10-20], [20-30], [30-40], [40-55], [55-70], [>70].
- **Pb+Pb central (peripheral) collisions**:
  - 50 events in pool.
  - z vertex bin 2 centimeter bin, 10 bins from -10 to 10 cm.
  - 2% wide bin with 5 bins to 0-10% centrality, 10% wide bin with 3 bins to 60-90% centrality.
  - Reaction plane ("V0" method), 3 bins between 0 and π radians.

For mixed events we get $N_{\mathrm{pair}}^{\mathrm{mixed}}(\Delta\varphi, \Delta\eta)$ and $N_{\mathrm{trig}}^{\mathrm{mixed}}$ $(= N_{\mathrm{trig}}^{\mathrm{same}})$. In an ideal case, the mixed event distribution is expected to have a constant flat distribution as function of $\Delta\varphi$ and a triangular shaped distribution in $\Delta\eta$ deriving from the limited

η acceptance of the detector. To get the acceptance corrected correlations for a given p_{T} trigger bin and p_{T} associated bin, one can apply the following formula:

$$\frac{d^2N^{\mathrm{raw1}}(\Delta\varphi,\Delta\eta)}{d\Delta\varphi,\Delta\eta} = \frac{1}{N_{\mathrm{trig}}}\frac{d^2N^{\mathrm{same}}/d\Delta\varphi d\Delta\eta}{d^2N^{\mathrm{mixed}}/d\Delta\varphi d\Delta\eta}\cdot\alpha \tag{6.4}$$

where the factor α is chosen to normalize the background distribution such that it is unity for pairs at $\Delta\varphi = \Delta\eta \approx 0$. In our analysis, only $\frac{1}{N_{\mathrm{trig}}}\frac{dN}{d\Delta\varphi}$ distribution is focused. Therefore, the factor $\alpha = \frac{dN^{\mathrm{mixed}}}{d\Delta\varphi}|_{\Delta\varphi=0}$ is used. If one wants to subtract the

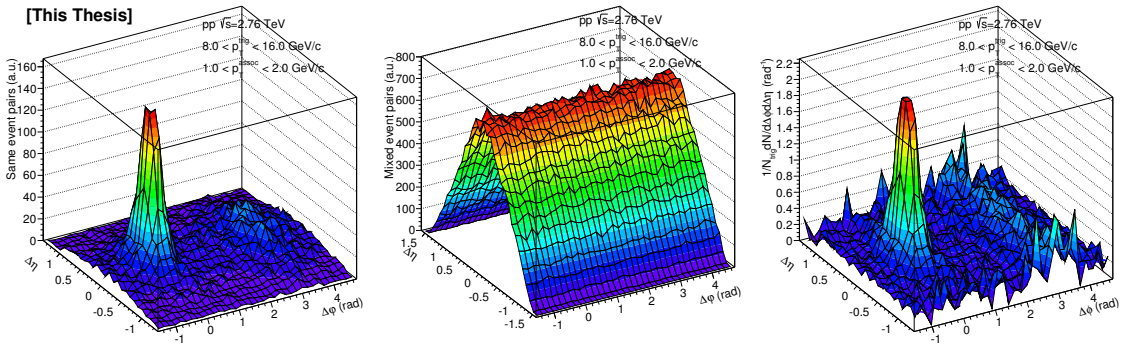

Figure 6.11: Same event (left), mixed event (middle) and the acceptance corrected correlation distribution (right) as $\Delta\varphi - \Delta\eta$ in π^0 trigger transverse momentum of $8.0 < p_{\mathrm{T}}^{\mathrm{trig}} < 16.0$ GeV/c, associated charged hadrons transverse momentum of $1.0 < p_{\mathrm{T}}^{\mathrm{assoc}} < 2.0$ GeV/c in pp at $\sqrt{s} = 2.76$ TeV.

underlying event contributions to the correlations, one more step can be used as:

$$\frac{dN^{\mathrm{raw}}(\Delta\varphi)}{d\Delta\varphi} = \frac{1}{N_{\mathrm{trig}}}(\frac{dN^{\mathrm{raw1}}}{d\Delta\varphi} - \beta\cdot\frac{dN^{\mathrm{mixed}}}{d\Delta\varphi}) \tag{6.5}$$

Calculating the factor β in $\Delta\varphi$ region from 1 to 1.5, where it is expected the background is dominant, as written in Eq. 6.6, is similar to do a ZYAM discussed later.

$$\beta = \int_1^{1.5}\frac{dN^{\mathrm{raw1}}}{d\Delta\varphi}d\Delta\varphi / \int_1^{1.5}\frac{dN^{\mathrm{mixed}}}{d\Delta\varphi}d\Delta\varphi \tag{6.6}$$

Fig. 6.11 shows 2-D correlation distributions as $\Delta\varphi - \Delta\eta$ of the same event (left), mixed event (middle) and the acceptance corrected correlation distribution by Eq.6.4 in π^0 trigger at $8.0 < p_{\mathrm{T}}^{\mathrm{trig}} < 16.0$ GeV/c and associated at $1.0 < p_{\mathrm{T}}^{\mathrm{trig}} < 2.0$ GeV/c in pp at 2.76 TeV. Fig. 6.12 shows azimuthal angle correlation distributions of the same event (left), mixed event (middle), and the corrected acceptance and subtracted the background from underlying events correlation distribution by Eq.6.5 in π^0 trigger at $8.0 < p_{\mathrm{T}}^{\mathrm{trig}} < 16.0$ GeV/c and associated at $1.0 < p_{\mathrm{T}}^{\mathrm{trig}} < 2.0$ GeV/c in pp at 2.76 TeV.

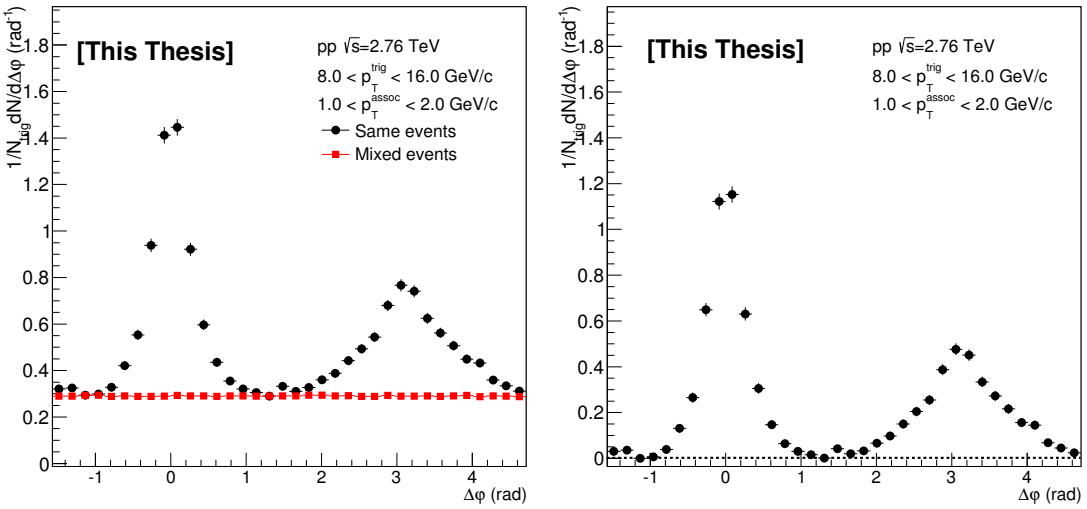

Figure 6.12: Azimuthal angle correlation distribution in Same events (left, black), mixed event (left, red) and the corrected acceptance and subtracted background correlation distribution (right) in π^0 trigger transverse momentum of $8.0 < p_{\mathrm{T}}^{\mathrm{trig}} < 16.0$ GeV/c, associated charged hadrons transverse momentum of $1.0 < p_{\mathrm{T}}^{\mathrm{assoc}} < 2.0$ GeV/c in pp at $\sqrt{s} = 2.76$ TeV.

6.3.2 Azimuthal correlations

In EMCal, two methods can be used to identify π^0, invariant mass and the cluster splitting, as mentioned in Sec. 6.2.1 and App. 7.3, respectively. To be sure that both identification criteria give similar results, we compare the azimuthal correlation with the both identification techniques at low $p_{\mathrm{T}}^{\mathrm{assoc}}$ bins, where we have enough statistic with the invariant mass technique. Fig. 6.13 shows that both methods give very similar correlation results. Fig. 6.14 gives the comparison of the uncorrected per-

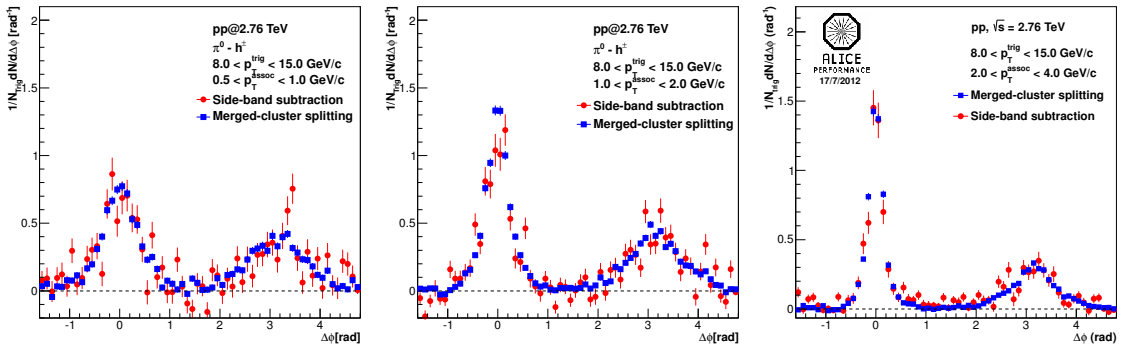

Figure 6.13: Azimuthal correlation of π^0 measured in pp collisions at $\sqrt{s} = 2.76$ TeV with transverse momentum between $8.0 < p_{\mathrm{T}}^{\mathrm{trig}} < 15.0$ GeV/c and charged hadrons, in three $p_{\mathrm{T}}^{\mathrm{assoc}}$ bins. The π^0 is identified via invariant mass in red and cluster splitting in blue. The mixed event contribution has been subtracted following Eq. 6.4 and Eq. 6.6.

trigger yield between pp data at $\sqrt{s} = 2.76$ TeV and Pythia 6 MC in azimuthal correlation distribution with trigger $8.0 < p_{\mathrm{T}}^{\mathrm{trig}} < 12.0$ GeV/c and $12.0 < p_{\mathrm{T}}^{\mathrm{trig}} < 16.0$ GeV/c.

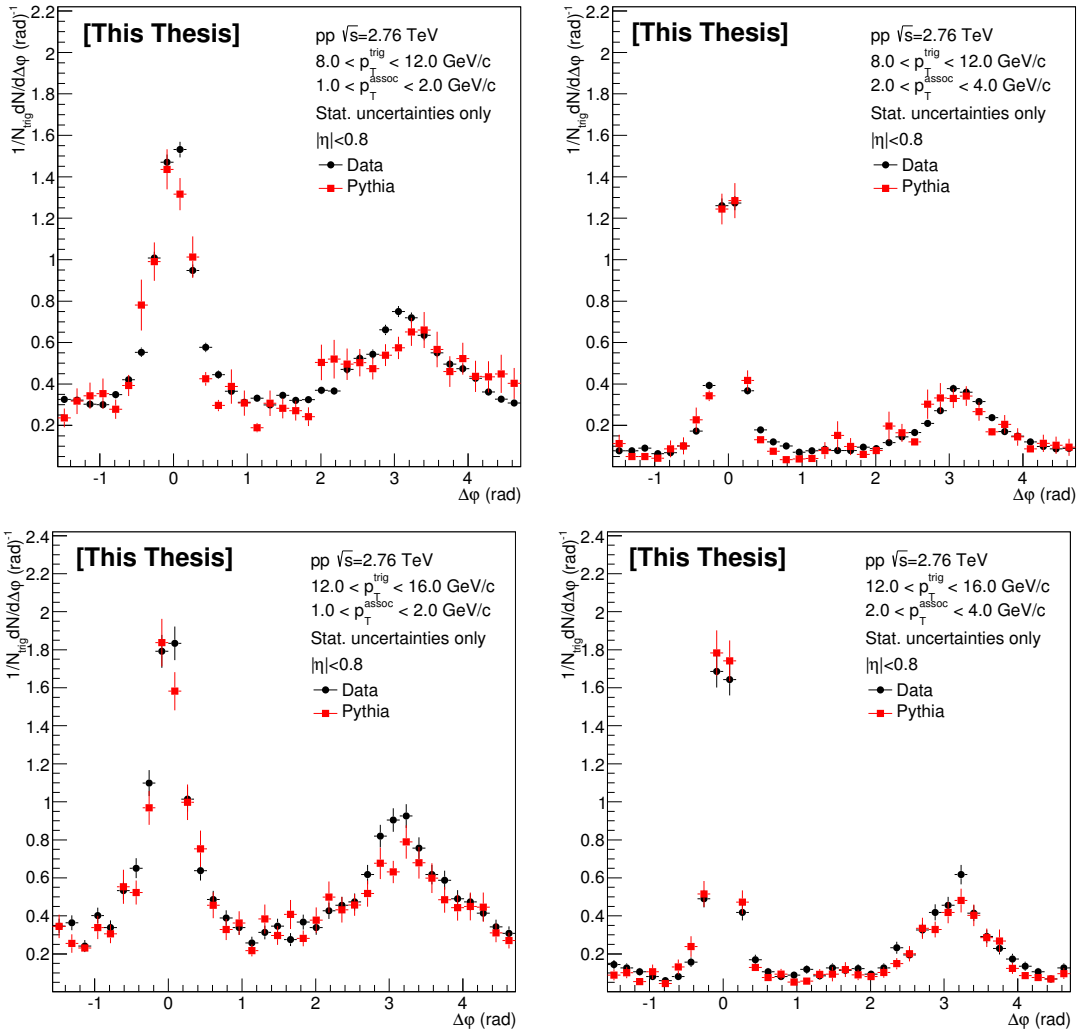

Figure 6.14: Azimuthal correlations of comparisons between pp data (red) and Pythia 6 MC (black) at $\sqrt{s} = 2.76$ TeV for the cluster splitting method with trigger p_{T} bins at $8.0 < p_{\mathrm{T}}^{\mathrm{trig}} < 12.0$ GeV/c, $12.0 < p_{\mathrm{T}}^{\mathrm{trig}} < 16.0$ GeV/c and charged hadrons, in two $p_{\mathrm{T}}^{\mathrm{assoc}}$ bins.

6.3.3 Extraction of associated per-trigger yield

The counting pairs technique is used to extract the correlated and un-correlated yield of charged hadrons in different $\Delta\varphi$ width. Pedestal (or ZYAM) subtraction is used to extract correlated yield of charged hadrons.

6.3.3.1 Yield extraction

Subsequently, the yield on the near (away) side is summed over a region of 0 (π) $\pm$ some width. In our analysis, two regions are taken into account to extract the yield.

- Near side $|\Delta\varphi| < 0.7$ *radians*
- Away side $|\Delta\varphi - \pi| < 0.7$ *radians*

The regions are illustrated in Fig. 6.15. The red and green regions are the correlated pairs, and the blue region is un-correlated (underlying event contributions).

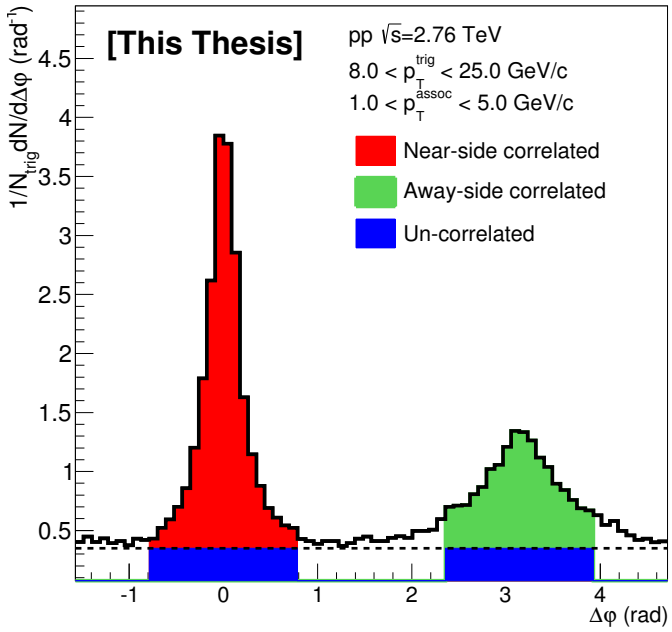

Figure 6.15: Red and green regions are the signal correlated pairs, and the blue is the un-correlated (underlying event contributions), respectively.

6.3.3.2 Pedestal subtraction

In the pedestal subtraction, the uncorrelated background is considered as a flat distribution in $\Delta\varphi$. The pedestal uncorrelated background is determined in three ways, which are used to estimate the systematic uncertainty of subtraction of the uncorrelated background:

- 1. Six minimum points in 60 points are selected at $\Delta\varphi = \Delta\varphi_0 \pm 0.2$. The yield (correlated+un-correlated) $Y(\Delta\varphi_0)$ is minimum at $1 < |\Delta\varphi| < \frac{\pi}{2}$. Generally,

there are two minimum. Fig. 6.16 shows the possible selection of φ_0 in pp (left) and Pb+Pb (right).

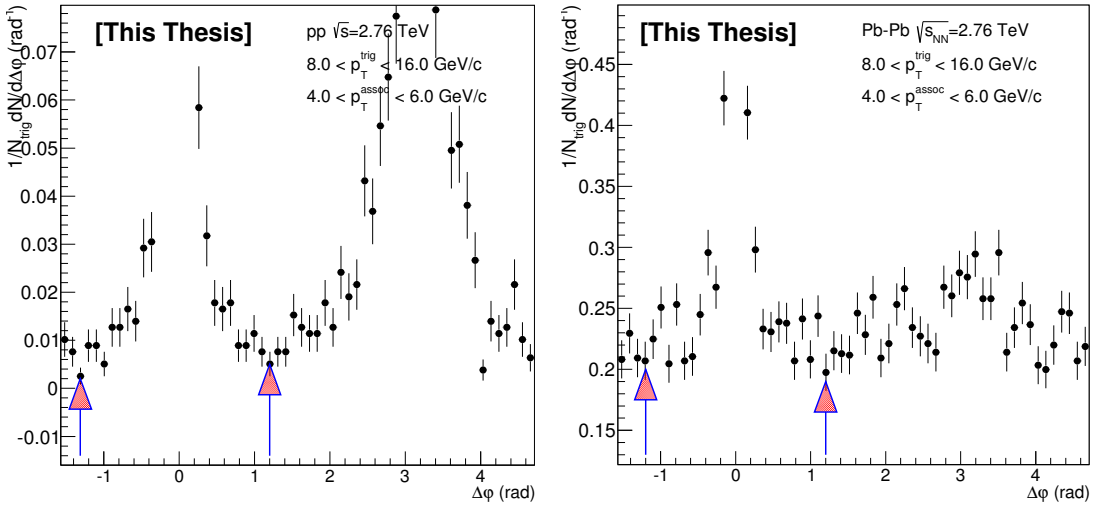

Figure 6.16: Possible selection of φ_0 in pp (left) and Pb+Pb (right) according to method 1.

- 2. Constant fit in $1 < |\Delta\varphi| < \frac{\pi}{2}$. Fig. 6.17 shows the constant fit in $1 < |\Delta\varphi| < \frac{\pi}{2}$ in pp (left) and Pb+Pb (right).

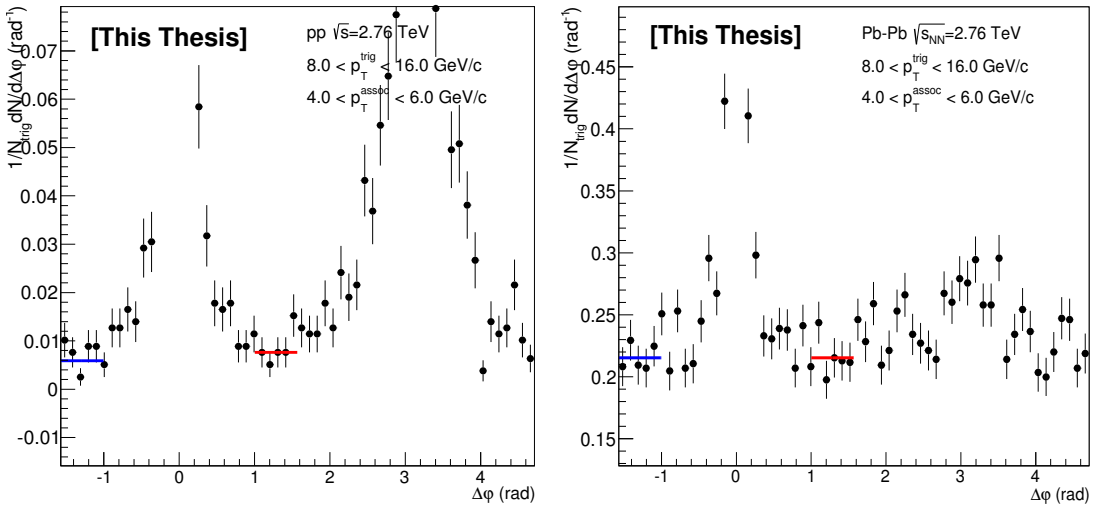

Figure 6.17: Constant fits in $1 < |\Delta\varphi| < \frac{\pi}{2}$ in pp (left) and Pb+Pb (right) according to method 2.

- 3. Average value of the eight smallest points in full $|\Delta\varphi|$ range.

Fig. 6.18 and Fig. 6.19 show the results of the per-trigger yield of hadrons calculated by the three methods in two analyzed regions in pp at $\sqrt{s} = 2.76$ TeV and

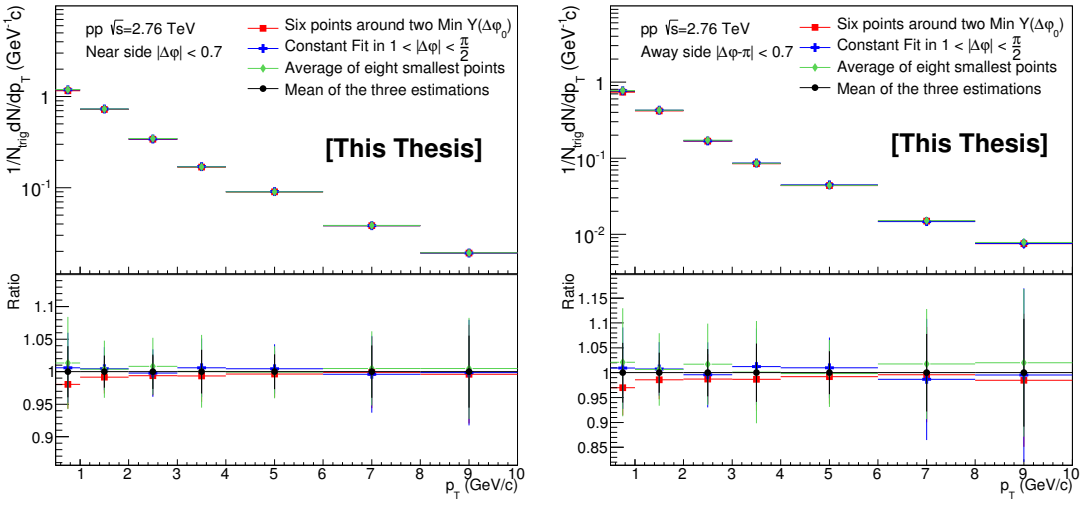

Figure 6.18: The difference of the three pedestal subtractions on Near side $|\Delta\varphi| < 0.7$ (left), Away side $|\Delta\varphi - \pi| < 0.7$ (right) in pp at $\sqrt{s} = 2.76$ TeV, respectively. The ratio is calculated with respect to the average distribution of the three pedestal determinations.

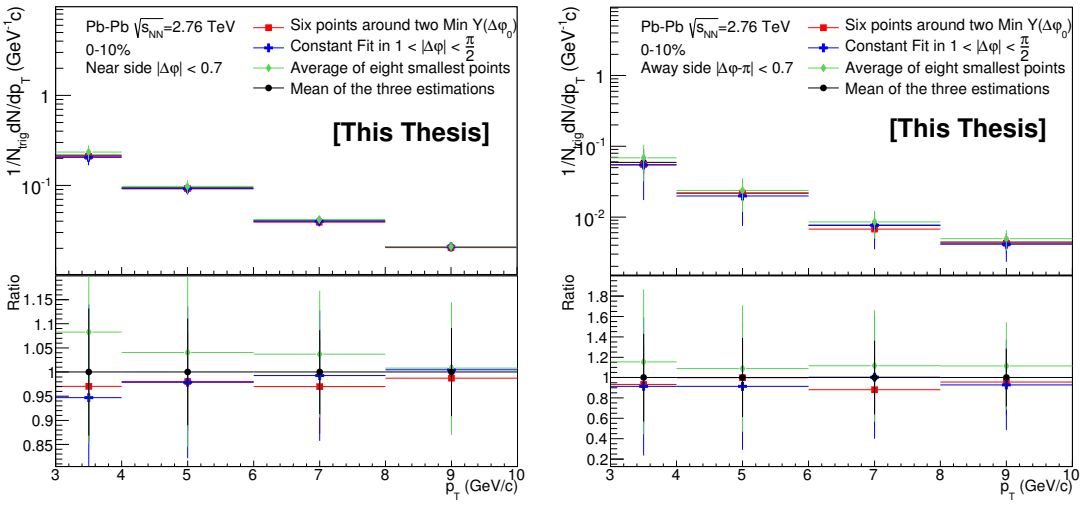

Figure 6.19: The difference of the three pedestal subtractions on Near side $|\Delta\varphi| < 0.7$ (left), Away side $|\Delta\varphi - \pi| < 0.7$ (right) in Pb+Pb 0-10% at $\sqrt{s_{\rm NN}} = 2.76$ TeV, respectively. The ratio is calculated respect to the average distribution of the three pedestal determinations.

Pb+Pb at $\sqrt{s_{\rm NN}}$ = 2.76 TeV, respectively. Their difference determines the systematic uncertainty due to the pedestal determination, which is shown in Fig. 6.20 in pp at $\sqrt{s}$ = 2.76 TeV and Fig. 6.21 in Pb+Pb at $\sqrt{s_{\rm NN}}$ = 2.76 TeV. The effect is larger in the away side than in the near side due to the smaller signal.

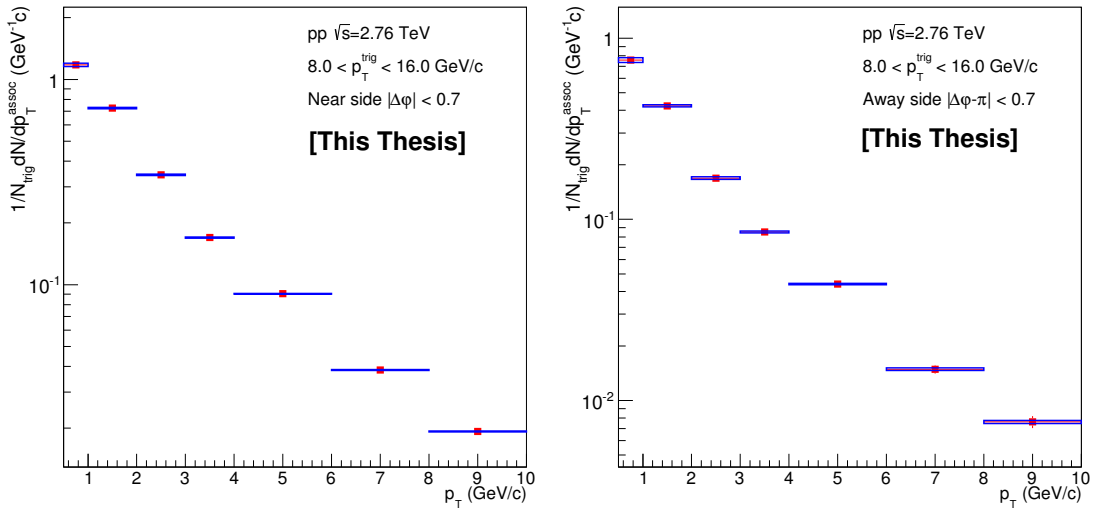

Figure 6.20: The systematic uncertainty from the three pedestal subtractions of the yield on Near side $|\Delta\varphi| < 0.7$ (left), Away side $|\Delta\varphi - \pi| < 0.7$ (right) in pp at $\sqrt{s}$ = 2.76 TeV, respectively. The blue boxed is the systematic uncertainty.

6.3.3.3 Flow subtraction

In Sec. 6.3.3.2, we present to subtract the background which is considered as a flat distribution. This makes sense in pp collisions. While the background in Pb-Pb collisions is not flat due to the flow contribution. To estimate the contribution of flow (we only consider v_2 in this analysis) to the measured yields, we use the extracted v_2 from the flow group. Since the v_2 of π^0 has not been obtained at ALICE, the v_2 of charged pions is used instead of the v_2 of π^0. The v_2 of charged pions and charged hadrons are shown in the left and right panel of Fig. 6.22 [284]. The fluctuation of charged pions v_2 is a little large at $p_{\rm T} > 6.0$ GeV/c. To estimate the flow value at $8.0 < p_{\rm T} < 16.0$ GeV/c, Polynomial0 function is used to fit the distribution in the $p_{\rm T}$ range. The fit error is considered to estimate the systematic uncertainty at $8.0 < p_{\rm T} < 16.0$ GeV/c. The fit result is 0.0347 ± 0.0043, which gives the systematic uncertainty of $\sim 12.4\%$. To the charged hadron flow, it has $\sim 2\%$ systematic uncertainty at $p_{\rm T} > 6.0$ GeV/c. Finally, the jet-like correlations is obtained by

$$J(\Delta\varphi) = C(\Delta\varphi) - b_0(1 + 2\langle v_2^{trig} v_2^{assoc}\rangle \cos(2\Delta\varphi)) \quad (6.7)$$

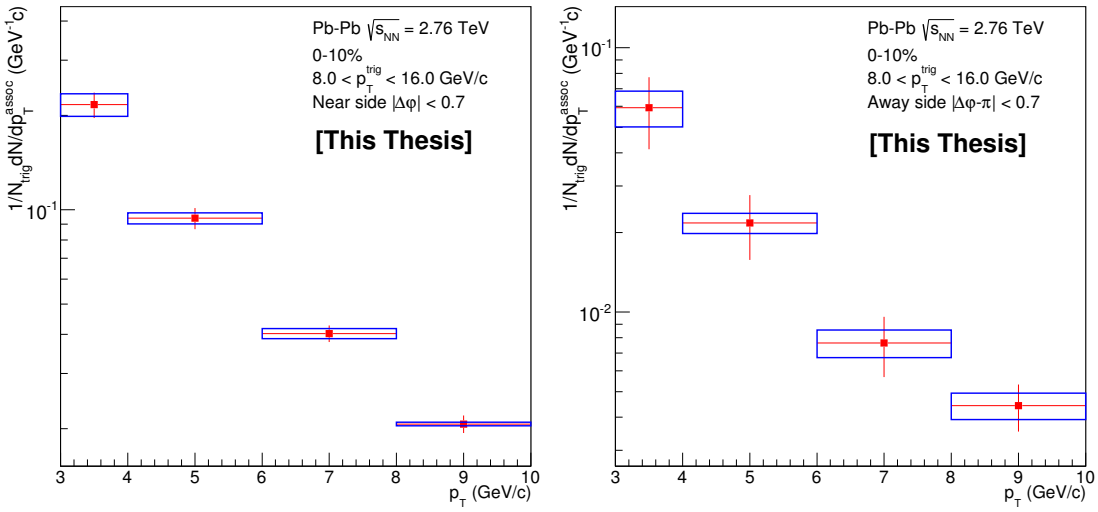

Figure 6.21: The systematic uncertainty from the three pedestal subtractions of the yield on Near side $|\Delta\varphi| < 0.7$ (left), Away side $|\Delta\varphi - \pi| < 0.7$ (right) in Pb+Pb 0-10% at $\sqrt{s_{\rm NN}}$ = 2.76 TeV, respectively. The blue boxed is the systematic uncertainty.

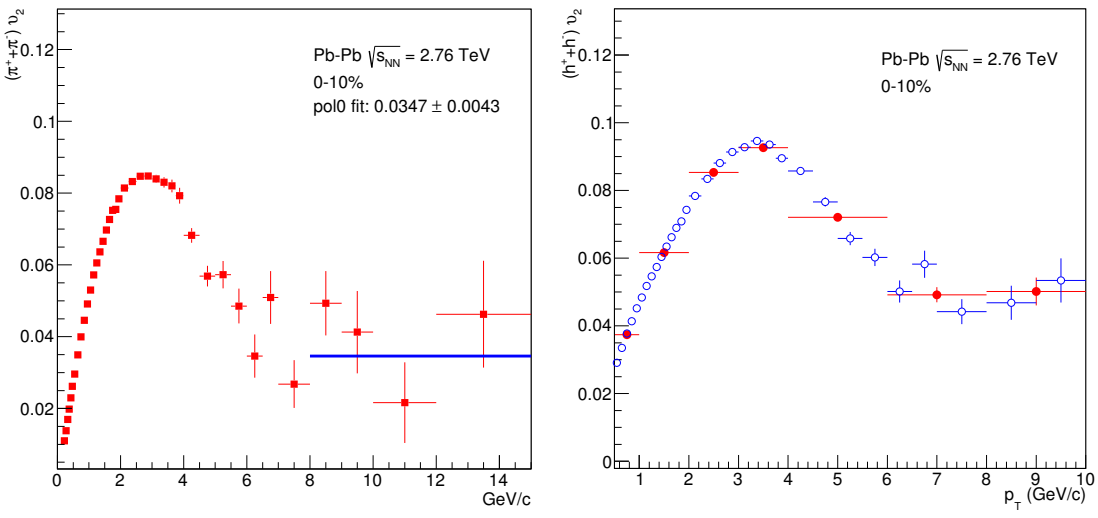

Figure 6.22: v_2 flow of charged pions (left) and charged hadrons (right) in Pb-Pb 0-10% at $\sqrt{s_{\rm NN}}$ = 2.76 TeV. In the left, the blue line is the fit value at $8.0 < p_{\rm T} < 16.0$ GeV/c with0.0347 ± 0.0043. The fit error is used to estimate the systematic uncertainty of flow.

where $J(\Delta\varphi)$ and $C(\Delta\varphi)$ are the jet-like correlations and all correlations obtained by Eq. 6.4, respectively; v_2^{trig} and v_2^{assoc} are the elliptic flow coefficients of trigger particles and associated particles, respectively; b_0 is the background scaled factor, which is generally determined by a pedestal subtraction employing the zero-yield-at-minimum (ZYAM) method shown in Sec. 6.3.3.2.

6.4 Correction analysis

When analyzing MC, the N_{pair} and N_{trig} histograms are filled at different steps to allow the extraction of the necessary corrections to the yields. Tab.6.4 shows the various steps.

Step	Trigger π^0	Associated Tracks	Detector Effect
0	reconstructed candidate π^0	all reconstructed tracks	
1	reconstructed π^0	all reconstructed tracks	π^0 contamination
2	reconstructed π^0 (gen. p_{T})	all reconstructed tracks	π^0 p_{T} resolution
3	all input π^0 MC	all reconstructed tracks	π^0 efficiency
4		primary+secondary MC tracks if reconstructed	track p_{T} resolution
5		primary MC tracks if reconstructed	track contamination
6		all input primary MC tracks	track efficiency

Table 6.4: List of corrections.

The steps in above table can be explained as:

- **step 0 → step 1**: correlations are corrected by π^0 contamination, details shown in 6.4.1.
- **step 1 → step 2**: correlations are corrected by π^0 resolution, details shown in 6.4.3.
- **step 2 → step 3**: correlations are corrected by π^0 efficiency, details shown in 6.4.2.
- **step 3 → step 4**: correlations are corrected by track resolution, details shown in 6.4.3.
- **step 4 → step 5**: correlations are corrected by track contamination, details shown in 6.4.4.

- **step 5 → step 6**: correlations are corrected by track efficiency, details shown in 6.4.4.

In step 5 and 6 the MC parameters of reconstructed tracks are used to fill the histograms. In this way the effect of efficiency and contamination can be estimated without being affected by tracking resolution.

6.4.1 π^0 contamination correction

For the cluster splitting method, the π^0 contamination can be calculated, which is shown in Sec. 6.2.1. In principle, the real π^0-hadron correlations should be extracted as:

$$Y_S = Y_{S+B}(1 + \frac{1}{f_{S/B}}) - \frac{Y_B}{f_{S/B}} \tag{6.8}$$

where Y_{S+B}, Y_S and Y_B are the yield of reconstructed candidate π^0-hadron correlations, reconstructed π^0-hadron correlations and fake (contamination) π^0-hadron correlations, respectively, and $f_{S/B}$ is the ratio of reconstructed π^0 (signal) to π^0 contamination (background). Since the fake π^0 includes photons and hadrons, whose statistics is very low, it is difficult to obtain a good fake π^0-hadron correlation, and the π^0 identification purity is high, 90% in pp and 85% in Pb+Pb. So in our analysis, a simple ratio of reconstructed candidate π^0-hadron correlations to true reconstructed π^0-hadron correlations is calculated with generated p_{T} as the correction factor for π^0 contamination, named pair purity correction factor. Written as:

$$P(Gen.p_{\mathrm{T}}, pair) = \frac{\text{reconstructed candidate } \pi^0 - h^{\pm}(Gen.p_T)}{\text{reconstructed true } \pi^0 - h^{\pm}(Gen.p_T)} \tag{6.9}$$

Since there is no enough statistics of LHC12a15a for pp at $\sqrt{s}$ =2.76 TeV to analyze correction factors, especially resolution correction factor presented later, therefore LHC12f2a simulation for pp at $\sqrt{s}$ = 7 TeV is used for correction factor estimation analysis. To believe the correction factors for LHC12f2a can be used on pp data at $\sqrt{s}$ =2.76 TeV, the pair purity factors from LHC12a15a and LHC12f2a are compared as shown in Fig. 6.23. The comparison shows that both simulations give the same pair purity factors.

The factor as a function of $\Delta\varphi$ is shown in Fig. 6.24 with π^0 trigger bins $8.0 < p_{\mathrm{T}}^{\mathrm{trig}} < 12.0$ GeV/c and $12.0 < p_{\mathrm{T}}^{\mathrm{trig}} < 16.0$ GeV/c, associated in $1.0 < p_{\mathrm{T}}^{\mathrm{assoc}} < 2.0$ GeV/c and $2.0 < p_{\mathrm{T}}^{\mathrm{assoc}} < 4.0$ GeV/c in LHC12f2a (Pythia6). A constant is used to fit the distribution, and three $\Delta\varphi$ regions ($|\Delta\varphi| < 1.0$, $2.0 < |\Delta\varphi| < 4.0$ and full $\Delta\varphi$) are selected to to fit and to estimate the systematic uncertainty from the

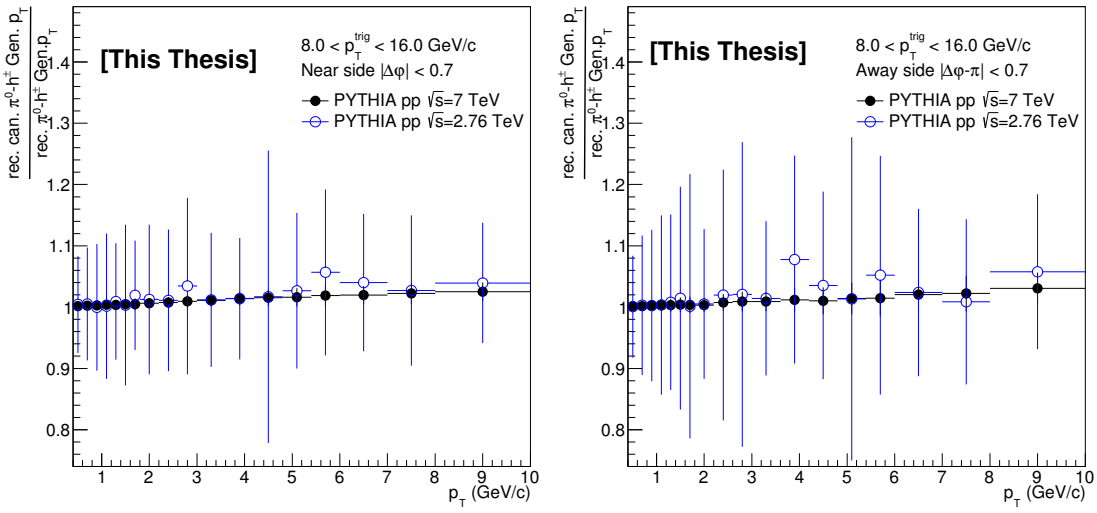

Figure 6.23: Comparison of pair purity correction factors from LHC12a15a simulation for pp at $\sqrt{s} = 2.76$ TeV and LHC12f2a for pp at $\sqrt{s} = 7$ TeV on Near side $|\Delta\varphi| < 0.7$ (left), and Away side $|\Delta\varphi - \pi| < 0.7$ (right).

fitting. The results of the 3 fits are summarized in Tab. 6.5 for the pp (LHC12f2a) simulation.

$p_{\mathrm{T}}^{\mathrm{trig}}$ and $p_{\mathrm{T}}^{\mathrm{assoc}}$ (GeV/c)	$-\frac{\pi}{2} < \Delta\varphi < \frac{3\pi}{2}$	$-1.0 < \Delta\varphi < 1.0$	$2.0 < \Delta\varphi < 4.0$
$8.0 < p_{\mathrm{T}}^{\mathrm{trig}} < 12.0$ $1.0 < p_{\mathrm{T}}^{\mathrm{assoc}} < 2.0$	1.006±0.004	1.008±0.006	1.006±0.007
$8.0 < p_{\mathrm{T}}^{\mathrm{trig}} < 12.0$ $2.0 < p_{\mathrm{T}}^{\mathrm{assoc}} < 4.0$	1.016±0.006	1.020±0.007	1.015±0.010
$12.0 < p_{\mathrm{T}}^{\mathrm{trig}} < 16.0$ $1.0 < p_{\mathrm{T}}^{\mathrm{assoc}} < 2.0$	1.008±0.006	1.008±0.009	1.010±0.011
$12.0 < p_{\mathrm{T}}^{\mathrm{trig}} < 16.0$ $2.0 < p_{\mathrm{T}}^{\mathrm{assoc}} < 4.0$	1.016±0.008	1.018±0.010	1.016 ±0.014

Table 6.5: Result of constant fit to pair purity in different $\Delta\varphi$ regions in trigger p_{T} bins in $8.0 < p_{\mathrm{T}}^{\mathrm{trig}} < 12.0$ GeV/c and $12.0 < p_{\mathrm{T}}^{\mathrm{trig}} < 16.0$ GeV/c, associated in $0.5 < p_{\mathrm{T}}^{\mathrm{assoc}} < 1.0$ GeV/c and $1.0 < p_{\mathrm{T}}^{\mathrm{assoc}} < 2.0$ GeV/c in LHC12f2a simulation.

Similarly, the analysis in $8.0 < p_{\mathrm{T}}^{\mathrm{trig}} < 12.0$ GeV/c and $12.0 < p_{\mathrm{T}}^{\mathrm{trig}} < 16.0$ GeV/c, associated in $1.0 < p_{\mathrm{T}}^{\mathrm{assoc}} < 2.0$ GeV/c and $2.0 < p_{\mathrm{T}}^{\mathrm{assoc}} < 4.0$ GeV/c is done in Pb+Pb simulation, and the results are shown in Fig. 6.25. The results of the 3 fits are summarized in Tab. 6.6 for the Pb+Pb (LHC12d17d_fix) simulation.

Fig. 6.26 and Fig. 6.27 show the pair purity correction factors as a function of

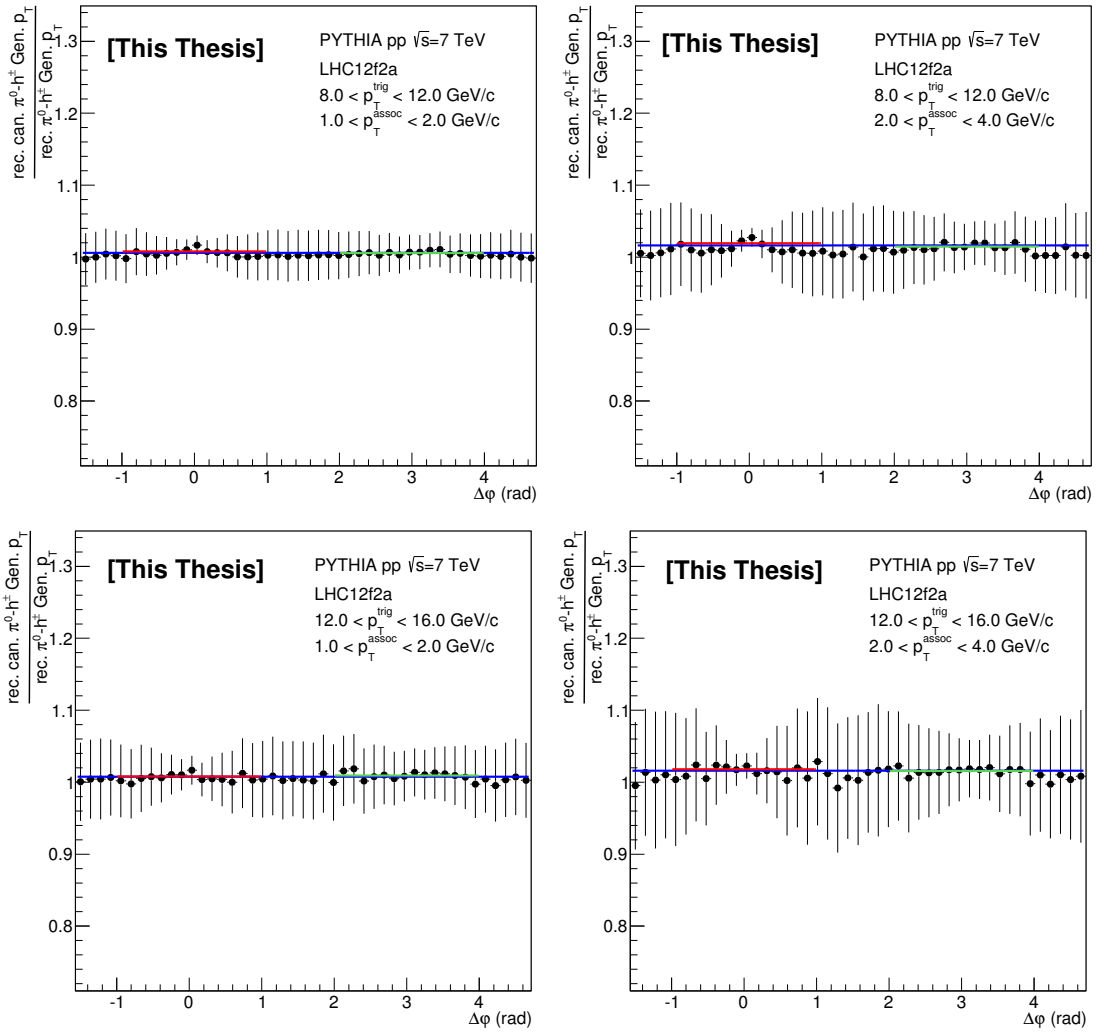

Figure 6.24: Pair purity correction factor as a function of $\Delta\varphi$ with π^0 trigger bins $8.0 < p_{\mathrm{T}}^{\mathrm{trig}} < 12.0$ GeV/c and $12.0 < p_{\mathrm{T}}^{\mathrm{trig}} < 16.0$ GeV/c, associated in $1.0 < p_{\mathrm{T}}^{\mathrm{assoc}} < 2.0$ GeV/c and $2.0 < p_{\mathrm{T}}^{\mathrm{assoc}} < 4.0$ GeV/c in LHC12f2a for pp data. A constant is used to fit the distribution in three different $\Delta\varphi$ ranges, which is used to estimated the fitting systematic uncertainty.

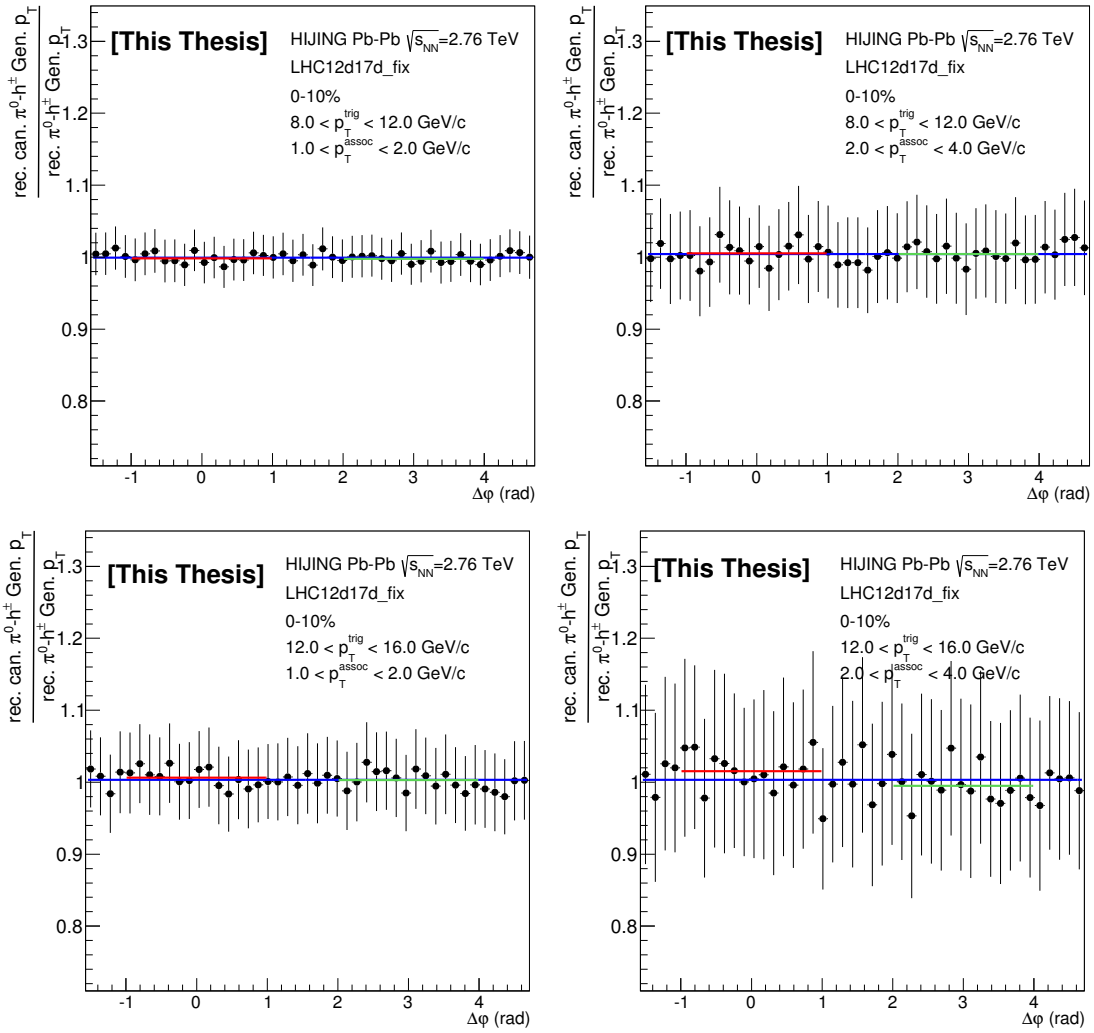

Figure 6.25: Pair purity correction factor as a function of $\Delta\varphi$ with π^0 trigger bins $8.0 < p_{\mathrm{T}}^{\mathrm{trig}} < 12.0$ GeV/c and $12.0 < p_{\mathrm{T}}^{\mathrm{trig}} < 16.0$ GeV/c, associated in $1.0 < p_{\mathrm{T}}^{\mathrm{assoc}} < 2.0$ GeV/c and $2.0 < p_{\mathrm{T}}^{\mathrm{assoc}} < 4.0$ GeV/c in LHC12a17d_fix for Pb+Pb data. A constant is used to fit the distribution in three different $\Delta\varphi$ ranges, which is used to estimated the fitting systematic uncertainty.

$p_{\mathrm{T}}^{\mathrm{trig}}$ and $p_{\mathrm{T}}^{\mathrm{assoc}}$ (GeV/c)	$-\frac{\pi}{2} < \Delta\varphi < \frac{3\pi}{2}$	$-1.0 < \Delta\varphi < 1.0$	$2.0 < \Delta\varphi < 4.0$
$8.0 < p_{\mathrm{T}}^{\mathrm{trig}} < 12.0$ $1.0 < p_{\mathrm{T}}^{\mathrm{assoc}} < 2.0$	0.999±0.004	0.998±0.008	0.998±0.008
$8.0 < p_{\mathrm{T}}^{\mathrm{trig}} < 12.0$ $2.0 < p_{\mathrm{T}}^{\mathrm{assoc}} < 4.0$	1.004±0.009	1.005±0.017	1.004±0.017
$12.0 < p_{\mathrm{T}}^{\mathrm{trig}} < 16.0$ $1.0 < p_{\mathrm{T}}^{\mathrm{assoc}} < 2.0$	1.003±0.008	1.006±0.015	1.003±0.015
$12.0 < p_{\mathrm{T}}^{\mathrm{trig}} < 16.0$ $2.0 < p_{\mathrm{T}}^{\mathrm{assoc}} < 4.0$	1.003±0.017	1.016±0.031	0.995±0.031

Table 6.6: Result of constant fit to pair purity in different $\Delta\varphi$ regions in trigger p_{T} bins in $8.0 < p_{\mathrm{T}}^{\mathrm{trig}} < 12.0$ GeV/c and $12.0 < p_{\mathrm{T}}^{\mathrm{trig}} < 16.0$ GeV/c, associated in $1.0 < p_{\mathrm{T}}^{\mathrm{assoc}} < 2.0$ GeV/c and $2.0 < p_{\mathrm{T}}^{\mathrm{assoc}} < 4.0$ GeV/c in LHC12a17d_fix simulation.

p_{T} on Near side $|\Delta\varphi| < 0.7$ (left), Away side $|\Delta\varphi - \pi| < 0.7$ (right) for pp at $\sqrt{s}$ = 2.76 TeV and Pb+Pb 0-10% at $\sqrt{s_{\mathrm{NN}}}$ = 2.76 TeV, respectively. In consideration of the correction factor statistics error from the simulation analysis, more than one functions fitting are also used to obtain the factor value and estimate the fitting systematic uncertainty.

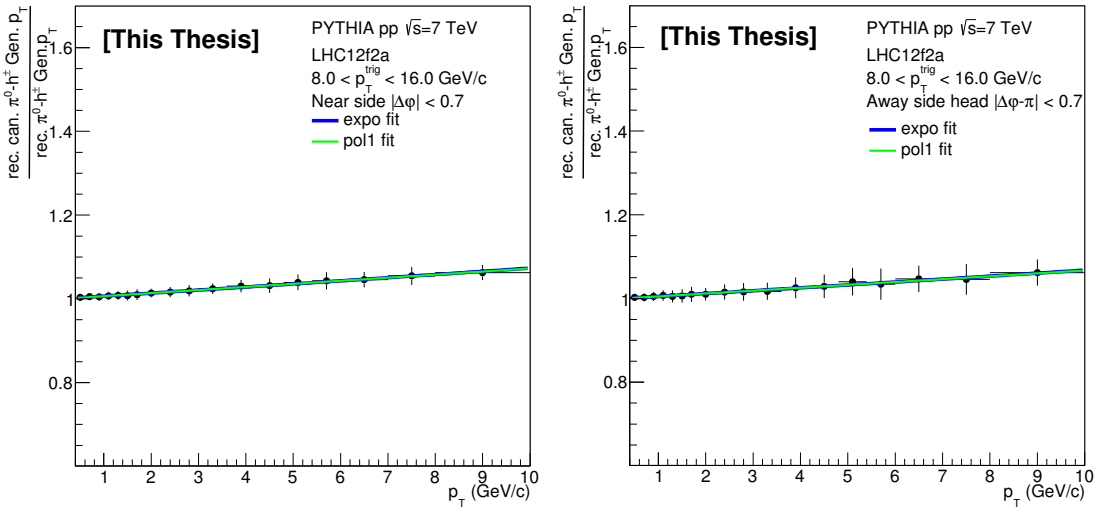

Figure 6.26: Pair purity correction factors as a function of p_{T} on Near side $|\Delta\varphi| < 0.7$ (left), Away side $|\Delta\varphi - \pi| < 0.7$ (right) from LHC12f2a (Pythia6) for pp data. Two functions (Exponential and Polynomial1) are used to fit the distribution to estimate the systematic uncertainty of the fit.

Compared to Pb+Pb results, the pair purity ratio in pp goes up with a certain slope. This result is from the cluster track matching effect. The pair purity results in

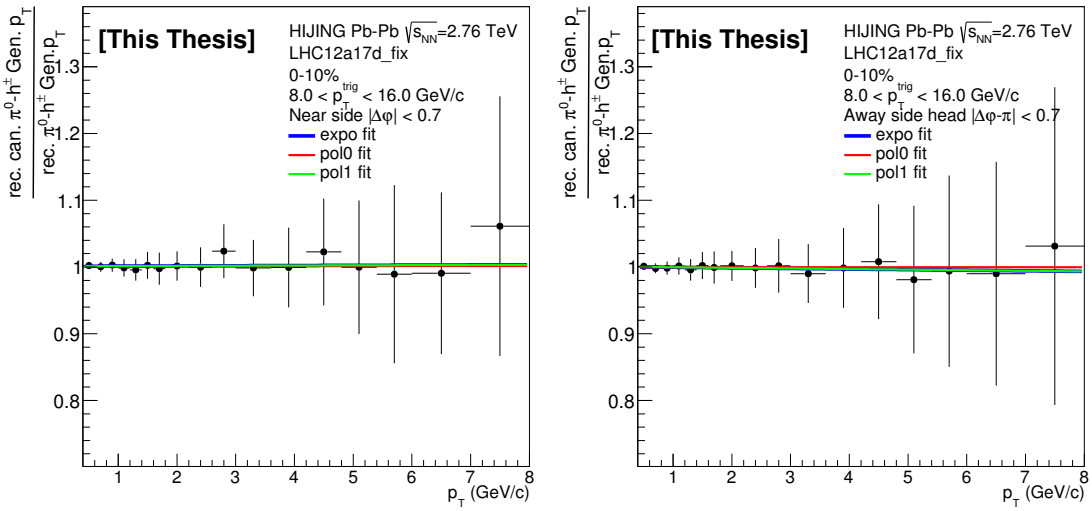

Figure 6.27: Pair purity correction factors as a function of p_{T} on Near side $|\Delta\varphi| < 0.7$ (left), Away side $|\Delta\varphi - \pi| < 0.7$ (right) from LHC12a17d_fix (HIJING) for Pb+Pb 0-10% data. Three functions (Exponential, Polynomial0 and Polynomial1) are used to fit the distribution to estimate the systematic uncertainty of the fit.

pp with and without the track matching (Here, match cluster with tracks selected by TPC-Only track cuts) are compared, see Fig. 6.28. The comparison indicates that the slope of with track matching is larger than without track matching. Therefore, the conclusion is that the efficiency of track matching rejecting clusters produced by charged hadrons is not high.

6.4.2 π^0 efficiency correction

Fig. 6.9 shows the π^0 reconstruction efficiency of the cluster splitting technique in pp at $\sqrt{s} = 2.76$ and 7 TeV (left), and centrality 0-10% Pb+Pb at $\sqrt{s_{\mathrm{NN}}} = 2.76$ TeV (right), respectively. Since the efficiency as a function of p_{T} is not flat , it needs to be taken into account. For correction with the trigger π^0 efficiency, the azimuthal correlations are corrected by the efficiency:

$$\frac{1}{N_{\mathrm{trig}}^{corrected}}\frac{dN_{\mathrm{pair}}^{\mathrm{corrected}}}{d\Delta\varphi} = \frac{1}{\sum_{\Delta p_{\mathrm{T(i)}}}\frac{1}{\varepsilon_i}N_{\mathrm{trig(i)}}(\Delta p_{\mathrm{T}}^{\mathrm{trig}})}\sum_{\Delta p_{\mathrm{T(i)}}}\frac{1}{\varepsilon_i}\frac{dN_{\mathrm{pair(i)}}^{Raw}}{d\Delta\varphi}(\Delta p_{\mathrm{T}}^{\mathrm{trig}}) \quad (6.10)$$

In order to correct the effect of π^0 efficiency to a p_{T} bin trigger more exactly, the minimum p_{T} bin, $\Delta p_T = 1.0$ GeV/c, is set to the trigger in the calculation. Fig. 6.30 shows the comparison of with and without π^0 efficiency correction to azimuthal angle correlations in trigger $8.0 < p_{\mathrm{T}}^{\mathrm{trig}} < 12.0$ GeV/c, $12.0 < p_{\mathrm{T}}^{\mathrm{trig}} < 16.0$ GeV/c and

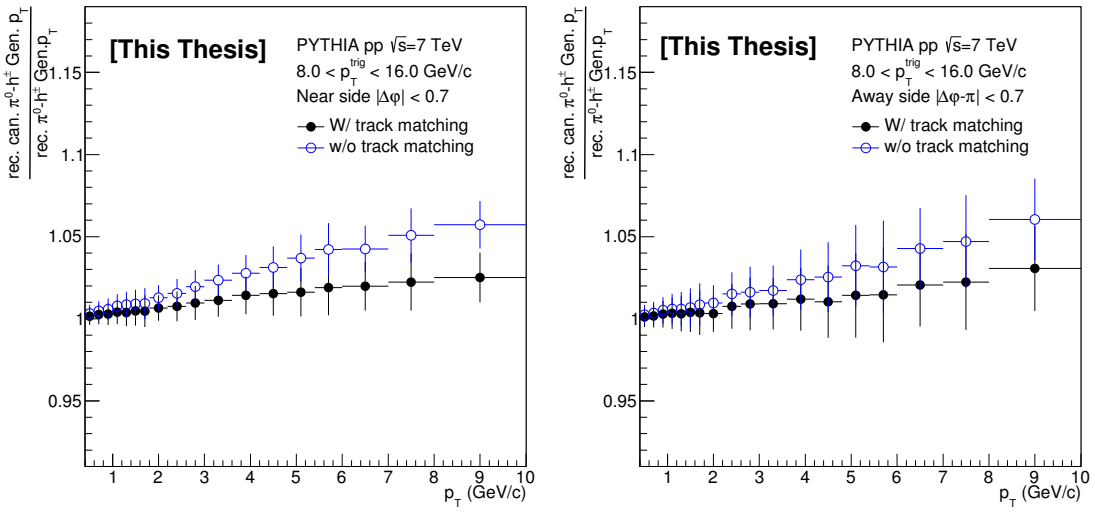

Figure 6.28: Pair purity factor comparison between with track matching and without track matching on Near side $|\Delta\varphi| < 0.7$ (left), Away side $|\Delta\varphi - \pi| < 0.7$ (right) in pp at $\sqrt{s} = 7$ TeV.

associated $1.0 < p_{\mathrm{T}}^{\mathrm{assoc}} < 2.0$ GeV/c in pp and Pb+Pb 0-10% collisions. The difference between with and without π^0 efficiency in azimuthal correlations is less than 2% at this p_{T} range. Fig. 6.29 shows the comparison of with and without π^0 efficiency correction to per-trigger yield of hadrons in trigger $8.0 < p_{\mathrm{T}}^{\mathrm{trig}} < 16.0$ GeV/c on Near side in pp and Pb+Pb 0-10% collisions. The difference between with and without π^0 efficiency in per-trigger yield of hadrons is $p_{\mathrm{T}}^{\mathrm{assoc}}$dependent.

6.4.3 π^0 and track p_{T} resolution correction

Fig. 6.31 shows the π^0 p_{T} resolution of the cluster splitting method for LHC12a15a (Pythia6). Fig. 6.32 shows the track p_{T} resolution for LHC12a15a. Similar study is shown in Fig. 6.33 for the π^0 and track p_{T} resolution in 0-10% Pb+Pb at $\sqrt{s_{\mathrm{NN}}} =$ 2.76 TeV (LHC12a17d_fix).

From Fig. 6.31 and Fig. 6.32, we found the π^0 p_{T} resolution is not very good, especially at high p_{T}, while track p_{T} resolution is better at below $p_{\mathrm{T}} < 10$ GeV/c. Because of statistics limit of Pb+Pb simulation, we did not give more detail analysis to the π^0 and track p_{T} resolution. The figures indicate that it necessary to correct the p_{T} resolution effects of trigger π^0 and associated tracks. In our analysis, the trigger π^0 and associated track p_{T} resolution corrections are taken into account together as one factor, namely pair resolution, which is a ratio of reconstructed π^0-hadron correlations with reconstructed p_{T} to reconstructed π^0-hadron correlations

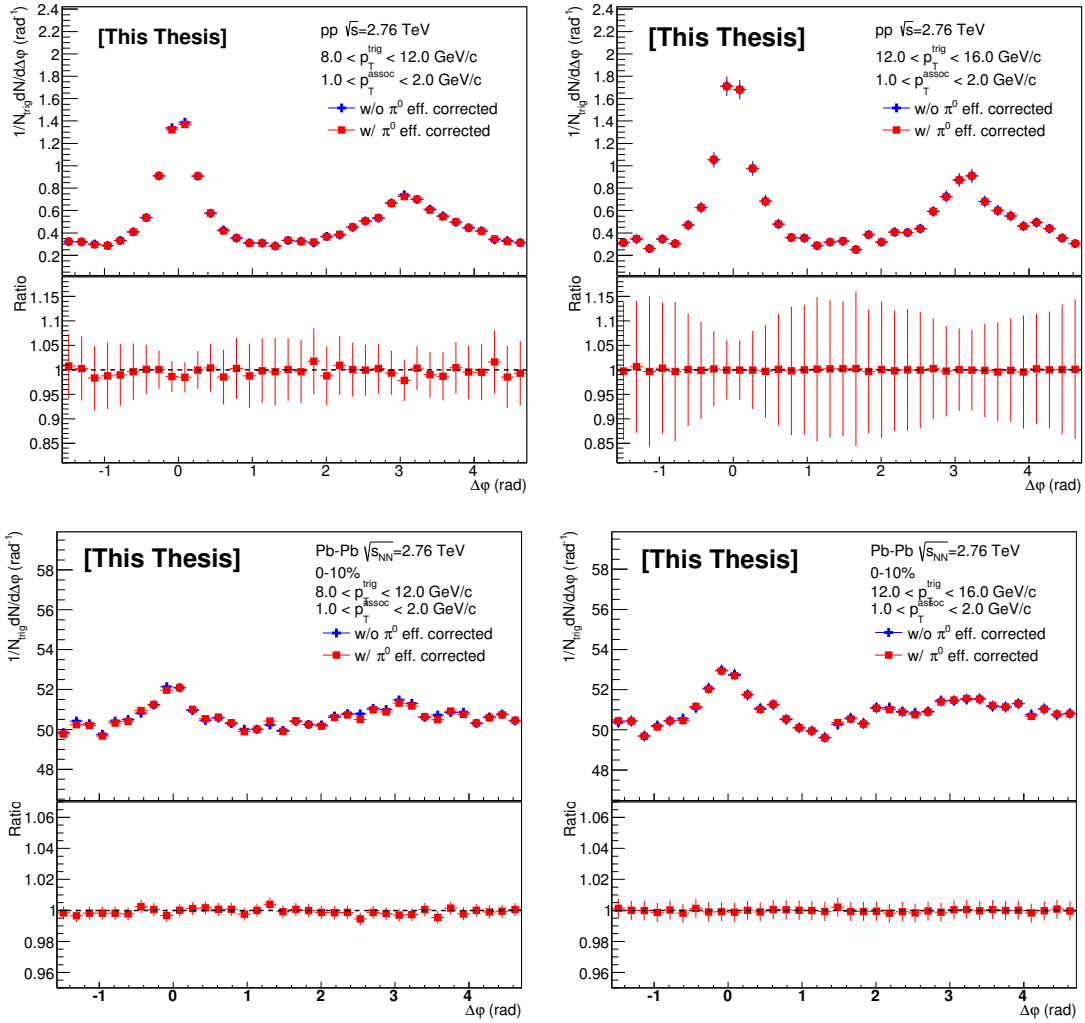

Figure 6.29: Comparison of azimuthal correlations with and without π^0 trigger efficiency correction in pp (top two) and Pb+Pb 0-10% (bottom two).

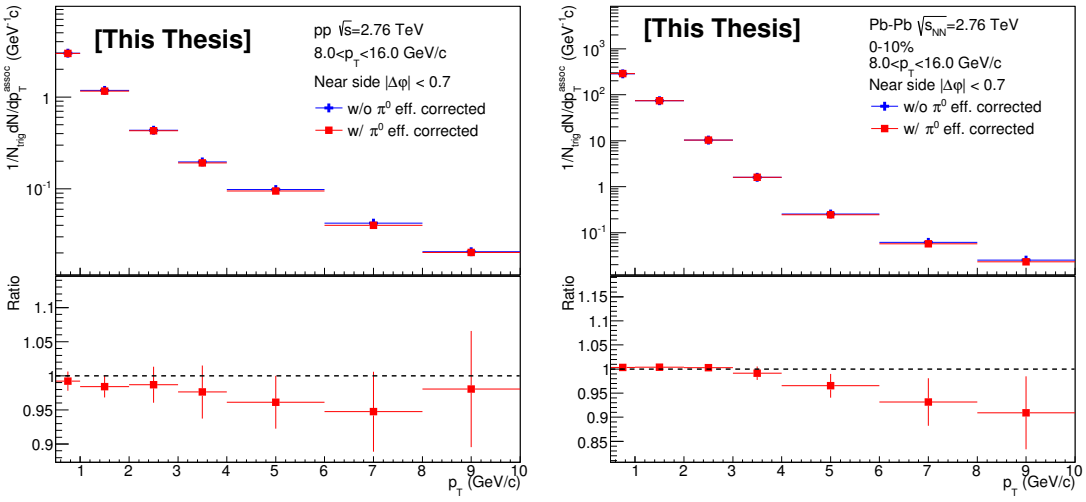

Figure 6.30: Comparison of per-trigger yield of hadrons with and without π^0 trigger efficiency correction in pp (left) and Pb+Pb 0-10% (right).

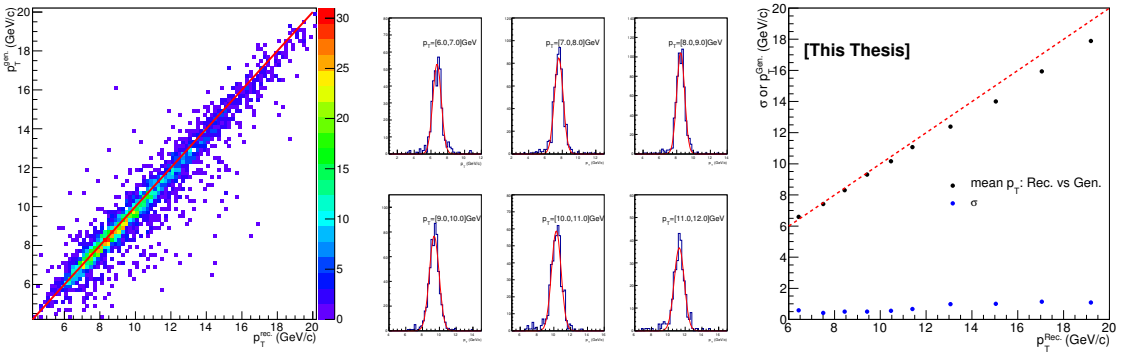

Figure 6.31: π^0 p_{T} resolution for the cluster splitting method in pp (LHC12a15a). The left panel shows the reconstructed vs generated p_{T} for reconstructed true π^0, the middle the projection to generated p_{T} in a fixed reconstructed p_{T} bin fitted by a Gaussian, and the right the Gaussian mean and sigma as a function of reconstructed p_{T}.

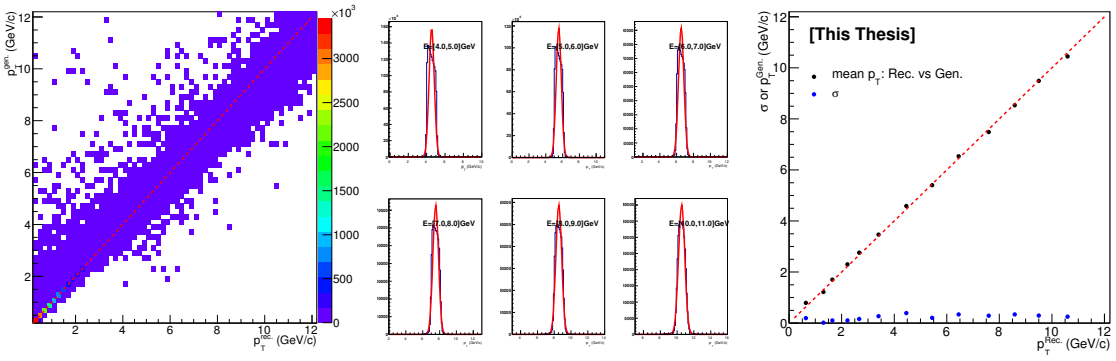

Figure 6.32: Track p_{T} resolution pp (LHC12a15a). The left panel shows the reconstructed vs generated p_{T} for tracks, the middle the projection to generated p_{T} in a fixed reconstructed p_{T} bin fitted by a Gaussian, and the right the Gaussian mean and sigma as a function of reconstructed p_{T}.

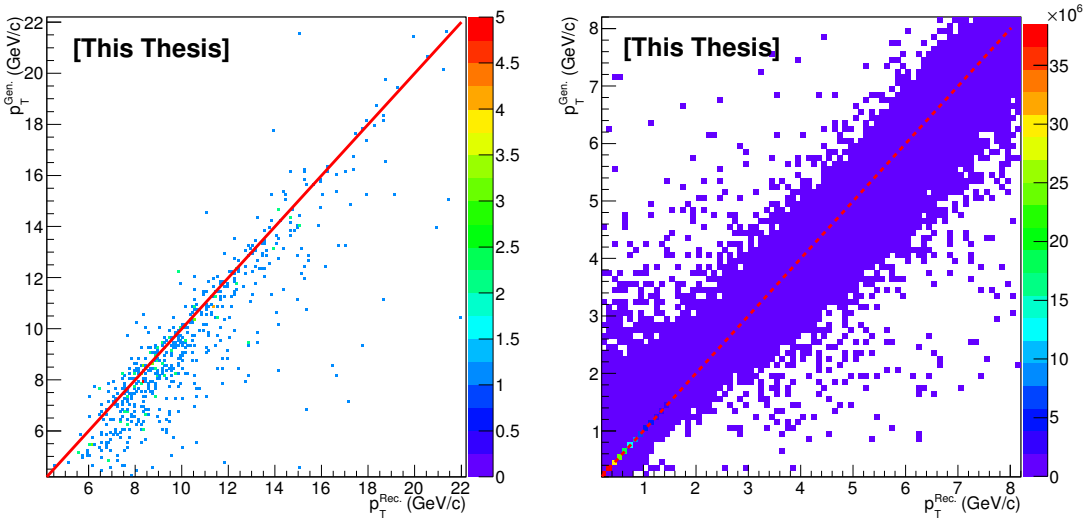

Figure 6.33: Generated p_{T} vs reconstructed p_{T} of the reconstructed π^0 (left), track (right) in centrality 0-10% in LHC12a17d_fix for Pb+Pb data.

with generated p_{T}. Written as:

$$R(Rec.p_{\mathrm{T}}, Gen.p_{\mathrm{T}}, pair) = \frac{\text{reconstructed true } \pi^0 - h^{\pm}(Rec.p_T)}{\text{reconstructed true } \pi^0 - h^{\pm}(Gen.p_T)} \tag{6.11}$$

Fig. 6.34 and 6.35 show the pair p_{T} resolution as a function of $\Delta\varphi$ from LHC12f2a and in LHC12a17d_fix, respectively. In each plot, constants are used to fit the distribution in three different $\Delta\varphi$ ranges, which are used to estimate the fitting systematic uncertainty of pair p_{T} resolution. In pp (LHC12f2a), the pair p_{T} resolution does not appear to be flat, perhaps because of the lack of statistics in the MC, whereas in 0-10% Pb+Pb (LHC12a17d_fix) it is. The results of the fits to the pair p_{T} resolution are given in Table 6.7 and Table 6.8 for pp and 0-10% Pb+Pb, respectively.

$p_{\mathrm{T}}^{\mathrm{trig}}$ and $p_{\mathrm{T}}^{\mathrm{assoc}}$ (GeV/c)	-$\frac{\pi}{2} < \Delta\varphi < \frac{3\pi}{2}$	$-1.0 < \Delta\varphi < 1.0$	$2.0 < \Delta\varphi < 4.0$
$8.0 < p_{\mathrm{T}}^{\mathrm{trig}} < 12.0$ $1.0 < p_{\mathrm{T}}^{\mathrm{assoc}} < 2.0$	1.002±0.004	1.004±0.006	1.001±0.007
$8.0 < p_{\mathrm{T}}^{\mathrm{trig}} < 12.0$ $2.0 < p_{\mathrm{T}}^{\mathrm{assoc}} < 4.0$	1.007±0.006	1.007±0.007	1.006±0.010
$12.0 < p_{\mathrm{T}}^{\mathrm{trig}} < 16.0$ $1.0 < p_{\mathrm{T}}^{\mathrm{assoc}} < 2.0$	1.009±0.006	1.009±0.009	1.004±0.011
$12.0 < p_{\mathrm{T}}^{\mathrm{trig}} < 16.0$ $2.0 < p_{\mathrm{T}}^{\mathrm{assoc}} < 4.0$	1.008±0.008	1.013±0.011	1.001±0.014

Table 6.7: Result of constant fit to pair p_{T} resolution in different $\Delta\varphi$ regions in trigger p_{T} bins in $8.0 < p_{\mathrm{T}}^{\mathrm{trig}} < 12.0$ GeV/c and $12.0 < p_{\mathrm{T}}^{\mathrm{trig}} < 16.0$ GeV/c, associated in $1.0 < p_{\mathrm{T}}^{\mathrm{assoc}} < 2.0$ GeV/c and $2.0 < p_{\mathrm{T}}^{\mathrm{assoc}} < 4.0$ GeV/c in LHC12f2a simulation.

Similar consideration, the pair p_{T} resolution results as a function of p_{T} on Near side $|\Delta\varphi| < 0.7$ (left), Away side $|\Delta\varphi - \pi| < 0.7$ (right) with trigger $8.0 < p_{\mathrm{T}}^{\mathrm{trig}} < 16.0$ GeV/c, in pp from LHC12f2a, and Pb+Pb 0-10% from LHC12a17d_fix are shown in Fig. 6.36 and Fig. 6.37, respectively. Because of limited statistical precision, fits, Exponential and Polynomial1 are used to fit the ratio in each pp and Pb+Pb and to estimate systematic uncertainty from using the fit.

6.4.4 Track efficiency and contamination correction

The tracking efficiency and contamination for hybrid tracks reconstructed in the ITS and TPC are evaluated with event and detector simulations. The generated

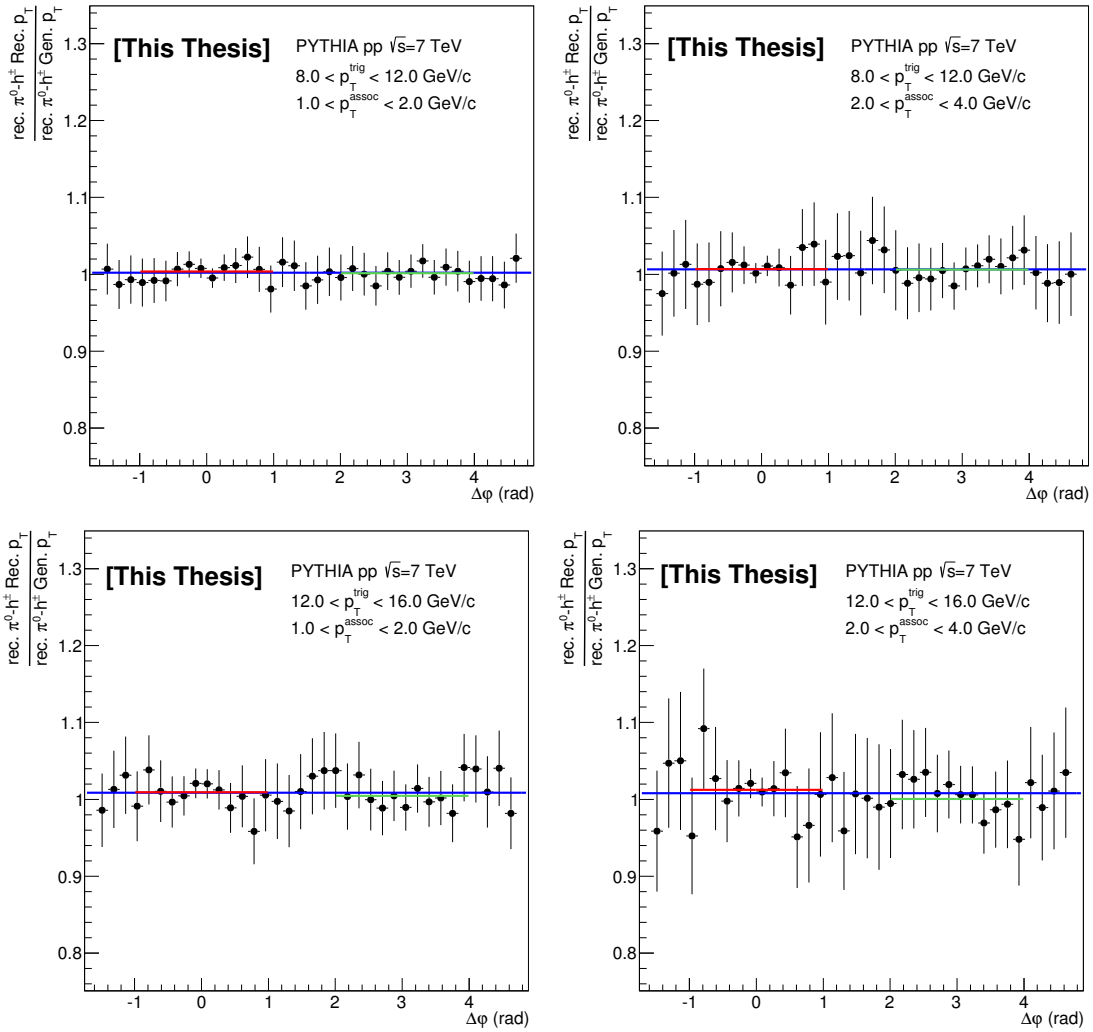

Figure 6.34: Pair p_{T} resolution correction factor as a function of $\Delta\varphi$ with trigger π^0 $8.0 < p_{\mathrm{T}}^{\mathrm{trig}} < 12.0$ GeV/c (left), $12.0 < p_{\mathrm{T}}^{\mathrm{trig}} < 16.0$ GeV/c (right) and associated hadron $1.0 < p_{\mathrm{T}}^{\mathrm{trig}} < 5.0$ GeV/c from LHC12f2a for pp data.

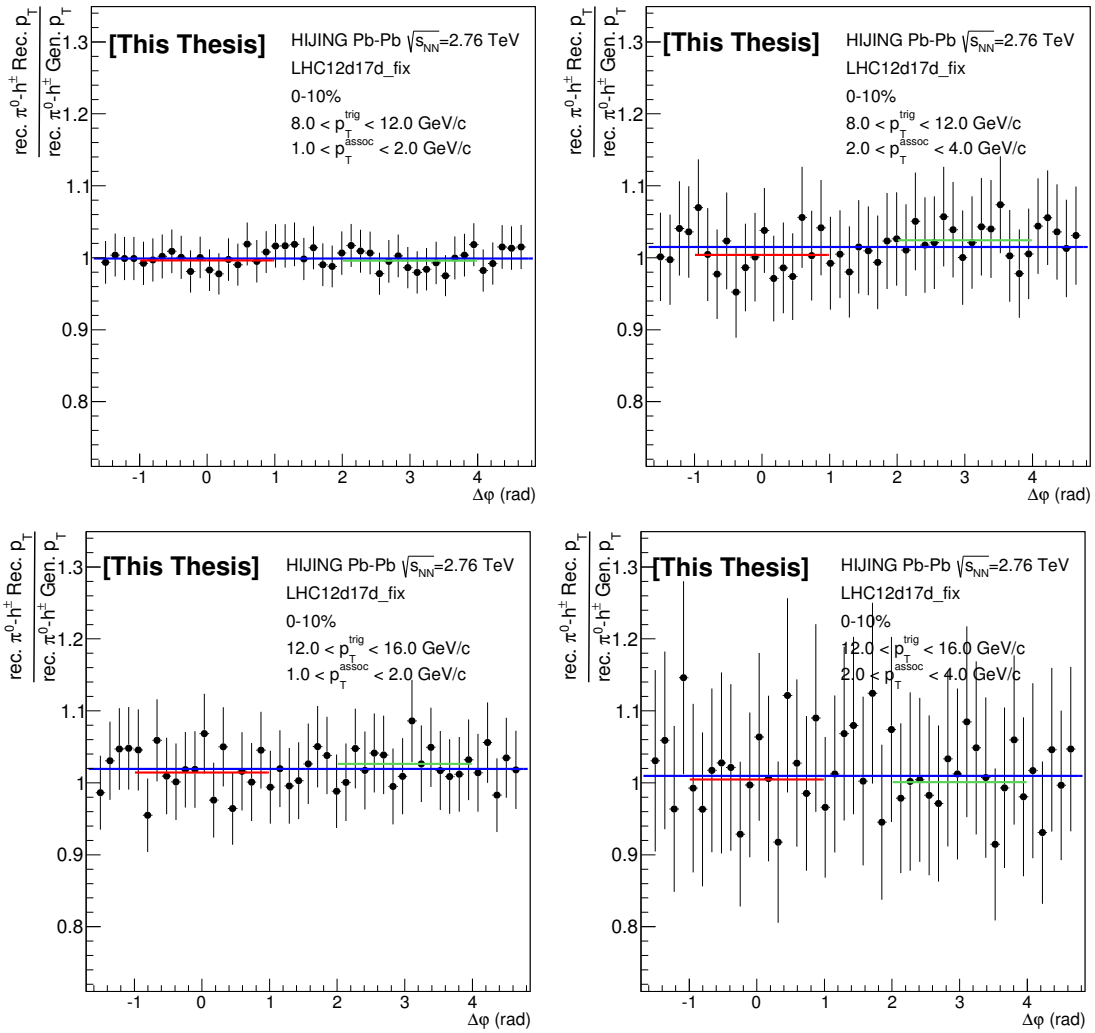

Figure 6.35: Pair p_{T} resolution correction factor as a function of $\Delta\varphi$ with trigger π^0 $8.0 < p_{\mathrm{T}}^{\mathrm{trig}} < 12.0$ GeV/c, $12.0 < p_{\mathrm{T}}^{\mathrm{trig}} < 16.0$ GeV/c and associated hadron $1.0 < p_{\mathrm{T}}^{\mathrm{trig}} < 2.0$ GeV/c, $2.0 < p_{\mathrm{T}}^{\mathrm{trig}} < 4.0$ GeV/c from LHC12a17d_fix for Pb+Pb 0-10% data.

$p_{\mathrm{T}}^{\mathrm{trig}}$ and $p_{\mathrm{T}}^{\mathrm{assoc}}$ (GeV/c)	$-\frac{\pi}{2} < \Delta\varphi < \frac{3\pi}{2}$	$-1.0 < \Delta\varphi < 1.0$	$2.0 < \Delta\varphi < 4.0$
$8.0 < p_{\mathrm{T}}^{\mathrm{trig}} < 12.0$ $1.0 < p_{\mathrm{T}}^{\mathrm{assoc}} < 2.0$	0.999±0.004	0.996±0.008	0.996±0.008
$8.0 < p_{\mathrm{T}}^{\mathrm{trig}} < 12.0$ $2.0 < p_{\mathrm{T}}^{\mathrm{assoc}} < 4.0$	1.015±0.010	1.004±0.017	1.024±0.018
$12.0 < p_{\mathrm{T}}^{\mathrm{trig}} < 16.0$ $1.0 < p_{\mathrm{T}}^{\mathrm{assoc}} < 2.0$	1.019±0.008	1.014±0.014	1.026±0.015
$12.0 < p_{\mathrm{T}}^{\mathrm{trig}} < 16.0$ $2.0 < p_{\mathrm{T}}^{\mathrm{assoc}} < 4.0$	1.010±0.017	1.004±0.031	1.001±0.031

Table 6.8: In pair p_{T} resolution as a function of $\Delta\varphi$, three constant fitting results in different $\Delta\varphi$ regions in trigger p_{T} bins in $8.0 < p_{\mathrm{T}}^{\mathrm{trig}} < 12.0$ GeV/c and $12.0 < p_{\mathrm{T}}^{\mathrm{trig}} < 16.0$ GeV/c, associated in $1.0 < p_{\mathrm{T}}^{\mathrm{assoc}} < 2.0$ GeV/c and $2.0 < p_{\mathrm{T}}^{\mathrm{assoc}} < 4.0$ GeV/c in LHC12a17d_fix simulation.

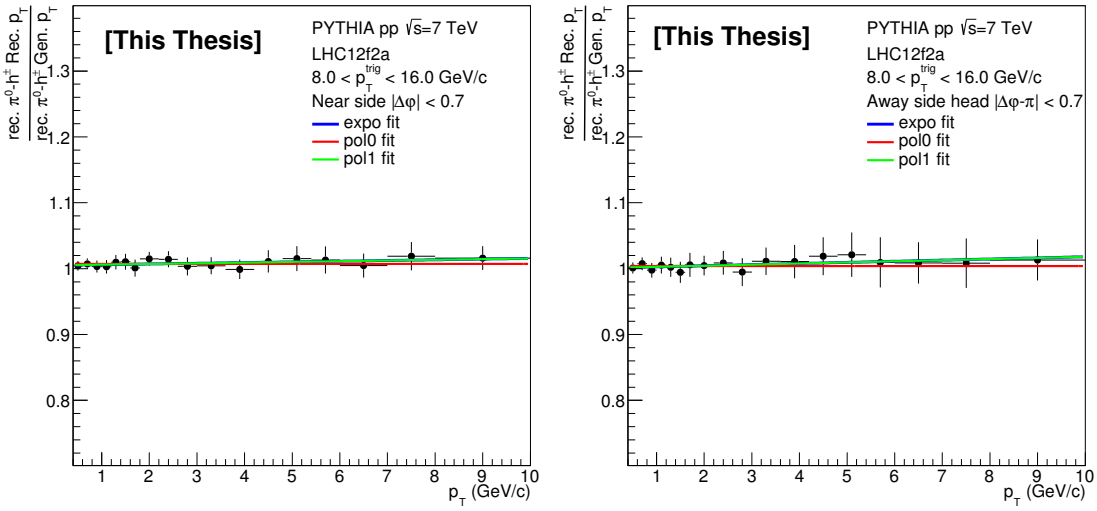

Figure 6.36: Pair p_{T} resolution correction factor as a function of p_{T} on Near side $|\Delta\varphi| < 0.7$ (left), Away side $|\Delta\varphi - \pi| < 0.7$ (right) with trigger $8.0 < p_{\mathrm{T}}^{\mathrm{trig}} < 16.0$ GeV/c (right) from LHC12f2a for pp data. Two functions (Exponential and Polynomial1) are used to to fit the distribution and to estimate the systematic uncertainty of the fit.

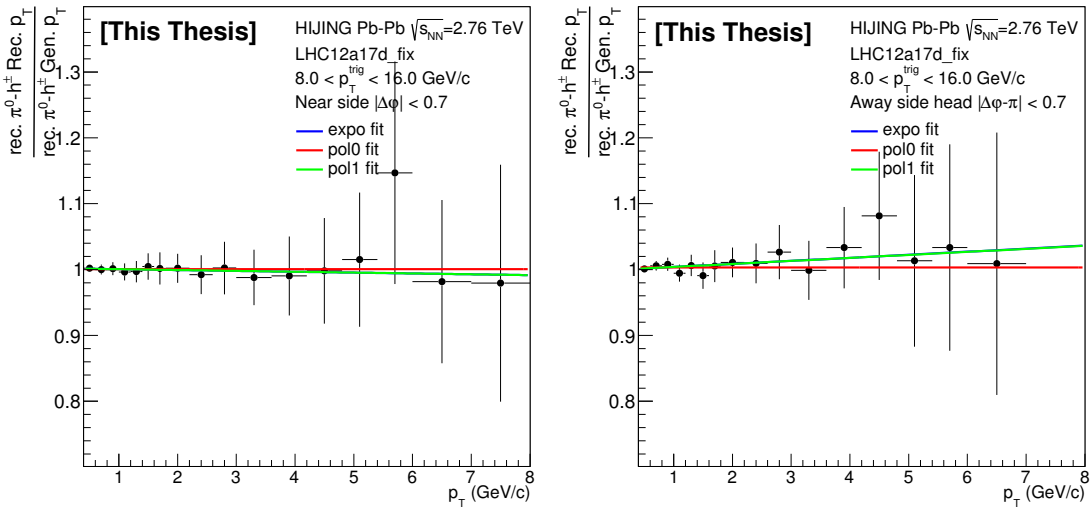

Figure 6.37: Pair p_{T} resolution correction factor as a function of p_{T}on Near side $|\Delta\varphi| < 0.7$ (left), Away side $|\Delta\varphi - \pi| < 0.7$ (right) with trigger $8.0 < p_{\mathrm{T}}^{\mathrm{trig}} < 16.0$ GeV/c (right) from LHC12a17d_fix for Pb+Pb (0-10%) data. Three functions (Exponential, Polynomial0 and Polynomial1) are used to to fit the distribution and to estimate the systematic uncertainty of the fit.

physical primary charged particles is defined as all the generated charged primary pions, protons, kaons and electrons within $|\eta| < 0.8$. Reconstructed physical primary tracks are tracks which pass the track selection and originate from a primary charged pion, kaon, proton or electron. The track efficiency and contamination are defined as:

$$\varepsilon(Gen.p_{\mathrm{T}}) = \frac{\text{Reconstructed physical primary tracks } (Gen.\ p_{\mathrm{T}})}{\text{True physical primary charged hadrons } (Gen.\ p_{\mathrm{T}})} \tag{6.12}$$

$$C(Rec.p_{\mathrm{T}}) = \frac{\text{Reconstructed secondary tracks } (Rec.\ p_{\mathrm{T}})}{\text{Reconstructed primary} + \text{secondary tracks } (Rec.p_{\mathrm{T}})} \tag{6.13}$$

For pp collisions, the track efficiency and contamination are calculated using 3 different simulations, LHC12a15a (Pythia6), LHC12f1a (Pythia8) and LHC12f1b (Phojet), shown in Fig. 6.38. The average is used to correct the raw correlation yields. The systematic uncertainty are estimated based on the spread of the 3 simulations.

For 0-10% Pb+Pb collisions, the track efficiency and contamination are estimated using HIJING (LHC12a17d_fix), shown in Fig. 6.39.

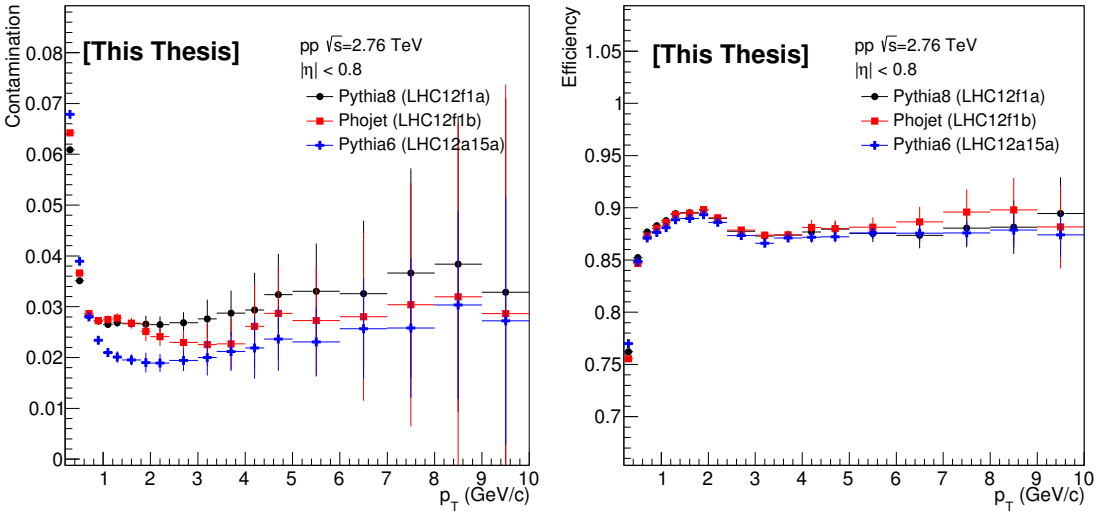

Figure 6.38: Track contamination (left) and efficiency (right) with Hybrid track cuts in three simulations, Pythia6 (blue), Pythia8 (black) and Phojet (red) for pp data.

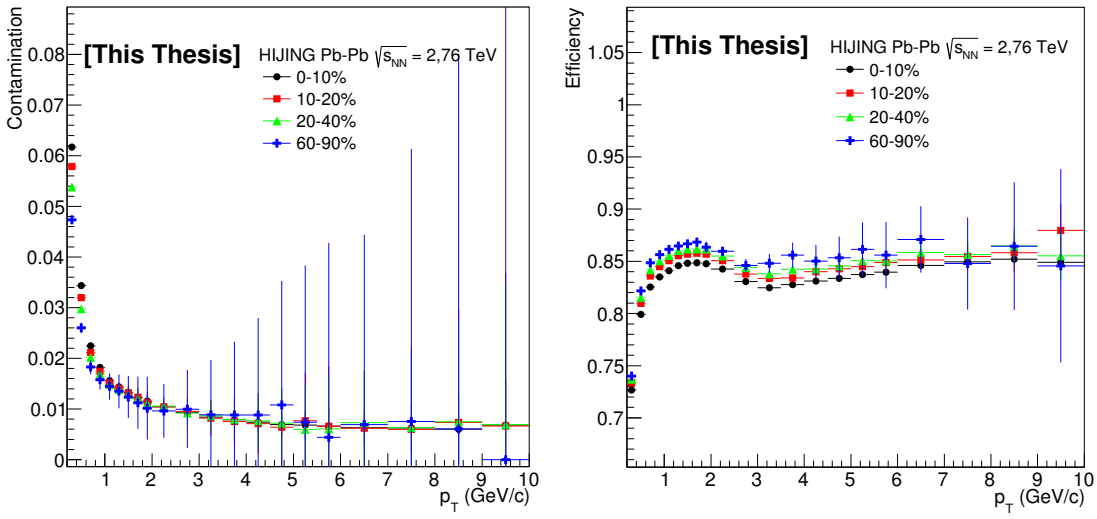

Figure 6.39: Track contamination (left) and efficiency (right) with Hybrid track cuts in LHC12a17d_fix for Pb+Pb (0-10%) data.

6.4.5 Applying the corrections

The complete correction procedure can be summarized as:

$$\begin{aligned} Y^{corrected}(\Delta\varphi, p_T^{trig}, p_T^{assoc}) &= Y^{raw}(\Delta\varphi, p_T^{trig}, p_T^{assoc}) \\ &\cdot f1_{CorrelatedTrigContam}(\Delta\varphi, p_T^{trig}, p_T^{assoc}) \\ &\cdot f2,4_{TirgAssocResolution}(p_T^{trig}, p_T^{assoc}) \\ &\cdot f3_{TrigEff}(p_T^{trig}) \\ &\cdot f5_{TrackContam}(p_T^{assoc}) \\ &\cdot f6_{TrackEff}(p_T^{assoc}) \end{aligned} \tag{6.14}$$

Notice: the correction factor for the trigger pi0 efficiency is applied to the raw yield before the normalization by N_{trig}, (see Eq. 6.10).

As a "MC closure check", the correction procedure is tested on MC simulations, shown in Fig. 6.40. It shows the comparison of azimuthal distribution in pp (top two) and in Pb+Pb (bottom two).

6.5 Systematic uncertainties

In this section, the systematic uncertainties of the π^0-hadron correlations in pp and Pb+Pb analysis are discussed. As discussed in Section 6.4, functions are used to fit the pair purity, pair resolution. The systematic uncertainty due to the fit estimated by variation of the fit functions. In pp, the uncertainties on the track efficiency and contamination is estimated from using Pythia6, Pythia8 and Phojet. In Pb+Pb, the uncertainties still need to be evaluated. The systematic uncertainties from shower shape cuts, invariant mass window selections and track cuts are estimated below. To a changed cut, all the correction factors are re-calculated. The systematic uncertainty estimation in per-trigger yield of hadrons, all pairs (correlated pairs and uncorrelated pairs together) in a region are used in order to avoid the fluctuation effects from estimating uncorrelated background.

6.5.1 Shower shape cuts

- **pp analysis**: As baseline, the cut on the shower shape long axis with a band criterion as Eq. 6.2 is used. To estimate the uncertainty introduced by this cut,

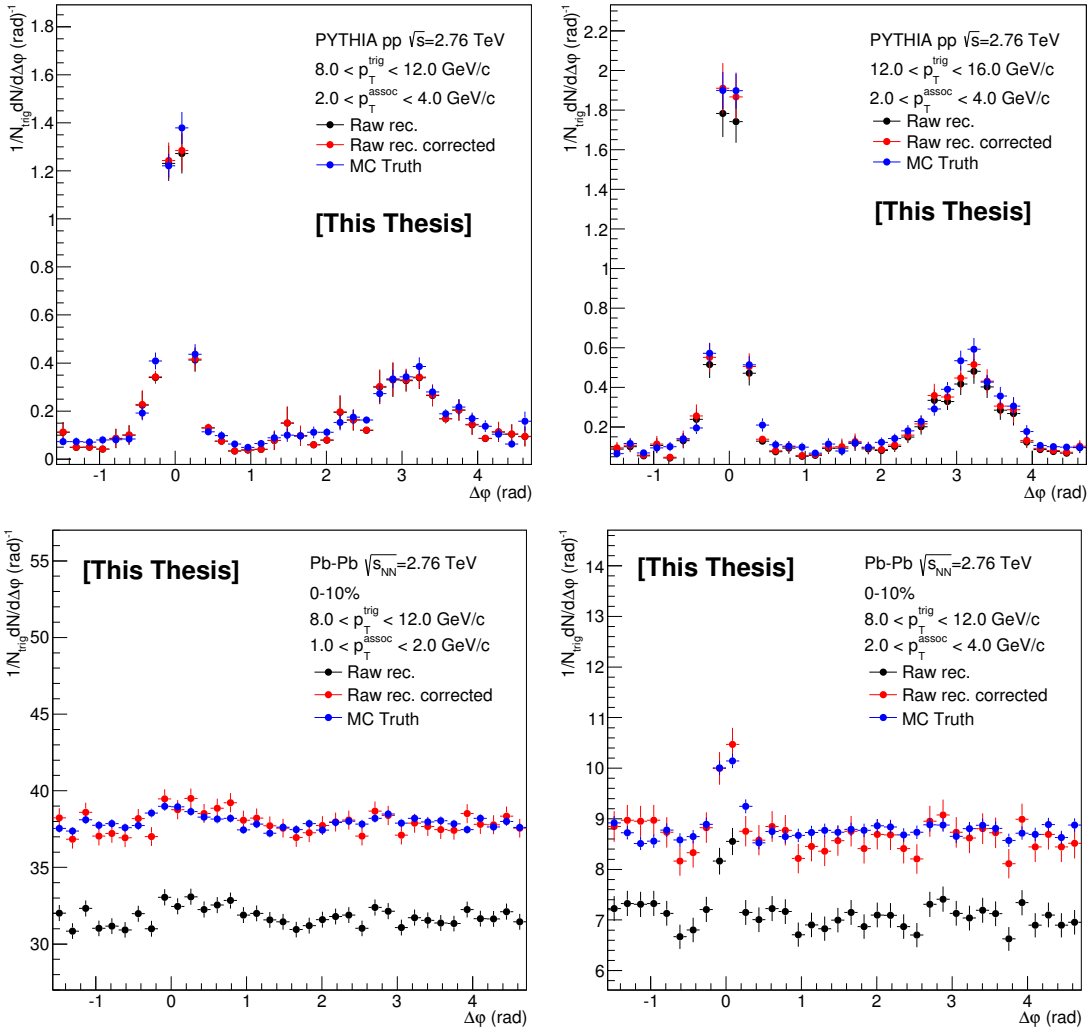

Figure 6.40: The correction procedure applied to MC simulations as a closure test for pp LHC12a15a (top) and Pb+Pb LHC12a17d_fix (bottom).

a new cut, $0.3 < \lambda_0^2 < 5$, is used. Fig. 6.41 shows the effect on the azimuthal $\Delta\varphi$ distribution for $8.0 < p_{\mathrm{T}}^{\mathrm{trig}} < 12.0$ GeV/c and $12.0 < p_{\mathrm{T}}^{\mathrm{trig}} < 16.0$ GeV/c with $1.0 < p_{\mathrm{T}}^{\mathrm{assoc}} < 2.0$ GeV/c, and Fig. 6.42 shows the comparison of the per-trigger yields between the two different shower shape cuts with π^0 trigger at $8.0 < p_{\mathrm{T}}^{\mathrm{trig}} < 16.0$ GeV/c in three $\Delta\varphi$ regions in pp at $\sqrt{s} = 2.76$ TeV.

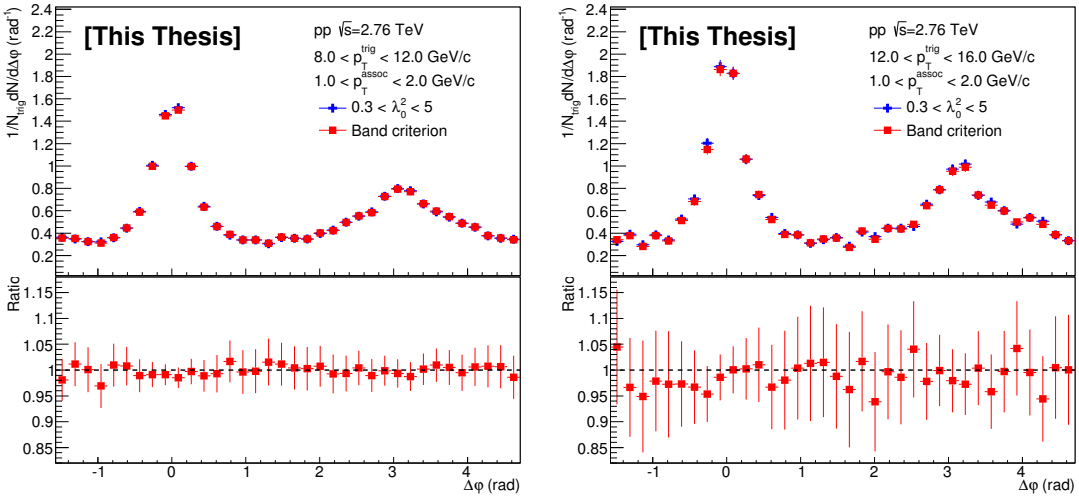

Figure 6.41: Comparison of the azimuthal distributions for two different shower shape cuts ($\lambda_{0,min}^2 < \lambda_0^2 < \lambda_{0,max}^2$ as Eq. 6.2 and $0.3 < \lambda_0^2 < 5$) in trigger p_{T} at $8.0 < p_{\mathrm{T}}^{\mathrm{trig}} < 12.0$ GeV/c and $12.0 < p_{\mathrm{T}}^{\mathrm{trig}} < 16.0$ GeV/c in pp collisions at $\sqrt{s} = 2.76$ TeV.

- **Pb+Pb analysis**: As baseline, the cut on the shower shape long axis with a band criterion same as in pp is used. To estimate the uncertainty introduced by this cut, a new cut on the shower shape, $0.3 < \lambda_0^2 < 5$, is used. Fig. 6.43 shows the effect on the azimuthal $\Delta\varphi$ distribution for $8.0 < p_{\mathrm{T}}^{\mathrm{trig}} < 12.0$ GeV/c and $12.0 < p_{\mathrm{T}}^{\mathrm{trig}} < 16.0$ GeV/c with $1.0 < p_{\mathrm{T}}^{\mathrm{assoc}} < 2.0$ GeV/c, and Fig. 6.44 shows the comparison of the per-trigger yields between the two different shower shape cuts with π^0 trigger at $8.0 < p_{\mathrm{T}}^{\mathrm{trig}} < 16.0$ GeV/c in three $\Delta\varphi$ regions in Pb+Pb 0-10% at $\sqrt{s_{\mathrm{NN}}} = 2.76$ TeV.

6.5.2 π^0 invariant mass window cuts

- **pp analysis**: As baseline, the cut on the reconstructed π^0 invariant mass window is $mean - 3\sigma < M_{\gamma\gamma} < mean + 3\sigma$, where $mean$ and σ are defined in Eq. 6.3. To estimate the uncertainty introduced by this cut, we change the cut to $mean - 2.5\sigma < M_{\gamma\gamma} < mean + 2.5\sigma$. The comparison of the azimuthal correlations between the two different cuts is shown in Fig. 6.45 for

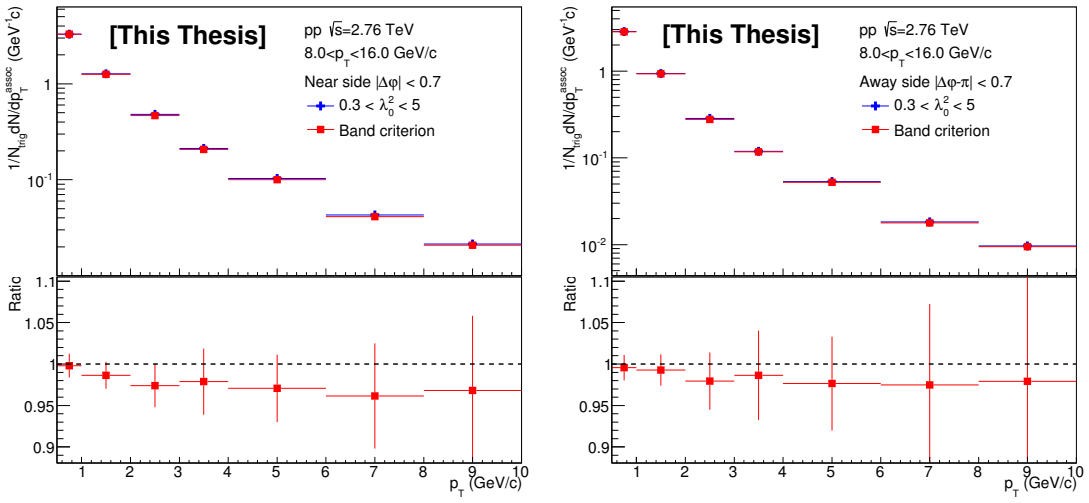

Figure 6.42: Comparison of the per-trigger yields for two different shower shape cuts ($(\lambda^2_{0,min} < \lambda^2_0 < \lambda^2_{0,max}$ as Eq. 6.2 and $0.3 < \lambda^2_0 < 5$) in trigger p_{T} at $8.0 < p_{\mathrm{T}}^{\mathrm{trig}} < 16.0$ GeV/c in pp at $\sqrt{s} = 2.76$ TeV.

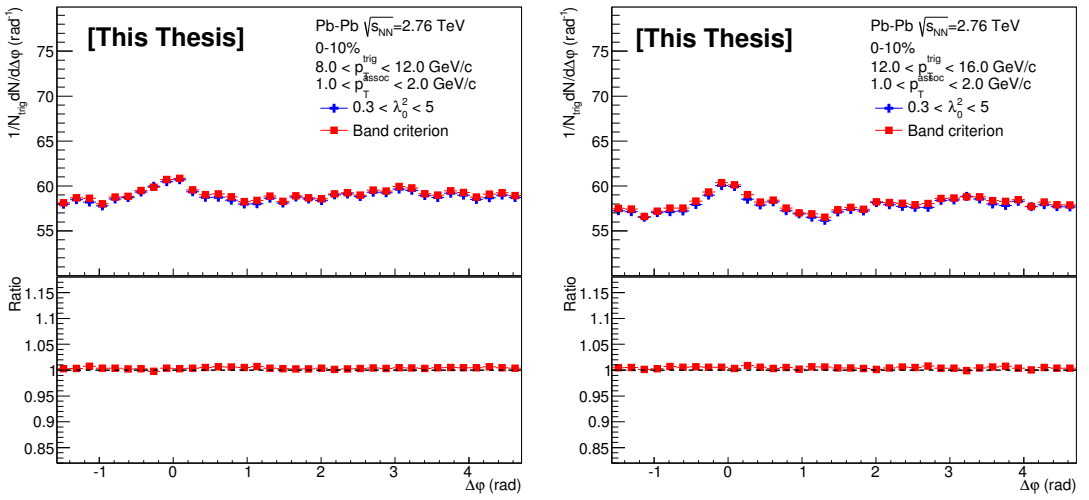

Figure 6.43: Comparison of the azimuthal distributions for two different shower shape cuts ($(\lambda^2_{0,min} < \lambda^2_0 < \lambda^2_{0,max}$ as Eq. 6.2 and $0.3 < \lambda^2_0 < 5$) in trigger p_{T} at $8.0 < p_{\mathrm{T}}^{\mathrm{trig}} < 12.0$ GeV/c and $12.0 < p_{\mathrm{T}}^{\mathrm{trig}} < 16.0$ GeV/c in Pb+Pb 0-10% at $\sqrt{s_{\mathrm{NN}}} = 2.76$ TeV.

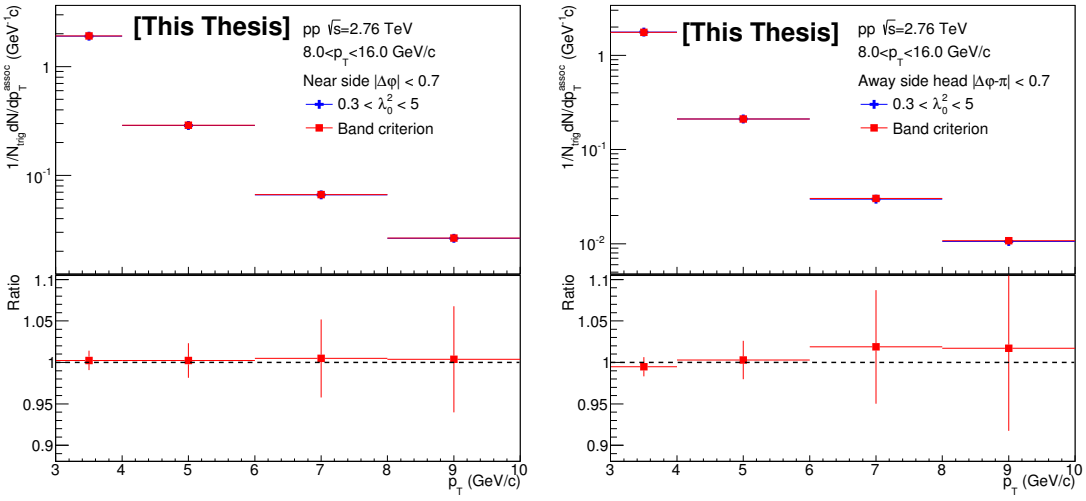

Figure 6.44: Comparison of the per-trigger yields for two different shower shape cuts ($(\lambda^2_{0,min} < \lambda^2_0 < \lambda^2_{0,max}$ as Eq. 6.2 and $0.3 < \lambda^2_0 < 5$) in trigger p_{T} at $8.0 < p_{\mathrm{T}}^{\mathrm{trig}} < 16.0$ GeV/c in Pb+Pb 0-10% at $\sqrt{s_{\mathrm{NN}}} = 2.76$ TeV.

$8.0 < p_{\mathrm{T}}^{\mathrm{trig}} < 12.0$ GeV/c and $12.0 < p_{\mathrm{T}}^{\mathrm{trig}} < 16.0$ GeV/c with $1.0 < p_{\mathrm{T}}^{\mathrm{assoc}} < 2.0$ GeV/c, and Fig. 6.46 shows the comparison of the per-trigger yields with π^0 trigger at $8.0 < p_{\mathrm{T}}^{\mathrm{trig}} < 16.0$ GeV/c in three $\Delta\varphi$ regions in pp collisions at $\sqrt{s} = 2.76$ TeV.

- **Pb+Pb analysis**: As baseline, the cut on the reconstructed π^0 invariant mass window is is $mean - 3\sigma < M_{\gamma\gamma} < mean + 3\sigma$, where $mean$ and σ are defined in Eq. 6.3. To estimate the uncertainty introduced by this cut, a changed π^0 invariant mass window, $mean - 2.5\sigma < M_{\gamma\gamma} < mean + 2.5\sigma$, is used. The comparison of the azimuthal correlations between the two different cuts is shown in Fig. 6.47 for $8.0 < p_{\mathrm{T}}^{\mathrm{trig}} < 12.0$ GeV/c and $12.0 < p_{\mathrm{T}}^{\mathrm{trig}} < 16.0$ GeV/c with $1.0 < p_{\mathrm{T}}^{\mathrm{assoc}} < 2.0$ GeV/c, and Fig. 6.48 shows the comparison of per-trigger yields in the two different π^0 invariant mass window selections with π^0 trigger at $8.0 < p_{\mathrm{T}}^{\mathrm{trig}} < 16.0$ GeV/c in three $\Delta\varphi$ regions at 0-10% in Pb+Pb collisions at $\sqrt{s_{\mathrm{NN}}} = 2.76$ TeV.

6.5.3 Track cuts

- **pp analysis**:
  As baseline, the cut on the associated tracks are selected by Hybrid cuts. To estimate the uncertainty introduced by this cut, the TPC-Only track cuts are used. Fig. 6.49 shows the comparison of the azimuthal correlations in the two

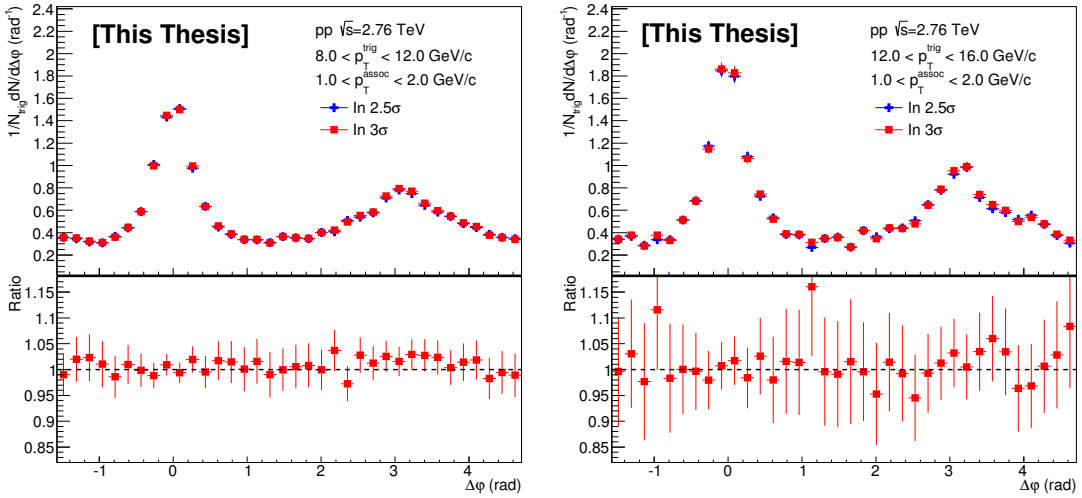

Figure 6.45: Comparison of the azimuthal distributions for two different π^0 invariant mass window selections ($mean \pm 3\sigma$ and $mean \pm 2.5\sigma$) in trigger p_{T} at $8.0 < p_{\mathrm{T}}^{\mathrm{trig}} < 12.0$ GeV/c and $12.0 < p_{\mathrm{T}}^{\mathrm{trig}} < 16.0$ GeV/c in pp collisions at $\sqrt{s} = 2.76$ TeV.

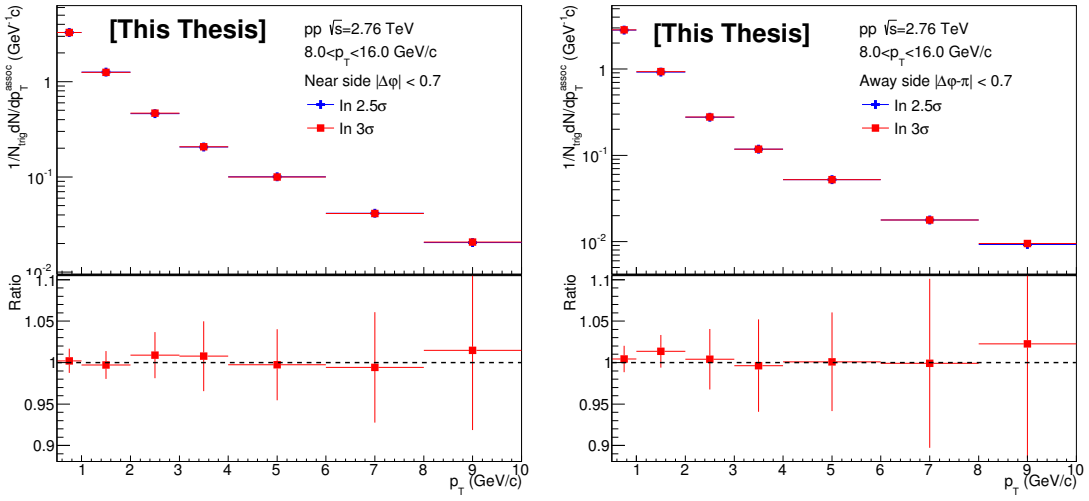

Figure 6.46: Comparison of the per-trigger yields for two different π^0 invariant mass window selections ($mean \pm 3\sigma$ and $mean \pm 2.5\sigma$) in trigger p_{T} at $8.0 < p_{\mathrm{T}}^{\mathrm{trig}} < 16.0$ GeV/c in pp collisions at $\sqrt{s} = 2.76$ TeV.

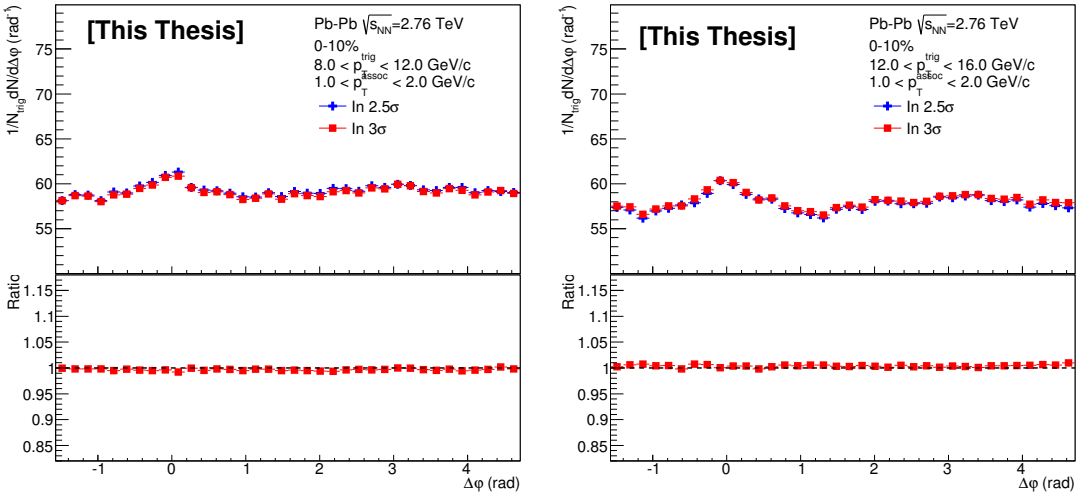

Figure 6.47: Comparison of the azimuthal distributions for two different π^0 invariant mass window selections ($mean \pm 3\sigma$ and $mean \pm 2.5\sigma$) in trigger p_{T} at $8.0 < p_{\mathrm{T}}^{\mathrm{trig}} < 12.0$ GeV/c and $12.0 < p_{\mathrm{T}}^{\mathrm{trig}} < 16.0$ GeV/c in Pb+Pb 0-10% at $\sqrt{s_{\mathrm{NN}}} = 2.76$ TeV.

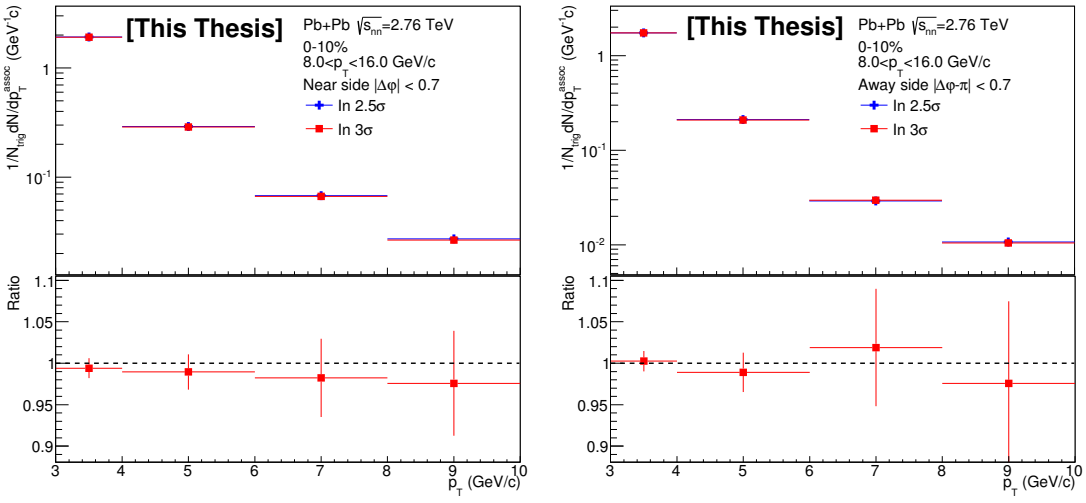

Figure 6.48: Comparison of the per-trigger yields for two different π^0 invariant mass window selections ($mean \pm 3\sigma$ and $mean \pm 2.5\sigma$) in trigger p_{T} at $8.0 < p_{\mathrm{T}}^{\mathrm{trig}} < 16.0$ GeV/c at 0-10% in Pb+Pb 0-10% at $\sqrt{s_{\mathrm{NN}}} = 2.76$ TeV.

different track cuts for $8.0 < p_{\mathrm{T}}^{\mathrm{trig}} < 12.0$ GeV/c and $12.0 < p_{\mathrm{T}}^{\mathrm{trig}} < 16.0$ GeV/c with $1.0 < p_{\mathrm{T}}^{\mathrm{assoc}} < 2.0$ GeV/c, and Fig. 6.50 shows the comparison of per-trigger yields in the two different track cut selections with π^0 trigger at $8.0 < p_{\mathrm{T}}^{\mathrm{trig}} < 16.0$ GeV/c.

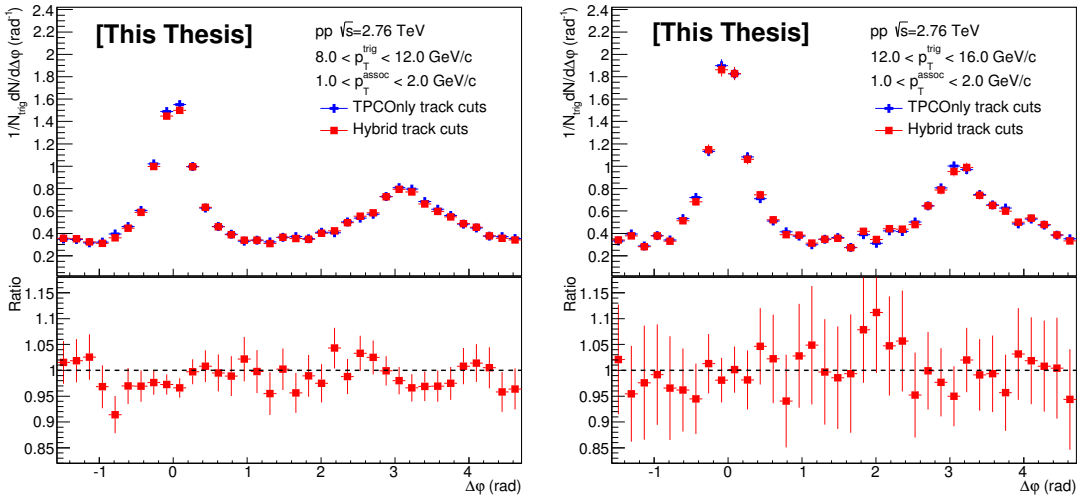

Figure 6.49: Comparison of the azimuthal distributions for two different track cuts (Hybrid track cuts and TPC-Only track cuts) in trigger p_{T} at $8.0 < p_{\mathrm{T}}^{\mathrm{trig}} < 12.0$ GeV/c and $12.0 < p_{\mathrm{T}}^{\mathrm{trig}} < 16.0$ GeV/c in pp at $\sqrt{s} = 2.76$ TeV.

- **Pb+Pb analysis**:
  As baseline, the cut on the associated tracks are selected by Hybrid cuts. To estimate the uncertainty introduced by this cut, the TPC-Only track cuts are used. Fig. 6.51 shows the comparison of the azimuthal correlations in the two different track cuts for $8.0 < p_{\mathrm{T}}^{\mathrm{trig}} < 12.0$ GeV/c and $12.0 < p_{\mathrm{T}}^{\mathrm{trig}} < 16.0$ GeV/c with $1.0 < p_{\mathrm{T}}^{\mathrm{assoc}} < 2.0$ GeV/c, and Fig. 6.54 shows the comparison of per-trigger yields in the two different different track cuts with π^0 trigger at $8.0 < p_{\mathrm{T}}^{\mathrm{trig}} < 16.0$ GeV/c.

6.5.4 Tracking efficiency and contamination

In the analysis, the Hybrid track cuts are used to select the tracks. To estimate this track selection systematic uncertainty in tracking efficiency and contamination. Some main setting in Hybrid track cuts are changed, and results from different cuts are compared. Four changes are set as: a) Standard cuts; b) and c) tighter and looser cuts w.r.t the standard cuts; and d) the ratio of the number of found over findable clusters as well as its tighter and looser cuts in e) and f) (Only in Pb+Pb).

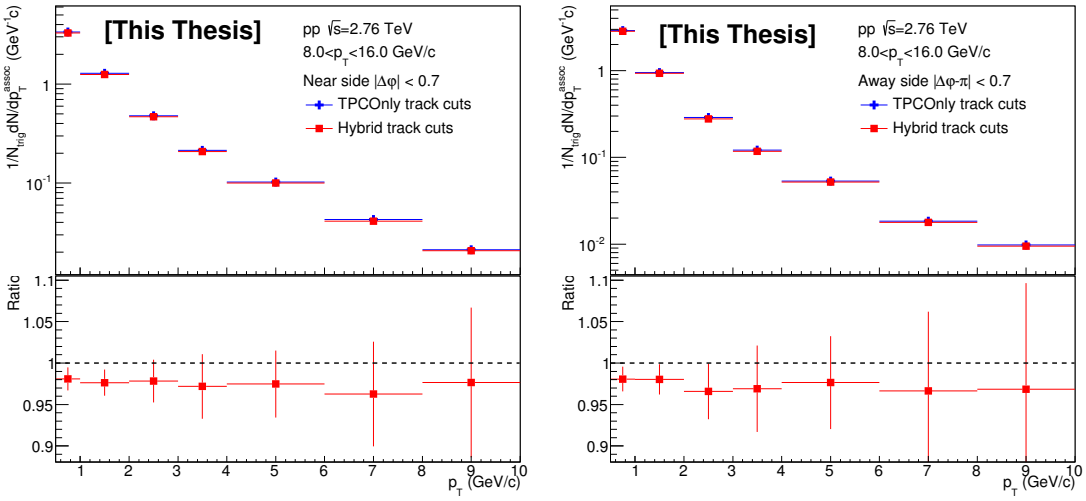

Figure 6.50: Comparison of the per-trigger yields for two different track cuts (Hybrid track cuts and TPC-Only track cuts) in trigger p_{T} at $8.0 < p_{\mathrm{T}}^{\mathrm{trig}} < 16.0$ GeV/c in pp at $\sqrt{s} = 2.76$ TeV.

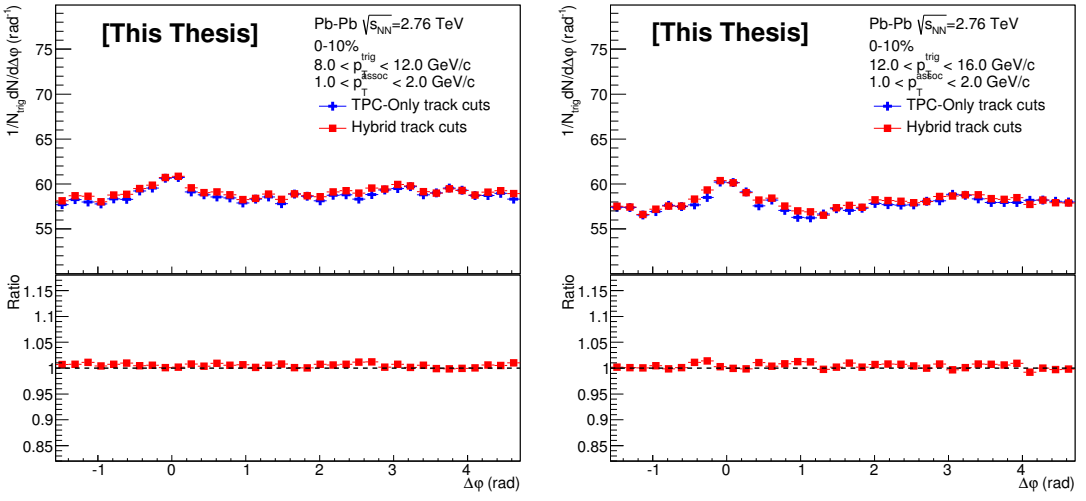

Figure 6.51: Comparison of the azimuthal distributions for two different track cuts (TPC-Only track cuts and Hybrid track cuts) in trigger p_{T} at $8.0 < p_{\mathrm{T}}^{\mathrm{trig}} < 12.0$ GeV/c and $12.0 < p_{\mathrm{T}}^{\mathrm{trig}} < 16.0$ GeV/c in Pb+Pb 0-10% at $\sqrt{s_{\mathrm{NN}}} = 2.76$ TeV.

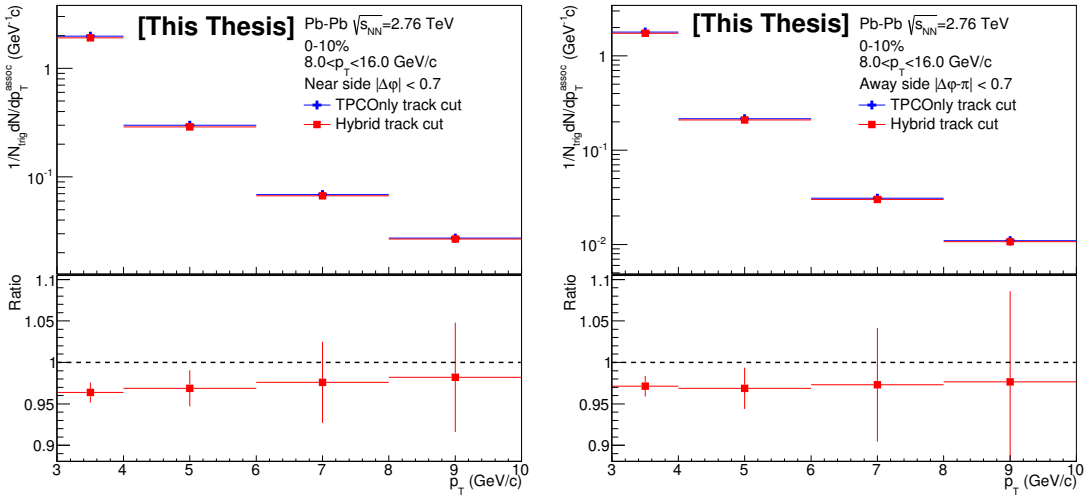

Figure 6.52: Comparison of the per-trigger yields for two different track cuts (Hybrid track cuts and TPC-Only track cuts) in trigger p_{T} at $8.0 < p_{\mathrm{T}}^{\mathrm{trig}} < 16.0$ GeV/c at 0-10% in Pb+Pb collisions at $\sqrt{s_{\mathrm{NN}}} = 2.76$ TeV.

Since the Hybrid track cuts in LHC11a pp data and LHC11h Pb+Pb data are a little different, therefore, the changed details are summarized in the following.

- **pp analysis**

  Tab. 6.9 summarizes the selection in pp data, only mentioned the cuts which are different w.r.t. the standard selection: Fig. 6.53 shows the difference from

cut	a)	b)	c)	d)
Number of clusters	70	80	60	–
Chi2/cluster	4	3	5	–
d_{xy} (cm)	2.4	1.9	2.9	2.4
d_z (cm)	3.2	2.7	3.7	3.2
Crossed rows	–	–	–	70
Crossed rows/findable clusters	–	–	–	0.8

Table 6.9: Summary of changed settings in Hybrid track cuts for tracking efficiency and contamination systematic uncertainties calculation in pp at $\sqrt{s}$ =2.76 TeV.

  different setting used in tracking efficiency and contamination.

- **Pb+Pb analysis**

  Tab. 6.10 summarizes the selection in Pb+Pb data, only mentioned the cuts which are different w.r.t. the standard selection:

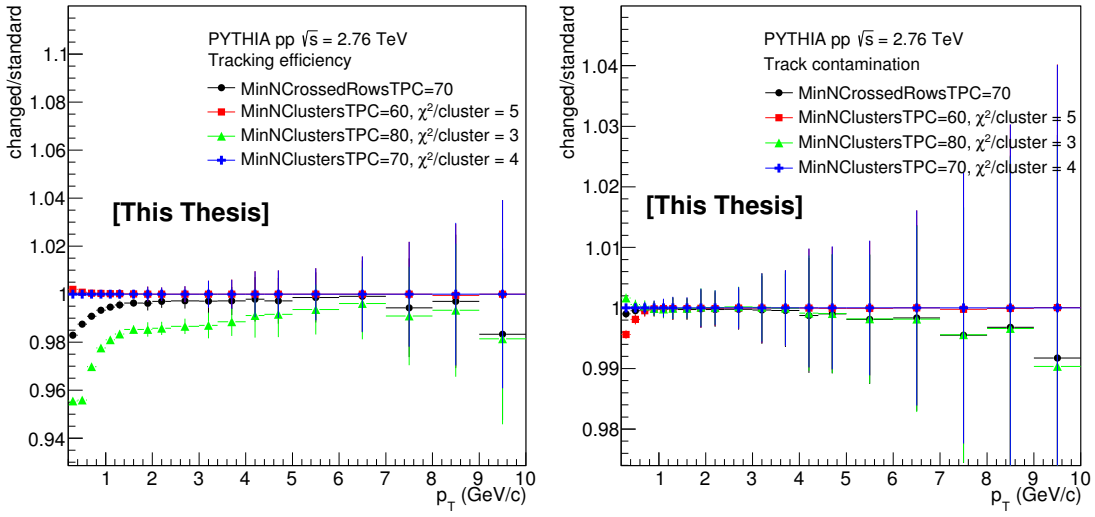

Figure 6.53: Comparison of tracking efficiency (left) and contamination (right) among different changed settings in Hybrid track cuts in LHC12a15a simulation for pp at $\sqrt{s} = 2.76$ TeV.

cut	a)	b)	c)	d)	e)	f)
Number of clusters	50	60	40	–	–	–
d_{xy} (cm)	2.4	1.9	2.9	2.4	2.9	1.7
d_z (cm)	3.2	2.7	3.7	3.2	3.7	2.7
Chi2perClusterTPC	4	3	5	4	5	3
Chi2perClusterITS	36	25	49	36	49	25
Chi2TPCConstrainedGlobal	36	25	49	36	49	25
FractionSharedTPCClusters	0.4	0.2	1	0.4	1	0.2
Crossed rows	–	–	–	70	60	80
Crossed rows/findable clusters	–	–	–	0.8	0.7	0.9

Table 6.10: Summary of changed settings in Hybrid track cuts for tracking efficiency and contamination systematic uncertainties calculation in Pb+Pb at $\sqrt{s_{\rm NN}} = 2.76$ TeV.

Fig. 6.54 shows the difference from different setting used in tracking efficiency and contamination.

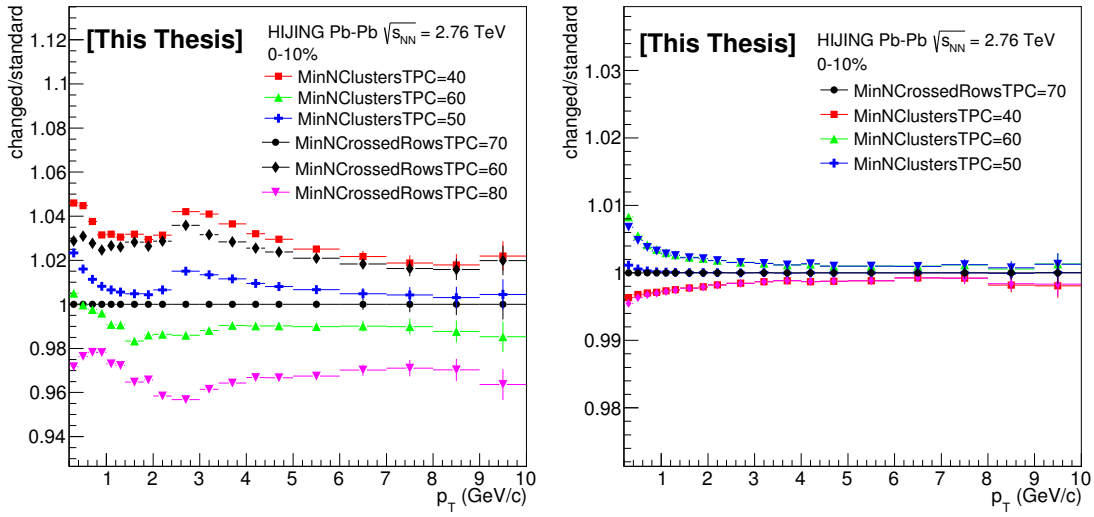

Figure 6.54: Comparison of tracking efficiency (left) and contamination (right) among different changed settings in Hybrid track cuts in LHC12a17d_fix simulation for Pb+Pb 0-10% at $\sqrt{s_{\mathrm{NN}}}$ = 2.76 TeV.

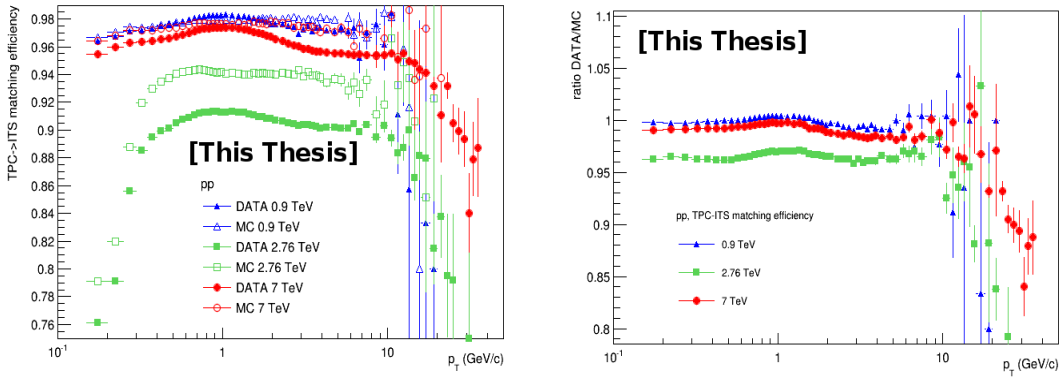

Figure 6.55: Left: TPC+ITS matching efficiency in data as well as corresponding to simulation in pp. Right: TPC+ITS matching efficiency ratio in data to simulation in pp. The plots are taken from [307]

Besides the systematic uncertainty from track selections, another part of the total systematic uncertainty is from the tracking efficiency by comparing the difference in the matching efficiency between data and MC. The matching efficiency is defined as a ratio of the number of tracks reconstructed in the TPC and ITS detectors to the number of tracks reconstructed using TPC stand-alone (TPC+ITS/TPC stand-alone) determined as a function of p_{T} in MC and data. This method is based on

assumption that the TPC is fully efficient for the tracks selected in this analysis. In fact, the method checks the overall efficiency (tracking efficiency and acceptance) of the ITS, the quality of space point calibration in the TPC, and the quality of alignment of the TPC and the ITS detectors. The systematic uncertainty on tracking efficiency is 3% in pp and 5% in Pb+Pb. The results are shown in Fig. 6.55 in pp and Fig. 6.56 in Pb+Pb. More analysis details and results can be found in [307].

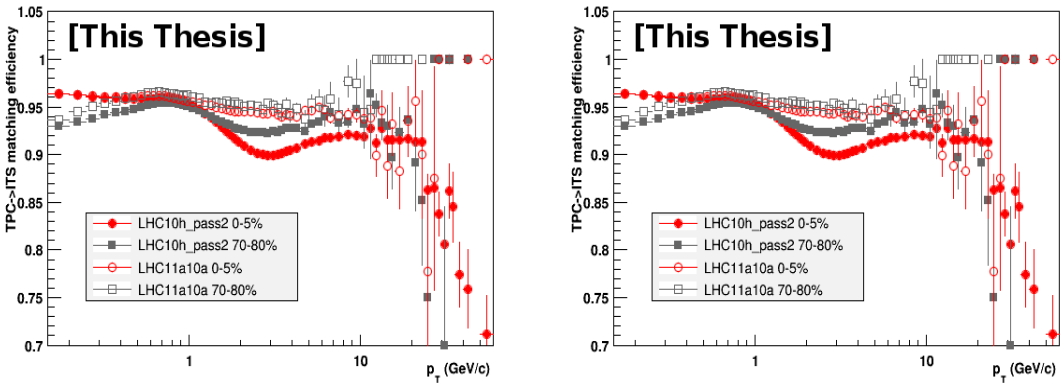

Figure 6.56: Left: TPC+ITS matching efficiency in data as well as corresponding to simulation in Pb+Pb. Right: TPC+ITS matching efficiency ratio in data to simulation in Pb+Pb. The plots are taken from [307]

6.5.5 Summary of systematic uncertainties

The relative systematic uncertainty to a given source is estimated as:

$$\varepsilon = \frac{\sigma}{Y^{\text{standard}}(\Delta\varphi, p_{\text{T}}^{trig}, p_{\text{T}}^{assoc})} = \frac{|\max(Y_i(\Delta\varphi, p_{\text{T}}^{trig}, p_{\text{T}}^{assoc}) - Y^{\text{standard}}(\Delta\varphi, p_{\text{T}}^{trig}, p_{\text{T}}^{assoc}))|}{Y^{\text{standard}}(\Delta\varphi, p_{\text{T}}^{trig}, p_{\text{T}}^{assoc})} \tag{6.15}$$

To calculate the total systematic uncertainty, we use standard error propagation. The total systematic uncertainty includes correction factor systematic uncertainties and changed cut systematic uncertainties. Firstly, calculate the total correction factor systematic uncertainty which includes pedestal subtraction in per-trigger yields . For simplicity, correction procedure Eq. 6.14 is rewritten as:

$$Y^{corrected} = \frac{y^{raw} * P_{pair} * (1 - C_{h^{\pm}})}{\epsilon_{\pi^0} * \epsilon_{h^{\pm}} * R_{pair}} \tag{6.16}$$

where y^{raw} is the raw distribution extracted from data, P_{pair} is the pair purity correction factor, R_{pair} is the pair resolution correction factor, $C_{h^{\pm}}$ is the track contamination correction factor, ϵ_{π^0} is the π^0 efficiency correction factor and $\epsilon_{h^{\pm}}$ is

the tracking efficiency. The relative systematic uncertainty of them therefore can be written as:

$$\frac{\delta Y^{corrected}}{Y^{corrected}} = \sqrt{(\frac{\delta y^{raw}}{y^{raw}})^2 + (\frac{\delta P_{pair}}{P_{pair}})^2 + (\frac{\delta R_{pair}}{R_{pair}})^2 + (\frac{\delta C_{h^{\pm}}}{C_{h^{\pm}}})^2 + (\frac{\delta \epsilon_{\pi^0}}{\epsilon_{\pi^0}})^2 + (\frac{\delta \epsilon_{h^{\pm}}}{\epsilon_{h^{\pm}}})^2} \tag{6.17}$$

Except for δy^{raw}, the other δ_i is the correction factor systematic uncertainty. The δy^{raw} is only formed in per-trigger yield by pedestal subtraction.

Secondly, calculate the total systematic uncertainty from three main changed cuts, cluster shower shape cut, π^0 invariant mass window cut and track selection cut, in the analysis. It can be calculated as:

$$\delta Y^{cut} = \sqrt{(\delta Y^{SScut})^2 + (\delta Y^{Masscut})^2 + (\delta Y^{Trackcut})^2} \tag{6.18}$$

At last, the full total systematic uncertainty is obtained by combining the total correction factor systematic uncertainty and the total changed cut systematic uncertainty as:

$$\delta Y^{total} = \sqrt{(\delta Y^{corrected})^2 + (\delta Y^{cut})^2} \tag{6.19}$$

The systematic uncertainty of each source for the per-trigger yield on near side, away side in pp and 0-10% Pb+Pb are shown in Fig. 6.57 and Fig. 6.58, respectively.

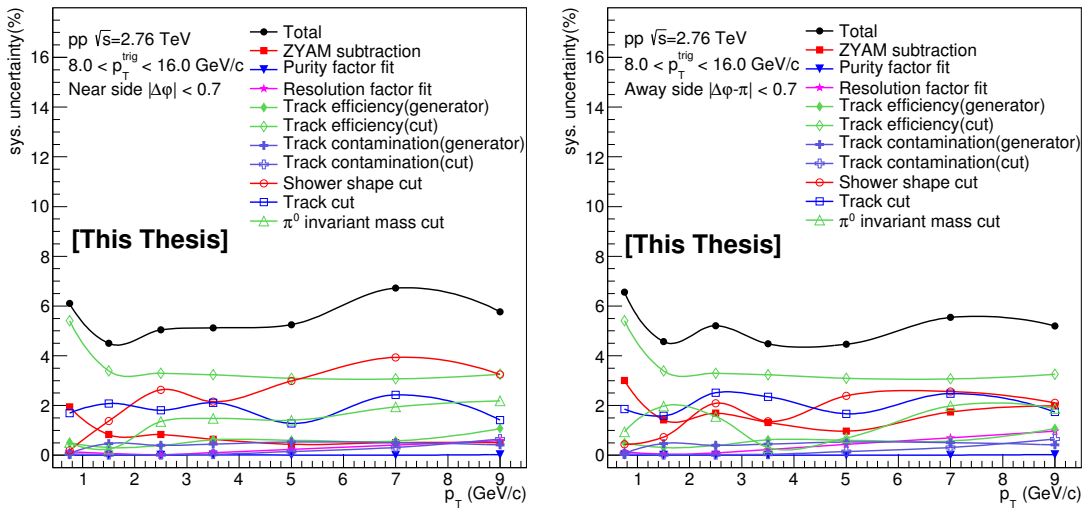

Figure 6.57: Systematic uncertainties for the per-trigger yield on the near side (left), away side (right) for trigger p_{T} at $8.0 < p_{\mathrm{T}}^{\mathrm{trig}} < 16.0$ GeV/c in pp at $\sqrt{s} = 2.76$ TeV.

The systematic uncertainties in azimuthal correlations and per-trigger yields in pp and Pb+Pb at 0-10% at $\sqrt{s_{\mathrm{NN}}} = 2.76$ TeV are summarized in Tab. 6.11. In

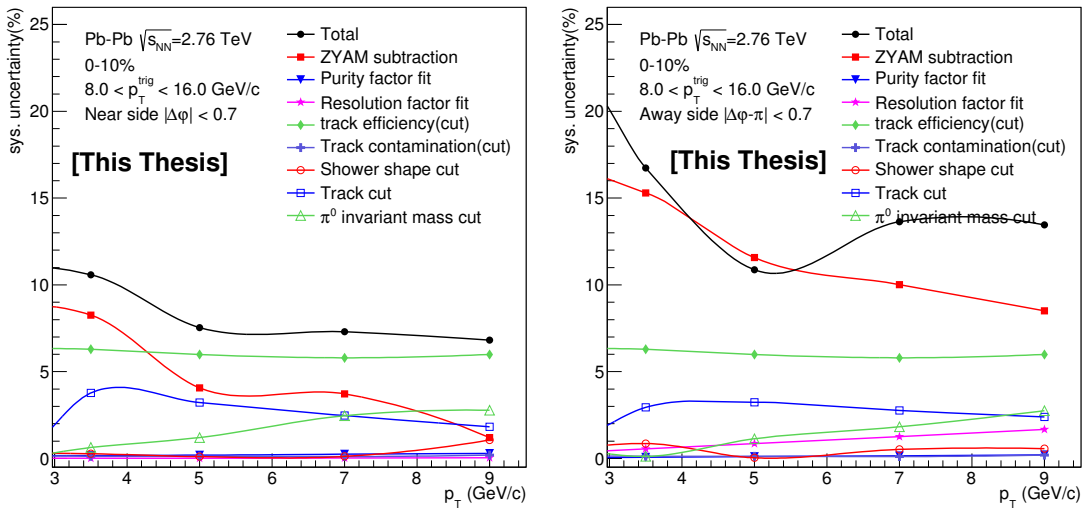

Figure 6.58: Systematic uncertainties for the per-trigger yield on the near side (left), away side (right) for trigger p_{T} at $8.0 < p_{\mathrm{T}}^{\mathrm{trig}} < 16.0$ GeV/c in Pb+Pb 0-10%at $\sqrt{s_{\mathrm{NN}}} = 2.76$ TeV.

	pp		Pb+Pb 0-10%	
source	$Y(\Delta\varphi)$	$Y(p_{\mathrm{T}})$	$Y(\Delta\varphi)$	$Y(p_{\mathrm{T}})$
Pair purity fit	$< 0.3\%$	$< 0.03\%$	$< 1.1\%$	$< 0.5\%$
Pair resolution fit	$< 1.0\%$	$< 0.2\%$	$< 1.1\%$	$< 2.0\%$
π^0 efficiency	–	–	–	–
Tracking efficiency (generator)	$< 1.0\%$	$< 1.0\%$	–	–
Tracking efficiency (cut)	$< 5.5\%$	$< 5.5\%$	$< 6.5\%$	$< 6.5\%$
Track contamination (generator)	$< 0.5\%$	$< 0.5\%$	–	–
Track contamination (cut)	$< 0.5\%$	$< 0.5\%$	$< 0.9\%$	$< 0.9\%$
Shower shape cut	$< 1.2\%$	$< 2.5\%$	$< 0.7\%$	$< 2.0\%$
Invariant mass window	$< 1.3\%$	$< 2.0\%$	$< 1.0\%$	$< 2.5\%$
Track cut	$< 1.0\%$	$< 2.5\%$	$< 3.5\%$	$< 4.0\%$
Pedestal subtraction	–	$< 3.0\%$	–	$< 17.0\%$
Total	$< 6.5\%$	$< 7.0\%$	$< 7.5\%$	$< 21.0\%$

Table 6.11: Summary of systematic uncertainties for the azimuthal correlations and per-trigger yields in pp and 0-10% Pb+Pb.

Tab. 6.11, the total systematic uncertainty of per-trigger yields of charged hadrons is only the results of flat background subtraction. If subtracting the flow contribution, another systematic uncertainty of 8% from the flow of charged poins and charged hadrons needs to be considered.

6.6 Results

In this section, the corrected results for the azimuthal correlations and per-trigger yields are shown.

6.6.1 Azimuthal correlations

6.6.1.1 pp collisions results

Fig. 6.59 and Fig. 6.60 show the azimuthal correlations for π^0 trigger p_{T} bins at $8.0 < p_{\mathrm{T}}^{\mathrm{trig}} < 12.0$ GeV/c and $12.0 < p_{\mathrm{T}}^{\mathrm{trig}} < 16.0$ GeV/c with four associated hadrons p_{T} bins ($0.5 < p_{\mathrm{T}}^{\mathrm{assoc}} < 1.0$ GeV/c, $1.0 < p_{\mathrm{T}}^{\mathrm{assoc}} < 2.0$ GeV/c, $2.0 < p_{\mathrm{T}}^{\mathrm{assoc}} < 4.0$ GeV/c, $4.0 < p_{\mathrm{T}}^{\mathrm{assoc}} < 6.0$ GeV/c) in pp collisions at $\sqrt{s} = 2.76$ TeV, respectively. The shown results are obtained without subtraction underly event contributions.

6.6.1.2 Pb+Pb collisions results

Fig. 6.61 shows the azimuthal correlations for π^0 trigger p_{T} bins at $8.0 < p_{\mathrm{T}}^{\mathrm{trig}} < 12.0$ GeV/c and $12.0 < p_{\mathrm{T}}^{\mathrm{trig}} < 16.0$ GeV/c with two associated hadrons p_{T} bins $1.0 < p_{\mathrm{T}}^{\mathrm{assoc}} < 2.0$ GeV/c, $2.0 < p_{\mathrm{T}}^{\mathrm{assoc}} < 4.0$ GeV/c) at 0-10% centrality in Pb+Pb collisions at $\sqrt{s_{\mathrm{NN}}} = 2.76$ TeV. The results are obtained without subtraction underlying event contributions, and flow has not been subtracted either.

6.6.2 Integrated per-trigger yield

6.6.2.1 pp collisions results

Fig. 6.62 shows the per-trigger yield of charged hadrons on near side, away side in pp at $\sqrt{s} = 2.76$ TeV.

Fig. 6.63 shows the same results of the per-trigger yield of charged hadrons on near side, away side in pp at $\sqrt{s} = 2.76$ TeV as Fig. 6.62, but in one figure.

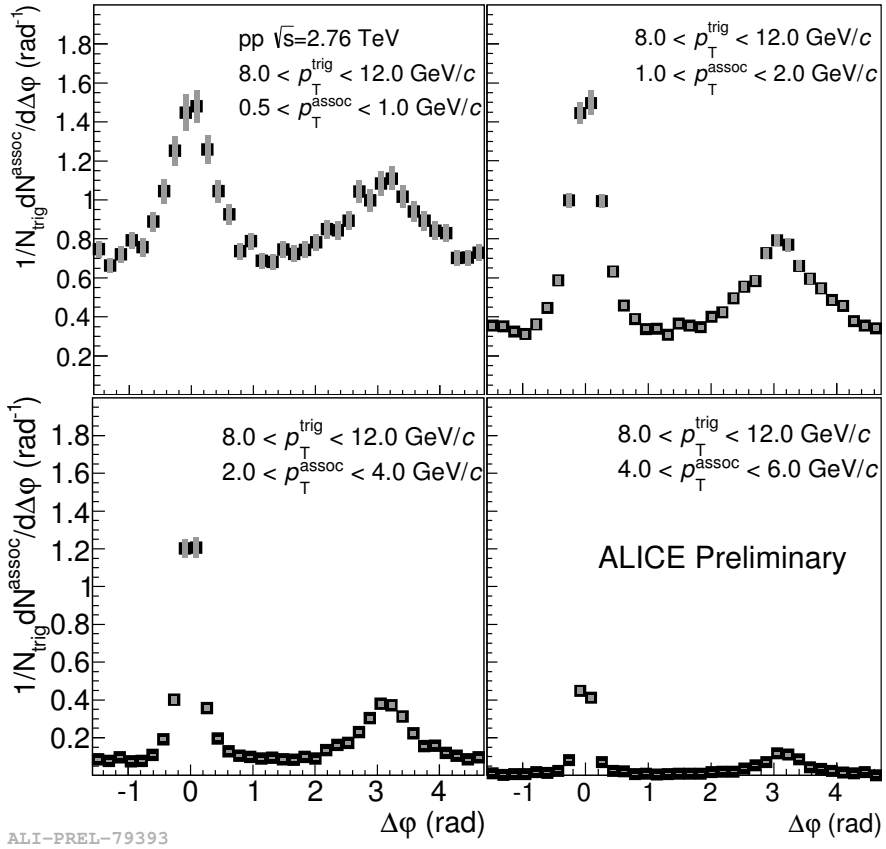

Figure 6.59: Azimuthal correlations for trigger p_{T} at $8.0 < p_{\mathrm{T}}^{\mathrm{trig}} < 12.0$ GeV/c and associated hadrons p_{T} at $0.5 < p_{\mathrm{T}}^{\mathrm{assoc}} < 1.0$ GeV/c, $1.0 < p_{\mathrm{T}}^{\mathrm{assoc}} < 2.0$ GeV/c, $2.0 < p_{\mathrm{T}}^{\mathrm{assoc}} < 4.0$ GeV/c, $4.0 < p_{\mathrm{T}}^{\mathrm{assoc}} < 6.0$ GeV/c in pp at $\sqrt{s} = 2.76$ TeV. The blue boxes are the total systematic uncertainty.

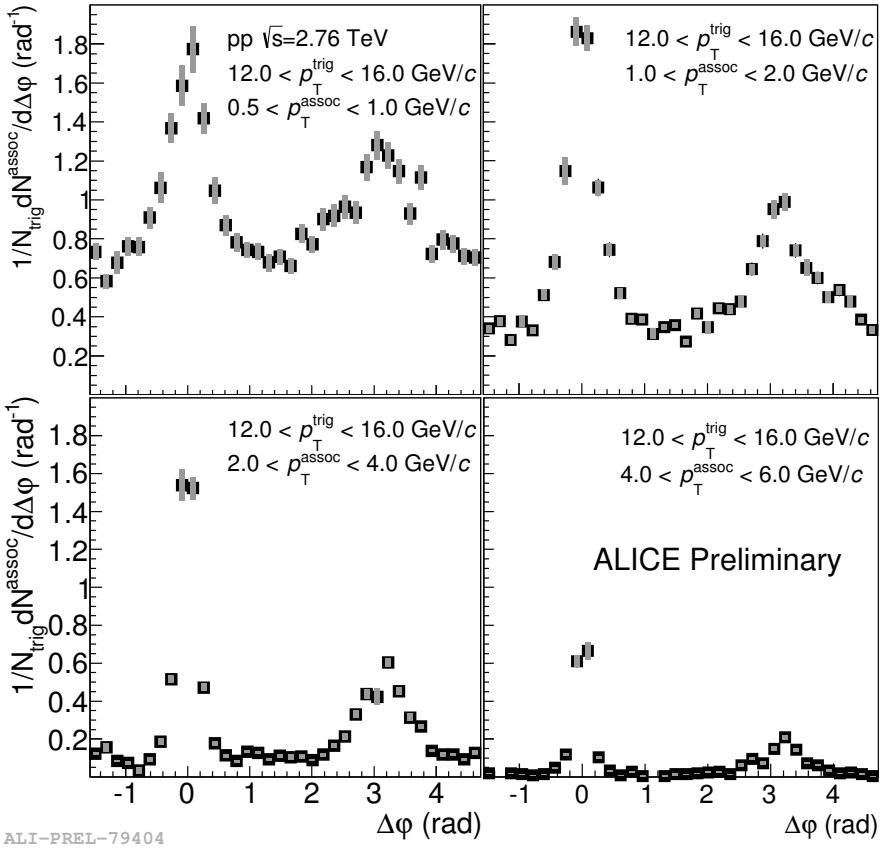

Figure 6.60: Azimuthal correlations for trigger p_{T} at $12.0 < p_{\mathrm{T}}^{\mathrm{trig}} < 16.0$ GeV/c and associated hadrons p_{T} at $0.5 < p_{\mathrm{T}}^{\mathrm{assoc}} < 1.0$ GeV/c, $1.0 < p_{\mathrm{T}}^{\mathrm{assoc}} < 2.0$ GeV/c, $2.0 < p_{\mathrm{T}}^{\mathrm{assoc}} < 4.0$ GeV/c, $4.0 < p_{\mathrm{T}}^{\mathrm{assoc}} < 6.0$ GeV/c in pp at $\sqrt{s} = 2.76$ TeV. The blue boxes are the total systematic uncertainty.

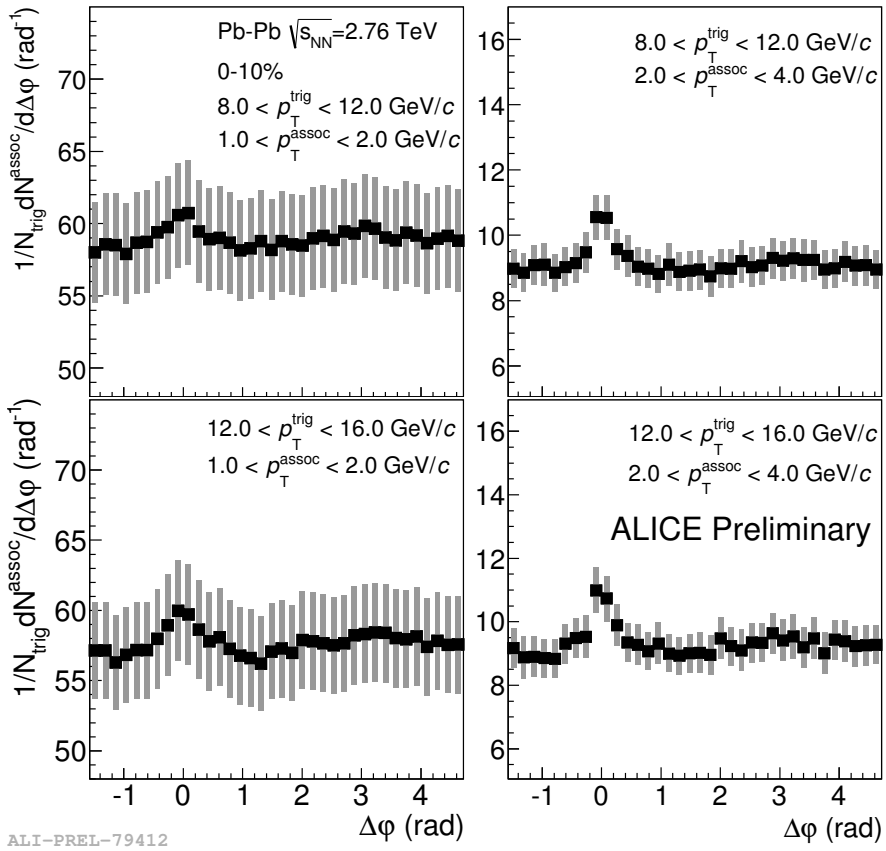

Figure 6.61: Corrected results of azimuthal distributions in trigger p_{T} at $8.0 < p_{\mathrm{T}}^{\mathrm{trig}} < 12.0$ GeV/c and $12.0 < p_{\mathrm{T}}^{\mathrm{trig}} < 16.0$ GeV/c, and associated hadrons p_{T} at $1.0 < p_{\mathrm{T}}^{\mathrm{assoc}} < 2.0$ GeV/c and $2.0 < p_{\mathrm{T}}^{\mathrm{assoc}} < 4.0$ GeV/c in Pb+Pb 0-10% at $\sqrt{s_{\mathrm{NN}}}$ =2.76 TeV. The blue boxes are the total systematic uncertainty.

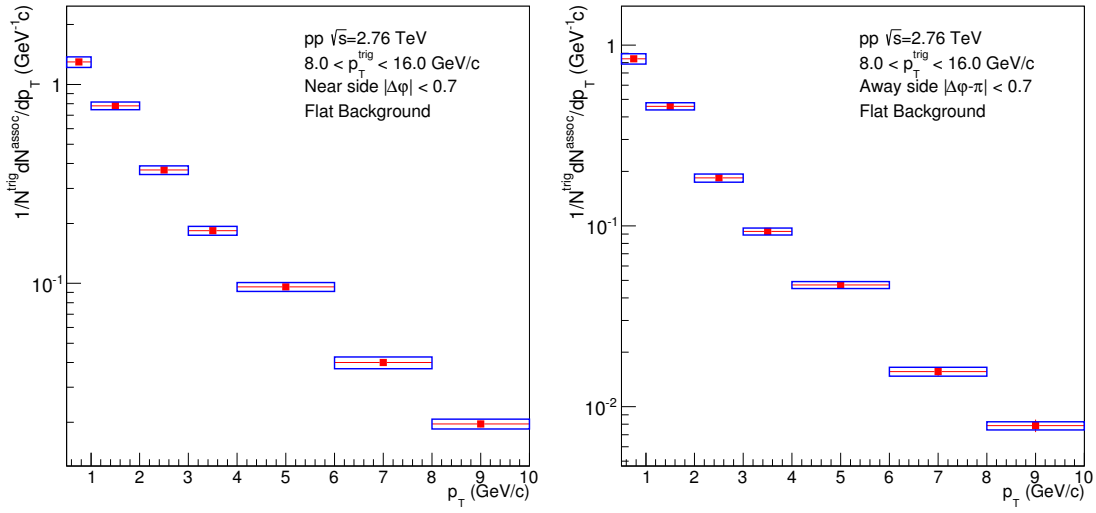

Figure 6.62: Per-trigger yield of charged hadrons on near side $|\Delta\varphi| < 0.7$ (left), away side $|\Delta\varphi - \pi| < 0.7$ (right) in trigger p_{T} at $8.0 < p_{\mathrm{T}}^{\mathrm{trig}} < 16.0$ GeV/c in pp at $\sqrt{s} = 2.76$ TeV. The blue boxes are the total systematic uncertainty.

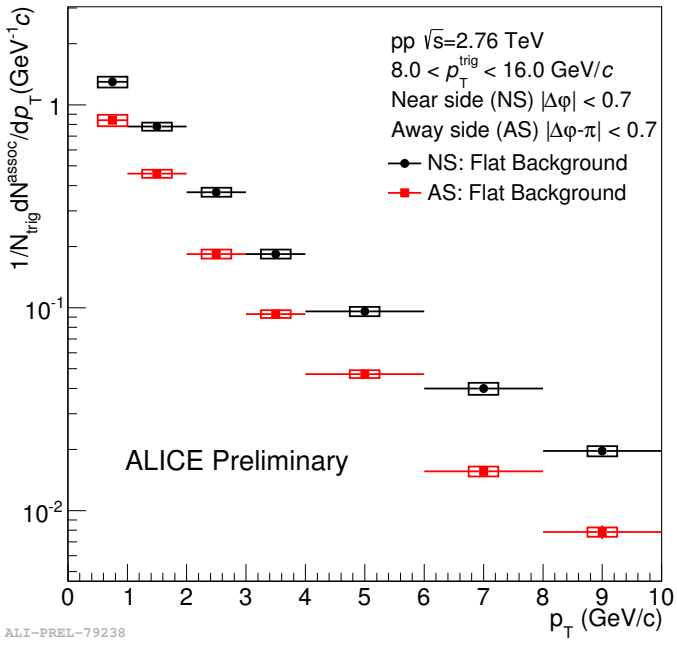

Figure 6.63: Per-trigger yield of charged hadrons on near side $|\Delta\varphi| < 0.7$ (black), away side $|\Delta\varphi - \pi| < 0.7$ (red) in trigger p_{T} at $8.0 < p_{\mathrm{T}}^{\mathrm{trig}} < 16.0$ GeV/c in pp at $\sqrt{s} = 2.76$ TeV. The boxes are the total systematic uncertainty.

6.6.2.2 Pb+Pb collisions results

Flat background:

Taking into account the flat background, the per-trigger yield of charged hadrons on near side, away side in in Pb+Pb collisions 0-10% centrality at $sNN = 2.76$ TeV are obtained, shown in Fig. 6.64.

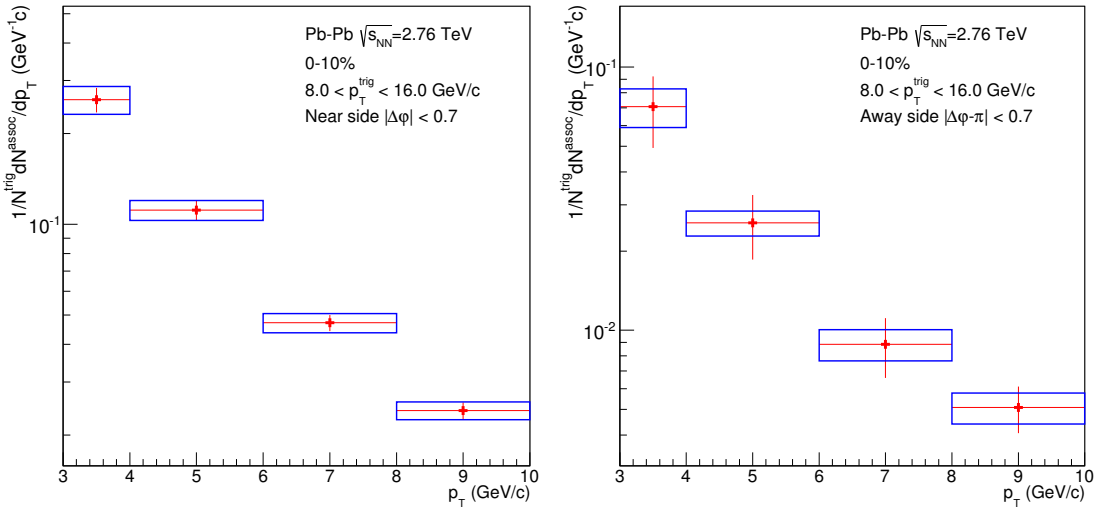

Figure 6.64: Per-trigger yield of charged hadrons distributions subtracted flat background on near side $|\Delta\varphi| < 0.7$ (left), away side $|\Delta\varphi - \pi| < 0.7$ (right) in trigger p_{T} at $8.0 < p_{\mathrm{T}}^{\mathrm{trig}} < 16.0$ GeV/c in Pb+Pb 0-10% at $\sqrt{s_{\mathrm{NN}}} = 2.76$ TeV. The blue boxes are the total systematic uncertainty.

Flow background:

Taking into account the background of flow, the per-trigger yield of charged hadrons on near side, away side in in Pb+Pb collisions 0-10% centrality at $\sqrt{s_{\mathrm{NN}}} = 2.76$ TeV are obtained, shown in Fig. 6.65.

Fig. 6.66 shows the same results of the per-trigger yield of charged hadrons on near side, away side in in Pb+Pb collisions 0-10% centrality at $\sqrt{s_{\mathrm{NN}}} = 2.76$ TeV as Fig. 6.64 and Fig. 6.65, but in one figure.

6.6.3 Yield modification factor

In this section, the yield modification factors, I_{AA} and I_{CP}, are calculated. The factors can be written as

$$I_{\mathrm{AA}}(p_{\mathrm{T}}^{\pi^0}, p_{\mathrm{T}}^{h^\pm}) = \frac{Y^{\mathrm{PbPb}}(p_{\mathrm{T}}^{\pi^0}, p_{\mathrm{T}}^{h^\pm})}{Y^{\mathrm{pp}}(p_{\mathrm{T}}^{\pi^0}, p_{\mathrm{T}}^{h^\pm})}; \tag{6.20}$$

$$I_{\mathrm{CP}}(p_{\mathrm{T}}^{\pi^0}, p_{\mathrm{T}}^{h^\pm}) = \frac{Y^{\mathrm{PbPb}}_{\mathrm{central}}(p_{\mathrm{T}}^{\pi^0}, p_{\mathrm{T}}^{h^\pm})}{Y^{\mathrm{PbPb}}_{\mathrm{peripheral}}(p_{\mathrm{T}}^{\pi^0}, p_{\mathrm{T}}^{h^\pm})} \tag{6.21}$$

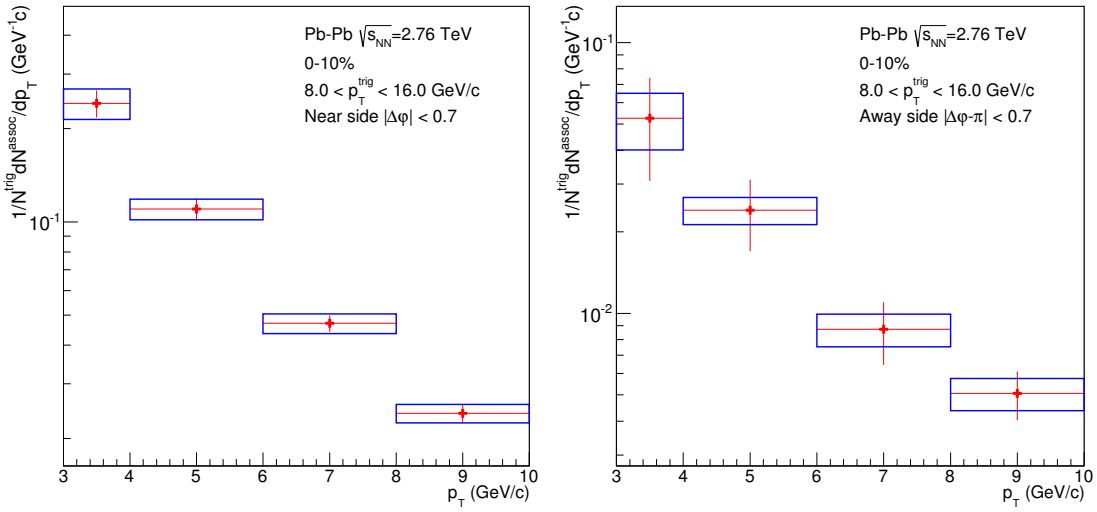

Figure 6.65: Per-trigger yield of charged hadrons distributions subtracted flow background on near side $|\Delta\varphi| < 0.7$ (left), away side $|\Delta\varphi - \pi| < 0.7$ (right) in trigger p_{T} at $8.0 < p_{\mathrm{T}}^{\mathrm{trig}} < 16.0$ GeV/c in Pb+Pb 0-10% at $\sqrt{s_{\mathrm{NN}}} = 2.76$ TeV. The blue boxes are the total systematic uncertainty.

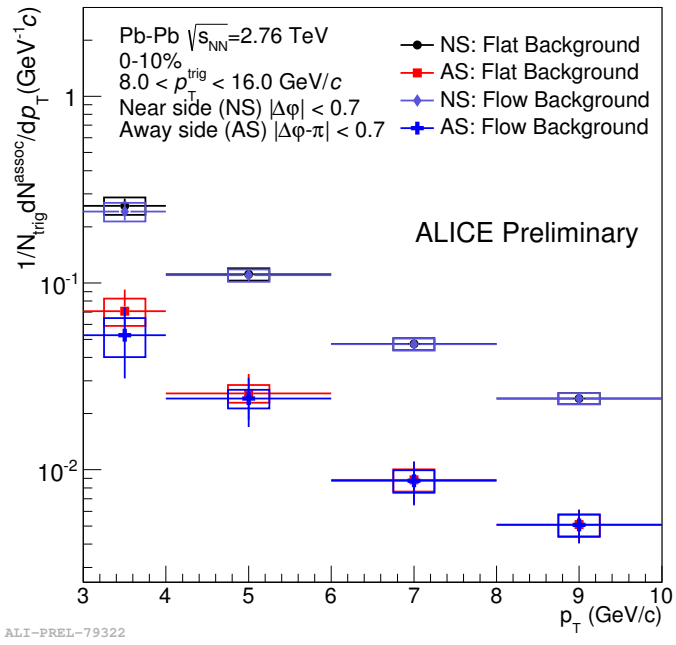

Figure 6.66: Per-trigger yield of charged hadrons on near side $|\Delta\varphi| < 0.7$ (full circle and full diamond), away side $|\Delta\varphi - \pi| < 0.7$ (full square and full cross) in trigger p_{T} at $8.0 < p_{\mathrm{T}}^{\mathrm{trig}} < 16.0$ GeV/c in Pb+Pb 0-10% at $\sqrt{s_{\mathrm{NN}}} = 2.76$ TeV. The boxes are the total systematic uncertainty.

Flat background:

Fig. 6.67 shows the modification factor, $I_{\rm AA}$, as a function of $p_{\rm T}$ on near side, away side in 0-10% Pb+Pb collisions. The results subtracted flat background from the π^0-hadron correlations are compared to the published similar results from hadron-hadron correlations [286]. The measurements of π^0-hadron correlations are good agreement with di-hadron correlations in all shown $p_{\rm T}$ range within the errors.

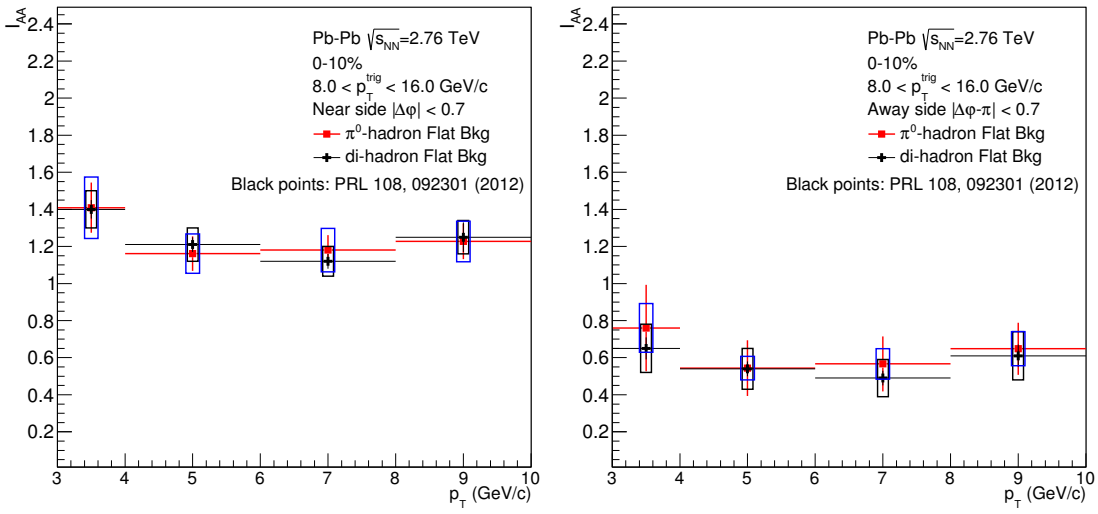

Figure 6.67: Considering the flat background in Pb+Pb, $I_{\rm AA}$ yield modification factors on near side $|\Delta\varphi| < 0.7$ (left), away side $|\Delta\varphi - \pi| < 0.7$ (right) in π^0-hadron correlations at $8.0 < p_{\rm T}^{\rm trig} < 16.0$ GeV/c (red). The blue boxes are the total systematic uncertainty. The black points and boxes are the $I_{\rm AA}$ results in hadron-hadron correlations.

Flow background:

Fig. 6.68 shows the modification factor, $I_{\rm AA}$, as a function of $p_{\rm T}$ on near side, away side in 0-10% Pb+Pb collisions. The results subtracted flow background from the π^0-hadron correlations are compared to the published similar results from hadron-hadron correlations [286]. The measurements of π^0-hadron correlations are good agreement with di-hadron correlations in all shown $p_{\rm T}$ range within the errors.

Fig. 6.69 shows the same modification factor, $I_{\rm AA}$, as a function of $p_{\rm T}$ on near side, away side in 0-10% Pb+Pb collisions as in Fig. 6.67 and Fig. 6.68. The reulsts subtracted flat and flow backgrounds from the π^0-hadron correlations are compared to the published similar results from hadron-hadron correlations [286].

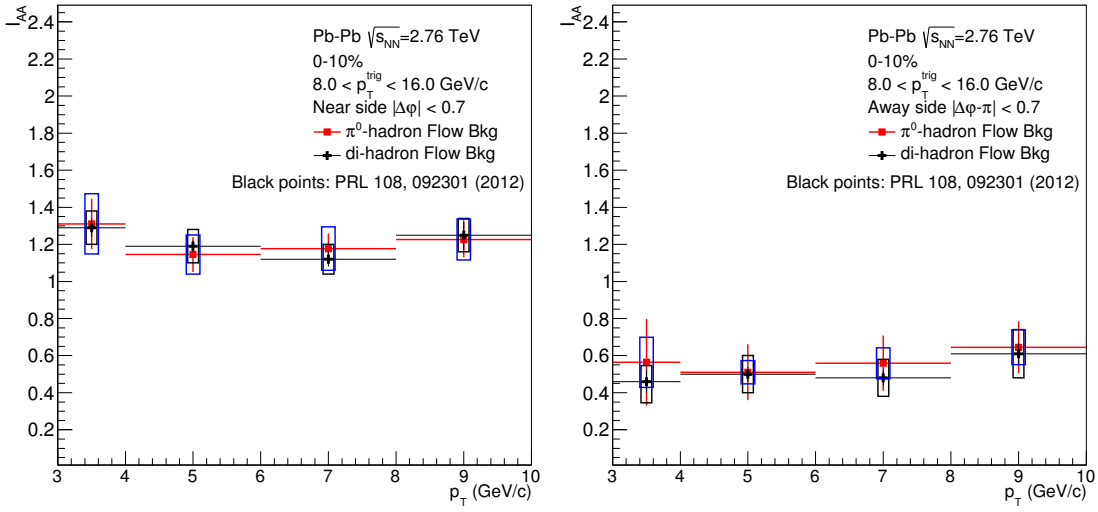

Figure 6.68: Considering the flow background in Pb+Pb, $I_{\rm AA}$ yield modification factors on near side $|\Delta\varphi| < 0.7$ (left), away side $|\Delta\varphi - \pi| < 0.7$ (right) in π^0-hadron correlations at $8.0 < p_{\rm T}^{\rm trig} < 16.0$ GeV/c (red). The blue boxes are the total systematic uncertainty. The black points and boxes are the $I_{\rm AA}$ results in hadron-hadron correlations.

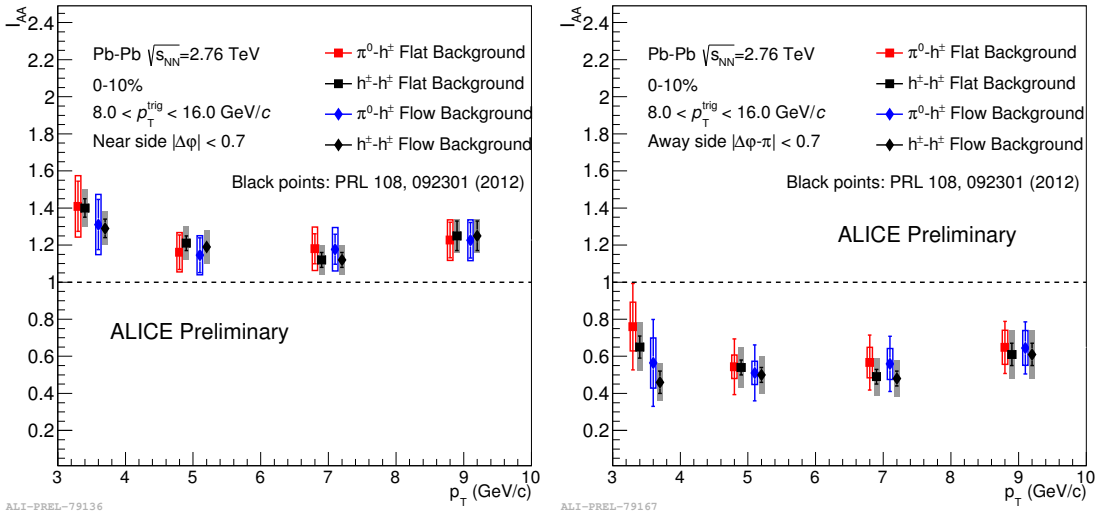

Figure 6.69: Considering the flat and flow backgrounds in Pb+Pb, $I_{\rm AA}$ yield modification factors on near side $|\Delta\varphi| < 0.7$ (left), away side $|\Delta\varphi - \pi| < 0.7$ (right) in π^0-hadron correlations at $8.0 < p_{\rm T}^{\rm trig} < 16.0$ GeV/c (red). The blue boxes are the total systematic uncertainty. The black points and gray boxes are the $I_{\rm AA}$ results in hadron-hadron correlations.

6.7 Summary

In this chapter, the π^0-hadron correlations are measured in pp and Pb+Pb collisions at a center-of-mass energy of $\sqrt{s_{\rm NN}}$ = 2.76 TeV. The two main observables, azimuthal correlations $\Delta\varphi = \varphi^{\rm trig} - \varphi^{\rm assoc}$ and charged hadrons yields as a function of their $p_{\rm T}$, are measured to study the properties of the medium. Especially, the per-trigger yield modification factors, $I_{\rm AA}(p_{\rm T}^{\pi^0}, p_{\rm T}^{h^\pm}) = \frac{Y^{\rm PbPb}(p_T^{\pi^0}, p_T^{h^\pm})}{Y^{\rm pp}(p_{\rm T}^{\pi^0}, p_T^{h^\pm})}$ and $I_{\rm CP} = \frac{Y^{\rm PbPb}_{\rm central}(p_{\rm T}^{\pi^0}, p_T^{h^\pm})}{Y^{\rm PbPb}_{\rm peripheral}(p_{\rm T}^{\pi^0}, p_{\rm T}^{h^\pm})}$, are analyzed at $8.0 < p_{\rm T}^{\rm trig} < 16.0$ GeV/c and $3.0 < p_{\rm T}^{\rm assoc} < 10.0$ GeV/c. While the $I_{\rm CP}$ is not measured due to no enough statistics in Pb+Pb peripheral simulation for extracting the correction factors. But the measurements will be updated soon when the enough simulations are produced.

The opening angle of two decay photons from a neutral meson becomes smaller with increasing of the neutral meson energy due to the Lorentz boost. In the EMCal of ALICE, when the energy of the π^0 (η) is larger than 5-6 GeV ($\sim$ 22 GeV), the two photons start to be close, and their two electromagnetic showers overlap in the calorimeter cells. Based on this performance of clusters, a new identification π^0 method, cluster splitting method, is used to identify π^0 for measuring the π^0-hadron correlations. This method can achieve to high-$p_{\rm T}$ and improve the statistics of the triggers of π^0, which be shortly summarized as following several steps. First of all, clusters with large shower shape long axis λ_0^2 and one or two local maxima are selected as the inputs for using the cluster splitting method. Secondly, the filtered clusters are split two new sub-clusters with the two highest local maxima cells and aggregate all the cells around them with 3×3 clusters clusterization. At last, the two new sub-clusters are paired to calculate their invariant mass for obtaining the trigger π^0 of the correlations. The associated charged hadrons is reconstructed in the Central tracking System, ITS and TPC.

The per-trigger yield of charged hadrons at central Pb+Pb collisions is obtained by subtracting the flat and flow backgrounds. In the flat background estimation, three methods are used to estimate the minimum value of the background. The charged pion flow is used instead of π^0 flow in the flow background estimation. The yield modification factors of $I_{\rm AA}$ at central Pb+Pb collisions on the near side and away side are estimated by comparing to the measurements in pp collisions. An away-side suppression from in-medium energy loss is observed ($I_{\rm AA} \approx 0.6$), which is from the effects of partons energy loss. Moreover, there is an enhancement above unity of ($I_{\rm AA} \approx 1.2$) on the near side which has not been observed with any

significance at lower collision energies. The significant near-side enhancement of I_{AA} in the p_{T} region observed shows that the near-side parton is also subject to medium effects. I_{AA} is sensitive to (i) a change of the fragmentation function, (ii) a possible change of the quark/gluon jet ratio in the final state due to the different coupling to the medium, and (iii) a bias on the parton p_{T} spectrum after energy loss due to the trigger particle selection. It needs to point out that the π^0-hadron correlations analysis is an important step to measure direct photon-hadron correlations.

Chapter 7

Direct photon-hadron correlations

Direct photon-hadron correlation, offers two major advantages as compared to di-jet measurements because of the nature of the photon. First of all, in contrast to partons, photons do not carry color charge and hence do not interact strongly when traversing the medium[292]. Secondly, the direct photon production at leading-order (LO) in pp and A+A collisions is dominated by the QCD Compton scattering process, $q+g \rightarrow q+\gamma$ and $q+\bar{q} \rightarrow g+\gamma$ annihilation process, and the photon momentum in the center-of-mass frame is approximately balanced by that of the recoil parton when considering the initial transverse momentum, k_{T}, of the colliding partons inside the nucleons. In nucleus-nucleus collisions, the direct photon contributions from next-to-leading-order (NLO) processes, such as fragmentation photons and thermal photons, are expected to be small ($\sim 10\%$) at high-p_{T} [293]. For these reasons, direct photon-hadron correlations have been considered as a "golden channel" for studying the properties of parton energy loss including parton fragmentation function without the need of the jet reconstruction [294, 295]. At RHIC, the measurements of correlations between direct photons and charged hadrons extracted by isolation method and Statistical Subtraction method were introduced briefly in Sec. 4.4. In ALICE, both methods are also used together to extract the direct photon-hadron correlations, which will presented in this chapter.

In this chapter, it begins with the introduction of measurement observables from the direct photon-hadron correlations in Sec. 7.1, which is followed by the analysis of the direct photon-hadron correlations with the isolation method in Sec. 7.2. In Sec. 7.3, another extraction method, Statistical Subtraction method, is used to measured the direct photon-hadron correlations.

7.1 Measurement observables

Direct photon production at leading-order is dominated by the QCD Compton scattering process, $q + g \to q + \gamma$ and $q + \bar{q} \to g + \gamma$ annihilation process shown in panel a and b of Fig. 7.1. It generally is called *prompt* photon. The production from next-to-leading-order, such as fragmentation photons and other additional medium induced contributions (thermal, jet conversion), contributes with about 10% (corresponding Feynman graphs shown in panel c and d of Fig. 7.1). Experimentally,

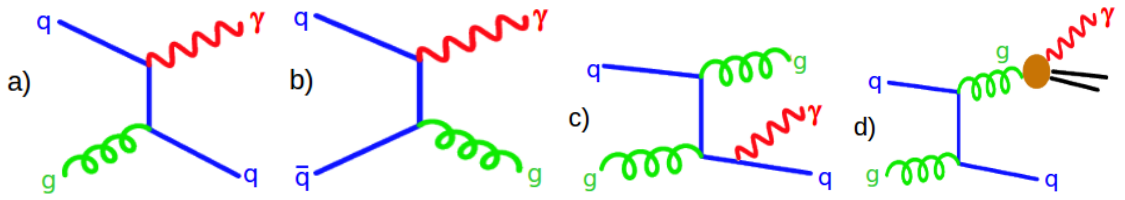

Figure 7.1: Feynman graphs of the main production processes for direct photons in initial hard scatterings, quark-gluon plasma phase thermalization and parton fragmentation: (a) quark-gluon Compton scattering, (b) quark-antiquark annihilation, (c) Bremsstrahlung and (d) parton fragmentation.

it is accessible using the momentum of prompt photon to balance the momentum of the opposite jet, $p_{\mathrm{T}}^{\gamma} \approx p_{\mathrm{T}}^{jet}$. This balance is only approximate due to the transverse momentum, k_{T}, of the colliding partons inside nucleons. In this analysis, the azimuthal angle distribution and jet fragmentation function are measured by the direct photon-hadron correlations. At LO direct photon-hadron correlations, hadrons are ideally produced from the away side parton fragmentation, see a schematic view in the left panel of Fig. 7.2. This would result in the azimuthal angle difference of $\Delta\varphi = \varphi^{\gamma} - \varphi^{track}$ with non-zero distribution on the away side. The away side distribution provides a measurement of the jet fragmentation function defined as $D(z) = 1/(N_{jet})(dN(z)/dz)$, where $z = p^{h^{\pm}}/p^{jet}$. In leading order pQCD, the fragmentation function of the recoil jet from the away side parton should be given to a good approximation by the imbalance parameter x_{E} distribution defined as:

$$x_{\mathrm{E}} = -\frac{\vec{p}_{\mathrm{T}}^{\gamma} \cdot \vec{p}_{\mathrm{T}}^{h^{\pm}}}{|\vec{p}_{\mathrm{T}}^{\gamma}|^2} = -\frac{|p_{\mathrm{T}}^{h^{\pm}}| \cos\Delta\varphi}{|p_{\mathrm{T}}^{\gamma}|} \tag{7.1}$$

where $\Delta\varphi$ is the azimuthal angle between isolated photons and hadrons. As it was mentioned, the transverse and longitudinal momenta of away side parton does not exactly balance with the prompt photon. Hence, the parameter x_{E} is an approximation rather than an exact measurement to the fragmentation function of the away

side jet [298]. This analysis is only performed with pp collisions at $\sqrt{s} = 7$ TeV. The right panel of Fig. 7.2 shows the x_{E} distribution computed from Diphox γ-jet production [308] and comparison with DSS quark and gluon fragmentation function [309, 310]. It indicates that the x_{E} distribution mainly follows the quark fragmentation behaviour in a large range (0.2 to 0.8) because of the dominant contribution of Compton scattering process.

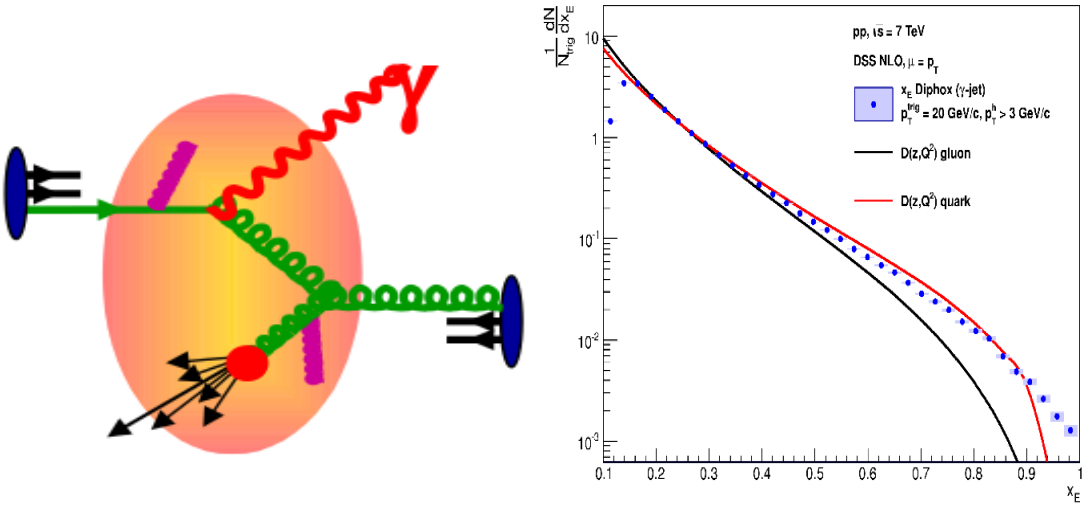

Figure 7.2: Left: Schematic view of γ-jet in A+A collisions; Right: x_{E} distribution from γ-jet production produced by Diphox, and compared to DSS quark and gluon fragmentation [311].

7.2 Isolation method

Experimentally, isolation method is a good technique to select the prompt photon. In this section, the jet fragmentation function measured by isolated photon-hadron correlations is presented briefly. The main analysis procedures are:

- Obtain photon candidates by filtering all clusters measured at EMCal with the photon identification cuts defined in Sec. 5.3.1.
- Study a isolation criterion with the γ+jet simulation production.
- Use the isolation criterion to obtain isolated photon candidates, and make azimuthal angle correlations between the isolated photon candidates with highest p_{T} (leading photon candidates) and charged hadrons.
- The isolated leading photon candidates are not pure photons, which include a fraction of contamination, such as charged hadron clusters and π^0 clusters.

Therefore, the isolation photon purity is calculated by a so-called binned likelihood method based on the distribution of cluster shower shape long axis λ_0^2 [312].

- Extract isolated photon-hadron correlations by subtracting the contamination and underlying events contributions.

- Correction factors, such as track contamination and efficiency, are calculated and used in the analysis.

7.2.1 Isolation criterion

Clusters filtered by EMCal photon identification cuts, photon candidates, are dominated by a large fraction of decay photons of neutral mesons (mostly π^0). The fraction is reduced about 80% by applying isolation criteria. In this analysis, the isolation criterion requires no particles including charged and neutral particles with $p_{\mathrm{T}} > 0.5$ GeV/c in a cone of radius $R = \sqrt{\Delta\varphi^2 + \Delta\eta^2} = 0.4$ around a photon candidate with highest p_{T} in one event. In Fig. 7.3, the left panel shows the schema of this isolation criterion, and the right panel presents the isolation efficiencies of direct photons calculated from the γ-jet simulation at $\sqrt{s} = 7$ TeV and π^0 obtained from pp collisions at $\sqrt{s} = 7$ TeV. The efficiency results indicate that ~80% direct photons are isolated by this isolation criterion, while ~10% π^0 are isolated.

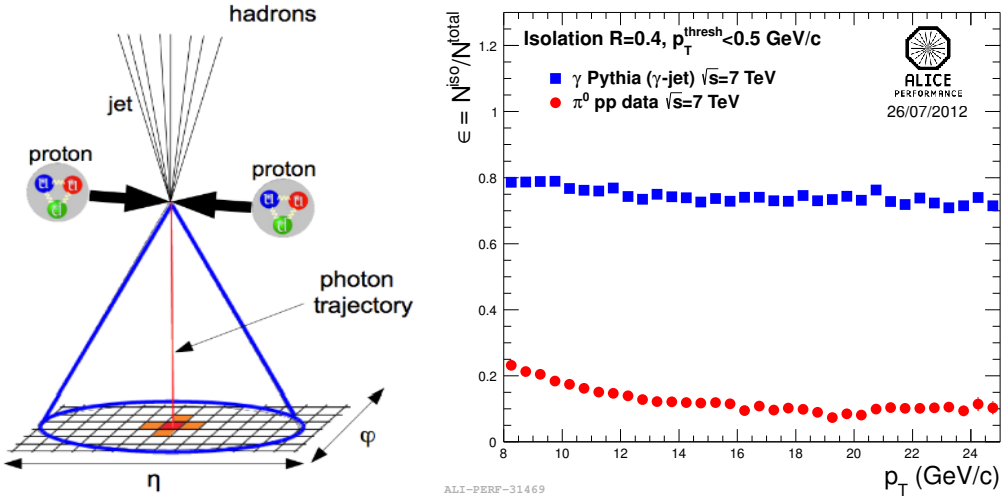

Figure 7.3: Left: Schema of isolation method with a cone radius of $R = \sqrt{\Delta\varphi^2 + \Delta\eta^2}$ around the leading photon candidate. Right: Isolation efficiencies of direct photons (blue) from the γ-jet simulation at $\sqrt{s} = 7$ TeV and π^0 (red) from pp collisions at $\sqrt{s} = 7$ TeV [311].

7.2.2 Isolated cluster-hadron correlations

The isolated cluster (photon candidate) with highest p_{T} in one event is used as the trigger to correlate with charged hadrons. The imbalance parameter x_{E} is calculated by Eq. 7.1 at a region of $|\Delta\varphi - \pi| < \frac{\pi}{2}$ on the away side in the correlations. Fig. 7.4 presents the x_{E} distribution from isolated cluster-hadron correlations with the isolated leading clusters p_{T} at $8 < p_{\mathrm{T}}^{\mathrm{trig}} < 12$ GeV/c (black), $12 < p_{\mathrm{T}}^{\mathrm{trig}} < 16$ GeV/c (red), and $16 < p_{\mathrm{T}}^{\mathrm{trig}} < 25$ GeV/c (blue). To the isolated cluster-hadron correlations, the underlying events x_{E} contributions which are estimated at two different regions of $\frac{\pi}{3} < \Delta\varphi < \frac{2\pi}{3}$ and $\frac{4\pi}{3} < \Delta\varphi < \frac{5\pi}{3}$ are subtracted.

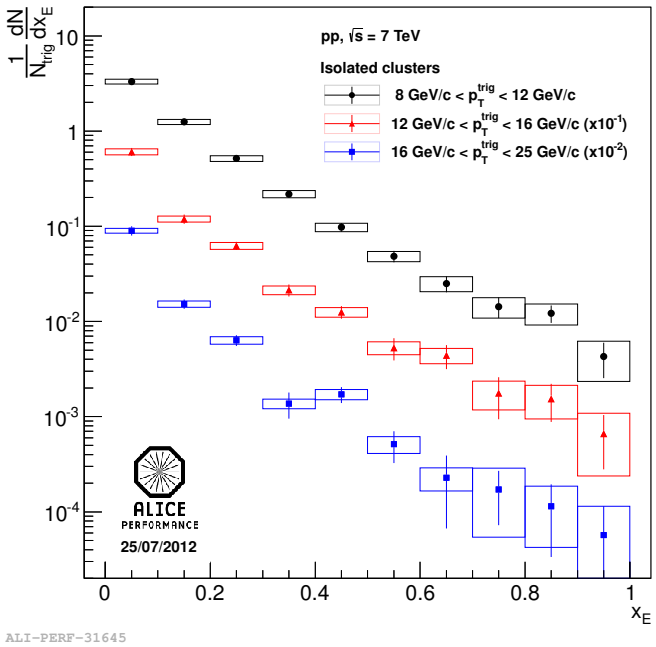

Figure 7.4: x_{E} distributions of isolated cluster-hadron correlations in three $p_{\mathrm{T}}^{\mathrm{trig}}$ bins and $p_{\mathrm{T}}^{\mathrm{assoc}} > 0.2$ GeV/c [311].

7.2.3 Isolated π^0-hadron correlations

As it is presented in the right panel of Fig. 7.3, ~10% π^0 at high-p_{T} are isolated with the defined isolation criterion. This is because two decay photons from high-p_{T} π^0 are generally close and their two electromagnetic showers overlapping in the calorimeter cells are clustered. A fraction of these clusters rejected unsuccessfully by the photon identification cuts are the dominant contamination of isolated photons. In order to estimate and subtract the contamination, the x_{E} distribution of

isolated π^0-hadron correlations is measured, where the π^0 is identified by Cluster Splitting method introduced in Sec. 6.2.1. The underlying event contribution to $x_{\rm E}$ is also subtracted with similar analysis in isolated cluster-hadron correlations. The final results of $x_{\rm E}$ distribution of isolated π^0-hadron correlations at three $p_{\rm T}^{\rm trig}$ are presented in the left panel of Fig. 7.5. Compared to inclusive π^0, the isolated π^0 equally carries the fraction of its parent parton energy from 0.5 to 0.8. An exponential slope is extracted from fitting the $x_{\rm E}$ distribution of isolated π^0-hadron correlations with a function of Ae^{-B} and compared to DSS fragmentation functions shown in the right panel of Fig. 7.5. The comparison indicates that the isolated π^0 is a parton fragmentation product and $p_{\rm T}^{\pi^0} < p_{\rm T}^{\rm parton}$.

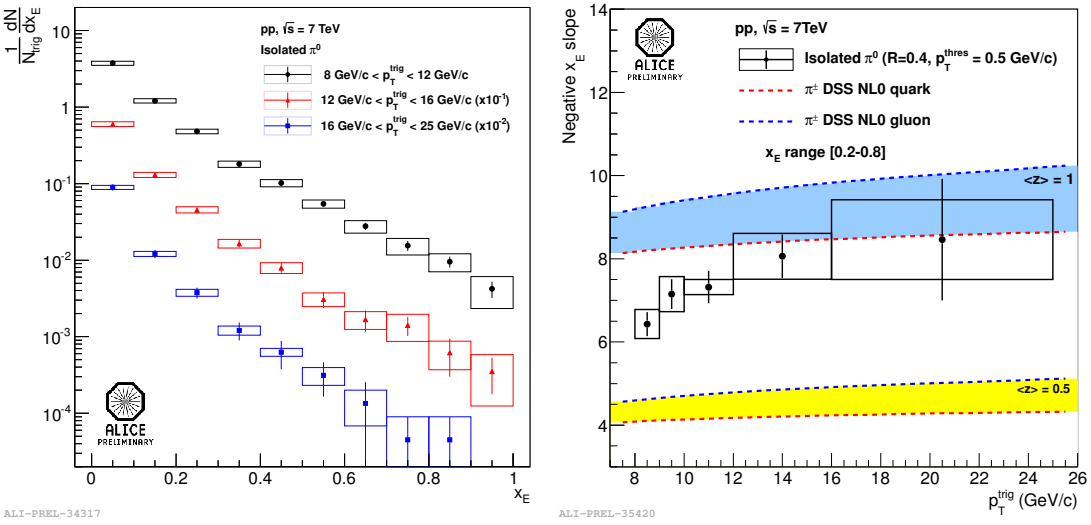

Figure 7.5: Left: $x_{\rm E}$ distributions of isolated π^0-hadron correlations in three $p_{\rm T}^{\rm trig}$ bins. Right: Slopes extracted from exponential fit of isolated π^0-hadron correlations and compared to DSS quark-gluons fragmentation functions [311].

7.2.4 Isolated photon-hadron correlations

To subtract the contamination contribution to the $x_{\rm E}$ distribution, the isolated photon purity is estimated firstly by two-component binned likelihood method: a mix of scaled signal and contamination distribution is used to fit all clusters in pp collision data at the distribution of the shower shape long axis λ_0^2. An example fitting with this method at $16 < p_{\rm T} < 25$ GeV/c is shown in the left panel of Fig. 7.6. Here, the signal component is obtained from γ-jet events generated with PYTHIA and propagated through the detectors with GEANT3, and the contamination component is extracted from data by selecting events which are failed in the isolation criteria.

The typical purity values obtained from this method in $8 < p_{\mathrm{T}} < 25$ GeV/c increase from about 5% to 70%. The x_{E} distribution of isolated π^0-hadron correlations scaled with respect to the isolated photon purity estimated previous is subtracted from isolated cluster-hadron correlations. The subtraction analysis is to sum up at $8 < p_{\mathrm{T}}^{\mathrm{trig}} < 25$ GeV/c with the trigger p_{T} interval of $\Delta p_{\mathrm{T}} = 1$ GeV/c:

$$D(x_{\mathrm{E}}^{\gamma,iso}) = \sum_{p_{\mathrm{T}}=8}^{25\ \mathrm{GeV}/c} \frac{1}{p_i} D_i(x_{\mathrm{E}}^{cluster,iso}) + \frac{p_i - 1}{p_i} D_i(x_{\mathrm{E}}^{\pi^0,iso}) \tag{7.2}$$

where the $D(x_{\mathrm{E}}^{\gamma,iso})$, $D_i(x_{\mathrm{E}}^{cluster,iso})$, and $D_i(x_{\mathrm{E}}^{\pi^0,iso})$ are the imbalance parameter x_{E} distributions of isolated photon-hadron correlations, isolated cluster-hadron correlations and isolated π^0-hadron correlations; p_i is the isolated photon purity calculated by binned likelihood fitting in each trigger interval. The x_{E} distribution of isolated photon-hadron correlations at $8 < p_{\mathrm{T}}^{\mathrm{trig}} < 25$ GeV/c is shown in the right panel of Fig. 7.6, and a slope 7.8 ± 0.9 is obtained from the fitting of x_{E} distribution at $0.2 < x_{\mathrm{E}} < 0.8$ with the function of Ae^{-B}. More details about this analysis can be found in [311].

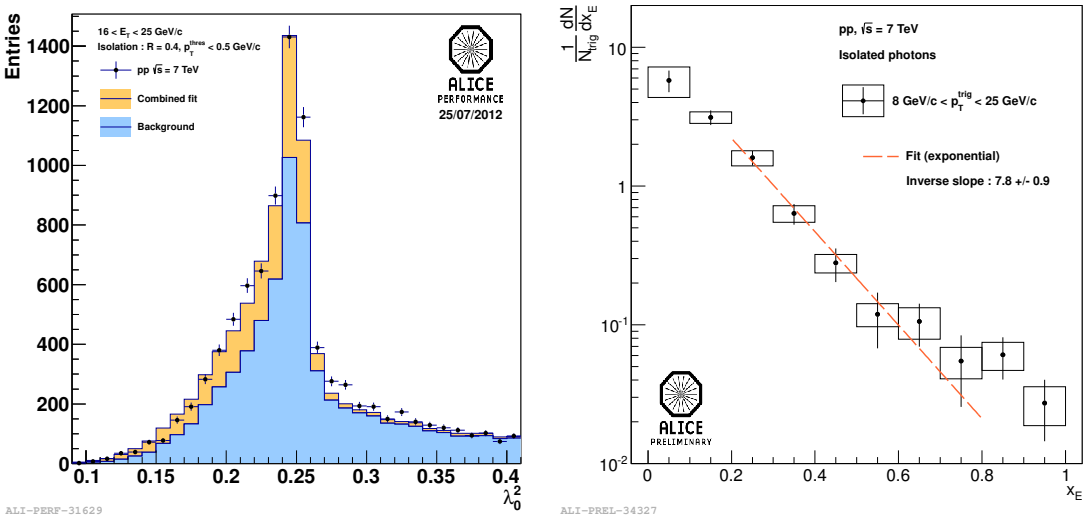

Figure 7.6: Left: Isolated cluster shower shape long axis λ_0^2 distribution fitted by a two-component binned likelihood. Right: x_{E} distributions of isolated photon-hadron correlations at $8 < p_{\mathrm{T}}^{\mathrm{iso}\ \gamma} < 25$ GeV/c [311].

7.3 Statistical Subtraction method

In this section, a detail description about the measurement of the direct-hadron correlations with Statistical Subtraction method is presented. The inclusive photon

($\gamma_{\rm inclusive}$) sample that we measure in the data, can be distinguished into two types of photons: decay photons and direct photons. Decay photons ($\gamma_{\rm decay}$) are from meson decays such as $\pi^0 \to 2\gamma$, and direct photons ($\gamma_{\rm direct}$) are the rest. In summary,

$$N_{\rm direct} = N_{\rm inclusive} - N_{\rm decay} \tag{7.3}$$

Ideally, the direct photon component can be extracted from the inclusive photon sample in an event-by-event basis and then correlated with charged hadrons. Since the contribution of photons from hadron decays is dominant by a couple of orders of magnitude compared to the direct photons, this measurement is challenging.

In the Statistical Subtraction method, the $\gamma_{\rm direct}$-hadron correlations are obtained by subtracting the $\gamma_{\rm decay}$-hadron correlations from the $\gamma_{\rm inclusive}$-hadron correlations. The $\gamma_{\rm inclusive}$-hadron correlations require a high-$p_{\rm T}$ photon trigger (*i.e.* $p_{\rm T} > 8.0$ GeV/c) constructed $\Delta\varphi$ and $\Delta\eta$ distributions with associated charged hadrons in the events. The $\gamma_{\rm decay}$-hadron correlations are estimated from measured π^0-hadron and η-hadron correlations with a weighting factor from Monte-Carlo study that a π^0/η with a given $p_{\rm T}$ produces a decay photon within a certain $p_{\rm T}$ bin. Based on Eq. 7.3, the relationship between the per-trigger yield, Y, for $\gamma_{\rm direct}$-hadron, $\gamma_{\rm inclusive}$-hadron and $\gamma_{\rm decay}$-hadron correlations can be expressed as:

$$N_{\rm direct}Y_{\rm direct} = N_{\rm inclusive}Y_{\rm inclusive} - N_{\rm decay}Y_{\rm decay} \tag{7.4}$$

According to Eq. 7.4, the statistical subtraction equation used to determine the direct photon-hadron correlation is written as:

$$Y_{\rm direct} = \frac{R_\gamma Y_{\rm inclusive} - Y_{\rm decay}}{R_\gamma - 1} \tag{7.5}$$

where R_γ is the ratio of inclusive to decay photons, called Double Ratio, which is written as:

$$R_\gamma = \frac{N_{\rm inclusive}}{N_{\rm decay}} = 1 - \frac{N_{\rm direct}}{N_{\rm decay}} \tag{7.6}$$

$R_\gamma > 1$ indicates the signal of direct photons exists. More details about the statistical subtraction method are summarized in Tab. 7.1.

In the imbalance parameter analysis, the detector effects, such as track contamination and tracking efficiency, are taken into account directly during filling the raw histograms with a weighting factor. The weighting factor w is calculated as:

$$w = \frac{1 - C_{\rm track}^{contam}}{\epsilon_{\rm track}^{eff}} \tag{7.7}$$

Step	Input measurement	Correction source	Output (Like generated-level)
1	Inclusive candidate γ-h	γ purity, efficiency, correlation resolution	Inclusive γ-h
2	Raw π^0/η-h	π^0/η identification efficiency correlation resolution	π^0/η-h
3	π^0/η-h from Step 2	π^0/η MC truth map	π^0/η decay γ-h
4	π^0/η decay γ-h from Step 3	$Ratio = \frac{all\ decay\ \gamma}{decay\ \gamma\ from\ \pi^0}$	All decay γ-h
5	Inclusive γ-h All decay γ-h	$R_\gamma = \frac{inclusive\ \gamma}{all\ decay\ \gamma}$	Direct γ-h

Table 7.1: Summary of analysis steps of direct photon-hadron correlations with the Statistical Subtraction method.

where the $C_{\text{track}}^{contam}$ and $\epsilon_{\text{track}}^{eff}$ are the track contamination and tracking efficiency, respectively. Their calculation are defined in Sec. 6.4.4. Both of the results are obtained from the simulation production for pp at $\sqrt{s} = 7$ TeV, as shown in Fig. 7.7.

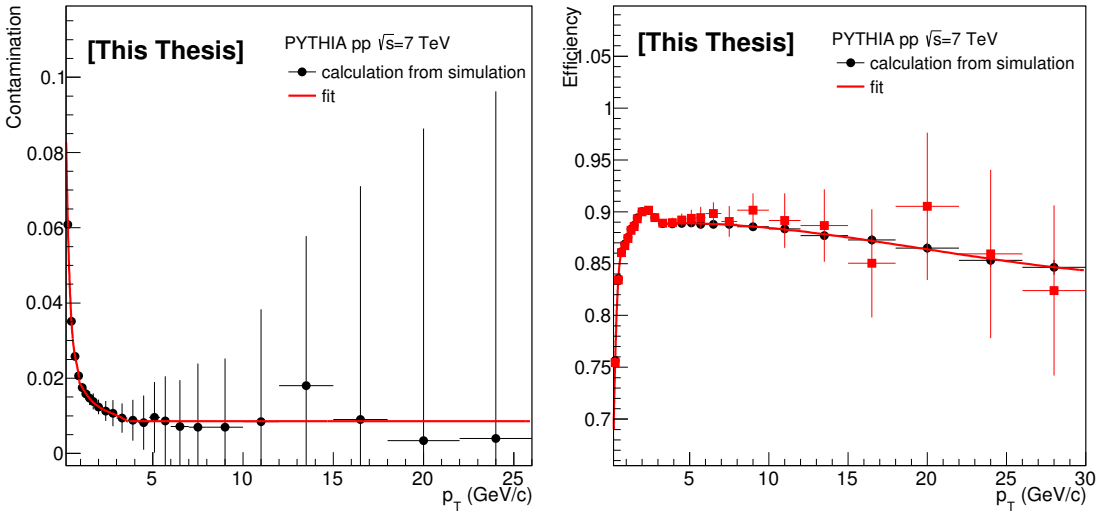

Figure 7.7: Track contamination (left) and tracking efficiency (right) obtained from the PYTHIA simulation production of pp at $\sqrt{s} = 7$ TeV. In the efficinecy calculation, results from two simulation productions are used to make comparison, and similar results are found.

In the following sections, more details about each step analysis, including the calculation of the R_γ factor, are introduced.

7.3.1 Inclusive γ-hadron correlations

In the inclusive γ-hadron correlations analysis, the V1 clusterzation is used to reconstruct the cluster at EMCal.

7.3.1.1 Photon purity

The photons are identified from the reconstructed clusters by some cluster cuts (photon identification) as presented in Sec. 5.3.1. Not all the clusters obtained after using of the cluster cuts are photon clusters. Because some fraction of clusters are created by charged hadrons, merged π^0 and electrons, *etc.* Fig. 7.8 shows the fraction of different composition in the clusters. The result shows that the fraction

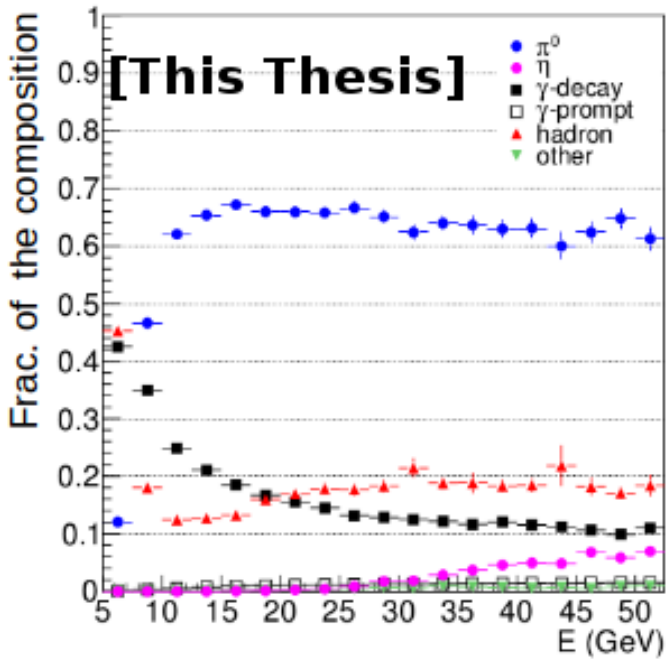

Figure 7.8: Fraction of the composition in the clusters with V1 clusterzation at EMCal in PYTHIA jet-jet simulation for the pp collisions at $\sqrt{s}$ = 7 TeV. π^0 clusters (blue filled circles) generated by the two decay photons; η clusters (pink filled circles) generated by the two decay photons; decay photon clusters (filled square) generated by only one of the meson decay photons, hadron clusters (red triangle)generated by a hadron; prompt photon clusters (open black squares); Remaining contributions (inverse green triangle) are electrons, muons, or cases that could not be classified. The plot was taken from [305].

of merged π^0 clusters becomes larger with the cluster p_{T} increasing. This can be explained when the energy of the π^0 (η) is larger than 5-6 GeV ($\sim$ 22 GeV), the two photons start to be close, and their two electromagnetic showers overlap in the

calorimeter cells, as discussed in Sec.6.2.1.

It is impossible to extract the pure photon cluster with any photon PID cuts at EMCal. The purity of photon needs to be calculated for extracting inclusive γ-hadron correlations. Since the used jet-jet simulation does not include the process of prompt photon production, and the shower shape parameter of the cluster in the simulation does not well re-produce the data, the purity calculation is estimated from the data or from the data together with simulations. As the isolated photon purity, the binned likelihood method is used in this purity calculation with the shower shape λ_0^2 distribution. Three main components are used as the inputs for the binned likelihood fitting, which are signal part of photon clusters from the data or the simulation, and background parts of charged hadron clusters and merged π^0 clusters from the data. Each component is analyzed as follows:

- **photon cluster**:
  The shower shape λ_0^2 distribution of photon clusters is respectively extracted from the data and simulation for comparison. In the simulation, the photon cluster can be labeled by the tagged particle index in the event generation. Looping all clusters filtered by the photon identification cuts to get the label of each cluster, the label is used to determine the cluster is produced by a photon or other particles. Finally, all the clusters produced by photons are selected to analyze their shower shape λ_0^2 distribution. The distribution is presented in Fig. 7.9 with the blue line. Since the simulation does not well re-produce the data, the λ_0^2 of photon clusters is also estimated from data by reconstruction of π^0 and η. All clusters from data are paired to calculate their invariant mass. Each two clusters with invariant mass around the mass peaks of π^0 and η are considered as the photon clusters. Fig 7.16 shows the Gaussian+Polynomial2 fit to the invariant mass peaks of π^0 and η at $8.0 < p_{\mathrm{T}} < 12$ GeV/c in the left and right, respectively. The shower shape λ_0^2 of the clusters with the invariant mass at different widths (different times of Gaussian σ) in the mass peaks of π^0 and η are shown in the Fig. 7.9. The λ_0 probability distributions are similar at different widths in the π^0 and η peaks from data, which means most of selected clusters under the peak are photon clusters. The distribution extracted from π^0 peak is very different from η peak due to a little fraction of clusters formed by decay photons from high-p_{T} π^0 are merged. Hence the distributions extracted from the π^0 peak can not be considered as the full photon clusters shower shape λ_0^2 probability distributions. The figure also

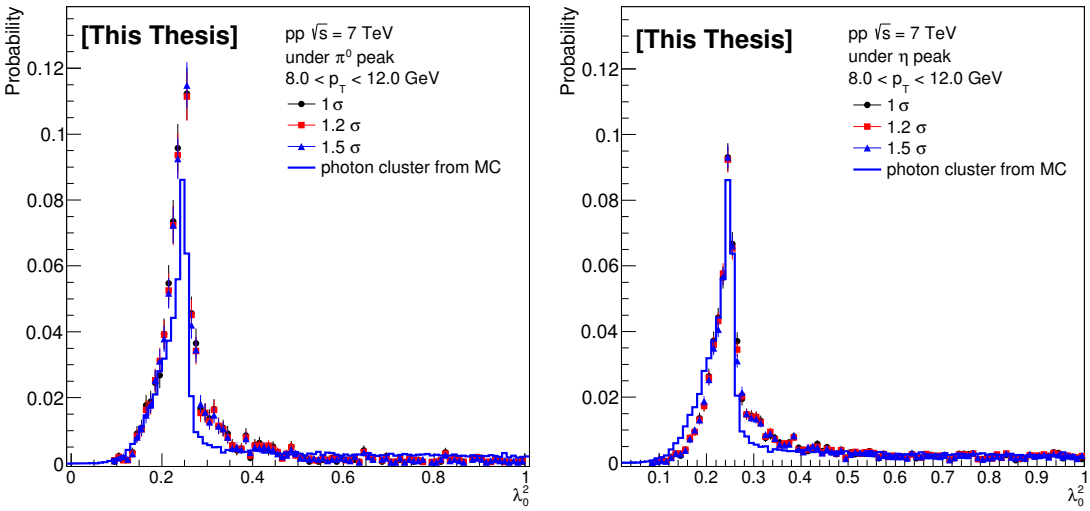

Figure 7.9: Shower shape λ_0^2 probability distributions of the clusters from different widths in the invariant mass peaks of π^0 (left) and η (right), and comparison with photon clusters from the simulation (blue line) of pp at $\sqrt{s} = 7$ TeV are shown.

indicates that the λ_0 probability distributions of photon clusters between the data and the simulation are very different, which reveals the simulation can not re-produce the data. In order to have high probability to select photon clusters, it would be better to select the clusters at narrower widths in the invariant mass peak. But taking into account the statistics, the estimation from the width of 1.2σ is used as the input of the photon cluster shower shape distribution for binned likelihood fitting.

- **charged hadron cluster**:
  At EMCal, a fraction of clusters are produced by charged hadrons, *e.g.* $\pi^{\pm}$, $K^{\pm}$. The track matching cuts discussed in Sec. 5.3.1 are able to reject a large fraction of charged hadron clusters. According to this performance, the shower shape parameter of charged hadron clusters can be obtained from the clusters rejected by the track matching cuts. In Fig. 5.10, the residual distributions of matched track-cluster pairs are shown with $\Delta\eta$ versus energy and $\Delta\varphi$ versus energy. The projection distributions are presented as function of $\Delta\eta$ and $\Delta\varphi$ in Fig. 7.10. A clear peak is shown in each residual distribution. The λ_0^2 probability of matched clusters in different $\Delta\eta$ and $\Delta\varphi$ widths are shown in left and right panel of Fig. 7.11. From the figure, we find tighter cuts give higher probability. Because of the limited statistics, the fluctuation of the result is a little large at the tightest cut. In this case, the λ_0^2 probability

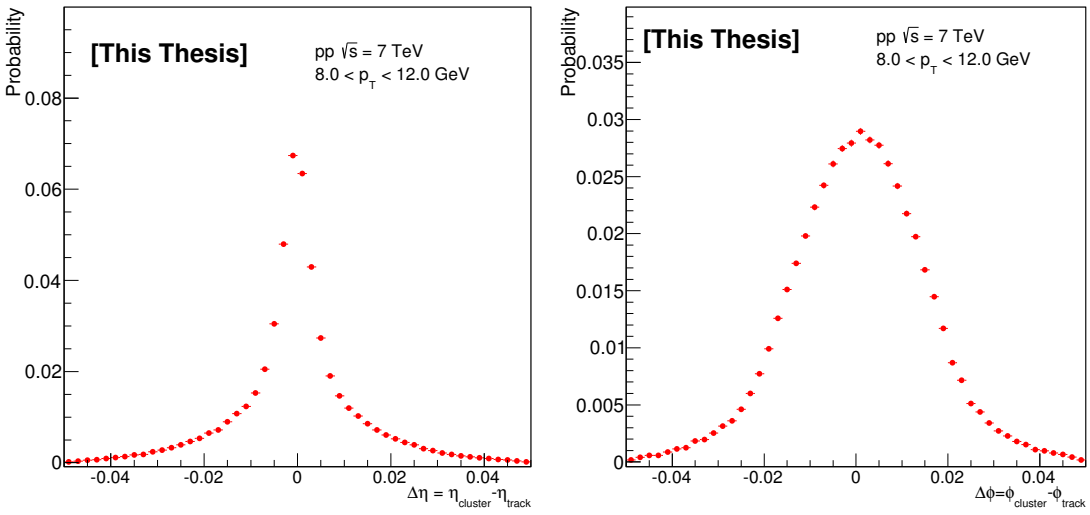

Figure 7.10: $\Delta\eta$ (left) and $\Delta\varphi$ (right) distributions of the clusters matched by tracks at $8.0 < p_{\mathrm{T}} < 12.0$ GeV/c from pp at $\sqrt{s} = 7$ TeV.

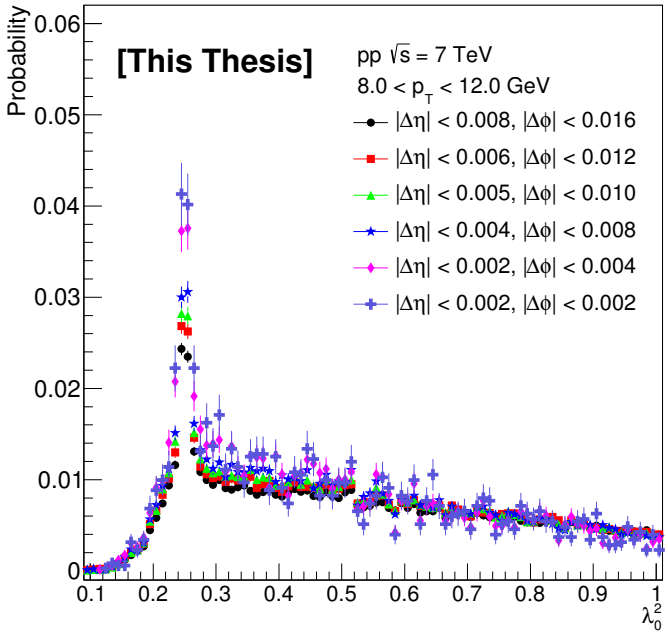

Figure 7.11: Shower shape λ_0^2 probability distribution of the cluster matched by tracks in different $\Delta\eta$ and $\Delta\varphi$ widths at $8.0 < p_{\mathrm{T}} < 12.0$ GeV/c from pp at $\sqrt{s} = 7$ TeV.

distribution at width of $\Delta\eta < 0.002$ and $\Delta\varphi < 0.004$ is considered from the charged hadron clusters.

- **merged π^0 cluster**:
  As it was mentioned previous, when the energy of the π^0 (η) is larger than 5-6 GeV ($\sim$ 22 GeV), both of its decay photons start to be close, and their two electromagnetic showers overlap in the calorimeter cells. Therefore, a large fraction of clusters are formed by π^0, so-called merged π^0 clusters. The fraction is larger with the increasing of π^0 energy. The merged π^0 clusters mainly exist in the V1 clusterzation, and a little fraction in V2 clusterzation only when clusters with very large energy. Fig. 7.8 shows the fraction of merged π^0 clusters in V1 clusterzation. The shower shape parameter λ_0^2 of merged π^0 clusters is obtained from the merged π^0 clusters identified by the cluster splitting method discussed in Sec. 6.2.1. In Sec. 6.2.1, a cluster is considered as the merged π^0 cluster in 3σ width of the split sub-clusters invariant mass. Fig 7.12 shows the λ_0^2 probability distributions in different widths of the split sub-clusters invariant mass. The results show that the probability distribution

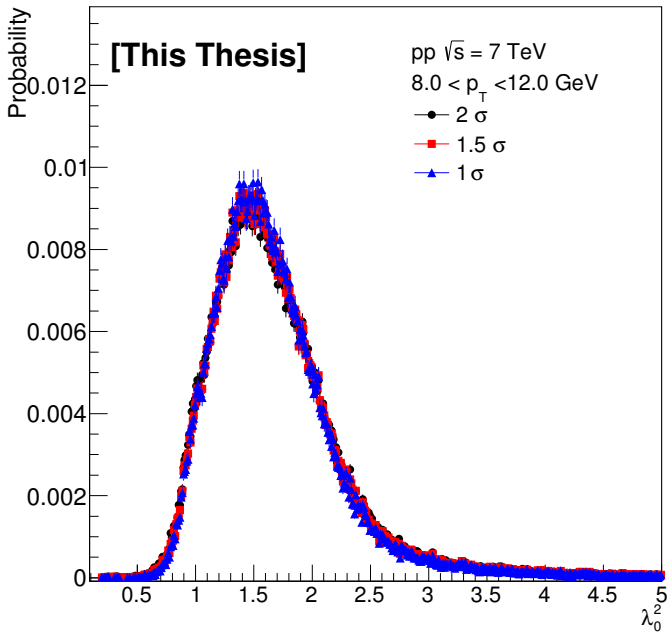

Figure 7.12: Shower shape λ_0^2 probability distributions of the considered merged π^0 clusters in different widths of the sub-cluster invariant mass by splitting method at $8.0 < p_{\rm T} < 12.0$ GeV/c from pp collisions at $\sqrt{s} = 7$ TeV.

is highly larger with decreasing the widths of invariant mass. This indicates that narrower width has higher probability to select the merged π^0 clusters.

When taking into account the statistical errors of the distribution, the width of 1.5σ is better to be used for the λ_0^2 probability estimation of the merged π^0 clusters.

The λ_0^2 probabilities of three sources discussed above are used as the inputs to fit the λ_0^2 distribution of inclusive clusters with the binned likelihood method. Two different fitting results are obtained with the signal distribution from the simulation and the data, respectively. In Fig. 7.13, the first fit result with the λ_0^2 of photon clusters estimated from the simulation is shown. We find that the fit is not good at

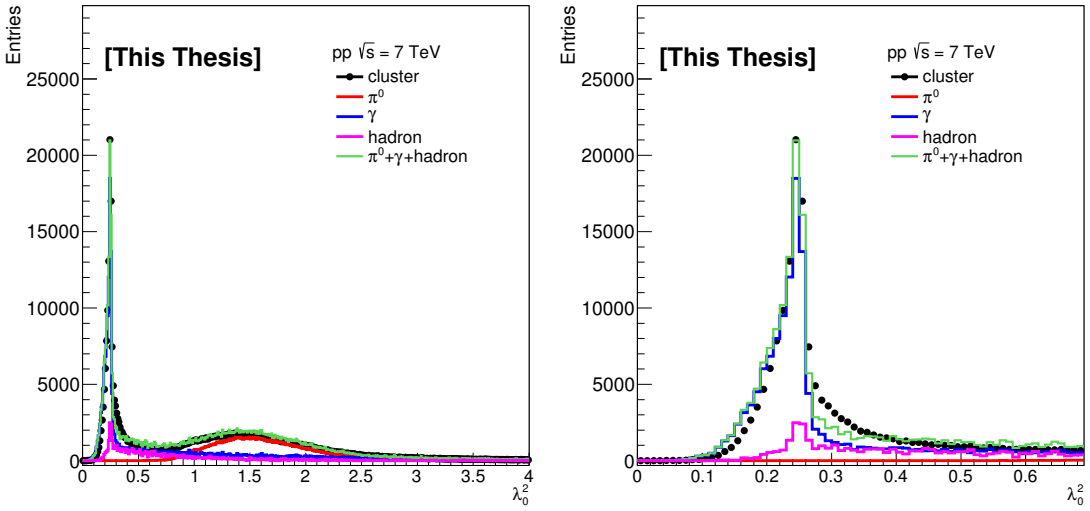

Figure 7.13: Zoom in (left) and zoom out (right) binned likelihood fitting results to the λ_0^2 of inclusive clusters with signal of photon clusters from simulation and background of charged hadrons and merged π^0 clusters from data at $8.0 < p_{\mathrm{T}} < 12.0$ GeV/c from pp at $\sqrt{s} = 7$ TeV.

$0.1 < \lambda_0^2 < 0.4$. The reason is that the λ_0^2 of photon clusters from the simulation does not well re-produce the data. The second fit with the λ_0^2 of photon clusters estimated in η peak from the data is shown in Fig. 7.14. The second fitting performs well in the full λ_0^2 range. The photon purity value is about 0.94, which is calculated by a ratio of the blue line distribution to the inclusive cluster distribution by integrating at a range of $0.10 < \lambda_0^2 < 0.27$.

7.3.1.2 Inclusive γ-hadron correlations

The clusters filtered by some cuts are used as the trigger particles to construct correlations with charged hadrons in the azimuthal angle difference $\Delta\varphi = \varphi^{\mathrm{trig}} - \varphi^{\mathrm{assoc}}$ and pseudo-rapidity difference $\Delta\eta = \eta^{\mathrm{trig}} - \eta^{\mathrm{assoc}}$ as Eq. 4.1. These correlations are not inclusive γ-hadron correlations due to the trigger clusters including not only

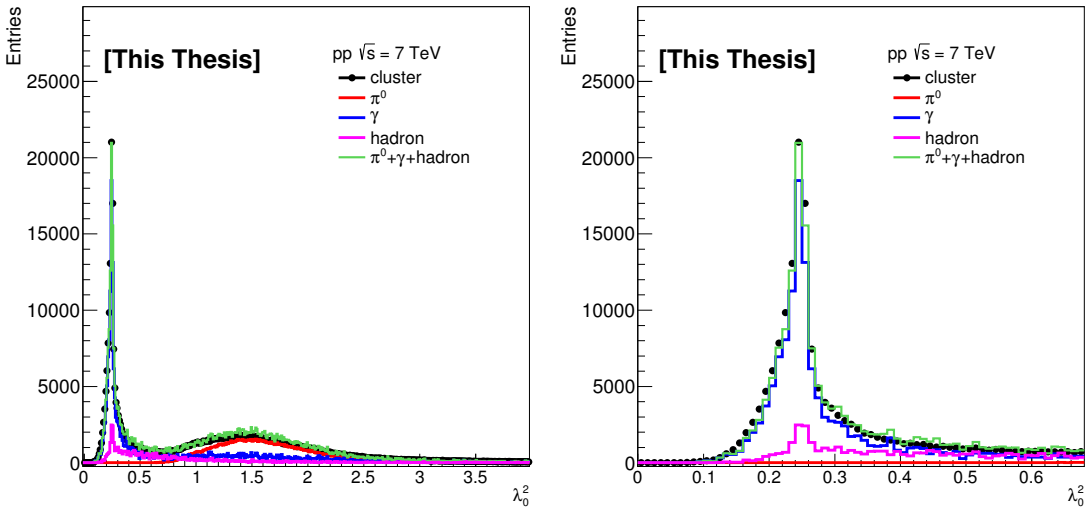

Figure 7.14: Zoom in (left) and zoom out (right) binned likelihood fitting results to the λ_0^2 of inclusive clusters with both signal of photon clusters under η peak and background of charged hadrons and merged π^0 clusters from data at $8.0 < p_{\mathrm{T}} < 12.0$ GeV/c from pp at $\sqrt{s} = 7$ TeV.

photon clusters but also other source clusters. Therefore, the correlations are called inclusive candidate photon-hadron correlations as shown in Fig. 7.15 with black points, which need to be subtracted the background contributions of non-photon trigger correlations. Since most of the non-photon clusters are formed by merged π^0 and charged hadrons, therefore the non-photon trigger correlations are characterized by π^0-hadron correlations as shown with red square in Fig. 7.15. The details analysis of π^0-hadron correlations will be discussed in Sec. 7.3.2. The inclusive γ-hadron correlations can be obtained by subtracting merged π^0-hadron correlations from inclusive candidate γ-hadron correlations according to:

$$Y_{\gamma} = \frac{1}{p} Y_{can.\ \gamma} - \frac{1-p}{p} Y_{\pi^0} \tag{7.8}$$

where Y_{γ}, $Y_{can.\ \gamma}$ and Y_{π^0} are the per-trigger yield of correlations with the triggers of inclusive γ, inclusive candidate γ and π^0, respectively; p is the photon purity calculated in Sec. 7.3.1.1.

7.3.2 π^0/η-hadron correlations

In Chap. 6, the identification of π^0 via the cluster splitting method with V1 clusterization and the measurement of π^0-hadron correlations in pp and Pb+Pb at $\sqrt{s_{\mathrm{NN}}} = 2.76$ TeV are discussed in details. In this section, π^0 and η are reconstructed with V2 clusterization by selecting two-cluster invariant mass around the PDG mass

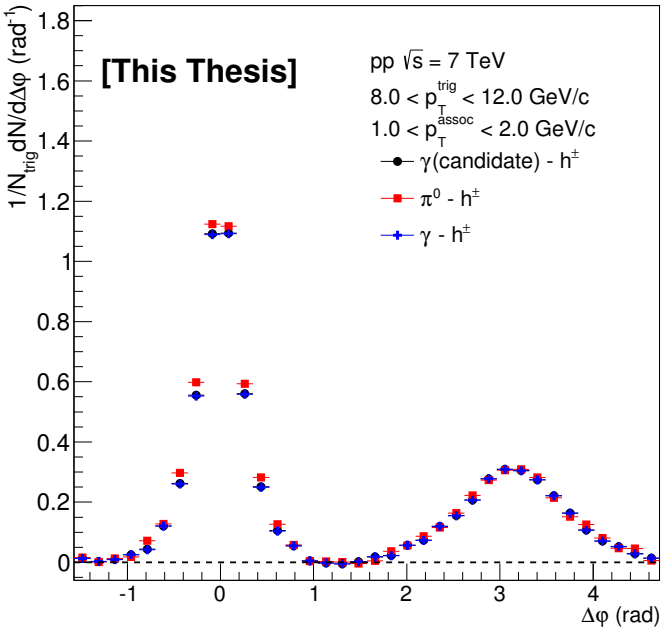

Figure 7.15: Azimuthal angle distribution of correlations with trigger as inclusive candidate γ (black circle), π^0 (red square) and inclusive γ (blue cross) at $8.0 < p_{\mathrm{T}}^{\mathrm{trig}} < 12.0$ GeV/c and $1.0 < p_{\mathrm{T}}^{\mathrm{assoc}} < 2.0$ GeV/c in pp at $\sqrt{s} = 7$ TeV.

of π^0 and η, respectively. A Side Band Subtraction method is used to subtract the fake π^0/η-hadron correlations for extracting π^0/η-hadron correlations.

7.3.2.1 π^0 and η reconstruction

No matter which method, cluster splitting or two-cluster invariant mass, is used to identified π^0 and η mesons, the invariant mass needs to be calculated according to Eq. 6.1. The difference is that cluster splitting method is based on one cluster which is split two sub-cluster for invariant mass calculation, and two-cluster invariant mass method starts from two independent clusters for the invariant mass calculation.

In the method of two clusters invariant mass, the selected clusters are reconstructed with V2 clusterization which can unfold most of merged π^0 clusters at a certain high energy range (below 25 GeV). The merged π^0 clusters above 25 GeV can not be unfolded. Fig. 7.16 shows two clusters invariant mass fit by a Guassian+Polynomial2 function at around π^0 PDG mass 0.135 GeV/c^2 and η PDG mass 0.58 GeV/c^2 at $8.0 < p_{\mathrm{T}} < 12.0$ GeV/c. The reconstruction efficiency of $\pi^0(\eta)$ is calculated by embedding single $\pi^0(\eta)$ with a flat distribution into real pp collisions at $\sqrt{s} = 7$ TeV events. The final pairs were weighted according to the published $\pi^0(\eta)$ spectrum in [68]. The efficiencies are shown in the left and right panel of

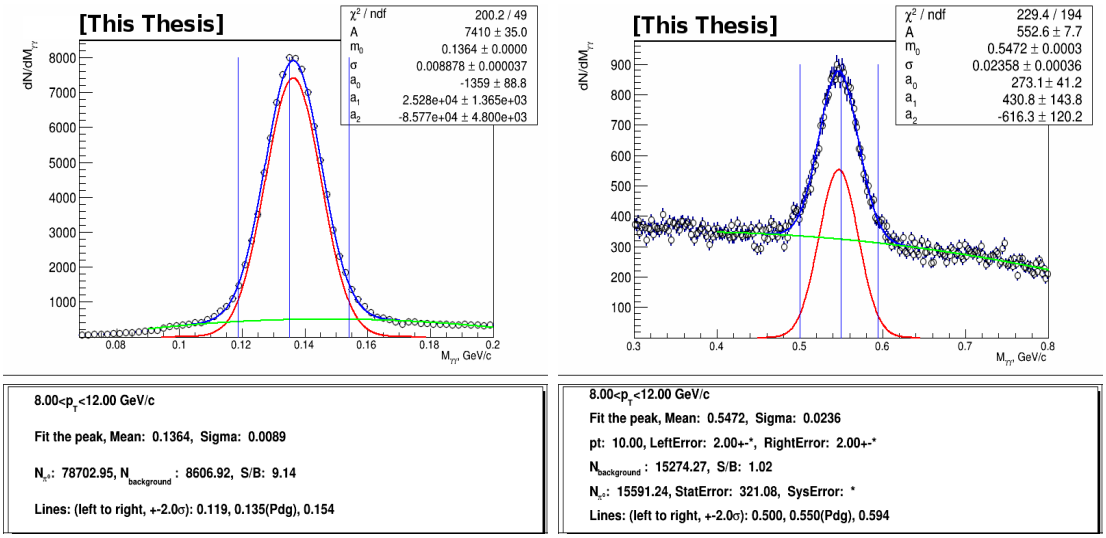

Figure 7.16: Invariant mass distribution of two clusters fit by the function of Gaussian+Polynomial2 for π^0 (left) and η (right) at $8.0 < p_{\rm T} < 12.0$ GeV/c in pp collisions at $\sqrt{s}$ = 7 TeV. The green line and red Gaussian estimate the background and signal contributions, respectively. The blue like Gaussian is the sum of red and green, while the two vertical lines are 2σ width around the peak mean. S/B is the ratio of signal to background in 2σ width.

Fig 7.17 for π^0 and η, respectively.

7.3.2.2 π^0/η-hadron correlations

In the measurement of π^0/η-hadron correlations, a Side Band Subtraction is used to subtract the fake π^0/η-hadron correlations. This method is expressed by three steps as following:

1. A pair of two-clusters with their invariant mass in 2σ width around the peak mean is considered as the π^0/η candidate. The candidate is used as the trigger to make correlations with charged hadrons as a function of $\Delta\varphi$ and $\Delta\eta$. The ratio of signal (π^0/η) to background (fake π^0/η) can be calculated via the fit results.

2. Inside the peak, a fraction of pairs, fake π^0 and η, whose trigger correlations need to be subtracted from the candidate π^0/η-hadron correlations obtained in the step 1. The fake π^0/η trigger correlations are estimated via the correlations with the triggers selected from cluster pairs whose invariant mass ranges are within $4\sigma < |M_{\gamma\gamma} - mean| < 6\sigma$ around the mass peak. While fake π^0-hadron correlations are only estimated with the triggers of fake π^0 with the invariant mass at right side due to the invariant mass distribution at left side going down

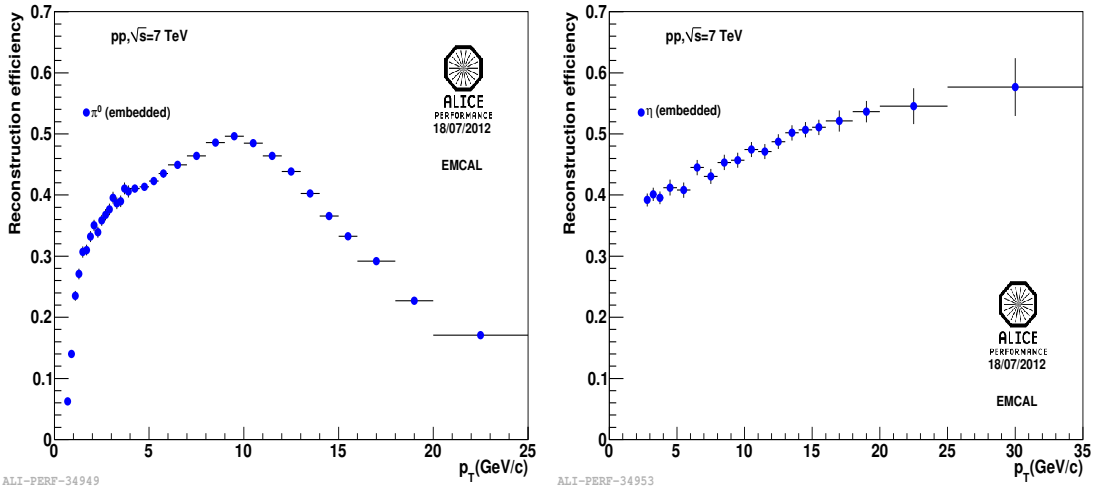

Figure 7.17: Reconstruction efficiency of π^0 (left) and η (right) calculated by embedding single $\pi^0(\eta)$ with a flat distribution into real pp collisions at $\sqrt{s}$ = 7 TeV events. The final pairs were weighted according to the published $\pi^0(\eta)$ spectrum in [68].

sharply. A schematic view of the candidate π^0/η and fake π^0/η selection is shown in Fig. 7.18.

3. According to the candidate π^0/η-hadron correlations from step 1 and fake π^0/η-hadron correlations from step2, the π^0/η-hadron correlations can be obtained by a calculation:

$$Y_S = Y_{S+B}(1+\frac{1}{f_{bkg}}) - Y_B/f_{bkg} \tag{7.9}$$

where Y_S, Y_{S+B} and Y_B are the per-trigger yield of correlations with the triggers of π^0/η, candidate π^0/η and fake π^0/η, respectively; f_{bkg} is a ratio of signal to background calculated from the fit of the invariant mass distributions. More details about the equation can be found in App. A.3. As an example of π^0 trigger correlations, the three per-trigger distributions as a function of azimuthal angle $\Delta\varphi$ are presented at the left panel of Fig. 7.19. As shown in the left panel of Fig. 7.19, the relation of $Y_B > Y_{S+B} > Y_S$ is found. In order to explain this relation, a new schema of the regions of signal+background and background of π^0 is presented in the right panel of Fig. 7.19. As one can see, the region "A" goes down sharply. Hence the pairs with the variant mass in this region are not used to construct correlations with charged hadrons for fake π^0-hadron correlations. The per-trigger yield of correlations with the triggers from the right side band region (region "C") is same as the triggers from the background pairs under the

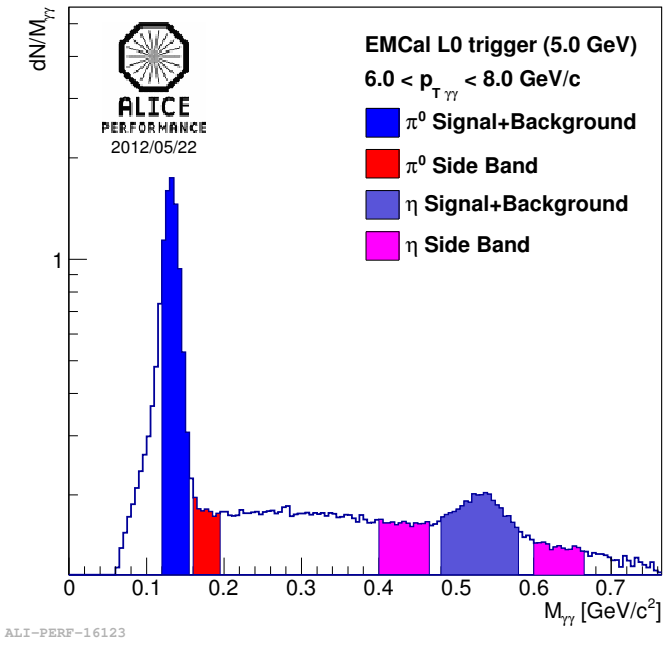

Figure 7.18: Schematic view of the candidate π^0/η and fake π^0/η selection according to the invariant mass of two cluster. The higher blue region and lower blue region are considered as the regions of candidate π^0 and η, respectively. The left red region at $mean + 4\sigma < M_{\gamma\gamma} < mean + 6\sigma$ is considered as the full fake π^0 region, and the two right red reions at $mean - 6\sigma < M_{\gamma\gamma} < mean - 4\sigma$ and $mean + 4\sigma < M_{\gamma\gamma} < mean + 6\sigma$ are considered as the regions of the full fake η region.

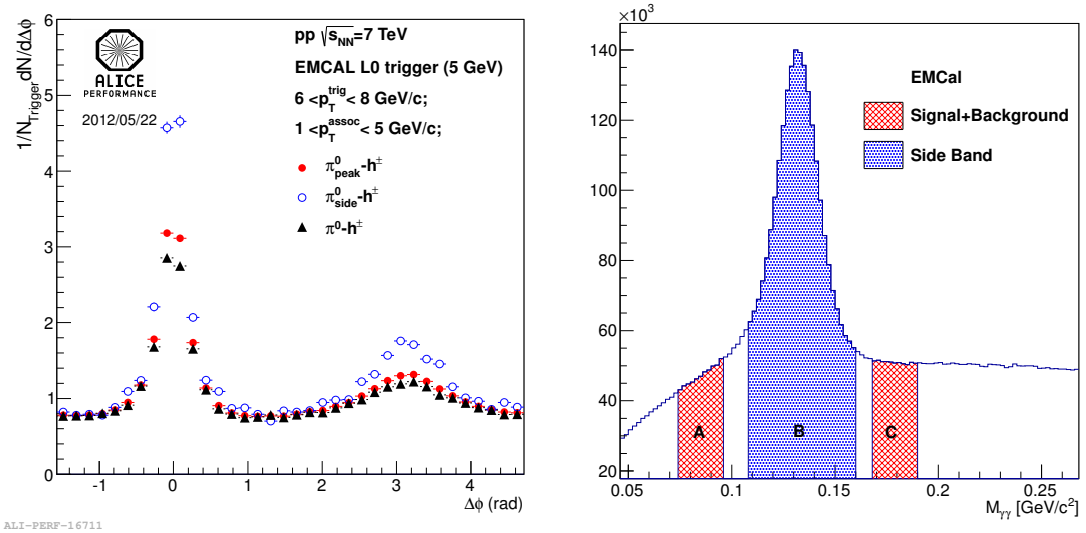

Figure 7.19: Left: Three per-trigger yields with triggers of π^0 (fill triangle), candidate π^0 (fill circle) and fake π^0 (open circle) at $6.0 < p_{\mathrm{T}}^{\mathrm{trig}} < 8.0$ GeV/c and $1.0 < p_{\mathrm{T}}^{\mathrm{assoc}} < 5.0$ GeV/c in pp at $\sqrt{s} = 7$ TeV. Right: A schema of two types regions, signal+background (tagged by "B") and background (tagged by "A" and "C").

peak (region "B"). The per-trigger yields with the triggers in the region "B" and "C" are noted by Y_{S+B} and Y_B, respectively. The fake π^0 and η may be a pair with two clusters from the following cases:

- One cluster is formed by a photon of π^0 decays and the other one is from η.
- One cluster is formed by a photon and the other one is created by the charged hadron.
- Two clusters are created by two photons which are decays from two different $\pi^0(\eta)$.
- Two clusters are produced by charged hadrons.

In each case, the parton which result in Y_B has higher energy than the parton giving Y_{S+B} and Y_S, so $Y_{S+B} > Y_S$. Because Y_{S+B} includes a fraction of Y_B, hence $Y_{S+B} > Y_S$ make sense.

In this analysis, the correlations are measured with the triggers of π^0 and η at $8.0 < p_{\mathrm{T}}^{\mathrm{trig}} < 12.0$ GeV/c. Their per-trigger yields of Y_{S+B}, Y_B and Y_S are shown in Fig. 7.20. Each distribution is corrected by the track contamination and tracking efficiency. Here, the per-trigger yields of correlations with triggers of π^0 and η are not corrected by the reconstruction efficiencies of π^0 and η. In π^0 trigger correlations,

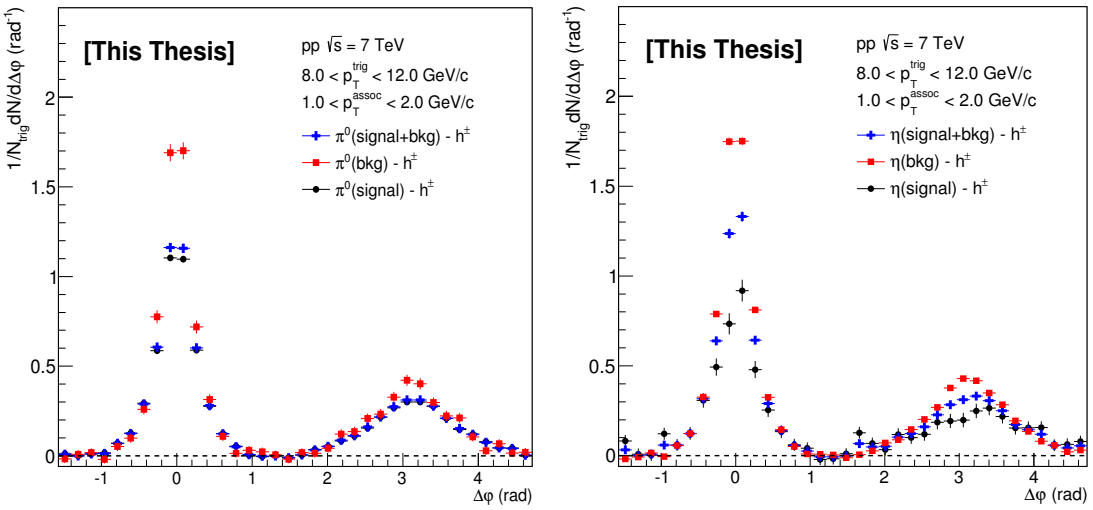

Figure 7.20: Three per-trigger yields, Y_{S+B} (blue cross), Y_B (red square) and Y_S (black circle), of π^0 (left) and η (right) at $8.0 < p_{\mathrm{T}} < 12.0$ GeV/c and $1.0 < p_{\mathrm{T}} < 2.0$ GeV/c.

the ratio of signal to background is large, so we observe that the Y_S is very close to Y_{S+B}. While for η trigger correlations, the ratio is small which results in Y_{S+B} much higher than Y_S.

7.3.3 Decay γ-hadron correlations

The correlations with the triggers of decay photons from π^0 (Y_{γ,π^0}) and from η ($Y_{\gamma,\eta}$) can to be determined by weighting the measurements of π^0-hadron correlations (Y_{π^0}) and η-hadron correlations (Y_{η}) in pair-by-pair procedure. The weighting factor called decay map probability factor is obtained from a Monte-Carlo study discussed later. All decay γ-hadron correlations are estimated from the correlations with triggers of decay photons from π^0 and η via a ratio of all decay photons to decay photons from π^0. In this analysis, only decay photons from π^0 and η are taken into account, and other meson contributions (*e.g.* ω, η', ϕ ...) are not measured and are considered to be equivalent to Y_{η}.

7.3.3.1 Pair-by-pair weighting

Taking the analysis of decay photon-hadron correlations with the decay photons from π^0 as an example, the weighting determination includes two independent procedures which are weight analysis of number of triggers and correlation pairs. In a real detector however, the reconstructed π^0 differs in both momentum and position from the true distribution due to the π^0 identification cuts and detector effects. The π^0 identification efficiency is taken into account in the pair-by-pair weighting procedure for obtaining the true π^0 triggers and true π^0-hadron correlations. For a given π^0 distribution, the number of its decay photons in a p_{T} bin (*e.g.* $a < p_{\mathrm{T}} < b$ GeV/c) can be obtained by a calculation as:

$$N^{\gamma(\pi^0)}(a < p_{\mathrm{T}}^{\gamma} < b) = \int_a^{\infty} \wp_{\pi^0}(p_{\mathrm{T}}^{\gamma}, p_{\mathrm{T}}^{\pi^0}) \cdot \frac{N^{\pi^0}(p_{\mathrm{T}}^{\pi^0})}{\varepsilon_{\pi^0}} dp_{\mathrm{T}}^{\pi^0} \tag{7.10}$$

where $\wp_{\pi^0}(p_{\mathrm{T}}^{\gamma}, p_{\mathrm{T}}^{\pi^0})$ is the decay map probability obtained from a given π^0 with $p_{\mathrm{T}}^{\pi^0}$ to decay into a photon of p_{T}^{γ}, and ε_{π^0} is the π^0 identification efficiency. In principle, the calculation of decay map probability function needs to implement the EMCal acceptance, smearing effects, resolutions of energy and position. While as summarized in Tab. 7.1, the obtained π^0 reconstruction reach "generator level" by using some of correction factors (In this analysis, only the reconstruction efficiencies of π^0 and η are considered for the correction). Therefore, the probability function can be determined analytically and/or from the PYTHIA simulation and will be discussed later. Similarly, the correlation pairs are obtained by following calculation:

$$N^{\gamma-h(\pi^0-h)}(a < p_{\mathrm{T}}^{\gamma} < b) = \int_a^{\infty} \wp_{\pi^0}(p_{\mathrm{T}}^{\gamma}, p_{\mathrm{T}}^{\pi^0}) \cdot N^{\pi^0-h}(p_{\mathrm{T}}^{\pi^0}) dp_{\mathrm{T}}^{\pi^0} \tag{7.11}$$

Theoretically, the $N^{\gamma(\pi^0)}(a < p_{\rm T}^{\gamma} < b)$ and $N^{\gamma-h(\pi^0-h)}(a < p_{\rm T}^{\gamma} < b)$ need to be estimated by weighting π^0 contributions at $p_{\rm T} > a$ GeV/c. However, the momentum range of the measured π^0 and its trigger correlations is limit. For example, the measured momentum range can only go up to 20.0 GeV/c to π^0 and 25.0 GeV/c to η in this analysis. To estimate the contributions above this momentum, a Cut-Off method is used by fitting the π^0-hadron correlations as a function of π^0 $p_{\rm T}$ with the Power law function. More details about this method will be discussed in Sec. 7.3.3.3.

7.3.3.2 Decay map probability

As it is discussed, the detector effects need to be considered when calculating the decay map probability. While the $\pi^0(\eta)$-hadron correlations are measured with all correction factors to go to the "generation level". In this case, the decay map probability function can be estimated analytically and/or from the PYTHIA simulation.

The analytical calculation shows that this probability distribution should be flat for a given π^0 with $p_{\rm T}^{\pi^0}$ to its decay photons at any $p_{\rm T}$. In this case, the likelihood of yielding a photon at any $p_{\rm T}^{\gamma}$ can be written in terms of the decay phase space as $dN_{\gamma}/dp_{\rm T}^{\gamma} = 2/p_{\rm T}^{\pi^0}$ where 2 reflects the number of decay photons. The probability value should be zero at $p_{\rm T}^{\pi^0} < p_{\rm T}^{\gamma,{\rm dec}}$ because the decay photon can not have higher energy than its parent π^0. Generally, the decay map probability function, $\wp_{\pi^0}(p_{\rm T}^{\pi^0})$, for a decay photon $p_{\rm T}$ interval of $a < p_{\rm T}^{\gamma} < b$, can be expressed as:

$$\wp_{a-b}(p_{\rm T}^{\pi^0}) = \begin{cases} = 0, & p_{\rm T}^{\pi^0} < a \\ \displaystyle\int_a^{p_{\rm T}^{\pi^0}} dp_{\rm T}^{\gamma} \frac{2}{p_{\rm T}^{\gamma}} = 2\left(1 - \frac{a}{p_{\rm T}^{\pi^0}}\right), & a < p_{\rm T}^{\gamma} < b \\ \displaystyle\int_a^{b} dp_{\rm T}^{\gamma} \frac{2}{p_{\rm T}^{\gamma}} = 2\left(\frac{b-a}{p_{\rm T}^{\pi^0}}\right), & p_{\rm T}^{\gamma} > b \end{cases} \tag{7.12}$$

An example of the weight probability function determined analytically and estimated from simulation MC truth for decay photon $p_{\rm T}$ interval of $8.0 < p_{\rm T} < 12.0$ GeV/c is shown in Fig. 7.21.

7.3.3.3 Cut-Off correction

As presented in Eq. 7.11, the number of decay photons N^{γ} at $a < p_{\rm T} < b$ should theoretically come from π^0/η at $p_{\rm T} > b$ up to infinite $p_{\rm T}$. In fact, the mesons can not reach a certain $p_{\rm T}$ due to the limit of system collision energy $\sqrt{s}$. In this analysis,

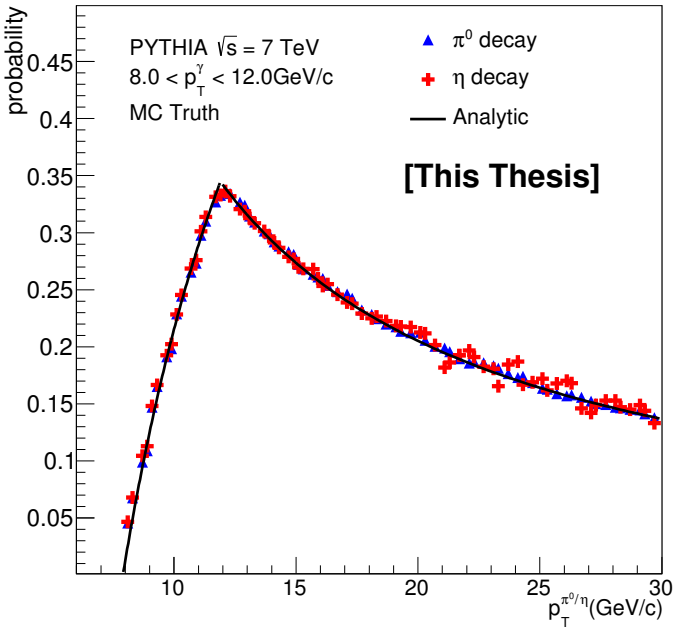

Figure 7.21: Decay map probability (normalized to one photon) for the photon at $8.0 < p_{\mathrm{T}}^{\gamma} < 12.0$ GeV/c as a function of $p_{\mathrm{T}}^{\pi^0}$ and p_{T}^{η} from simulation truth and analytically.

the p_{T} of π^0 and η can only go up to 20 GeV/c and 25 GeV/c in V2 clusterization, respectively. A correction is included to decay yields to account for the contribution from mesons at higher p_{T}. The correction factor can be estimated from a fitting to the meson-hadron correlations yield as a function of trigger p_{T} with a function of power law, which is calculated as:

$$C_{cutoff} = \frac{\int_{<p_{\mathrm{T}}^{max}} dp_{\mathrm{T}}^{meson-h} \wp(p_{\mathrm{T}}^{meson-h}) \frac{dN^{meson-h}}{dp_{\mathrm{T}}^{meson-h}} / \int_{\infty} dp_{\mathrm{T}}^{meson-h} \wp(p_{\mathrm{T}}^{meson-h}) \frac{dN^{meson-h}}{dp_{\mathrm{T}}^{meson-h}}}{\int_{<p_{\mathrm{T}}^{max}} dp_{\mathrm{T}}^{meson} \wp(p_{\mathrm{T}}^{meson}) \frac{dN^{meson}}{dp_{\mathrm{T}}^{meson}} / \int_{\infty} dp_{\mathrm{T}}^{meson} \wp(p_{\mathrm{T}}^{meson}) \frac{dN^{meson}}{dp_{\mathrm{T}}^{meson}}} \tag{7.13}$$

where p_{T}^{max} is 20 GeV/c to π^0 and 25 GeV/c to η. Because of the limited simulation and data statistics, the cut-off correction factor can not be analyzed above 20 GeV/c to π^0 and 25 GeV/c to η. But according to the results at PHINEX, the contribution is less than 1% above 20 GeV/c to correlations at $8.0 < p_{\mathrm{T}}^{\mathrm{trig}} < 12.0$ GeV/c and $1.0 < p_{\mathrm{T}}^{\mathrm{assoc}} < 2.0$ GeV/c [313].

7.3.3.4 Decay γ-hadron correlations

Based on the π^0/η-hadron correlations, the corresponding decay photon trigger correlations can be obtained by using the pair-by-pair weighting and cut-off correction for high-p_{T} contributions. The per-trigger yields of correlations with the

trigger of decay photon from π^0 and η are shown in Fig. 7.22. Here, the per-trigger yields of correlations with triggers of π^0 and η are corrected by the reconstruction efficiencies of π^0 and η presented in Fig. 7.17. Total decay γ-hadron correlations

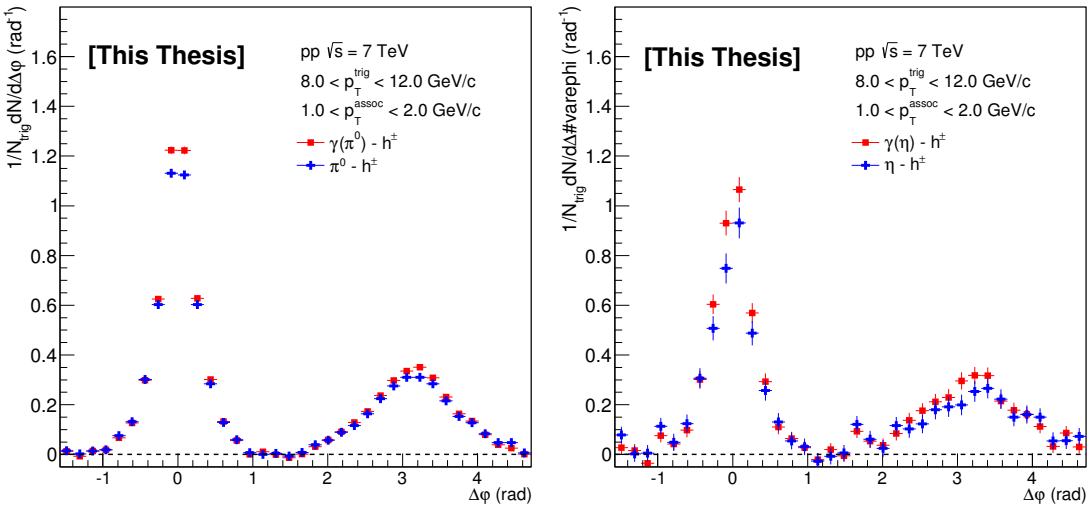

Figure 7.22: Per-trigger yields of correlations with trigger as decay photon from π^0 (left, red) and η (right, red) at $8.0 < p_{\mathrm{T}}^{\mathrm{trig}} < 12.0$ GeV/c and $1.0 < p_{\mathrm{T}}^{\mathrm{assoc}} < 2.0$ GeV/c in pp collisions at $\sqrt{s} = 7$ TeV.

are estimated from the correlations with the triggers of decay photon from π^0 and η via a ratio of all decay photons to decay photons from π^0. In this analysis, only decay photons from π^0 and η are analyzed, and other meson contributions (*e.g.* ω, η', ϕ ...) are not measured and considered to be equivalent to Y_η. Finally, the total decay per-trigger yield can be calculated according to:

$$Y_{\mathrm{decay}} = \frac{1}{\delta} * Y_{\mathrm{decay}}(\pi^0) + (1 - \frac{1}{\delta}) * Y_{\mathrm{decay}}(\eta) \tag{7.14}$$

where δ is the ratio of the total number of decay photons to the number of decay photons from π^0. The ratio is calculated by analyzing a Cocktail Generator simulation with π^0 and η from ALICE measurements [68] and other sources from m_{T} scaling [315, 316] as discussed in Sec. 7.3.4. The left panel of Fig. 7.23 shows this ratio as a function of p_{T}. The value at $8.0 < p_{\mathrm{T}} < 12.0$ GeV/c is estimated about 1.21 ± 0.01. According to Eq. 7.14 and the ratio of all decay photon to π^0 decay photon, the per-trigger yield of inclusive γ-hadron correlations can be obtained and shown in the right panel of Fig. 7.23.

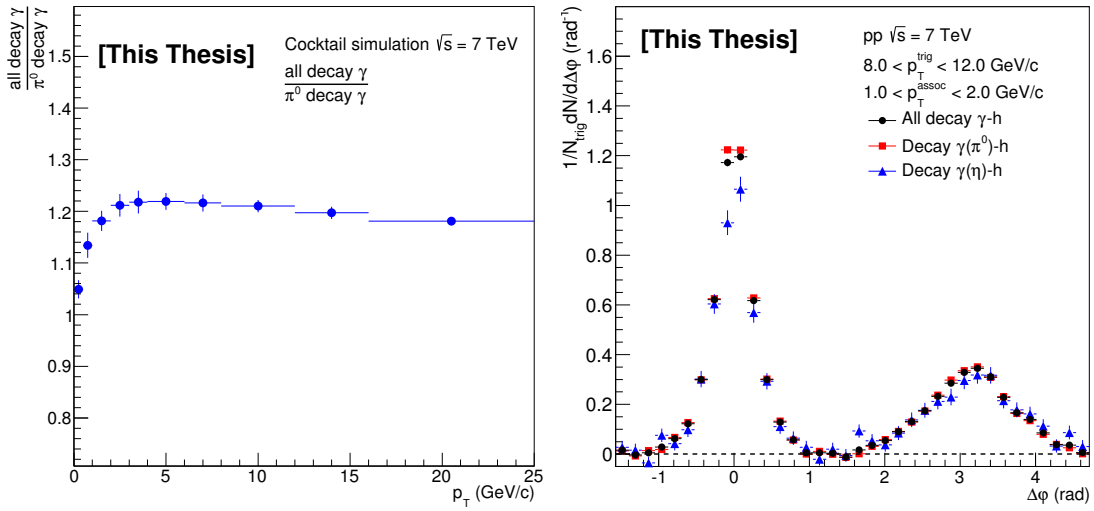

Figure 7.23: Left: Ratio of all decay photon to π^0 decay photon as a function of p_{T} calculated by Cocktail simulation at $\sqrt{s}$ = 7 TeV, taken from [314]; Right: Per-trigger yield of correlations as trigger of all decay photon estimated from decay photon of π^0/η-hadron correlations in pp at $\sqrt{s}$ = 7 TeV.

7.3.4 R_γ calculation

In the statistical subtraction method, the last important variable is the Double Ratio, R_γ, as defined in Eq. 7.6 to achieve the direct γ-hadron correlations according Eq. 7.5. Experimentally, R_γ is calculated generally as:

$$R_\gamma = \frac{N_{\gamma_{inc}}/N_{\pi^0}|_{\mathrm{data}}}{N_{\gamma_{decay}}/N_{\pi^0}|_{\mathrm{cocktail}}} \approx \frac{N_{\gamma_{inc}|_{\mathrm{data}}}}{N_{\gamma_{decay}}|_{\mathrm{cocktail}}} \tag{7.15}$$

After the approximate canceling of the π^0 contributions in the two input ratios, this ratio describes the ratio of the measured inclusive primary photon to the simulated decay photon spectrum. If this ratio rises above unity, it means more inclusive photons are measured than expected from meson decays and indicates the direct photon signal exists. Using this calculation, many effects are canceled in the data measurements, which include:

- The energy scale error which completely cancels if it is an overall scale factor.
- The uncertainty in the efficiency calculation which partially cancels as the single photon efficiency has a direct impact on the two-photon efficiency needed for the invariant mass analysis of the π^0.
- The systematic error due to the conversion correction, which partially cancels for the same reason.

- The overall normalization uncertainty of the trigger if using EMCal triggered events for the analysis.

In this analysis, the used R_γ is calculated from photon conversion method. The numerator in Eq. 7.15 includes two measurements which are inclusive photon and π^0. The inclusive π^0 measurement in pp at $\sqrt{s} = 7$ TeV is taken from [68], and the corrected inclusive γ is measured by photon conversion method as shown in the left panel of Fig. 7.24. The ratio of inclusive photon to π^0 is calculated by combining with the measurement of π^0, as shown in the right panel of Fig. 7.24.

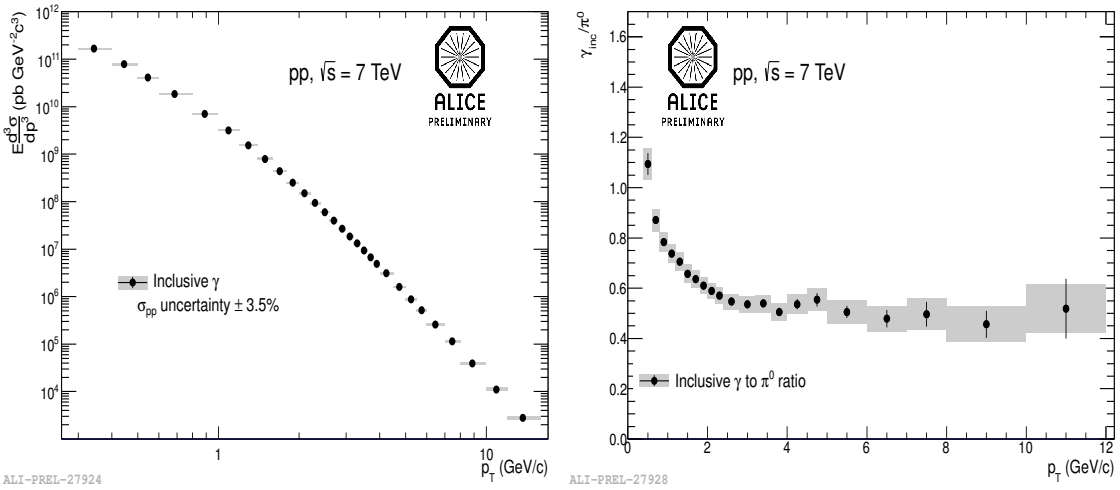

Figure 7.24: Left: Fully corrected γ invariant cross section as a function of p_{T} in pp collisions at $\sqrt{s} = 7$ TeV; Right: Ratio of inclusive photon to π^0 measured in pp at $\sqrt{s} = 7$ TeV. Taken from [314].

In the denominator of Eq. 7.15, the distributions of all decay photon and π^0 are estimated from a Cocktail simulation by m_{T} scaling. Two most contributions to decay photons are from π^0 and η by the two-photon decay channel. The decay photon from π^0 and η provides about 80% and 15% of all decay photons, respectively. The remaining about 5% is distributed between the decay products of ϕ, η', ω and ρ^0 meson, the Σ^0 baryon and other decays. The largest contribution from theses additional sources is from the decay of the ω with the order of 2%. The cocktail generator is used to fit the meson spectra as inputs. In the pp collisions, the π^0 and η spectra are measured and the corresponding fits are used as the inputs to simulate the decay photon spectra. To simulate the decay photon spectra from other mesons, their spectra have to be estimated by m_{T} scaling. The m_{T} is defined as:

$$m_{\mathrm{T}} = \sqrt{p_{\mathrm{T}}^2 + m_{\pi^0}^2} \tag{7.16}$$

The m_{T} scaling phenomenology was found by the WA80 collaboration [315] and was extended to a broader set of different mesons [316]. Taking η as an example, its m_{T} spectrum can be estimated according to:

$$E\frac{dN}{dp^3} = C_m \cdot P_{\pi^0}\sqrt{p_{\mathrm{T}}^2 + m_\eta} \tag{7.17}$$

where C_m represents the relative normalization of the η-m_{T} spectrum to the neutral π^0-m_{T} spectrum and must be obtained from experimental results. P_{π^0} is a parametrization of the π^0 spectrum and m_η is the mass of the η meson. The considered hadron contributions and their m_{T} scaling factors are listed in Tab. 7.2. In

Meson	Mass (MeV/c^2)	m_{T} factor (C_m)	Decay Branches	Branching ratio
π^0	134.98	–	$\gamma\gamma$	98.789%
			$e^+e^-\gamma$	11.1198%
η	547.3	0.46	$\gamma\gamma$	39.21%
			$\pi^+\pi^-\gamma$	4.77%
			$e^+e^-\gamma$	4.9×10^{-3}
ρ^0	770.0	1.0	$\pi^+\pi^-\gamma$	9.9×10^{-3}
			$\pi^0\gamma$	7.9×10^{-4}
ω	781.9	0.9	$\pi^0\gamma$	8.5%
			$\eta\gamma$	6.5×10^{-4}
η'	957.8	0.25	$\rho^0\gamma$	30/2%
			$\omega\gamma$	3.01%
			$\gamma\gamma$	2.11%
ϕ	1019.5	0.35	$\eta\gamma$	1.3%
			$\pi^0\gamma$	1.25×10^{-3}
			$\omega\gamma$	$<5\%$
Σ^0	1192.6	0.49	$\Lambda\gamma$	100%
			$\Lambda\gamma\gamma$	$< 3\%$

Table 7.2: Dominant sources of decay photons from hadronic decays and the employed m_{T} factor scaling relative to the π^0 measurement. The masses, decay branches, and branching ratios of different hadrons are listed, taken from [314].

the Cocktail simulation, all the hadrons listed in Tab. 7.2 are as the inputs. From the simulation, the decay photon spectra from different hadrons obtained for pp collisions at $\sqrt{s} = 7$ TeV are shown in the left panel of Fig. 7.25, and the ratios of

corresponding decay γ to π^0 as well as the ratio of all decay γ to π^0 are presented in the right panel of Fig. 7.25.

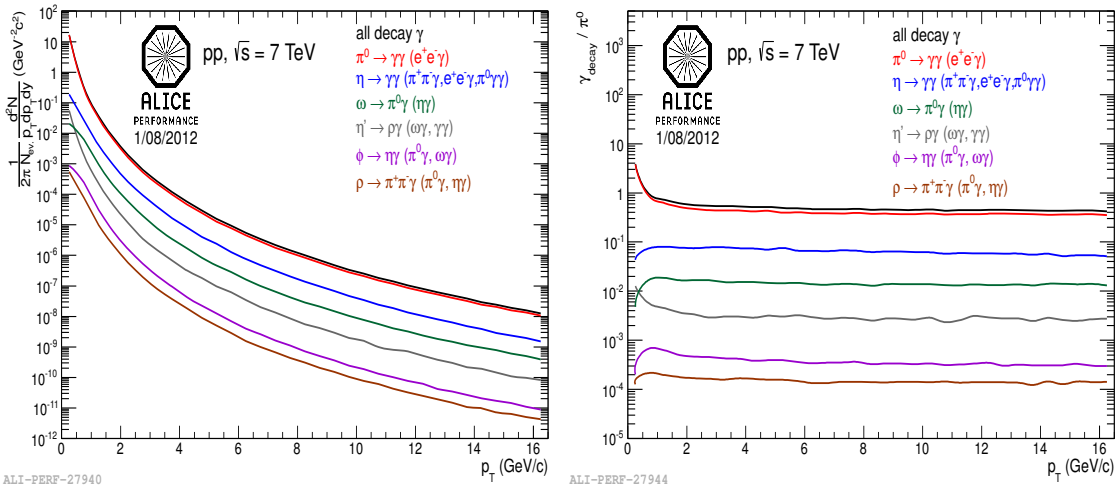

Figure 7.25: Left: Decay photon spectra from different hadrons obtained for in pp collisions at $\sqrt{s}$ = 7 TeV; Right: Ratios of corresponding decay γ to π^0 as well as the ratio of all decay γ to π^0. Taken from [314].

When the ratio of inclusive γ to π^0 measured from pp data together the ratio of all decay γ to π^0 obtained from Cocktail generator is calculated, the Double Ratio, R_γ, defined in Eq. 7.6, can be calculated according to formula Eq. 7.15. The final result including NLO pQCD predictions is shown in Fig. 7.26. The NLO pQCD prediction is calculated as:

$$\Re_{NL0} = 1 + (N_{coll} \cdot \frac{N_{\gamma_{direct,NLO}}}{N_{\gamma_{decay}}|_{\text{cocktail}}}) \tag{7.18}$$

Three predictions with different momentum scales (μ = 0.5, 1.0, 2.0 p_{T}) are calculated and shown in the figure. The width of the band is given by the differences in the scales with central value obtained from $\mu = 1$. In pp collisions, the N_{coll} is set to one. The prediction from the pQCD calculation is consistent with the measurement result. Both of the measurement and predication indicate the signal of direct photon is not strong at p_{T} below 12.0 GeV/c. Higher p_{T} results are expected to be measured in the future soon.

7.3.5 Direct γ-hadron correlations

The direct photon-hadron correlations can be extracted by subtracting all decay photon-hadron correlations from the inclusive photon-hadron correlations according

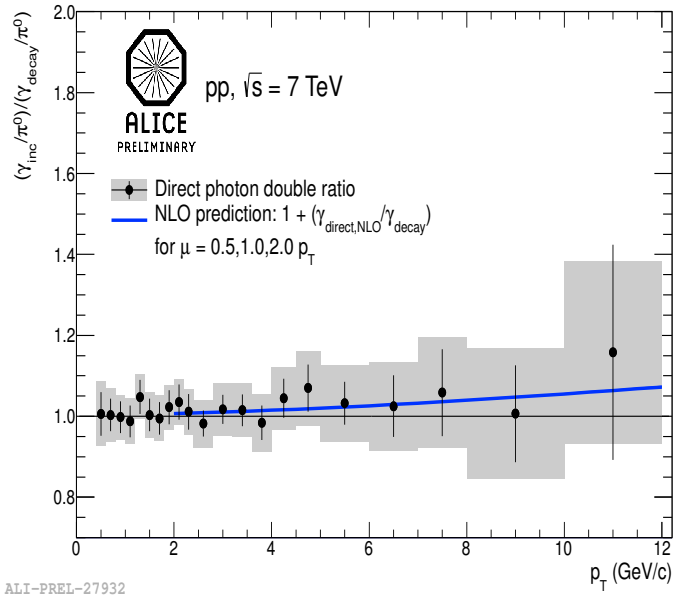

Figure 7.26: Direct photon signal presented via the double ratio $\frac{N_{\gamma_{inc}}/N_{\pi^0}|_{\rm data}}{N_{\gamma_{decay}}/N_{\pi^0}|_{\rm cocktail}}$ for pp collisions at $\sqrt{s} = 7$ TeV. Different NLO calculations for three momentum scales are plotted as a blue band. Taken from [314].

to Eq. 7.5. The per-trigger yield of direct photon at $8.0 < p_{\rm T}^{\rm trig} < 12.0$ GeV/c and $1.0 < p_{\rm T}^{\rm assoc} < 2.0$ GeV/c is shown in Fig. 7.27. The R_γ at $8.0 < p_{\rm T} < 12.0$ GeV/c is estimated from the average of two values at $8.0 < p_{\rm T} < 10.0$ GeV/c and $10.0 < p_{\rm T} < 12.0$ GeV/c. This result indicates it is impossible to extract a enough significant measurement of the direct photon trigger correlations from current statistics of pp collisions at $\sqrt{s} = 7$ TeV. But the yield is zero consistent with systematic errors on the near side and a significant peak above zero on the away side are observed from the preliminary measurement.

7.4 Summary

Direct photons mainly consist of prompt photons produced at the leading-order from Compton and annihilation QCD processes and fragmentation photons at next-to-leading-order processes. In addition, one more contributions to direct photons at nucleus-nucleus collisions are thermal photons and jet conversion from the interactions of the hot and dense QCD medium. Generally, the parton fragmentation function is considered to be characterized by the imbalance parameter $x_{\rm E} = -\frac{\vec{p}_{\rm T}^{\gamma}\cdot\vec{p}_{\rm T}^{h^\pm}}{|\vec{p}_{\rm T}^{\gamma}|^2}$ where the $p_{\rm T}^{\gamma}$ and $p_{\rm T}^{h^\pm}$ are the momenta of prompt photons and charged hadrons.

Experimentally, the processes producing the leading-order direct photons can

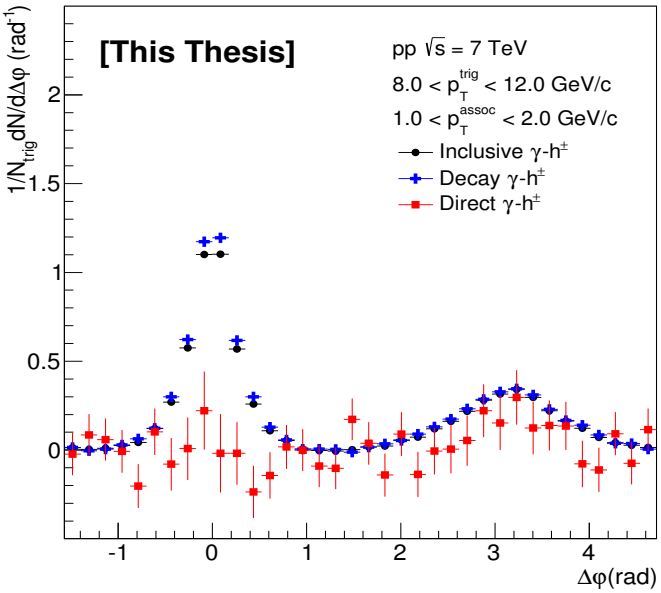

Figure 7.27: Per-trigger yield of direct photon-hadron correlations (red) is estimated by subtracting decay photon-hadron correlation (blue) from inclusive photon-hadron correlations (black) according to Eq. 7.5 at $8.0 < p_{\mathrm{T}}^{\mathrm{trig}} < 12.0$ GeV/c and $1.0 < p_{\mathrm{T}}^{\mathrm{assoc}} < 2.0$ GeV/c in pp collisions at $\sqrt{s} = 7$ TeV.

be tagged by identifying leading isolated photons and their correlated associated hadrons in opposite azimuth direction. In this analysis, the used isolation technique requires no particles including both charged and neutral particles with $p_{\mathrm{T}} > 0.5$ GeV/c in a cone of radius $R = \sqrt{\Delta\varphi^2 + \Delta\eta^2} = 0.4$ around a photon candidate with highest p_{T} in one event. The purity of isolated photons is estimated by a two-component binned likelihood method by fitting the cluster shower shape long axis λ_0^2 distribution with a mix of scaled signal (MC γ-jet) and contamination (non-isolated cluster) distributions. Isolated γ-hadron correlations are obtained by subtracting Isolated π^0-hadron correlations considered as the main contamination from isolated cluster-hadron correlations with the isolated photon purity. The slope of imbalance parameter x_{E} from isolated π^0-hadron correlations is compared to DSS fragmentation functions. Similarly, in the isolated γ-hadron correlations the slope of imbalance parameter x_{E} is calculated by fitting the imbalance parameter distribution with the function Ae^{-B} at $8.0 < p_{\mathrm{T}}^{iso\gamma} < 25.0$ GeV/c.

Another method, statistical subtraction, is used to extract the signal of direct photons for their trigger correlations with charged hadrons. The analysis method is based on a relation that total photons consist of direct photons and decay photons from hadrons. In this analysis, the direct photon-hadron correlations are obtained

by subtracting decay photon-hadron correlations from inclusive photon-hadron correlations. Firstly, the inclusive photon-hadron correlations are measured with the triggers of clusters filtered by photon identification and corrected with the photon purity and photon identification efficiency. The photon purity is calculated by binned likelihood fit to the cluster shaper shape long axis λ_0^2 distribution. In the binned likelihood fit, three λ_0^2 distributions of photon clusters, charged hadron clusters and merged π^0 clusters are used as inputs. The photon cluster λ_0^2 distribution is estimated from the clusters which are under π^0 and η peak in 1.2σ width. The charged hadron cluster λ_0^2 distribution is estimated from the clusters which are matched by cluster-matching algorithm where the $\Delta\varphi = \varphi_{cluster} - \varphi_{track} < 0.004$ and $\Delta\eta = \eta_{cluster} - \eta_{track} < 0.002$. The third contribution, merged π^0 cluster λ_0^2 distribution, is estimated from the clusters which are identified as π^0 by cluster splitting method. Secondly, the contamination, decay photon-hadron correlations, is obtained from π^0/η-hadron correlations by pair-by-pair weighting with the photon decay map probability function. The π^0/η-hadron correlations are measured by a Side Band subtraction method. The weight factor of photon decay map probability function is calculated by a Monte-Calo study. Thirdly, an important factor, Double Ratio R_γ, defined as a ratio of inclusive photons to decay photons, is calculated by a Cocktail simulation. At last, a limit esitmation of the direct photon-hadron correlations is measured by subtracting all decay photon-hadron correlations from the inclusive photon-hadron correlations by a so-called statistical subtraction method. This result indicates it is impossible to extract a enough significant measurement of the direct photon trigger correlations from current statistics of pp collisions at $\sqrt{s}$ = 7 TeV. But the yield is zero consistent with systematic errors on the near side and a significant peak above zero on the away side are observed from the preliminary measurement.

Chapter 8

Summary and outlook

The main goals of the ALICE experiment at CERN is to search for and study a new phase of strongly interacting matter called quark-gluon plasma (QGP) in nucleus-nucleus collisions at the LHC. In this new state, the quarks and gluons are no longer confined in the hadrons, but more freely over longer distances. It is well known that such a phase probably exists in a microsecond after the Big Bang, and is expected to be recreated in the laboratory via heavy-ion collisions at a sufficiently large energy density. It is a large experimental challenge to prove the fleeting existence of the QGP based on its characteristic signatures extracted from the final products of the heavy-ion collisions. The main work presented in this thesis is to study the medium effects by two-particle correlations with the triggers of neutral pions in pp and Pb+Pb collisions at a center-of-mass energy of $\sqrt{s_{\rm NN}} = 2.76$ TeV in the ALICE experiment at CERN/LHC. In addition, the correlations between direct photons and charged hadrons in pp collisions at $\sqrt{s} = 7$ TeV are measured by both isolation technique and statistical subtraction methods to study the azimuthal angle distribution and the parton fragmentation function. The ultimate objective of all the measurements is to study the properties of the hot and dense QCD matter.

8.1 Summary

The initial energetic partons are produced by short-distance hard-scatterings at the early stage during the collisions. The partons have to go through the hot and dense QGP medium and are expected to lose their energy due to the interactions between partons inside the medium via gluon bremsstrahlung and multiple collisionss with other partons in the medium. This parton energy loss, which is often

referred to as "jet quenching", depends on the color density of the medium and on the distance traversed inside the medium. The fragmentation of the reduced-energy parton will yield fewer particles at high p_{T} in the final state. That is to say the energy lost by a parton provides fundamental information on the thermodynamical and transport properties of the medium. A comparison of the final-state high-p_{T} particle yields in pp and A+A collisions will thus reveal the effect of jet-quenching.

At low jet transverse momenta ($p_{\mathrm{T,jet}} < 50$ GeV/c), background fluctuations due to the underlying event dominate and event-by-event jet reconstruction becomes difficult. Two-particle correlations allow the study of medium effects on the jet fragmentation without the need for jet reconstruction. In such an analysis, a particle is chosen from a p_{T} region and called the *trigger particle*. The so called *associated particles* from another p_{T} region are correlated to the trigger particle where $p_{\mathrm{T}}^{\mathrm{assoc}} < p_{\mathrm{T}}^{\mathrm{trig}}$. The associated per-trigger yield is measured as a function of the azimuthal angle difference $\Delta\varphi = \varphi_{\mathrm{trig}} - \varphi_{\mathrm{assoc}}$ and pseudo-rapidity difference $\Delta\eta = \eta_{\mathrm{trig}} - \eta_{\mathrm{assoc}}$. The medium effects are observed from the suppression of the correlation yield on the away side at high-$p_{\mathrm{T}}^{\mathrm{assoc}}$, enhancement and double-peak structure on the away side, and "ridge" on the near side at low both $p_{\mathrm{T}}^{\mathrm{trig}}$ and $p_{\mathrm{T}}^{\mathrm{assoc}}$. Direct photon-hadron correlations, offer two major advantages as compared to di-jet measurements because of the nature of the photon. First of all, in contrast to partons, photons do not carry color charge and hence do not interact strongly when traversing the medium. Secondly, the direct photon production at leading-order (LO) in pp and A+A collisions is dominated by the QCD Compton scattering process, $q + g \rightarrow q + \gamma$ and $q + \bar{q} \rightarrow g + \gamma$ annihilation process, and the photon momentum in the center-of-mass frame is approximately balanced by that of the recoil parton when considering the initial transverse momentum, k_{T}, of the colliding partons inside the nucleons. In nucleus-nucleus collisions, the direct photon contributions from next-to-leading-order (NLO) processes, such as fragmentation photons and thermal photons, are expected to be small ($\approx 10\%$) at high p_{T}. For these reasons, direct photon-hadron correlations have been considered as a "golden channel" for studying the properties of parton energy loss including parton fragmentation function without the need of the jet reconstruction.

8.1.1 Neutral pion-hadron correlations

The opening angle of decay photons from neutral mesons becomes smaller with increasing neutral mesons energy due to the Lorentz boost. In the EMCal at ALICE,

when the energy of the π^0 (η) is larger than 5-6 GeV ($\sim$ 22 GeV), the two photons start to be close, and their two electromagnetic showers overlap in the calorimeter cells. A new identification π^0 method, cluster splitting method, is used to identify π^0 for measuring the π^0-hadron correlations. This method can achieve to high $p_{\rm T}$ and improve statistics of the trigger number of π^0, which be shortly summarized as following several steps. First of all, clusters with large shower shape long axis λ_0^2 and one or two local maxima are selected to as the inputs for using splitting method. Secondly, the filtered clusters are split two new sub-clusters with the two highest local maxima cells and aggregate all the cells around them with 3×3 clusters clusterization. At last, the two new sub-clusters are paired to calculate their invariant mass for obtaining the trigger π^0 of the correlations. The associated charged hadrons are reconstructed in the central tracking System, ITS and TPC. The π^0-hadron correlations consist in studying the relative azimuthal and transverse momentum distributions of charged particles associated to a high-$p_{\rm T}$ π^0 selected as a trigger particle. The two main observables, azimuthal angle correlations $\Delta\varphi = \varphi_{\rm trig} - \varphi_{\rm assoc}$ and charged hadrons yields as a function of their $p_{\rm T}$, are measured to study the properties of medium. Especially, the per-trigger yield modification factors, $I_{\rm AA}(p_{\rm T}^{\pi^0}, p_{\rm T}^{h^\pm}) = \frac{Y^{\rm PbPb}(p_T^{\pi^0}, p_T^{h^\pm})}{Y^{\rm pp}(p_{\rm T}^{\pi^0}, p_T^{h^\pm})}$ and $I_{\rm CP} = \frac{Y^{\rm PbPb}_{\rm central}(p_{\rm T}^{\pi^0}, p_T^{h^\pm})}{Y^{\rm PbPb}_{\rm peripheral}(p_{\rm T}^{\pi^0}, p_{\rm T}^{h^\pm})}$, are analyzed. While the $I_{\rm CP}$ is not measured because of the limited statistics of Pb+Pb peripheral simulations for extracting the correction factors. But the measurements will be updated soon when the enough simulations are produced.

The per-trigger yield of charged hadrons at central Pb+Pb collisions is obtained by subtracting the flat and flow backgrounds. In the flat background estimation, three methods are used to estimate the minimum value of the background. The charged pion flow is used instead of π^0 flow in the flow background estimation. The yield modification factors of $I_{\rm AA}$ at central Pb+Pb collisions on the near side and away side are estimated by comparing to the measurements in pp collisions. An away-side suppression from in-medium energy loss is observed ($I_{\rm AA} \approx 0.6$), which is from the effects of partons energy loss. Moreover, there is an enhancement above unity of ($I_{\rm AA} \approx 1.2$) on the near side which has not been observed with any significance at lower collision energies. The significant near-side enhancement of $I_{\rm AA}$ in the $p_{\rm T}$ region observed shows that the near-side parton is also subject to medium effects. $I_{\rm AA}$ is sensitive to (i) a change of the fragmentation function, (ii) a possible change of the quark/gluon jet ratio in the final state due to the different coupling to the medium, and (iii) a bias on the parton $p_{\rm T}$ spectrum after energy loss due to the trigger particle selection. It needs to point out that the π^0-hadron correlations

analysis is an important step to measure the direct photon-hadron correlations.

8.1.2 Direct photon-hadron correlations

Direct photons mainly consist of prompt photons produced at the leading-order from Compton and annihilation QCD processes and fragmentation photons at next-to-leading-order processes. In addition, one more contributions to direct photons at nucleus-nucleus collisions are thermal photons and jet conversion from the interactions of the hot and dense QCD medium. Generally, the parton fragmentation function is considered to be characterized by the imbalance parameter $x_{\rm E} = -\frac{\vec{p}_{\rm T}^{\gamma}\cdot\vec{p}_{\rm T}^{h^{\pm}}}{|\vec{p}_{\rm T}^{\gamma}|^2}$ where the $p_{\rm T}^{\gamma}$ and $p_{\rm T}^{h^{\pm}}$ are the momenta of prompt photons and charged hadrons.

Experimentally, the processes producing the leading-order direct photons can be tagged by identifying leading isolated photons and their correlated associated hadrons in opposite azimuth direction. In this analysis, the used isolation technique requires no particles including both charged and neutral particles with $p_{\rm T} > 0.5$ GeV/c in a cone of radius $R = \sqrt{\Delta\varphi^2 + \Delta\eta^2} = 0.4$ around a photon candidate with highest $p_{\rm T}$ in one event. The purity of isolated photons is estimated by a two-component binned likelihood method by fitting the cluster shower shape long axis λ_0^2 distribution with a mix of scaled signal (MC γ-jet) and contamination (non-isolated cluster) distributions. Isolated γ-hadron correlations are obtained by subtracting Isolated π^0-hadron correlations considered as the main contamination from isolated cluster-hadron correlations with the isolated photon purity. The slope of imbalance parameter $x_{\rm E}$ from isolated π^0-hadron correlations is compared to DSS fragmentation functions. Similarly, in the isolated γ-hadron correlations the slope of imbalance parameter $x_{\rm E}$ is calculated by fitting the imbalance parameter distribution with the function Ae^{-B} at $8.0 < p_{\rm T}^{iso\gamma} < 25.0$ GeV/c.

Another method, statistical subtraction, is used to extract the signal of direct photons for their trigger correlations with charged hadrons. The analysis method is based on a relation that total photons consist of direct photons and decay photons from hadrons. In this analysis, the direct photon-hadron correlations are obtained by subtracting decay photon-hadron correlations from inclusive photon-hadron correlations. Firstly, the inclusive photon-hadron correlations are measured with the triggers of clusters filtered by photon identification and corrected with the photon purity and photon identification efficiency. The photon purity is calculated by binned likelihood fit to the cluster shaper shape long axis λ_0^2 distribution. In the binned likelihood fit, three λ_0^2 distributions of photon clusters, charged hadron

clusters and merged π^0 clusters are used as inputs. The photon cluster λ_0^2 distribution is estimated from the clusters which are under π^0 and η peak in 1.2σ width. The charged hadron cluster λ_0^2 distribution is estimated from the clusters which are matched by cluster-matching algorithm where the $\Delta\varphi = \varphi_{cluster} - \varphi_{track} < 0.004$ and $\Delta\eta = \eta_{cluster} - \eta_{track} < 0.002$. The third contribution, merged π^0 cluster λ_0^2 distribution, is estimated from the clusters which are identified as π^0 by cluster splitting method. Secondly, the contamination, decay photon-hadron correlations, is obtained from π^0/η-hadron correlations by pair-by-pair weighting with the photon decay map probability function. The π^0/η-hadron correlations are measured by a Side Band subtraction method. The weight factor of photon decay map probability function is calculated by a Monte-Calo study. Thirdly, an important factor, Double Ratio R_γ, defined as a ratio of inclusive photons to decay photons, is calculated by a Cocktail simulation. At last, a limit estimation of the direct photon-hadron correlations is measured by subtracting all decay photon-hadron correlations from the inclusive photon-hadron correlations by a so-called statistical subtraction method. This result indicates it is impossible to extract a enough significant measurement of the direct photon trigger correlations from current statistics of pp collisions at $\sqrt{s}$ = 7 TeV. But the yield is zero consistent with systematic errors on the near side and a significant peak above zero on the away side are observed from the preliminary measurement.

8.2 Outlook

In the work of this thesis, the flow background contribution to the neutral pion-hadron correlations was estimated by utilizing charged pions flow instead of π^0 flow. Meanwhile, the per-trigger yield modification factors of $I_{\rm CP}$ and $I_{\rm AA}$ at peripheral collisions are not calculated because of the limited statistics of simulations for extracting the correction factors. The measurements of neutral pion-hadron correlations need to be updated when the π^0 flow is measured at high-$p_{\rm T}$ and enough simulations at peripheral are produced.

In the direct photon-hadron correlation analysis, the final results of the azimuthal angle distribution and per-trigger yields are not extracted with the statistical subtraction method due to limited statistics of pp collisions at $\sqrt{s}$ = 7 TeV. But the analysis method at ALICE is developed and will be used to extract the direct photon-hadron correlations in the future pp and Pb+Pb collisions with enough statistics for studying the medium effects by measuring the parton fragmentation function.

List of publications and activities

1. **X. R. Zhu** and D.C. Zhou, "Gluon number fluctuations with heavy quarks at HERA", Chin. Phys. C **35**, 902 (2011).

2. **Xiangrong Zhu** (for the ALICE collaboration), "Two-particle Correlations in pp and Pb-Pb Collisions with ALICE", Int. J. Mod. Phys. Conf. Ser. **29**, 1460212 (2014), arXiv:1311.2394.

3. **Xiangrong Zhu** *et al.*, "Neutral pion-hadron correlations in pp and Pb+Pb collisions at $\sqrt{s_{\rm NN}}$=2.76 TeV with EMCal in ALICE", ALICE-ANALYSIS-NOTE:ANA-875 (**approved by ALICE Physics Board**), 2014.

4. Nicolas Arbor, ..., **Xiangrong Zhu** *et al.*, "Two-Particle correlations with charged and neutral triggers in pp collisions at $\sqrt{s}$=7 TeV", ALICE-ANALYSIS-NOTE:ANA-226 (**approved by ALICE Physics Board**), 2012.

5. J. Allen, ..., **X. Zhu** *et al.*, "ALICE DCal: An Addendum to the EMCal Technical Design Report Di-Jet and Hadron-Jet correlation measurements in ALICE", CERN-LHCC-2010-011, ALICE-TDR14-add-1.

6. D. C. Zhou, ..., **X. R. Zhu** *et al.*, "Potential physics measurement with ALICE electromagnetic calorimeters", Nucl. Phys. **A834**, 291c (2010).

7. **Xiangrong Zhu** (for the ALICE collaboration), "Isolated photon-hadron and π^0-hadron correlations in pp and Pb+Pb collisions with the ALICE experiment", Quark Matter conference poster presentation, Darmstadt, Germany, 2014.

8. **Xiangrong Zhu** (for the ALICE collaboration), "Neutral pion-hadron correlations in pp and Pb+Pb at $\sqrt{s_{\rm NN}}$ = 2.76 TeV with EMCal at ALICE", Quark Matter conference poster presentation, Washington D.C., USA, 2012.

9. Dana Huangmei and **Xiangrong. Zhu** (for the ALICE collaboration), "Charged-particle correlation with neutral triggers in pp collisions at $\sqrt{s}$=7 TeV with

the ALICE detector at the LHC", Hard Probes conference poster presentation, Cagliari, Italy, 2012.

10. **Xiangrong Zhu** "π^0-charged hadron correlations in pp and Pb+P collisions at $\sqrt{s_{\rm NN}}$ = 2.76 TeV with EMCal", ALICE Physics Week, 10-18 October, 2013, Wuhan, China.

11. **Xiangrong Zhu** (for the ALICE collaboration), "Two-particle Correlations in pp and Pb-Pb Collisions with ALICE", Oral presentation, Hadron Nuclear Physics (HNP) 2013, 18-22 July, 2013, Zhangjiajie, China.

12. **Xiangrong Zhu** (for the ALICE collaboration), "Correlations of charged hadrons relative to a neutral trigger particle in pp and Pb-Pb collisions with ALICE", Oral presentation, 8th International Workshop on High $p_{\rm T}$ Physics at LHC 2012, 21-24 October, 2012, Wuhan, China.

ALICE Collaboration publications:

1) B. Abelev, ..., **X. Zhu** *et al.* (ALICE Collaboration), "Neutral pion and eta meson production in proton-proton collisions at $\sqrt{s}$ = 0.9 TeV and $\sqrt{s}$ = 7 TeV", Phys. Lett. B **717**, 162 (2012).

2) B. Abelev, ..., **X. Zhu** *et al.* (ALICE Collaboration), "Particle-yield modification in jet-like azimuthal di-hadron correlations in Pb-Pb collisions at $\sqrt{s_{\rm NN}}$ = 2.76 TeV", Phys. Rev. Lett. **108**, 092301 (2012).

3) E. Abbas, ..., **X. Zhu** *et al.* (ALICE Collaboration), "Charmonium and e+e- pair photoproduction at mid-rapidity in ultra-peripheral Pb-Pb collisions at $\sqrt{s_{\rm NN}}$ = 2.76 TeV", Eur. Phys. J. C **73**, 2617 (2013).

4) B. Abelev, ..., **X. Zhu** *et al.* (ALICE Collaboration), "Multiplicity dependence of the average transverse momentum in pp, p-Pb, and Pb-Pb collisions at the LHC", Phys. Lett. B **727**, 371 (2013).

5) E. Abbas, ..., **X. Zhu** *et al.* (ALICE Collaboration), "J/psi Elliptic Flow in Pb-Pb Collisions at $\sqrt{s_{\rm NN}}$ = 2.76 TeV", Phys. Rev. Lett. **111**, 162301 (2013).

6) B. Abelev, ..., **X. Zhu** *et al.* (ALICE Collaboration), "Centrality determination of Pb-Pb collisions at $\sqrt{s_{\rm NN}}$ = 2.76TeV in the ALICE experiment", Phys. Rev. C **88**, 044909 (2013).

7) B. Abelev, ..., **X. Zhu** *et al.* (ALICE Collaboration), "Centrality dependence of Pion, Kaon, and Proton Production in Pb-Pb Collisions at $\sqrt{s_{\rm NN}}$ = 2.76 TeV", Phys. Rev. C **88**, 044910 (2013).

8) B. Abelev, ..., **X. Zhu** *et al.* (ALICE Collaboration), "Performance of the ALICE VZERO system", JINST **8** P10016 (2013).

9) B. Abelev, ..., **X. Zhu** *et al.* (ALICE Collaboration), "Centrality dependence of the pseudorapidity density distribution for charged particles in Pb-Pb collisions at $\sqrt{s_{\rm NN}}$ = 2.76 TeV", Phys. Lett. B **726** 610 (2013).

10) B. Abelev, ..., **X. Zhu** *et al.* (ALICE Collaboration), "Multiplicity dependence of two-particle azimuthal correlations in pp collisions at the LHC", JHEP **09** 049(2013).

11) B. Abelev, ..., **X. Zhu** *et al.* (ALICE Collaboration), "D meson elliptic flow in non-central PbPb collisions at $\sqrt{s_{\rm NN}}$=2.76 TeV", Phys. Rev. Lett. **111**, 102301 (2013).

12) B. Abelev, ..., **X. Zhu** *et al.* (ALICE Collaboration), "Long-range angular correlations of π, K and p in p-Pb collisions at $\sqrt{s_{\rm NN}}$=5.02 TeV", Phys. Lett. B **726**, 164 (2013).

13) B. Abelev, ..., **X. Zhu** *et al.* (ALICE Collaboration), "Mid-rapidity anti-baryon to baryon ratios in pp collisions at $\sqrt{s}$=0.9, 2.76 and 7 TeV measured by ALICE", Eur. Phys. J. C **73**, 2496 (2013).

14) B. Abelev, ..., **X. Zhu** *et al.* (ALICE Collaboration), "Measurement of inelastic, single- and double-diffraction cross sections in proton-proton collisions at the LHC with ALICE", Eur. Phys. J. C **73**, 2456 (2013).

15) B. Abelev, ..., **X. Zhu** *et al.* (ALICE Collaboration), "Charge correlations using the balance function in Pb+Pb collisions at $\sqrt{s_{\rm NN}}$=2.76 TeV", Phys. Lett. B **723**, 267 (2013).

16) B. Abelev, ..., **X. Zhu** *et al.* (ALICE Collaboration), "Measurement of the inclusive differential jet cross section in pp collisions at $\sqrt{s}$=2.76 TeV", Phys. Lett. B **722**, 262 (2013).

17) B. Abelev, ..., **X. Zhu** *et al.* (ALICE Collaboration), "Net-Charge Fluctuations in Pb-Pb Collisions at $\sqrt{s_{\rm NN}}$=2.76 TeV", Phys. Rev. Lett. **110**, 152301 (2013).

18) B. Abelev, ..., **X. Zhu** *et al.* (ALICE Collaboration), "Measurement of electrons from beauty hadron decays in pp collisions at $\sqrt{s}$=7 TeV", Phys. Lett. B **721**, 13 (2013).

19) B. Abelev, ..., **X. Zhu** *et al.* (ALICE Collaboration), "Charged kaon femtoscopic correlations in pp collisions at $\sqrt{s}$=7 TeV", Phys. Rev. D **87**, 052016 (2013).

20) B. Abelev, ..., **X. Zhu** *et al.* (ALICE Collaboration), "Centrality Dependence of Charged Particle Production at Large Transverse Momentum in Pb-Pb Collisions at $\sqrt{s_{\rm NN}}$=2.76 TeV", Phys. Lett. B **720**, 52 (2013).

21) B. Abelev, ..., **X. Zhu** *et al.* (ALICE Collaboration), "Transverse Momentum Distribution and Nuclear Modification Factor of Charged Particles in p-Pb Collisions at $\sqrt{s_{\rm NN}}$=5.02 TeV", Phys. Rev. Lett. **110**, 082302 (2013).

22) B. Abelev, ..., **X. Zhu** *et al.* (ALICE Collaboration), "Anisotropic flow of charged hadrons, pions and (anti-)protons measured at high transverse momentum in Pb+Pb collisions at $\sqrt{s_{\rm NN}}$=2.76 TeV", Phys. Lett. B **719**, 18 (2013).

23) B. Abelev, ..., **X. Zhu** *et al.* (ALICE Collaboration), "Pseudorapidity density of charged particles p-Pb collisions at $\sqrt{s_{\rm NN}}$=5.02 TeV", Phys. Rev. Lett. **110**, 032301 (2013).

24) B. Abelev, ..., **X. Zhu** *et al.* (ALICE Collaboration), "Long-range angular correlations on the near and away side in p-Pb collisions at $\sqrt{s_{\rm NN}}$=5.02 TeV", Phys. Lett. B **719**, 29 (2013).

25) B. Abelev, ..., **X. Zhu** *et al.* (ALICE Collaboration), "Charge separation relative to the reaction plane in Pb-Pb collisions at $\sqrt{s_{\rm NN}}$=2.76 TeV", Phys. Rev. Lett. **110**, 012301 (2013).

26) B. Abelev, ..., **X. Zhu** *et al.* (ALICE Collaboration), "Measurement of electrons from semileptonic heavy-flavour hadron decays in pp collisions at $\sqrt{s}$=7 TeV", Phys. Rev. D **86**, 112007 (2012).

27) B. Abelev, ..., **X. Zhu** *et al.* (ALICE Collaboration), "Measurement of the Cross Section for Electromagnetic Dissociation with Neutron Emission in Pb-Pb Collisions at $\sqrt{s_{\rm NN}}$=2.76 TeV", Phys. Rev. Lett. **109**, 252302 (2012).

28) B. Abelev, ..., **X. Zhu** *et al.* (ALICE Collaboration), "Pion, Kaon, and Proton Production in Central Pb-Pb Collisions at $\sqrt{s_{\rm NN}}$=2.76 TeV", Phys. Rev. Lett. **109**, 252301 (2012).

29) B. Abelev, ..., **X. Zhu** *et al.* (ALICE Collaboration), "Inclusive J/ψ production in pp collisions at $\sqrt{s}$=2.76 TeV", Phys. Lett. B **718**, 295 (2012).

30) B. Abelev, ..., **X. Zhu** *et al.* (ALICE Collaboration), "Coherent J/ψ photoproduction in ultra-peripheral Pb+Pb collisions at $\sqrt{s_{\rm NN}}$=2.76 TeV", Phys. Lett. B **718**, 1273 (2012).

31) B. Abelev, ..., **X. Zhu** *et al.* (ALICE Collaboration), "Measurement of prompt J/ψ and beauty hadron production production cross sections at mid-rapidity in pp collisions at $\sqrt{s}$=7 TeV", JHEP **11**, 065 (2012).

32) B. Abelev, ..., **X. Zhu** *et al.* (ALICE Collaboration), "Rapidity and transverse momentum dependence of inclusive J/ψ production in pp collisions at $\sqrt{s}$=7 TeV", Phys. Lett. B **718**, 692 (2012).

33) B. Abelev, ..., **X. Zhu** *et al.* (ALICE Collaboration), "Production of $K*0(892)$ and phi(1020) in pp collisions at $\sqrt{s}$=7 TeV", Eur. Phys. J. C **72**, 2183 (2012).

34) B. Abelev, ..., **X. Zhu** *et al.* (ALICE Collaboration), "ks0-ks0 correlations in pp collisions at $\sqrt{s}$=7 TeV from the LHC ALICE experiment", Phys. Lett. B **717**, 151 (2012).

35) B. Abelev, ..., **X. Zhu** *et al.* (ALICE Collaboration), "Suppression of high transverse momentum D mesons in central Pb-Pb collisions at $\sqrt{s_{\rm NN}}$=2.76 TeV", JHEP **9**, 112 (2012).

36) B. Abelev, ..., **X. Zhu** *et al.* (ALICE Collaboration), "Production of Muons from Heavy Flavor Decays at Forward Rapidity in pp and Pb-Pb collisions at $\sqrt{s_{\rm NN}}$=2.76 TeV", Phys. Rev. Lett. **109**, 112301 (2012).

37) B. Abelev, ..., **X. Zhu** *et al.* (ALICE Collaboration), "J/ψ suppression at forward rapidity in Pb-Pb collisions at $\sqrt{s_{\rm NN}}$=2.76 TeV", Phys. Rev. Lett. **109**, 072301 (2012).

38) B. Abelev, ..., **X. Zhu** *et al.* (ALICE Collaboration), "Underlying Event measurements in pp collisions at $\sqrt{s}$=0.9 and 7 TeV with the ALICE experiment at the LHC", JHEP **1207**, 116 (2012).

39) B. Abelev, ..., **X. Zhu** *et al.* (ALICE Collaboration), "J/ψ Production as a Function of Charged Particle Multiplicity in pp Collisions at $\sqrt{s}$=7 TeV", Phys.Lett. B **712**, 165 (2012).

40) B. Abelev, ..., **X. Zhu** *et al.* (ALICE Collaboration), "Light vector meson production in pp collisions at $\sqrt{s}$=7 TeV", Phys. Lett. B **710**, 557 (2012).

41) B. Abelev, ..., **X. Zhu** *et al.* (ALICE Collaboration), "D_s^+ meson production at central rapidity in proton-proton collisions at $\sqrt{s}$=7 TeV", Phys. Lett. B **718**, 279 (2012).

42) B. Abelev, ..., **X. Zhu** *et al.* (ALICE Collaboration), "Measurement of Event Background Fluctuations for Charged Particle Jet Reconstruction in Pb-Pb collisions $\sqrt{s_{\rm NN}}$=2.76 TeV", JHEP **03**, 053 (2012).

43) B. Abelev, ..., **X. Zhu** *et al.* (ALICE Collaboration), "Heavy flavor decay muon production at forward rapidity in proton-proton collisions at $\sqrt{s}$=7 TeV", Phys. Lett. B **708** 265 (2012).

44) K. Aamodt, ..., **X. Zhu** *et al.* (ALICE Collaboration), "Harmonic decomposition of two-particle angular correlations in Pb-Pb collisions at $\sqrt{s_{\rm NN}}$=2.76 TeV", Phys. Lett. B **708** 249 (2012).

45) K. Aamodt, ..., **X. Zhu** *et al.* (ALICE Collaboration), "J/ψ Polarization in pp Collisions at $\sqrt{s}$=7 TeV", Phys. Rev. Lett. **108**, 082001 (2012).

46) K. Aamodt, ..., **X. Zhu** *et al.* (ALICE Collaboration), "Measurement of charm production at central rapidity in proton-proton collisions at $\sqrt{s}$=7 TeV", JHEP **01**, 128 (2012).

Acknowledgments

It has been about seven years since I joined in the heavy-ion experiment analysis group at IOPP CCNU. Up to now, I still clearly remember the first homework given by my supervisor was to do self-study to $\ll C^{++}$ *Programming Language* $\gg$, $\ll$ *ROOT User's Guide* $\gg$ and $\ll PYTHIA6.4 \gg$, which made me so excited. It seems happened yesterday. When the writing of my thesis comes to *Acknowledgments*, it means my Ph.D work would be end. I would like to say "thank you" to many people with all my heart. Thanks for your many warm helps in both my life and work. Without your strong supports, this project can be finished so well.

Firstly, it is a great pleasure to express my sincere gratitude to three of my supervisors, Prof. Daicui Zhu, Dr. Constantinos Loizides, and Prof. Zhongbao Yin, for their advise, encouragement, support and friendship over the last four years. Their rich wisdom, broad-minded, human communication and wholehearted attitudes towards science have been a great influence on my research and personality. I appreciate Prof. Zhou to give me a chance to take part in the great international collaboration to follow the mordenest research of physics. He set us a super example in pursuing a career with his powerful energy and enthusiasm in the ALICE experiment. I also thanks to Prof. Daicui Zhou to give a lot of strong supports on my works and life. I would like to express my heartfelt thanks to Constantinos for his continuous encouragement, persevering guidance, detailed discussions and supports in my physics analysis at CERN in the past two years. Although he have been busy as a convenor of ALICE PWG-Gamma analysis group, he was willing to discuss whenever I had questions and went to his office. I have benefitted from his creativity, enthusiasm and amazing energy. I also would like to thank Prof. Zhongbao Yin for his long term guidance and helpful discussions in the past seven years. He always gives many helpful suggestions when I report my progress in our ALICE-Wuhan group meeting.

I am also particularly grateful to Dr. Gustavo Conesa Balbastre for many helpful discussions in my data analysis over these years. I would like to express many thanks

to Prof. Yves Schutz for his kind helps and discussions when I worked at CERN. Many thanks to Henner Buesching, Yuri Kharlov and Klaus Reyger for their strong supports and helpful discussions when I have been working at ALICE PWG-Gamma group. I would like to thank the funding support from CSC, which grants me to study at CERN for my Ph.D. work.

During working at CERN I enjoyed many discussions in analysis with Mauro Rogerio Cosentino, Ermes Braidot, Rongrong Ma, Michael Weber, Megan Elizabeth Connors, Tim Schuster, Marta Verweij, Shingo Sakai, Martin Wilde, Friederike Bock, Alexander Borissov, Catherine Silvestre, Anders Garritt Knospe, Rosi Jan Reed, Salvatore Aiola, Parask Evi Ganoti, Astrid Morreale, Jason Adrian Kamin. I would like to thank all of them and look forward to further collaborate with them. Especially, I also appreciate Mateusz Ploskon, and ALICE Secretariats, Ulla Tihinen, Audrey Deidda, Carnita Hervet and Helena Zerlauth for many helps.

I am grateful to Prof. Xu Cai, Prof. Nu Xu, Prof. Xinnian Wang, Prof. Enke Wang, Prof. Yadong Yang, Prof. Chunbin Yang, Prof. Feng Liu, Prof. Benwei Zhang, Prof. Fuming Liu, Mrs. Yanming Gao, Mr. Haitao Liu and Mr. Chao Liu, *et al* from IOPP for providing us a strong academic atmosphere and their teaching.

Many thanks to ALICE-Wuhan-group members, Yaping Wang, Xianbao Yuan, Yaxian Mao, Renzhuo Wan, Xiaoming Zhang, Dong Wang, Fang Zhang, Ping Yang, Changzhou Xiang, Jianlin Zhu, Mengliang Wang, Fengchu Zhou, Shuang Li, Xuan Yin, Jiebin Luo, Haitao Zhang, Jianhui Zhu, Hongsheng Zhu, Ruina Dang, Yonghong Zhang, Yang Zhan, Zuman Zhang, Wenzhao Luo, Xinye Peng and Kai Wang for their useful discussions and kind helps. I also thank my friends Wenchang Xiang, Hengtong Ding, Hongyan Yang, Dana Huangmei, Dag Toppe Larsen, Lijiao Liu, Bingfeng Jiang, Song Shu, Feng Bo, Qingquan Jiang, Ziqiang Zhang, Lei Yin, Yanping Zhu, Li Wen, Fang Qin, Yan Zhu, Zhihai Huang, Wei Chen, *etc* for many helps and having nice days together, and thank friends Prof. Yuehong Xie, Prof. Jianguo Bian, Zhenwei Yang, Liang Sun, Fanfan Jing, Haofei Luo, Xianguo Lu, You Zhou, Hai Chen, Jun Su, Qingjin Xu, Wenchao Zhang, Chenxin Zhao, Zhuo Zhou, *etc* for nice discussions and kind helps at CERN.

I would like to give my great gratitude to my dear father, mother, my father-in-law and mother-in-law and my younger brother for their great understanding and supports during my so long term studying towards the Ph.D. Finally, I would like to especially express sincere and great appreciations to my beloved wife, Kangfang Zhang, for her great comprehension, warm support, kind tolerance all the time.

My apologies to all of the people I may have forgotten!

Xiangrong Zhu

CERN Geneva

March 7, 2014

Bibliography

[1] S.L. Glashow, "Partial-symmetries of weak interactions", Nucl. Phys. **22**, 579 (1961).

[2] S. Weinberg, "A Model of Leptons", Phys. Rev. Lett. **19**, 1264 (1967).

[3] A. Salam, "Weak and electromagnetic interactions", Conf.Proc. **C680519**, 367 (1968).

[4] F. Englert and R. Brout, "Broken Symmetry and the Mass of Gauge Vector Mesons", Phys. Rev. Lett. **13**, 321 (1964).

[5] R. Brout and F. Englert, "Spontaneous Symmetry Breaking in Gauge Theories: A Historical Survey", arXiv:hep-th/9802142 (1998).

[6] P.W. Higgs, "Broken Symmetries and the Masses of Gauge Bosons", Phys. Rev. Lett. **13**, 508 (1964).

[7] G.S. Guralnik, C.R. Hagen and T.W.B. Kibble, "Global Conservation Laws and Massless Particles", Phys. Rev. Lett. **13**. 585 (1964).

[8] Standard Model at wikipedia, http://en.wikipedia.org/wiki/Standard_Model.

[9] M. Ablikim *et al.* (BESIII Collaboration), "Observation of a Charged Charmoniumlike Structure in $e^+e^- \to \pi^+\pi^- J/\psi$ at $\sqrt{s}$=4.26 GeV", Phys. Rev. Lett. **110**, 252001 (2013).

[10] Z.Q. Liu *et al.* (Belle Collaboration), "Study of $e^+e^- \to \pi^+\pi^- J/\psi$ and Observation of a Charged Charmoniumlike State at Belle", Phys. Rev. Lett. **110**, 252002 (2013).

[11] Particle Data Group, "Review of Particle Physics", J. Phys. G, **37**, 075021 (2010).

[12] Higgs boson at wikipedia, http://en.wikipedia.org/wiki/Higgs_boson.

[13] G. Aad *et al.* (ATLAS Collaboration), "Observation of a new particle in the search for the Standard Model Higgs boson with the ATLAS detector at the LHC", Phys. Lett. B **716**, 1 (2012).

[14] S. Chatrchyan *et al.* (CMS Collaboration), "Observation of a new boson at a mass of 125 GeV with the CMS experiment at the LHC", Phys. Lett. B **716**, 30 (2012).

[15] G. Dissertori and G.P. Salam (Particle Data Group), "Review of Particle Physics", J. Phys. G, **37**, 075021 (2010).

[16] P.Z. Skands, "Introduction to QCD", CERN-PH-TH-2012-196, (2012).

[17] G. 't Hooft, "A Planar Diagram Theory for Strong Interactions", Nucl. Phys. **B72**, 461 (1974).

[18] D.J. Gross and F. Wilczek. "Ultraviolet Behavior of Nonabelian Gauge Theories", Phys. Rev. Lett. **30**, 1343 (1973).

[19] H.D. Politzer. "Reliable Perturbative Results for Strong Interactions", Phys. Rev. Lett. **30**, 1346 (1973).

[20] J. Beringer *et al.* (Particle Data Group), "Review of Particle Physics", Phys. Rev. D **86**, 010001 (2012).

[21] D. Perkins. "Introduction to High-Energy Physics", Cambridge University Press, Cambridge, (2000).

[22] E.V. Shuryak, "Quantum Chromodynamics and the Theory of Superdense Matter", Phys. Rept. **61**, 71 (1980).

[23] K.G. Wilson, "CONFINEMENT OF QUARKS", Phys. Rev. D **10**, 2445 (1974).

[24] F. Karsch, "Lattice QCD at High Temperature and Density", Lect. Notes Phys. **583**, 209 (2002).

[25] F. Karsch, E. Laermann, and A. Peikert, "The Pressure in 2, 2+1 and 3 Flavour QCD", Phys. Lett. B **478**, 447 (2000).

[26] J.M. Lattimer and M. Prakash, "Neutron Star Observations: Prognosis for Equation of State Constraints", Phys. Rept. **442**, 109, (2007).

[27] M.G. Alford *et al.*, "Color superconductivity in dense quark matter", Rev. Mod. Phys. **80**, 1455 (2008).

[28] M.A. Stephanov, "QCD phase diagram and the critical point", Prog. Theor. Phys. Suppl. **153**, 139 (2004).

[29] Y. Aoki *et al.*, "The order of the quantum chromodynamics transition predicted by the standard model of particle physics", Nature **443**, 675 (2006).

[30] R.J. Glauber and G. Matthiae, "high-energy scattering of protons by nuclei", Nucl. Phys. B **21**, 135 (1970).

[31] M.L. Miller *et al.*, "Glauber Modeling in High Energy Nuclear Collisions", Ann. Rev. Nucl. Part. Sci. **57**, 205 (2007).

[32] J.D. Bjorken, "Highly relativistic nucleus-nucleus collisions: The central rapidity region", Phys. Rev. D **27**, 140 (1983).

[33] L. McLerranv, "Theoretical Concepts for Ultra-Relativistic Heavy Ion Collisions", arXiv:0911.2987, (2009).

[34] F. Gelis *et al.*, "The Color Glass Condensate", Ann. Rev. Nucl. Part. Sci. **60**, 463 (2010).

[35] J.L. Albacete, "CGC and initial state effects in Heavy Ion Collisions", J. Phys. Conf. Ser. **270**, 012052 (2011).

[36] J.J. Aubert *et al.* (EMC Collaboration), "The ratio of the nucleon structure functions F2N for iron and deuterium", Phys. Lett. B **123**, 275 (1983).

[37] K. J. Eskola, H. Paukkunen, and C. A. Salgado, "EPS09-a New Generation of NLO and LO Nuclear Parton Distribution Functions", JHEP **0904**, 065 (2009).

[38] D. de Florian *et al.*, "Global analysis of nuclear parton distributions", Phys. Rev. D **85**, 074028 (2012).

[39] D. de Florian and R. Sassot, "Nuclear parton distributions at next to leading order", Phys. Rev. D **69** 074028 (2004).

[40] M. Hirai, S. Kumano, and T.H. Nagai, "Determination of nuclear parton distribution functions and their uncertainties at next-to-leading order", Phys. Rev. C **76**, 065207 (2007).

[41] R. Vogt, "Cold nuclear matter effects on J/ψ and Υ production at energies available at the CERN Large Hadron Collider (LHC)", Phys. Rev. C **81**, 044903 (2010).

[42] R. Vogt, "x_F dependence of ψ and Drell-Yan production", Phys. Rev. C **61**, 035203 (2000).

[43] I. Vitev, "Initial state parton broadening and energy loss probed in d+Au at RHIC", Phys. Lett. B **562**, 36 (2003).

[44] D. Kharzeev and E. Levin, "Manifestations of high density QCD in the first RHIC data", Phys. Lett. B **523**, 79 (2001).

[45] D. Kharzeev, E. Levin, and M. Nardi, "The onset of classical QCD dynamics in relativistic heavy ion collisions", Phys. Rev. C **71**, 054903 (2005).

[46] V.N. Gribov and L.N. Lipatov, "Deep inelastic *ep* scattering in perturbation theory", Sov. J. Nucl. Phys. **15**, 438 (1972).

[47] G. Altarelli and G. Parisi, "Asymptotic Freedom in Parton Language", Nucl. Phys. B **126**, 298 (1977).

[48] L.N. Lipatov, "Reggeization of the Vector Meson and the Vacuum Singularity in Nonabelian Gauge Theories", Sov. J. Nucl. Phys. **23**, 338 (1976).

[49] E.A. Kuraev, L.N. Lipatov, and V.S. Fadin. "The Pomeranchuk Singularity in Nonabelian Gauge Theories", Sov. Phys. JETP, **45**, 199 (1977).

[50] I.I. Balitsky and L. N. Lipatov, "The Pomeranchuk Singularity in Quantum Chromodynamics", Sov. J. Nucl. Phys. **28**, 822 (1978).

[51] L. V. Gribov, E. M. Levin, and M. G. Ryskin, "Semihard Processes in QCD", Phys. Rept. 100 (1983).

[52] E.Iancu, "QCD in heavy ion collisions", arXiv:1205.0579, (2012).

[53] K. Geiger and B. Müller, "Dynamics of parton cascades in highly relativistic nuclear collisions", Nucl. Phys. B **369**, 600 (1992).

[54] K. Geiger and D. K. Srivastava, "Parton cascade description of relativistic heavy ion collisions at the CERN Super Proton Synchrotron at 158A GeV?", Phys. Rev. C **56**, 2718 (1997).

[55] B. Zhang, M. Gyulassy and C. M. Ko, "Elliptic flow from a parton cascade", Phys. Lett. B **455**, 45 (1999).

[56] V.V. Skokov and V.D. Toneev, "Hydrodynamics of an expanding fireball", Phys. Atom. Nucl. **70**, 109 (2007).

[57] J. D. Bjorken, "Highly relativistic nucleus-nucleus collisions: The central rapidity region", Phys. Rev. D **27**, 140 (1983).

[58] W.M. Alberico, Marzia Nardi, and Maria-Paola Lombardo, "Quark-gluon Plasma and Heavy Ion Collisions: A Meeting Held in the Framework of the Activities of the Italian Working Group on Strong Interactions", (2002).

[59] R. Rapp and E.V. Shuryak, "Resolving the Antibaryon-Production Puzzle in High-Energy Heavy-Ion Collisions", Phys. Rev. Lett. **86**, 2980 (2001).

[60] W. Florkowski, "Phenomenology of Ultra-relativistic Heavy-ion Collisions", World Scientific, (2010).

[61] A. Bialas, M. Bleszyński, and W. Czyz, "Multiplicity Distributions in Nucleus-nucleus Collisions at High Energies", Nucl. Phys. B **111**, 461 (1976).

[62] C. Y. Wong, "Introduction to High-Energy Heavy-Ion Collisions", World Scientific, (1994).

[63] J.C. Collins, D.E. Soper, and G. Sterman, "Factorization For Short Distance Hadron-Hadron Scattering", Nucl. Phys. B **261**, 104 (1985).

[64] M. Glück, E. Reya, and A. Vogt. "Dynamical parton distributions of the proton and small-x physics". Z. Phys. C **67**, 433 (1995).

[65] J. Pumplin *et al.*, "New generation of parton distributions with uncertainties from global QCD analysis", JHEP **0207**, 012 (2002).

[66] J. Binnewies, B.A. Kniehl, and G. Kramer, "Pion and Kaon Production in e^+e^- and ep Collisions at Next-to-Leading Order", Phys. Rev. D **52**, 4947 (1995).

[67] P. Aurenche *et al.*, " Large-p_{T} Inclusive π^0 Cross Sections and Next-to-Leading-Order QCD Predictions", Eur. Phys. J. C **13**, 347 (2000).

[68] B. Abelev *et al.* (ALICE Collaboration), "Neutral pion and η meson production in proton-proton collisions at $\sqrt{s} = 0.9$ TeV and 7 TeV", Phys. Lett. B **717**, 162 (2012).

[69] D. de Florian, R. Sassot, and M. Stratmann, "Global analysis of fragmentation functions for pions and kaons and their uncertainties", Phys. Rev. D **75**, 114010 (2007).

[70] J. Binnewies, B.A. Kniehl, and G. Kramer, "Next-to-Leading Order Fragmentation Functions for Pions and Kaons", Z. Phys. C **65**, 471 (1995).

[71] A. Adare *et al.* (PHENIX Collaboration), "Inclusive cross section and double helicity asymmetry for π^0 production in p+p collisions at $\sqrt{s} = 200$ GeV: Implications for the polarized gluon distribution in the proton", Phys. Rev. D **76**, 051106 (2007).

[72] J.D. Bjorken, "ENERGY LOSS OF ENERGETIC PARTONS IN QUARK-GLUON PLASMA: POSSIBLE EXTINCTION OF HIGH P(T) JETS IN HADRON-HADRON COLLISIONS", FERMILAB-PUB-82-059-THY, (1982).

[73] M. Gyulassy and M. Plümer, "Jet quenching in dense matter", Phys. Lett. B **243**, 432 (1990).

[74] X.N. Wang and M. Gyulassy, "Gluon Shadowing and Jet Quenching in A+A Collisions at $\sqrt{s_{\mathrm{NN}}} = 200$ GeV", Phys. Rev. Lett. **68**, 1480 (1992).

[75] M. Arneodo, "Nuclear effects in structure functions", Phys. Rept. **240**, 301 (1994).

[76] J.W. Cronin *et al.*, "Production of hadrons at large transverse momentum at 200, 300, and 400 GeV ", Phys. Rev. D **11**, 3105 (1975).

[77] X.N. Wang, "Systematic study of high hadron spectra in and collisions at ultrarelativistic energies", Phys. Rev. C **61**, 064910 (2000).

[78] B.Z. Kopeliovich *et al.*, "Cronin Effect in Hadron Production Off Nuclei", Phys. Rev. Lett. **88**, 232303 (2002).

[79] J.J. Aubert *et al.* (EMC Collaboration), "The ratio of the nucleon structure functions F_2^N for iron and deuterium", Phys. Lett. B **123**, 275 (1983).

[80] A. Bodek *et al.*, "Electron Scattering from Nuclear Targets and Quark Distributions in Nuclei", Phys. Rev. Lett. **50**, 1431 (1983).

[81] A. Bodek *et al.*, "Comparison of the Deep-Inelastic Structure Functions of Deuterium and Aluminum Nuclei", Phys. Rev. Lett. **51**, 534 (1983).

[82] M. Arneodo *et al.*, "The structure function ratios $F_2^{\rm Li}/F_2^D$ and F_2^C/F_2^D at small x". Nucl. Phys. **B441**, 12 (1995).

[83] P.R. Norton, "The EMC effect", Rept. Prog. Phys. **66**, 1253 (2003).

[84] A. Bodek and J.L. Ritchie, "Fermi Motion Effects in Deep Inelastic Lepton Scattering from Nuclear Targets", Phys. Rev. D **23** 1070 (1981).

[85] K.J. Eskola, V.J. Kolhinen, and C.A. Salgado, "The scale dependent nuclear effects in parton distributions for practical applications", Eur. Phys. J. C **9**, 61 (1999).

[86] K.J. Eskola, V.J. Kolhinen, and P.V. Ruuskanen, "Scale evolution of nuclear parton distributions", Nucl. Phys. **B535** 351 (1998).

[87] M. Hirai, S. Kumano, and M. Miyama, "Determination of nuclear parton distributions", Phys. Rev. D **64** 034003 (2001).

[88] M. Gyulassy and X.N. Wang, "Multiple collisions and induced gluon bremsstrahlung in QCD", Nucl. Phys. **B420**, 583 (1994).

[89] X.N. Wang, M. Gyulassy, and M. Plümer, "The LPM effect in QCD and radiative energy loss in a quark gluon plasma", Phys. Rev. D **51**, 3436 (1995).

[90] R. Baier, "Jet quenching". Nucl. Phys. **A715**, 209 (2003).

[91] R. Baier *et al.*, "Radiative energy loss of high energy quarks and gluons in a finite-volume quark-gluon plasma", Nucl. Phys. **B483**, 291 (1997).

[92] R. Baier *et al.*, "Radiative energy loss and $p_{\rm T}$-broadening of high energy partons in nuclei", Nucl. Phys. **B484**, 265 (1997).

[93] J.F. Gunion and G. Bertsch, "Hadronization by color bremsstrahlung ", Phys. Rev. D **25**, 746 (1982).

[94] C.A. Salgado and U. Wiedemann, "Calculating quenching weights", Phys. Rev. D **68**, 014008 (2003).

[95] C.A. Salgado and U. Wiedemann, "A dynamical scaling law for jet tomography", Phys. Rev. Lett. **89** 092303 (2002).

[96] A. Peshier, "QCD Collisional Energy Loss Reexamined", Phys. Rev. Lett. **97**, 212301 (2006).

[97] S. Peigné and A. Peshier, "Collisional energy loss of a fast heavy quark in a quark-gluon plasma", Phys. Rev. D **77**, 114017 (2008).

[98] B.G. Zakharov, "Parton energy loss in an expanding quark-gluon plasma: Radiative vs ollisional", JETP Lett. **86**, 444 (2007).

[99] R. Baier *et al.*, "Angular dependence of the radiative gluon spectrum and the energy loss of hard jets in QCD media", Phys. Rev. C **60**, 064902 (1999).

[100] Y.L. Dokshitzer, V.A. Khoze, and S.I. Troyan, "On specific QCD properties of heavy quark fragmentation ('dead cone')", J. Phys. G **17**, 1602 (1991);

[101] Y.L. Dokshitzer and D.E. Kharzeev, "Heavy quark colorimetry of QCD matter", Phys. Lett. B **519**, 199 (2001).

[102] S.Cao *et al.*, "Heavy-quark dynamics and hadronization in ultrarelativistic heavy-ion collisions: Collisional versus radiative energy loss", Phys. Rev. C **88**, 044907 (2013).

[103] R. Abir *et al.*, "Open heavy flavor and J/ψ at RHIC and LHC within a transport model", Phys. Lett. B **715**, 183 (2012).

[104] K. Krajczár (on behalf of the CMS Collaboration), "Charged hadron multiplicity and transverse energy densities in Pb+Pb collisions from CMS", J. Phys. G **38**, 124041 (2011).

[105] B.B. Back *et al.* (PHOBOS Collaboration), "The PHOBOS Perspective on Discoveries at RHIC", Nucl. Phys. **A757**, 28 (2005).

[106] I. Arsene *et al.* (BRAHMS collaboration), "Quark Gluon Plasma an Color Glass Condensate at RHIC? The perspective from the BRAHMS experiment", Nucl. Phys. **A757**, 1 (2005).

[107] K. Adcox *et al.* (PHENIX Collaboration), "Formation of dense partonic matter in relativistic nucleus-nucleus collisions at RHIC: Experimental evaluation by the PHENIX collaboration", Nucl. Phys. **A757**, 184 (2005).

[108] J. Adams *et al.* (STAR Collaboration, "Experimental and Theoretical Challenges in the Search for the Quark Gluon Plasma: The STAR Collaboration's Critical Assessment of the Evidence from RHIC Collisions", Nucl. Phys. **A757**, 102 (2005).

[109] K. Aamodt *et al.* (ALICE Collaboration), "Centrality dependence of the charged-particle multiplicity density at mid-rapidity in Pb+Pb collisions at $\sqrt{s_{\rm NN}}$ = 2.76 TeV", Phys. Rev. Lett. **106**, 032301 (2011).

[110] G. Aad *et al.* (ATLAS Collaboration), "Measurement of the centrality dependence of the charged particle pseudorapidity distribution in lead-lead collisions at $\sqrt{s_{\rm NN}}$ = 2.76 TeV with the ATLAS detector", Phys. Lett. B **710**, 363 (2012).

[111] S. Chatrchyan *et al.* (CMS Collaboration), "Dependence on pseudorapidity and centrality of charged hadron production in PbPb collisions at a nucleon-nucleon centre-of-mass energy of 2.76 TeV", JHEP **1108**, 141 (2011).

[112] S.S. Adler *et al.* (PHENIX Collaboration), "Systematic Studies of the Centrality and $\sqrt{s_{\rm NN}}$ Dependence of $dE_T/d\eta$ and $dN_{ch}/d\eta$ in Heavy Ion Collisions at Mid-rapidity", Phys. Rev. C **71**, 034908 (2005).

[113] B.I. Abelev *et al.* (STAR Collaboration), "Systematic Measurements of Identified Particle Spectra in pp, d+Au and Au+Au Collisions from STAR", Phys. Rev. C **79**, 034909 (2009).

[114] B. Alver *et al.* (PHOBOS Collaboration), "Phobos results on charged particle multiplicity and pseudorapidity distributions in Au+Au, Cu+Cu, d+Au, and p+p collisions at ultra-relativistic energies", Phys. Rev. C **83**, 024913 (2011).

[115] G.I. Kopylov and M.I. Podgoretsky, "Correlations of identical particles emitted by highly excited nuclei", Sov. J. Nucl. Phys. **15**, 219 (1972).

[116] G.I. Kopylov, V.L. Lyuboshits, and M.I. Podgoretsky, "Correlations Between the Particles Which Have Small Relative Momenta", JINR **P2**, 8069 (1974).

[117] K. Aamodt *et al.* (ALICE Collaboration), "Two-pion Bose-Einstein correlations in central PbPb collisions at $\sqrt{s_{\rm NN}}$ = 2.76 TeV", Phys. Lett. B **696**, 328 (2011).

[118] M.A. Lisa *et al.* (E895 Collaboration), "Bombarding Energy Dependence of π^- Interferometry at the Brookhaven AGS", Phys. Rev. Lett. **84**, 2798 (2000).

[119] C. Alt *et al.* (NA49 Collaboration), "Bose-Einstein correlations of $\pi^-\pi^-$ pairs in central Pb+Pb collisions at 20A, 30A, 40A, 80A and 158A GeV", Phys. Rev. C **77**, 064908 (2008).

[120] S.V. Afanasiev *et al.* (NA49 Collaboration), "Energy Dependence of Pion and Kaon Production in Central Pb+Pb Collisions", Phys. Rev. C **66**, 054902 (2002).

[121] D. Adamov *et al.* (CERES Collaboration), "Beam energy and centrality dependence of two-pion Bose-Einstein correlations at SPS energies", Nucl. Phys. **A714**, 124 (2003).

[122] B.I. Abelev *et al.* (STAR Collaboration), "Pion interferometry in Au+Au and Cu+Cu collisions at and 200 GeV", Phys. Rev. C **80**, 024905 (2009).

[123] B.B. Back *et al.* (PHOBOS Collaboration), "Transverse momentum and rapidity dependence of Hanbury-Brown-Twiss correlations in Au+Au collisions at $\sqrt{s_{\rm NN}}$= 62.4 and 200 GeV", Phys. Rev. C **73**, 031901 (2006).

[124] B.B. Back *et al.* (PHOBOS Collaboration), "Charged-particle pseudorapidity distributions in Au+Au collisions at $\sqrt{s_{\rm NN}}$= 62.4 GeV", Phys. Rev. C **74**, 021901 (2006).

[125] B.B. Back *et al.* (PHOBOS Collaboration), "Significance of the Fragmentation Region in Ultrarelativistic Heavy-Ion Collisions", Phys. Rev. Lett. **91**, 052303 (2003).

[126] J.D. Bjorken, "Highly Relativistic Nucleus-Nucleus Collisions: The Central Rapidity Region", Phys. Rev. D **27**, 140 (1983).

[127] H. Sorge, "Highly Sensitive Centrality Dependence of Elliptic Flow-A Novel Signature of the Phase Transition in QCD", Phys. Rev. Lett. **82**, 2048 (1999).

[128] J.Y. Ollitrault, "Anisotropy as a signature of transverse collective flow", Phys. Rev. D **46**, 229 (1992).

[129] S. Voloshin and Y. Zhang, "Flow Study in Relativistic Nuclear Collisions by Fourier Expansion of Azimuthal Particle Distributions", Z. Phys. C **70**, 665 (1996).

[130] J. Adams *et al.* (STAR Collaboration), "Experimental and theoretical challenges in the search for the quark gluon plasma: The STAR Collaboration,s critical assessment of the evidence from RHIC collisions", Nucl. Phys. **A757**, 102 (2005).

[131] R. Snellings (for the STAR and ALICE Collaborations), "Anisotropic flow from RHIC to the LHC", Eur. Phys. J. C **49**, 87 (2007).

[132] J. Adams *et al.* (STAR Collaboration), "Particle-type dependence of azimuthal anisotropy and nuclear modification of particle production in Au+Au collisions at $\sqrt{s_{\rm NN}} = 200$ GeV", Phys. Rev. Lett. **92**, 052302 (2004).

[133] J. Adler *et al.* (STAR Collaboration), "Pion Interferometry of $\sqrt{s_{\rm NN}} = 130$ GeV Au+Au Collisions at RHIC", Phys. Rev. Lett. **87**, 082301 (2001).

[134] A. Adare *et al.* (PHENIX Collaboration), "Scaling properties of azimuthal anisotropy in Au+Au and Cu+Cu collisions at $\sqrt{s_{\rm NN}} = 200$ GeV", Phys. Rev. Lett. **98**, 162301 (2007).

[135] K. Aamodt *et al.* (ALICE Collaboration), "Elliptic Flow of Charged Particles in Pb+Pb Collisions at $\sqrt{s_{\rm NN}} = 2.76$ TeV", Phys. Rev. Lett. **105**, 252302 (2010).

[136] Y. Bai, PhD thesis, "Anisotropic Flow Measurements in STAR at the Relativistic Heavy Ion Collider", Nikhef and Utrecht University (2007).

[137] B.I. Abelev *et al.* (STAR Collaboration), "Centrality dependence of charged hadron and strange hadron elliptic flow from $\sqrt{s_{\rm NN}} = 200$ GeV Au+Au collisions", Phys. Rev. C **77**, 054901 (2008).

[138] S.A. Voloshin, A.M. Poskanzer, and R. Snellings, in Landolt-Boernstein, "Relativistic Heavy Ion Physics", Vol. 1/23 Springer-Verlag, (2010).

[139] A. Andronic *et al.* (FOPI Collaboration), "Excitation function of elliptic flow in Au+Au collisions and the nuclear matter equation of state", Phys. Lett. B **612**, 173 (2005).

[140] C. Shen *et al.*, "Radial and elliptic flow in Pb+Pb collisions at the Large Hadron Collider from viscous hydrodynamic", Phys. Rev. C **84**, 044903 (2011).

[141] M. Krzewicki (for ALICE Collaboration), "Elliptic and triangular flow of identified particles measured with the ALICE detector at the LHC", J. Phys. G **38**, 124047 (2011).

[142] Z. Yin (for ALICE Collaboration), "Multi-strange baryon elliptic flow in Pb+Pb collisions at $\sqrt{s_{\rm NN}}$ = 2.76 TeV measured with the ALICE detector", arxiv:1202.0365, (2012).

[143] B. Abelev (for the ALICE Collaboration), "Elliptic flow of identified hadrons in Pb-Pb collisions at $\sqrt{s_{\rm NN}}$ = 2.76 TeV", arXiv:1405.4632, (2014).

[144] S. A. Voloshin, "Anisotropic flow", Nucl. Phys. **A715**, 379 (2003).

[145] R.J. Fries *et al.*, "Hadronization in heavy ion collisions: Recombination and fragmentation of partons", Phys. Rev. Lett. **90**, 202303 (2003).

[146] R.J Fries *et al.*s, "Hadron production in heavy ion collisions: Fragmentation and recombination from a dense parton phase", Phys.Rev. C **68**, 044902 (2003).

[147] V. Greco, C. M. Ko, and P. Lévai, "Partonic coalescence in relativistic heavy ion collisions", Phys. Rev. C **68** 034904 (2003).

[148] J. Rafelski and B. Müller, "Strangeness production in the quark-gluon plasma", Phys. Rev. Lett. **48**, 1066 (1982).

[149] J. Rafelski and B. Müller, "Strangeness production in the Quark-Gluon plasma", Phys. Rev. Lett. **56**, 2334 (1986).

[150] B.I. Abelev *et al.* (STAR Collaboration), "Enhanced strange baryon production in Au+Au collisions compared to p+p at 200 GeV", Phys. Rev. C **77**, 044908 (2008).

[151] B. Abelev (for the ALICE Collaboration), "Strangeness with ALICE: from pp to Pb+Pb", arXiv:1209.3285, (2012).

[152] D. d'Enterria, "Jet quenching", Springer Verlag. Landolt-Boernstein Vol. 1-23A, arXiv:0902.2011, (2009).

[153] M.M. Aggarwal *et al.* (WA98 Collaboration), "Transverse mass distributions of neutral pions from Pb-induced reactions at 158A GeV", Eur. Phys. J. C **23**, 225 (2002).

[154] D. d'Enterria, "Indications of suppressed high p_{T} hadron production in nucleus-nucleus collisions at CERN-SPS", Phys. Lett. B **596**, 32 (2004).

[155] A. Adare *et al.* (PHENIX Collaboration), "Suppression Pattern of Neutral Pions at High Transverse Momentum in Au+Au Collisions at $\sqrt{s_{\mathrm{NN}}}$ = 200 GeV and Constraints on Medium Transport Coefficients", Phys. Rev. Lett. **101**, 232301 (2008).

[156] J. Adams *et al.* (STAR Collaboration), "Transverse-Momentum and Collision-Energy Dependence of High-p_{T} Hadron Suppression in Au+Au Collisions at Ultrarelativistic Energies", Phys. Rev. Lett. **91**, 172302 (2003).

[157] K. Aamodt *et al.* (ALICE Collaboration), "Suppression of Charged Particle Production at Large Transverse Momentum in Central Pb+Pb Collisions at $\sqrt{s_{\mathrm{NN}}}$ = 2.76 TeV", Phys. Lett. B **696**, 30 (2011).

[158] Y. J. Lee (for the CMS Collaboration), "Nuclear modification factors from the CMS experiment", J. Phys. G **38**, 124015 (2011).

[159] A. Dainese, C. Loizides, and G. Paic, "Leading-particle suppression in high energy nucleus-nucleus collisions", Eur. Phys. J. C **38**, 461 (2005).

[160] I. Vitev and M. Gyulassy, "High-p_{T} Tomography of and at SPS, RHIC, and LHC", Phys. Rev. Lett. **89**, 252301 (2002).

[161] I. Vitev, "Jet tomography", J. Phys. G **30**, S791 (2004).

[162] T. Renk *et al.*, "Systematics of the charged-hadron p_{T} spectrum and the nuclear suppression factor in heavy-ion collisions from $\sqrt{s_{\mathrm{NN}}}$ = 200 GeV to $\sqrt{s_{\mathrm{NN}}}$ = 2.76 TeV", Phys. Rev. C **84**, 014906 (2011).

[163] H. Appelshäuser (for the ALICE Collaboration), "Particle Production at Large Transverse Momentum with ALICE", J. Phys. G **38**, 124014 (2011).

[164] A. Dainese A (for the ALICE Collaboration), "Heavy-flavour production in Pb+Pb collisions at the LHC, measured with the ALICE detector", J. Phys. G **38**, 124032 (2011).

[165] S. Chatrchyan *et al.* (CMS Collaboration), "Measurement of isolated photon production in pp and Pb+Pb collisions at $\sqrt{s_{\rm NN}}$ = 2.76 TeV", Phys. Lett. B **710**, 256 (2012).

[166] P. Steinberg (for the ATLAS Collaboration), "Recent Heavy Ion Results with the ATLAS Detector at the LHC", J. Phys. G **38**, 124004 (2011).

[167] S. Chatrchyan *et al.* (CMS Collaboration), "Study of Z boson production in Pb+Pb collisions at nucleon-nucleon centre of mass energy = 2.76 TeV", Phys. Rev. Lett. **106**, 212301 (2011).

[168] G. Aad *et al.* (ATLAS Collaboration), "Measurement of the centrality dependence of J/ψ yields and observation of Z production in lead-lead collisions with the ATLAS detector at the LHC", Phys. Lett. B **697**, 294 (2011).

[169] G. Aad *et al.* (ATLAS Collaboration), "Measurements of W Boson Yields in Pb+Pb Collisions at 2.76 TeV/nucleon via Single Muons with the ATLAS Detector", CERN Report No. ATLAS-CONF-2011-078, (2011) (unpublished).

[170] A. Milov (for the ATLAS Collaboration), "Centrality dependence of charged particle spectra and R_{CP} in Pb+Pb collisions at $\sqrt{s_{\rm NN}}$ = 2.76 TeV with the ATLAS detector at the LHC", J. Phys. G **38**, 124113 (2011).

[171] B. Abelev *et al.* (ALICE Collaboration), "J/ψ suppression at forward rapidity in Pb-Pb collisions at $\sqrt{s_{\rm NN}}$ = 2.76 TeV", Phys. Rev. Lett. **109** 072301 (2012).

[172] S. Chatrchyan S *et al.* (CMS Collaboration), "Suppression of non-prompt J/ψ, prompt J/ψ, and $\Upsilon(1S)$ in PbPb collisions at $\sqrt{s_{\rm NN}}$ = 2.76 TeV", JHEP **05**, 063 (2012).

[173] R. Sharma, I. Vitev, B. W. Zhang, "A light-cone wavefunction approach to open heavy flavor dynamics in QCD matter", Phys. Rev. C **80**, 054902 (2009).

[174] X. F. Chen *et al.*, "Suppression of high-$p_{\rm T}$ hadrons in Pb+Pb Collisions at LHC", Phys. Rev. C **84**, 034902 (2011).

[175] A. Majumder and C. Shen, "Suppression of the high $p_{\rm T}$ charged hadron R_{AA} at the LHC", Phys. Rev. Lett. **109**, 202301 (2011).

[176] K. C. Zapp, F. Krauss, U. Wiedemann, "Explaining jet quenching with perturbative QCD alone", IPPP-11-41; DCPT-11-82; MCNET-11-26; CERN-PH-TH-2011-299, (2011).

[177] B. Müller, J. Schukraft, and B. Wyslouch, "First Results from Pb+Pb collisions at the LHC", Annual Review of Nuclear and Particle Science **62**, 361 (2012).

[178] D. d'Enterria, "Quark-Gluon Matter", J. Phys. G **34** S53, (2007).

[179] G. Aad *et al.* (ATLAS Collaboration), "Observation of a Centrality-Dependent Dijet Asymmetry in Lead-Lead Collisions at $\sqrt{s_{\rm NN}}$ = 2.76 TeV with the ATLAS Detector at the LHC", Phys. Rev. Lett. **105**, 252303 (2010).

[180] S. Chatrchyan *et al.* (CMS Collaboration), "Observation and studies of jet quenching in PbPb collisions at nucleon-nucleon center-of-mass energy = 2.76 TeV", Phys. Rev. C **84**, 024906 (2011).

[181] M. Verweij (for the ALICE collaboration), "Measurement of jet spectra in Pb-Pb collisions at $\sqrt{s_{\rm NN}}$ =2.76 TeV with the ALICE detector at the LHC", arXiv:1208.6169, (2012).

[182] B.A. Cole (for the ATLAS Collaboration), "Jet probes of $\sqrt{s_{\rm NN}}$ = 2.76 TeV Pb+Pb collisions with the ATLAS detector ", J. Phys. G **38**, 124021 (2011).

[183] A. Adare *et al.* (PHENIX Collaboration), "Dihadron azimuthal correlations in Au+Au collisions at $\sqrt{s_{\rm NN}}$ = 200 GeV", Phys. Rev. C **78**, 014901 (2008).

[184] I. Vitev, "Large Angle Hadron Correlations from Medium-Induced Gluon Radiation", Phys. Lett. B **630**, 78 (2005).

[185] A.D. Polosa and C.A. Salgado, "Jet shapes in opaque media ", Phys. Rev. C **75**, 041901 (2007).

[186] J. Solanaa, E.V. Shuryaka, and D. Teaney, "Conical Flow induced by Quenched QCD Jets", Nucl. Phys. **A774**, 577 (2006).

[187] T. Renk and J. Ruppert, "Mach cones in an evolving medium", Phys. Rev. C **73**, 011901 (2006).

[188] C.B. Chiu and R.C. Hwa, "Away-side azimuthal distribution in a Markovian parton scattering model", Phys. Rev. C **74**, 064909 (2006).

[189] W. Li *et al.*, "Reaction plane angle dependence of dihadron azimuthal correlations from a multiphase transport model calculation", Phys. Rev. C **80**, 064913 (2009).

[190] V. Koch, A. Majumder, and X.N. Wang, "Cherenkov Radiation from Jets in Heavy-Ion Collisions", Phys. Rev. Lett. **96**, 172302 (2006).

[191] G.L. Ma *et al.*, "Di-hadron azimuthal correlation and Mach-like cone structure in parton/hadron transport model", Phys. Lett. B **641**, 362 (2006).

[192] B. Alver and G. Roland, "Collision-geometry fluctuations and triangular flow in heavy-ion collisions", Phys. Rev. C **81**, 054905 (2010).

[193] S.S. Adler *et al.* (PHENIX Collaboration), "Dense-Medium Modifications to Jet-Induced Hadron Pair Distributions in Au+Au Collisions at $\sqrt{s_{\rm NN}}$ = 200 GeV", Phys. Rev. Lett. **97**, 052301 (2006).

[194] N. Armesto *et al.*, "Measuring the Collective Flow with Jets", Phys. Rev. Lett. **93**, 242301 (2004).

[195] Majumder *et al.*, "QCD magnetic fields", hep-ph/0611035, (2006).

[196] P. Romantschke, "Momentum Broadening in an Anisotropic Plasma", Phys. Rev. C **75**, 014901 (2007).

[197] C.B. Chiu and R. C. Hwa, "Pedestal and peak structure in jet correlation", Phys. Rev. C **72**, 034903 (2005).

[198] S. Voloshin, "Transverse radial expansion in nuclear collisions and two particle correlations",Phys.Lett. B **632**, 490 (2006).

[199] C. Y. Wong, "Ridge Structure associated with the Near-Side Jet in the $\Delta\varphi-\Delta\eta$ Correlation", Phys. Rev. C **76**, 054908 (2007).

[200] R. Rapp and H. V. Hees, "Heavy Quarks in the Quark-Gluon Plasma", Quark Gluon Plasma 4, World Scientific, (2010).

[201] T. Matsui and H. Satz, "J/ψ suppression by quark-gluon plasma formation", Phys. Lett. B **178**, 416 (1986).

[202] R. Vogt, "Cold Nuclear Matter Effects on J/ψ and Υ Production at energies available at the CERN Large Hadron Collider (LHC)", Phys. Rev. C **81**, 044903 (2010).

[203] X. Zhao and R. Rapp, "Medium modifications and production of charmonia at LHC", Nucl. Phys. **A859**, 114 (2011).

[204] C. Baglin *et al.* (NA38 Collaboration), "ψ' and J/ψ production in p-W, p-U and S-U interactions at 200 GeV/nucleon", Phys. Lett. B **345**, 617 (1995).

[205] A. Adare *et al.* (PHENIX Collaboration), "J/ψ production versus centrality, transverse momentum, and rapidity in Au+Au collisions at $\sqrt{s_{\rm NN}} = 200$ GeV", Phys. Rev. Lett. **98**, 232301 (2007).

[206] A. Adare A *et al.* (PHENIX Collaboration), "J/ψ Production vs Centrality, Transverse Momentum, and Rapidity in Au+Au Collisions at $\sqrt{s_{\rm NN}} = 200$ GeV", Phys. Rev. Lett. **98**, 232301 (2007).

[207] A. Adare *et al.* (PHENIX Collaboration), "J/ψ suppression at forward rapidity in Au+Au collisions at $\sqrt{s_{\rm NN}} = 200$ GeV", Phys. Rev. C **84**, 054912 (2011).

[208] R. Reed (for the STAR Collaboration), "Measuring the Upsilon Nuclear Modification Factor at STAR", J. Phys. G **38**, 124185 (2011).

[209] G. Agakichiev *et al.* (CERES Collaboration), "Enhanced Production of Low-Mass Electron Pairs in 200 GeV/Nucleon S-Au Collisions at the CERN Super Proton Synchrotron", Phys. Rev. Lett. **75**, 1272 (1995).

[210] A. Adare *et al.* (PHENIX Collaboration), "Detailed measurement of the e^+e^- pair continuum in pp and Au+Au collisions at $\sqrt{s_{\rm NN}} = 200$ GeV and implications for direct photon production", Phys. Rev. C **81**, 034911 (2010).

[211] M.M. Aggarwal *et al.* (WA98 Collaboration), "Observation of Direct Photons in Central 158A GeV Pb+Pb Collisions", Phys. Rev. Lett. **85**, 3595 (2000).

[212] S. Afanasiev *et al.* (PHENIX Collaboration), "Measurement of Direct Photons in Au+Au Collisions at $\sqrt{s_{\rm NN}}$200 GeV", Phys. Rev. Lett. **109**, 152302 (2012).

[213] S. Chatrchyan *et al.* (CMS Collaboration), "Measurement of isolated photon production in pp and PbPb collisions at $\sqrt{s_{\rm NN}} = 2.76$ TeV", Phys. Lett. B **710** 256 (2012).

[214] S. Turbide *et al.*, "Electromagnetic radiation from nuclear collisions at ultra-relativistic energies", Phys. Rev. C **77**, 024909 (2008).

[215] I. Vitev and B.W. Zhang, "A systematic study of direct photon production in heavy ion collisions", Phys. Lett. B **669**, 337 (2008).

[216] C. Gale, "Photon Production in Hot and Dense Strongly Interacting Matter", Relativistic Heavy Ion Physics-Group I Elementary Particles, Nuclei and Atoms Volume **23**, (2010).

[217] F. Arleo *et al.*, "Inclusive prompt photon production in nuclear collisions at RHIC and LHC", JHEP **1104**, 055 (2011).

[218] A. Adare *et al.* (PHENIX Collaboration), "Enhanced production of direct photons in Au + Au collisions at $\sqrt{s_{\rm NN}} = 200$ GeV and implications for the initial temperature", Phys. Rev. Lett. **104**, 132301 (2010).

[219] A. Adare *et al.* (PHENIX Collaboration), "Observation of direct-photon collective flow in Au+Au collisions at $\sqrt{s_{\rm NN}} = 200$ GeV", Phys. Rev. Lett. **109**, 122302 (2012).

[220] ALICE home page, http://aliweb.cern.ch.

[221] LEP Collaboration, LEP Design Report: Vol 2, "The LEP Main Ring", CERN-LEP-84-01, (1984).

[222] L. Evans and P. Bryant, "LHC machine", JINST **3**, S08001 (2008).

[223] CERN public home page, http://home.web.cern.ch.

[224] C. Lefevre, "LHC: the guide", CERN-Brochure-2008-001-Eng, (2008).

[225] N. Angert *et al.*, "CERN Heavy Ion Facility Design Report", CERN 93-01, (1993).

[226] TeVI Group, "Design Report Tevatron 1 Project", FERMILAB-DESIGN-1982-01, (1982).

[227] M. Harrison, T. Ludlam, and S. Ozaki, "The Relativistic Heavy Ion Collider Project: RHIC and its Detectors", Nucl. Instrum. Meth. A **499**, 235 (2003).

[228] ATLAS home page, http://atlas.web.cern.ch/Atlas/Collaboration.

[229] CMS home page, http://cms.web.cern.ch.

[230] LHCb home page, http://lhcb.web.cern.ch/lhcb.

[231] TOTEM home page, http://totem.web.cern.ch/Totem.

[232] LHCf home page, http://www.stelab.nagoya-u.ac.jp/LHCf/LHCf/index.html.

[233] MoEDAL home page, http://moedal.web.cern.ch.

[234] CERN pages, "New results indicate that new particle is a Higgs boson", http://home.web.cern.ch/about/updates/2013/03/new-results-indicate-new-particle-higgs-boson.

[235] S.P. Martin, "A Supersymmetry Primer", arXiv:hep-ph/9709356, (1997).

[236] K. Aamodt *et al.* (ALICE Collaboration), "The ALICE experiment at the CERN LHC", JINST **3**, S08002 (2008).

[237] B. Alessandro *et al.* (ALICE Collaboration), "ALICE: physics performance report, volume I", J. Phys. G **30**, 1517 (2004).

[238] The LEP experiment, http://home.web.cern.ch/about/accelerators/large-electron-positron-collider.

[239] J. Allen *et al.*, "ALICE DCal: An Addendum to the EMCal Technical Design Report Di-Jet and Hadron-Jet correlation measurements in ALICE", CERN-LHCC-2010-011/ALICE-TDR-14-add-1, (2010).

[240] EMCal-DCal Projects, "Di-jet Calorimeter installation in ALICE", ALICE Matter, (2013).

[241] P.G. Kuijer (for the ALICE Collaboration), "Commissioning and Prospects for Early Physics with ALICE", Nucl. Phys. **A830**, 81c (2009).

[242] ALICE Collaboration, "ALICE Technical Design Report of the Inner Tracking System", CERN-LHCC-99-12, (1999).

[243] ALICE Collaboration, "ALICE Technical Design Report of the Time Projection Chamber", CERN-LHCC-2000-001, (2000).

[244] ALICE Collaboration, "ALICE Technical Design Report of the Transition Radiation Detector", CERN-LHCC-2001-021, (2001).

[245] ALICE Collaboration, "ALICE: Addendum to the Technical Design Report of the Time of Flight System (TOF)", CERN-LHCC-2002-016, (2002).

[246] ALICE Collaboration, "ALICE Technical Design Report of the High Momentum Particle Identification Detector", CERN-LHCC-98-19, (1998).

[247] ALICE Collaboration, "ALICE Electromagnetic Calorimeter Technical Design Report", CERN-LHCC-2008-014, (2008).

[248] ALICE Collaboration, "ALICE Technical Design Report of the Photon Spectrometer (PHOS)", CERN-LHCC-99-04, (1999).

[249] ALICE Collaboration, "ALICE Technical Design Report of the Zero Degree Calorimeter (ZDC)", CERN-LHCC-99-05, (1999).

[250] ALICE Collaboration, "ALICE Technical Design Report: Photon Multiplicity Detector (PMD)", CERN-LHCC-99-32, (1999).

[251] ALICE Collaboration, "ALICE Technical Design Report on Forward Detectors: FMD, T0 and V0", CERN-LHCC-2004-025, (2004).

[252] ALICE Collaboration, "ALICE Technical Design Report of the Dimuon Forward Spectrometer", CERN-LHCC-99-22, (1999).

[253] B. Abelev *et al.* (ALICE Collaboration), "Measurement of charm production at central rapidity in proton-proton collisions at $\sqrt{s} = 7$ TeV", CERN-PH-EP-2011-181, (2012).

[254] B. Abelev *et al.* (ALICE Collaboration), "Suppression of high transverse momentum D mesons in central Pb+Pb collisions at $\sqrt{s_{\rm NN}} = 2.76$ TeV", JHEP **09**, 112 (2012).

[255] B.B. Back *et al.* (PHOBOS Collaboration), "Identified hadron transverse momentum spectra in Au+Au collisions at $\sqrt{s_{\rm NN}} = 62.4$ GeV", Phys. Rev. C **75**, 024910 (2007).

[256] B. Alessandro *et al.* (ALICE Collaboration), "ALICE: physics performance report volume II", J. Phys. G **32**, 1295 (2006).

[257] A. Akindinov *et al.* (ALICE Collaboration), "Particle identification with the ALICE TOF detector at very high particle multiplicity", Eur. Phys. J. C **32**, s165 (2004).

[258] M. Ippolitov *et al.* (ALICE Collaboration), "Studies of lead tungstate crystals for the ALICE electromagnetic calorimeter PHOS", Nucl. Instrum. Meth. A **486**, 121 (2002).

[259] D.V. Aleksandrov *et al.* (ALICE Collaboration), "A high resolution electromagnetic calorimeter based on lead-tungstate crystals", Nucl. Instrum. Meth. A **550**, 169 (2005).

[260] B. Abelev *et al.* (ALICE Collaboration), "Measurement of the inclusive differential jet cross section for pp collisions at $\sqrt{s} = 2.76$ TeV ", Phys. Lett. B, **722**, 262 (2013).

[261] R.R. Ma, "Differential Inclusive Jet Spectrum in pp collisions at $\sqrt{s_{\rm NN}} = 2.76$ TeV", ALICE-ANALYSIS-Note-ANA533.

[262] C.H. Christensen *et al.*, "The ALICE Forward Multiplicity Detector", Int. J. Mod. Phys. E **16**, 2432 (2007).

[263] B. Abelev *et al.* (ALICE Collaboration), "Centrality determination of Pb+Pb collisions at $\sqrt{s_{\rm NN}} = 2.76$ TeV with ALICE", Phys. Rev. C **88**, 044909 (2013).

[264] ALICE Collaboration, "The Technical Design Report of the Trigger, Data-Acquisition, High Level Trigger, and Control System", CERN-LHCC-2003-062, (2003).

[265] S. Chapeland *et al.*, "Online processing in the ALICE DAQ The Detector Algorithms", J. of Phys.: Conf. Ser. **219**, 022004 (2010).

[266] P. Buncic *et al.*, "The architecture of the AliEn system", Proceedings of the Computing in High Energy Physics 2004, (2004).

[267] A. Szostak, "Operational experience with the ALICE High Level Trigger", J. Phys.: Conf. Ser. **396**, 012048 (2012).

[268] ALICE Offline, http://aliweb.cern.ch/Offline/AliRoot/Manual.html.

[269] ALICE Collaboration, "ALICE technical design report of the computing", CERN-LHCC-2005-018, (2005).

[270] ROOT, http://root.cern.ch/drupal.

[271] GEANT3, http://wwwinfo.cern.ch/asdoc/geantold/GEANTMAIN.html.

[272] GEANT4, http://wwwinfo.cern.ch/asd/geant4/geant4.html.

[273] FLUKA, http://www.slac.stanford.edu/econf/C0303241/proc/papers/MOMT004.PDF.

[274] S. Torbjorn *et al.*, "High-energy physics event generation with PYTHIA 6.1", Comput. Phys. Commun. **135**, 238 (2001).

[275] X.N. Wang and M. Gyulassy, "hijing: A Monte Carlo model for multiple jet production in pp, pA and AA collisions", Phys. Rev. D **44**, 3501 (1991).

[276] MONARC, http://www.cern.ch/MONARC.

[277] MonALISA Repository for ALICE-map, http://alimonitor.cern.ch/map.jsp.

[278] P. Saiz *et al.*, "AliEn-ALICE environment on the GRID", Nucl. Instrum. Meth. A **502** 437 (2003).

[279] AliEn home page, http://alien.cern.ch.

[280] D. d'Enterria, "in Nuclei-Relativistic Heavy Ion Physics", Landolt-Bornstein, Group I, Vol. 23 Springer-Verlag, Berlin, (2010).

[281] B. Abelev *et al.* (ALICE Collaboration), "Measurement of Event Background Fluctuations for Charged Particle Jet Reconstruction in Pb-Pb collisions at $\sqrt{s_{\rm NN}} = 2.76$ TeV", JHEP **03**, 053 (2012).

[282] J.F. Grosse-Oetringhaus (for the ALICE Collaboration), "Hadron Correlations Measured with ALICE", Nucl. Phys. **A910**, 58 (2013).

[283] A. Morsch (for the ALICE Collaboration), "Jet-like near-side peak shapes in Pb+Pb collisions at $\sqrt{s_{\rm NN}} = 2.76$ TeV with ALICE", Nucl. Phys. **A910**, 281 (2013).

[284] K. Aamodt *et al.* (ALICE Collaboration), "Higher harmonic anisotropic flow measurements of charged particles in Pb+Pb collisions at $\sqrt{s_{\rm NN}} = 2.76$ TeV", Phys. Rev. Lett. **107**, 032301 (2011).

[285] J. Adams *et al.* (STAR Collaboration), "Direct Observation of Dijets in Central Au+Au Collisions at $\sqrt{s_{\rm NN}}$ = 200 GeV", Phys. Rev. Lett. **97**, 162301 (2006).

[286] K. Aamodt *et al.* (ALICE Collaboration), "Particle-Yield Modification in Jet-like Azimuthal Dihadron Correlations in Pb-Pb Collisions at $\sqrt{s_{\rm NN}}$ = 2.76 TeV", Phys. Rev. Lett. **108**, 092301 (2012).

[287] J.F. Grosse-Oetringhaus (for the ALICE Collaboration), "Hadron correlations in Pb-Pb collisions at $\sqrt{s_{\rm NN}}$ = 2.76 TeV with ALICE", J. Phys. G **38**, 124028 (2011).

[288] A. Adare *et al.* (PHENIX Collaboration), "Trends in Yield and Azimuthal Shape Modification in Dihadron Correlations in Relativistic Heavy Ion Collisions", Phys. Rev. Lett. **104**, 252301 (2010).

[289] A. Adare *et al.* (PHENIX Collaboration), "Suppression Pattern of Neutral Pions at High Transverse Momentum in Au+Au Collisions at $\sqrt{s_{\rm NN}}$ = 200 GeV and Constraints on Medium Transport Coefficients", Phys. Rev. Lett. **101**, 232301 (2008).

[290] N. Armesto *et al.*, "Constraint fitting of experimental data with a jet quenching model embedded in a hydrodynamical bulk medium", J. Phys. G **37**, 025104 (2010).

[291] H. Zhang *et al.*, "Tomography of High-Energy Nuclear Collisions with Photon-Hadron Correlations", Phys. Rev. Lett. **103**, 032302 (2009).

[292] S. S. Adler *et al.* (PHENIX Collaboration), "Centrality Dependence of Direct Photon Production in $\sqrt{s_{\rm NN}}$ = 200 GeV Au+Au Collisions", Phys. Rev. Lett. **94**, 232301 (2005).

[293] G.Y. Qin *et al.*, "Jet energy loss, photon production, and photon-hadron correlations at energies available at the BNL Relativistic Heavy Ion Collider (RHIC)", Phys. Rev. C **80**, 054909 (2009).

[294] X.N. Wang and Z. Huang, "Medium-induced parton energy loss in gamma+jet events of high-energy heavy-ion collisions", Phys. Rev. C **55**, 3047 (1997).

[295] X.N. Wang, Z. Huang, and I. Sarcevic, "Jet Quenching in the Direction Opposite to a Tagged Photon in High-Energy Heavy-Ion Collisions", Phys. Rev. Lett. **77**, 231 (1996).

[296] S. Chatrchyan *et al.* (CMS Collaboration), "Studies of jet quenching using isolated-photon+jet correlations in PbPb and pp collisions at $\sqrt{s_{\rm NN}}$ = 2.76 TeV", Phys. Lett. B **718**, 773 (2013).

[297] A. Adare *et al.* (PHENIX Collaboration), "Medium Modification of Jet Fragmentation in Au+Au Collisions at $\sqrt{s_{\rm NN}}$ = 200 GeV Measured in Direct Photon-Hadron Correlations", Phys. Rev. Lett. **111**, 032301 (2013).

[298] A. Adare *et al.* (PHENIX Collaboration), "Photon-hadron jet correlations in pp and Au+Au collisions at $\sqrt{s_{\rm NN}}$ = 200 GeV", Phys. Rev. C **80**, 024908 (2009).

[299] N. Borghini and U. Wiedemann, "Distorting the Hump-backed Plateau of Jets with Dense QCD Matter", arXiv: 0506218, (2005).

[300] T. Renk, "Using hard dihadron correlations to constrain elastic energy loss", Phys. Rev. C **84**, 067902 (2011).

[301] ALICE Collaboration, "ALICE Run Condition Table by the MonALISA Repository for ALICE", http://alimonitor.cern.ch/configuration.

[302] B. Abelev *et al.* (ALICE Collaboration), "Measurement of the Cross Section for Electromagnetic Dissociation with Neutron Emission in Pb+Pb Collisions at $\sqrt{s_{\rm NN}}$ = 2.76 TeV", Phys. Rev. Lett. **109**, 252302 (2012).

[303] ALICE Collaboration, "EMCal offline documentation in ALICE-ROOT/EMCAL/doc/EMCALDocumentation.pdf", (2011).

[304] T.C. Awes *et al.*, "A simple method of shower localization and identification in laterally segmented calorimeters", Nucl Insttrum Meth. A **311**, 130 (1992).

[305] G.C. Balbastre *et al.*, "π^0 identification with EMCAL via shower shape and cluster splitting analysis methods in ALICE", ALICE-ANALYSIS-NOTE-ANA145, (2012).

[306] C. Silvestre "Isolated photon-hadron and neutral pion-hadron correlations with the EMCAL in pp collisions at $\sqrt{s}$=7 TeV in 2011 data", ALICE-ANALYSIS-NOTE-ANA976, (2013).

[307] ALICE Collaboration, "Systematic uncertainties related to track selection and tracking efficiency at ALICE", https://twiki.cern.ch/twiki/bin/viewauth/ALICE/TrackingEfficiencyCharged.

[308] T. Binoth *et al.*, "A full Next to Leading Order study of direct photon pair production in hadronic collisions", Eur. Phys. J. C **16**, 311 (2000).

[309] D. de Florian, R. Sassot and M. Stratmann, "Global analysis of fragmentation functions for pions and kaons and their uncertainties", Phys. Rev. D **75**, 114010 (2007).

[310] D. de Florian, R. Sassot and M. Stratmann, "Global analysis of fragmentation functions for protons and charged hadrons", Phys. Rev. D **76**, 074033 (2007).

[311] N. Arbor (for the ALICE Collaboration), "Isolated photon-hadron correlations in proton-proton collisions at image with the ALICE experiment", Nucl. Phys. **A904**, 697c (2013).

[312] S. Chatrchyan *et al.* (CMS Collaboration), "Measurement of isolated photon production in pp and Pb+Pb collisions at $\sqrt{s_{\rm NN}}$ = 2.76 TeV", Phys. Lett. B **710**, 256 (2012).

[313] M.E. Connors, PhD thesis, "Direct Photon Tagged Jets in 200 GeV Au+Au Collisions at PHENIX", (2011).

[314] M. Wilde *et al.*, "Measurement of direct photons in pp at 7 TeV and in Pb+Pb at 2.76 TeV via Conversions", ALICE-ANALYSIS-Note-ANA-227.

[315] R. Albrecht *et al.* (WA80 Collaboration), "Production of Eta-Mesons in 200 AGeV/c S+S and S+Au Reactions", Phys. Lett. B **361**, 14 (1995). WA80-Collaboration (1995).

[316] P.K. Khandai, P. Shukla, and V. Singh, "Meson spectra and m_T scaling in p+p, d+Au and Au+Au collisions at $\sqrt{s_{\rm NN}}$ = 200 GeV", Phys. Rev. C **84**, 054904 (2011).

Appendix A

Appendix

A.1 Glauber Model

The Glauber Model [30, 31] is used to calculate "geometric" quantities, which are typically expressed as impact parameter (b), number of participating nucleons (N_{part}) and number of binary nucleon-nucleon collisions (N_{coll}). In the model, all calculations of geometric parameters need to start from two most important inputs, nuclear charge density measured from low-energy electron scattering experiments and the energy dependence of the inelastic nucleon-nucleon cross section.

A.1.1 Glauber calculations inputs

Nuclear charge density

The nucleon density is usually parameterized by a Fermi distribution with three parameters:

$$\rho(r) = \rho_0 \frac{1 + \omega(r/R)^2}{1 + \exp(\frac{r-R}{a})} \tag{A.1}$$

where rho_0 corresponds to the nucleon density in the center of the nucleus, R corresponds to the nuclear radius, a to the "skin depth" and ω characterizes deviations from a spherical shape.

Inelastic nucleon-nucleon cross section:

The cross section involves many processes with low momentum transfer, and it is impossible to calculate it by using perturbative QCD. Therefore the inelastic nucleon-nucleon cross section ($\sigma_{\text{inel}}^{\text{NN}}$) need to be measured and is used as an input.

A.1.2 Glauber calculations

Thickness function

The nuclear thickness function of nucleus A is defined as:

$$T_A(\vec{s}) = \int d\rho_A(z, \vec{s}) \tag{A.2}$$

which is the number of nucleons per unit area along the direction z at a point from the center of the nucleus represented by a two-dimensional vector $\vec{s}$, where z is perpendicular to $\vec{s}$.

Overlap function

For a collision between nucleus A and nucleus B, the nuclear overlap function $T_{AB}(\vec{b})$ at impact parameter $\vec{b}$ is defined as:

$$T_{AB}(\vec{b}) = \int d^2s T_A(\vec{s}) T_B(\vec{b} - \vec{s}) \tag{A.3}$$

Number of participating nucleons

$$\begin{aligned} N_{part}(b) &= A \int \widehat{T}_A(s)\{1 - [1 - \widehat{T}_B(b-s)\sigma_{\text{inel}}^{\text{NN}}]^B\} d^2s \\ &\quad + B \int \widehat{T}_B(b-s)\{1 - [1 - \widehat{T}_A(s)\sigma_{\text{inel}}^{\text{NN}}]^A\} d^2s \end{aligned} \tag{A.4}$$

Number of binary nucleon-nucleon collisions

$$N_{coll}(b) = AB\widehat{T}_{AB}(b)\sigma_{\text{inel}}^{\text{NN}} \tag{A.5}$$

A.2 Sub-clusters invariant mass in Cluster Splitting method

Fig. A.1 shows the split sub-cluster invariant mass distributions at different energy intervals in π^0 reconstruction via cluster splitting method in pp collisions at $\sqrt{s} = 2.76$ TeV. Fig. A.2 shows the split sub-cluster invariant mass distributions at different energy intervals in π^0 reconstruction via cluster splitting method in Pb+Pb collisions at $\sqrt{s_{\text{NN}}} = 2.76$ TeV.

A.3 Meson trigger correlations in Side Band method

We assume that Y_S, Y_{S+B} and Y_B are the per-trigger yield of π^0/η, candidateπ^0/η (signal+background), and fake π^0/η, respectively; The ratio of signal to background,

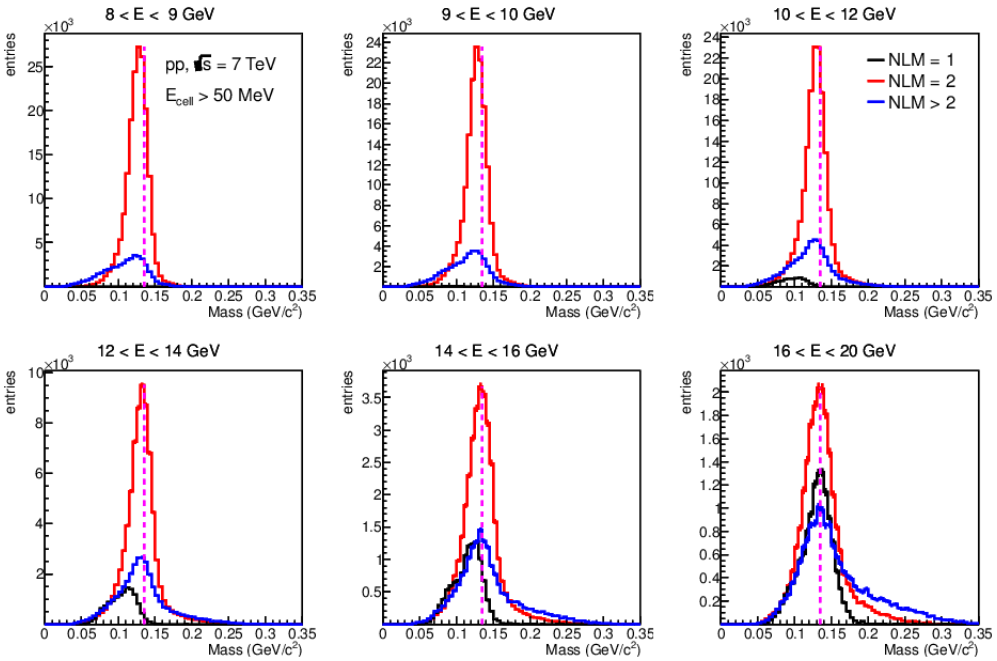

Figure A.1: Mass of split sub-clusters in data of pp collisions at $\sqrt{s} = 2.76$ TeV with EMCal triggered events in 6 cluster energy intervals at $NLM = 1, 2, > 2$, taken from [305].

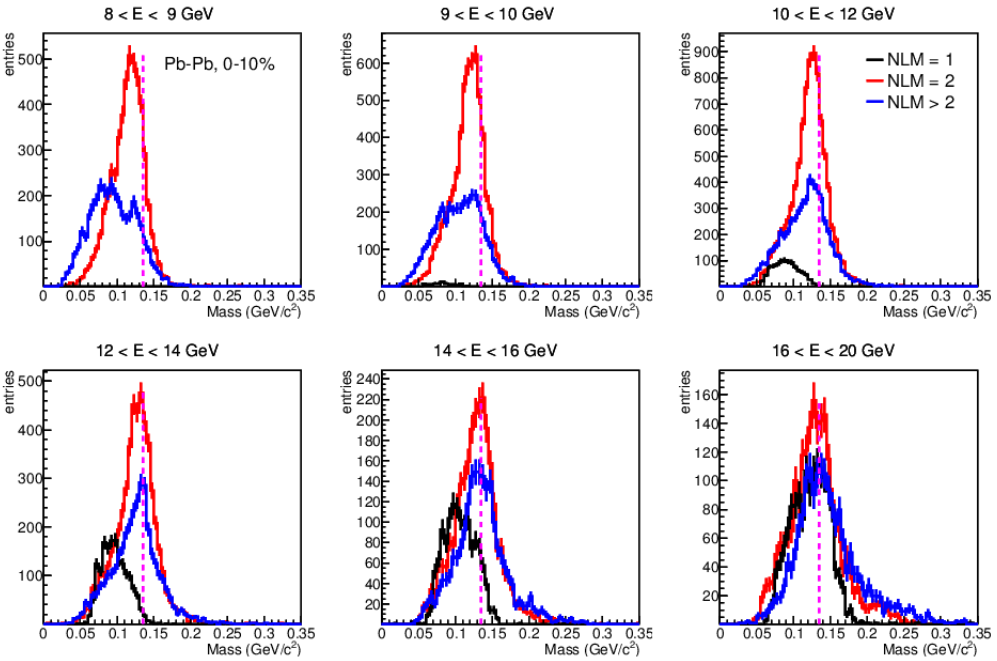

Figure A.2: Mass of split sub-clusters in data of Pb+Pb collisions at $\sqrt{s_{\mathrm{NN}}} = 2.76$ TeV with EMCal triggered events in 6 cluster energy intervals at $NLM = 1, 2, > 2$, taken from [305].

$f_{bkg} = N_S/N_B$, can be obtained from the two clusters invariant mass fitting; N^{ab} and N^a are the number of correlation pairs and triggers, respectively. The relation of the three per-trigger yields is written as

$$\begin{aligned}
Y_S &= \frac{N_S^{ab}}{N_S^a} = \frac{N_{S+B}^{ab} - N_B^{ab}}{N_{S+B}^a - N_B^a} \\
&= \frac{N_{S+B}^{ab} - N_B^{ab}}{f_{bkg} * N_B^a + N_B^a - N_B^a} = \frac{N_{S+B}^{ab} - N_B^{ab}}{f_{bkg} * N_B^a} \\
&= \frac{N_{S+B}^{ab}}{f_{bkg} N_B^a} - Y_B/f_{bkg} \\
&= \frac{Y_{S+B} * N_{S+B}^a}{f_{bkg} * N_B^a} - Y_B/f_{bkg} \\
&= \frac{Y_{S+B} * (N_S^a + N_B^a)}{f_{bkg} * N_B^a} - Y_B/f_{bkg} \\
&= Y_{S+B}\frac{f_{bkg}+1}{f_{bkg}} - Y_B/f_{bkg} \\
Y_S &= Y_{S+B}(1 + \frac{1}{f_{bkg}}) - Y_B/f_{bkg}
\end{aligned} \tag{A.6}$$